

Selective hydrogenation reactions in the synthesis of fragrances

Matthew B. Conway



Thesis submitted in accordance with the requirement of Cardiff University
for the degree of Doctor of Philosophy

School of Chemistry
Cardiff University
2021



Cardiff
Catalysis Institute
Sefydliad Catalysis
Caerdydd



Abstract

The partial reduction of alkyl-substituted indanes to tetrahydroindane products is an intermediate step in the synthesis of musk fragrances. Industrially, this process is performed solventless in a semi-batch reactor at 180 °C under 40 bar hydrogen pressure over a Pd/C catalyst to yield approximately 62–65 wt.% cycloolefins. Demand for downstream products has recently soared, and therefore yield enhancements are desired, which this thesis investigated.

Herein, a study of the effect of temperature and hydrogen pressure on the yield of the desired products was carried out and reaction conditions where a significant improvement in yield can be achieved were identified. This yield enhancement could not be attributed to equilibrium or mass transfer limitations. Rather, it was hypothesised that the greater adsorption strength of aromatics compared to cycloalkenes led to greater changes to surface coverages as temperature increased. Whereas higher hydrogen pressure disfavoured isomerisation reactions that afforded more reactive cycloalkenes, which gave a greater *trans/cis* ratio of saturated products.

The effect of metal (where M = Ru, Rh, Pd, Ir, Pt) on the partial reduction reaction was also studied using carbon-supported catalysts prepared in-house. The ordering of selectivity to cycloalkenes of these catalysts was sensitive to the thermal treatments used in their preparation. Catalysts that were only reduced gave cycloalkene selectivities which decreased in the order of Pd > Pt > Rh > Ir > Ru and calcination of these materials led to the selectivity to cyclic olefins of Rh rising above that of Pt. The metal ordering was ascribed to the differences in the reaction mechanism, whilst the beneficial effect of calcination was not conclusively identified. Lower yields of intermediate were obtained using the in-house Pd/C catalyst compared to the industrial catalyst under all conditions examined. This was attributed to the larger particles present in the in-house catalyst promoting the undesirable isomerisation reaction.

Acknowledgements

My research journey into the fascinating area of heterogeneous catalysis would not be possible if it weren't for the EPSRC-funded Centre for Doctoral Training in Catalysis, for the first year of this programme made this once aspiring main group chemist see the light. This centre is also responsible for providing me with 50% of my funding over the course of my PhD (and the entirety of my first year), so I would like to thank them for this monetary support. The other half of my funding came from International Flavors & Fragrances, who I am very appreciative to for financial support and will be sure to be buy IFF sourced fragrances where possible in the future.

The content presented in this thesis would not be possible without the help and support of many people. I would first like to thank my academic supervisor Professor Graham Hutchings for providing a lab, help, and guidance throughout my PhD. I am also grateful to my industrial supervisor Dr Carlos Lopez Cruz, who offered a very valuable industrial insight into the work and for hosting me for a week in Benicarló, Spain. A huge thank you is also necessary to Dr Mark Douthwaite for the supervision, advice, and prudent proof-reading of this never-ending thesis. I also thank Dr Rebecca Engel for her comprehensive training and help at the start of the project. Dr Thomas Davies is thanked for his assistance in obtaining then microscopy images as is Dr David Morgan for his help with X-ray photoelectron spectroscopy. I would also like to express my appreciation for Dr David Willock and Dr Julian Engel for useful discussions on density-functional theory.

There are also numerous people who have contributed to this work indirectly. I am grateful to the workshop (Mr Steve Morris and Mr Lee Wescombe) for fixing any broken equipment promptly. I also thank Dr Greg Shaw for his continued help and politely dealing with my many bizarre requests. I would also like to extend my gratitude to all CCI members for creating such a wonderful research environment.

Finally, I would like to thank my family, friends, my girlfriend Alex, and my two kitties Heidi and Lily, for their support and understanding over the past few years. Mum, you will be glad to know that my "course" is now over.

Publication list

- [1] R. Adishev, F. Arrigo, A. Baletto, V. Bordet, V. Bukhtiyarov, M. Carosso, R. Catlow, M. Conway, J. Davies, P. Davies, D. De Masi, C. Demirci, J. K. Edwards, C. Friend, S. Gallarati, J. Hargreaves, H. Huang, G. Hutchings, S. Lai, C. Lamberti, M. Macino, D. Marchant, T. Murayama, Y. Odarchenko, J. Peron, L. Prati, J. Quinson, N. Richards, S. Rogers, A. Russell, P. Selvam, P. Shah, M. Shoji, C.K. Skylaris, K. Soulantica, F. Spolaore, B. Tooze, L. Torrente-Murciano, A. Trunschke, B. Venezia, J. Walker, K. Whiston. *Faraday Discuss.*, 2018, **208**, 471–495.
- [2] M. Anand, F. Baletto, A. Bugaev, R. Catlow, M. Claeys, M. Conway, M. Davidson, P. Davies, N. de Leeuw, D. Eremin, N. Fischer, J. Hargreaves, G. Hutchings, J. Iyer, D. Jain, F. Jameel, A. R. Kamali, S. Kondrat, I. Kowalec, P. Kraus, C. Reece, R. Réocreux, D. Santos-Carballal, P. W. Seavill, M. Shoji, M. Sinev, V. Sinha, M. Stamatakis, D. Uner, A. Vojvodic, K. Whiston, D. Willock, M. Wolf, B. Yang, B. Zhu, *Faraday Discuss.*, 2021, **229**, 131–160.
- [3] M. Anand, A. M. Beale, M. Boronat, M. Bowker, A. L. Bugaev, V. I. Bukhtiyarov, C. R. A. Catlow, S. Chansai, M. Claeys, M. Conway, P. R. Davies, J. Edwards, J. El-Kadi, D. Eremin, N. Fischer, S. Guan, J. S. J. Hargreaves, C. Hess, G. J. Hutchings, F. Jameel, A. Reza Kamali, S. Kondrat, N. Lawes, D. Lennon, D. Li, P. Morgan, A. M. Oyarzún Aravena, C. Reece, R. Réocreux, P. W. Seavill, Y. Sekine, M. Shoji, I. Silverwood, M. Sinev, C. Smith, M. Stamatakis, L. Torrente Murciano, D. Uner, B. M. Weckhuysen, K. Whiston, M. Wolf, B. Yang, C. D. Zeinalipour-Yazdi, *Faraday Discuss.*, 2021, **229**, 378–421.
- [4] Ananikov, A. Bugaev, S. Chansai, M. Claeys, M. Conway, D. Eremin, M. Greaves, C. Hess, U. Hintermair, G. Hutchings, F. Jameel, A. R. Kamali, K. Koehler, A. Malkov, P. Morgan, A. M. Oyarzún Aravena, P. W. Seavill, M. Sinev, L. Torrente Murciano, D. Uner, K. Whiston, C. K. Williams, M. Wolf, *Faraday Discuss.*, 2021, **229**, 489–501.
- [5] K. Armstrong, S. Barbarino, X. E. Cao, F. Cassiola, R. A. Catlow, M. Claeys, M. Conway, A. J. Cowan, N. H. de Leeuw, G. R. M. Dowson, N. Fischer, A. Ghaderian, S. Ghosh, A. R. Kamali, S. Khan, S. Kyrimis, N. Lawes, W. Leitner, M. Maneiro, H. Manyar, W. Marquart, S. McCord, E. Moore, M. North, U. Olsbye, D. Pant, J. Poon, M. G. Quesne, M. Ranocchiari, L. Rossi, J. Ruiz Esquiús, M. Shoji, V. Sick, P. Styring, J. Tan, S. E. Tanzer, O. Thomas, K. Whiston, M. Wolf, *Faraday Discuss.*, 2021, **230**, 124–151.

Contents

| | | |
|----------|--|-----------|
| 1 | Introduction | 1 |
| 1.1 | Fragrances | 1 |
| 1.2 | Tetrahydropentamethyl indane: an important intermediate in the synthesis of fragrances | 4 |
| 1.2.1 | Overview | 4 |
| 1.2.2 | The industrial-scale synthesis of penthamethyl indane | 5 |
| 1.2.3 | The partial hydrogenation of pentamethyl indane to tetrahydropentamethyl indane | 6 |
| 1.3 | Products obtained from pentamethyl indane | 12 |
| 1.3.1 | Cashmeran | 12 |
| 1.3.2 | Further products from the Cashmeran process | 13 |
| 1.4 | The hydrogenation of aromatic compounds and cycloalkenes | 16 |
| 1.4.1 | Kinetic and mechanistic considerations | 16 |
| 1.4.2 | The partial hydrogenation of aromatic compounds | 32 |
| 1.4.3 | The partial reduction of alkyl-substituted benzenes | 32 |
| 1.5 | Summary | 41 |
| 1.6 | Thesis aims | 41 |
| 1.7 | References | 41 |
| 2 | Experimental | 59 |
| 2.1 | Materials | 59 |
| 2.2 | Catalyst preparation | 60 |
| 2.2.1 | Carbon-supported catalysts preparation | 60 |
| 2.3 | Reactions | 61 |
| 2.3.1 | Hydrogenation reactions of aromatics | 61 |
| 2.3.2 | Isomerisation reactions | 62 |
| 2.4 | Solution characterisation methods | 62 |
| 2.4.1 | Gas chromatography | 62 |
| 2.4.2 | Nuclear magnetic resonance spectroscopy | 65 |
| 2.4.3 | Viscosity | 67 |

| | | |
|----------|---|------------|
| 2.4.4 | Density-functional theory | 69 |
| 2.5 | Catalyst characterisation techniques | 70 |
| 2.5.1 | Microwave plasma and inductively-coupled plasma atomic emission spectroscopy | 70 |
| 2.5.2 | Thermal-analytical techniques | 72 |
| 2.5.3 | X-ray characterisation | 77 |
| 2.5.4 | Textural property analysis | 83 |
| 2.5.5 | Particle size and dispersion measurements | 90 |
| 2.5.6 | Volume and density measurements | 102 |
| 2.6 | References | 103 |
| 3 | The characterisation of galaxolide hydrocarbon and the typical industrial product mixture | 113 |
| 3.1 | Introduction | 113 |
| 3.2 | Aims | 114 |
| 3.3 | Results and discussion | 114 |
| 3.3.1 | GC analysis | 114 |
| 3.3.2 | NMR analysis | 120 |
| 3.3.3 | Density measurements | 121 |
| 3.3.4 | Viscosity measurements | 125 |
| 3.3.5 | Hydrogen solubility measurements | 130 |
| 3.4 | Conclusions | 131 |
| 3.5 | References | 131 |
| 4 | The effect of some process variables in the partial reduction of galaxolide hydrocarbon to cyclic alkene intermediates | 135 |
| 4.1 | Introduction | 135 |
| 4.2 | Aims | 137 |
| 4.3 | Results and discussion | 137 |
| 4.3.1 | Characterisation of the fresh industrial Pd/C catalyst | 137 |
| 4.3.2 | Process alignment | 143 |
| 4.3.3 | Effect of temperature and pressure | 148 |
| 4.3.4 | Apparent activation energies and compensation | 180 |
| 4.4 | Conclusions | 182 |
| 4.5 | References | 182 |
| 5 | The effect of metal (M = Ru, Rh, Pd, Ir, Pt) on the partial reduction of galax- olide hydrocarbon to cyclic alkenes | 189 |
| 5.1 | Introduction | 189 |
| 5.2 | Aims | 191 |

| | | |
|----------|---|------------|
| 5.3 | Results and Discussion | 191 |
| 5.3.1 | Catalyst characterisation | 191 |
| 5.3.2 | Kinetic data | 199 |
| 5.3.3 | Performance in the partial reduction reaction | 204 |
| 5.4 | Conclusions | 222 |
| 5.5 | References | 223 |
| 6 | Conclusions and future work | 229 |
| 6.1 | Introduction | 229 |
| 6.2 | Conclusions and future work relating to work presented in this thesis | 229 |
| 6.2.1 | Chapter 3: The characterisation of galaxolide hydrocarbon and an industrial product mixture | 229 |
| 6.2.2 | Chapter 4: The effect of some process variables in the partial reduction of galaxolide hydrocarbon to cyclic alkene intermediates | 233 |
| 6.2.3 | Chapter 5: The effect of metal in the partial reduction of galaxolide hydrocarbon to cycloalkene intermediates | 237 |
| 6.3 | Final comments | 241 |
| 6.4 | References | 243 |

Chapter 1

Introduction

1.1 Fragrances

SÜSKIND'S *Perfume* tells the tale of maestro *le nez* Jean-Baptiste Grenouille. His *raison d'être* is to create “*an angel's scent, so indescribably good and vital that whoever smelled it would be enchanted and with his whole heart would have to love him*”. Although fictitious, this tale is not too far away from reality. In 1995, a study asked a group of women to smell the unwashed t-shirt of several anonymous men, untainted with any scent but their own, and rate the intensity, pleasantness, and attractiveness of the t-shirts.¹ Unfortunately for Grenouille, there was no clear winner as women preferred men whose genetic makeup was most different than their own. It does however highlight the intimate relationship humans share with fragrance.

Indeed, the modern world exploits this fact—with almost every part of the modern human existence being scented, or it is at least where it is possible and profitable. There are obvious examples, such as scented laundry detergents and shower gels, with unperfumed equivalents carrying a premium price, to less obvious examples like seasonings for plant-based burgers.² Fragrances even find application in the medical field as shown during the ongoing covid-19 pandemic. As a subjective change in the sense of smell/taste are considered symptoms of infection, a team of researchers at Massachusetts General Hospital and International Flavors & Fragrances (IFF) developed a self-administered smell test in an attempt to detect the disease.³

With such widespread application, it leads to the question: what is the source of these compounds? For millennia, fragrances were obtained by distillation of plants to form “essential oils” that are still popular today. The development of organic chemistry in the late 1800s allowed for the large-scale production of compounds that could be used in fragrances, and most importantly this brought the cost down significantly. The birth of the modern fragrances industry arguably occurred with the release of Channel No 5., one of the first perfumes to contain fully synthetic aliphatic aldehydes. These synthetic compounds were cheaper to produce than their synthesised natural analogues and afforded other advantages:

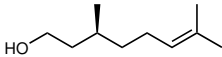
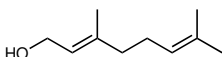
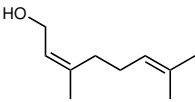
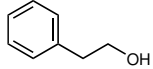
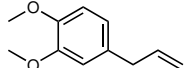
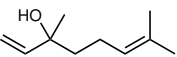
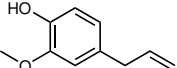
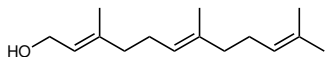
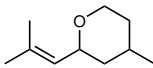
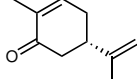
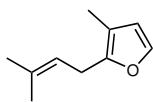
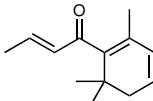
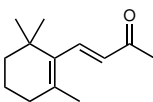
more chemically robust molecules could be envisaged—so that they could be included in, for example, highly oxidising media such as bleach—and entirely artificial scents could now be created. The profound impact synthetic compounds have had on the industry can be counted. A modern perfumer has easy access to more than 3,000 synthetic compounds and just several hundred natural fragrance ingredients.⁴

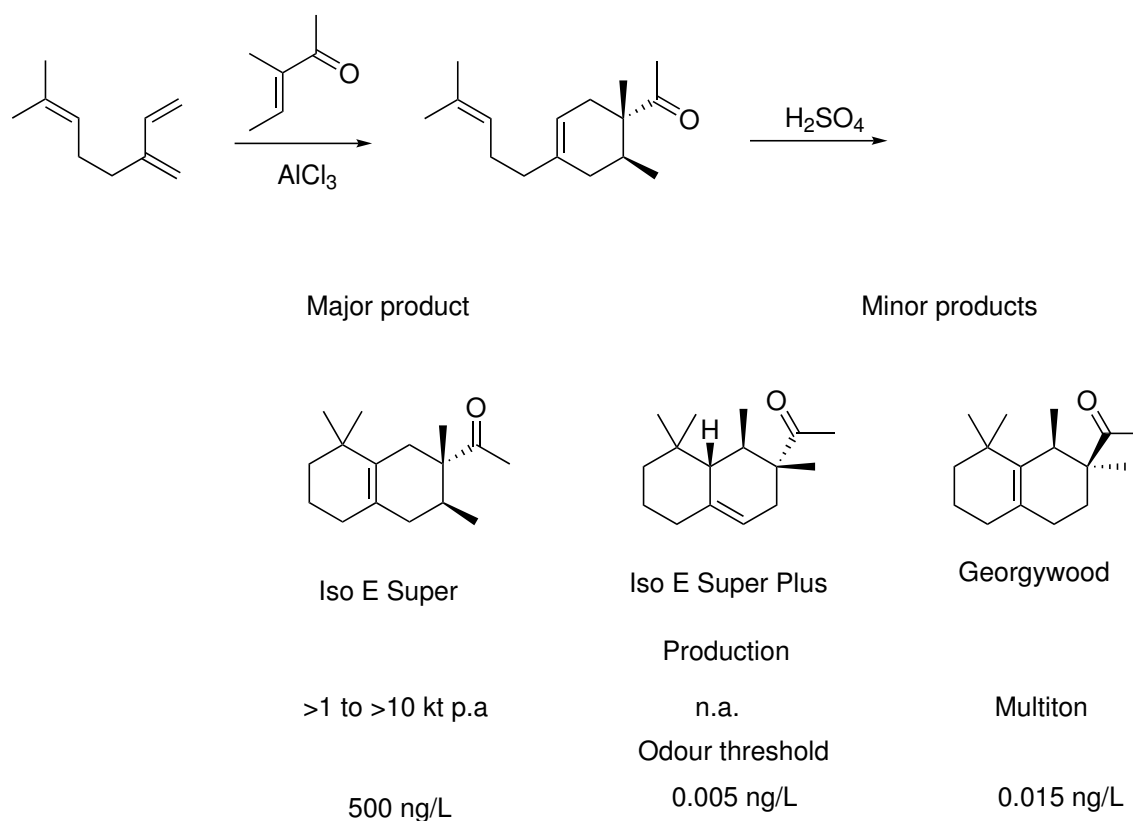
Consequently, one may wonder why natural fragrances are still used when so many cheaper synthetic compounds are available that can be tailored for a specific use. Take the example of Bulgarian rose oil, a widely used essential oil in the fragrances industry which costs thousands of dollars per kilogram of oil. Just nine compounds, which can be synthesised in bulk for a relatively low price, are present in quantities higher than 1% (Table 1.1). However, if this oil is produced its odour is vastly dissimilar to rose oil; it is the minor components that form only 1.2% of the oil that possess half the odour value of all the major components. So while in a toilet cleaner the fine distinctions between these two mixtures is irrelevant, when spritzing a costly perfume on the wrist or neck it may.

The minor component problem is not unique to fragrances of natural origin. At several stages of the production process encroachment of impurities is possible, whether that be from contamination from a reactor or through the formation of side- or by-products from the reaction itself. A particular good example of the latter point relates to IFF product, Iso E Super, a popular fragrant compound first marketed in the late 1970s. Its cheap and easy synthesis (Scheme 1.1) allows for widespread application in the industry. To IFF's misfortune, GC-olfactometry performed by rival Givaudan revealed that the major product of the synthesis is not the primary odourant, but a side product that constitutes only 5% of the product mixture.^{6,7} Givaudan subsequently developed and patented a synthesis of this compound, referred to internally as Iso E Super Plus,⁷⁻⁹ but large scale synthesis of this compound is still not commercially viable.¹⁰ They also secured a patent for the synthesis of a second impurity in the synthesis, trade name Georgywood, which has preferential olfactory characteristics and is now produced at the multi-ton scale.¹¹

There are clearly many areas of improvement to be made during the synthesis of fragrant compounds. These may come from developments in synthetic methodology or will come from the focus of this thesis: the study of catalytic technologies. This section has served to provide some context for the unique nature of the fragrances industry and the challenges it faces. The remainder of this chapter will provide an introduction into the industrial processes relevant to this thesis before providing a literature review on the relevant areas of chemistry, providing insight before any experimental results are discussed.

Table 1.1: Odour contributions and structures of 14 of the 275 constituents of Bulgarian rose oil. Table and caption adapted from [5].

| Compound | Structure | Concentration (wt.%) | Odour contribution (%) |
|-------------------------|---|----------------------|------------------------|
| (-)-Citronellol |  | 38 | 62 |
| Paraffins |  | 16 | 0 |
| Geraniol |  | 14 | 1.2 |
| Nerol |  | 7 | 0.15 |
| β -Phenyl ethanol |  | 2.8 | 0.024 |
| Methyl eugenol |  | 2.4 | 0.019 |
| Linalool |  | 1.4 | 1.5 |
| Eugenol |  | 1.2 | 0.26 |
| Farnesol |  | 1.2 | 0.39 |
| (-)-Rose oxide |  | 0.46 | 6 |
| (-)-Carvone |  | 0.41 | 0.05 |
| Rosefuran |  | 0.16 | 0.005 |
| β -Damascone |  | 0.14 | 0.09 |
| β -Ionone |  | 0.03 | 28 |



Scheme 1.1: Structures of Iso E Super, Iso E Super Plus, and Georgywood. Odour threshold values taken from [12] and production scale values for Iso E Super taken from [13]. The estimate for Georgywood taken from [11] as tonnage data considered “confidential” on REACH database.¹⁴

1.2 Tetrahydropentamethyl indane: an important intermediate in the synthesis of fragrances

1.2.1 Overview

Tetrahydropentamethylindane (THPMI) is an important intermediate in the synthesis of seven compounds (Figure 1.1) that are widely used in fragrance applications and is produced in the thousands of tonnes per year. It is prepared by the partial reduction of pentamethyl indane (1,1,2,3,3,-pentamethylindane, PMI) at 180 °C under 40 bar hydrogen pressure over a Pd/C catalyst. The discovery of fragrant compounds from THPMI came when researchers at IFF were investigating transformations of low cost indanes, which had recently been used to synthesise what is now the most widely used musk agent in the world, Galaxolide (Scheme 1.2),¹⁵ in the late 1960s. One product identified in these experiments was Cashmeran, the allylic ketone of THPMI. Cashmeran is now one of IFF’s flagship products and is the end product for most of the THPMI produced. More details on the Cashmeran process are outlined in Section 1.3.1. This section will discuss the production of THPMI, starting with chemicals widely available in the petrochemical industry.

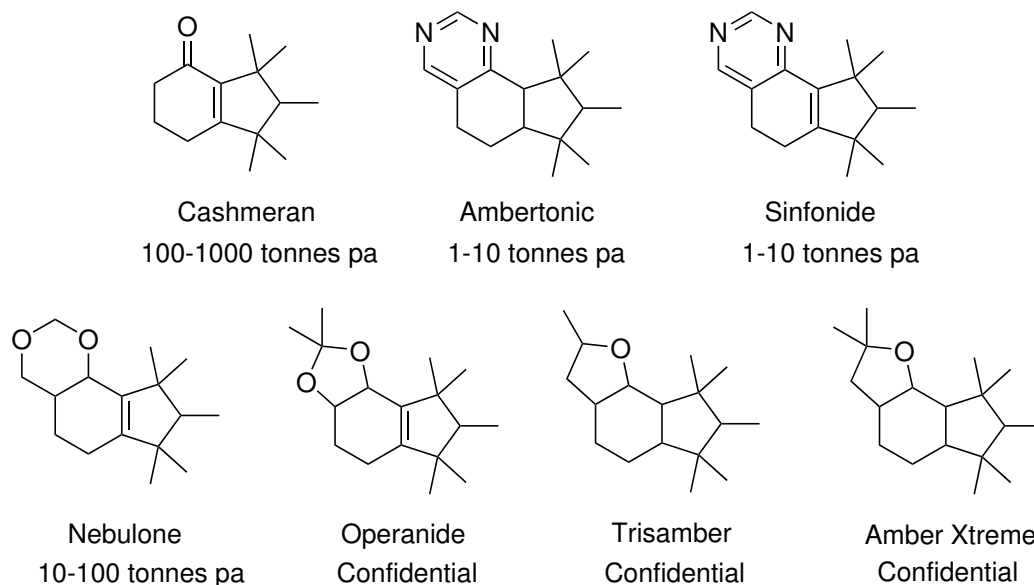
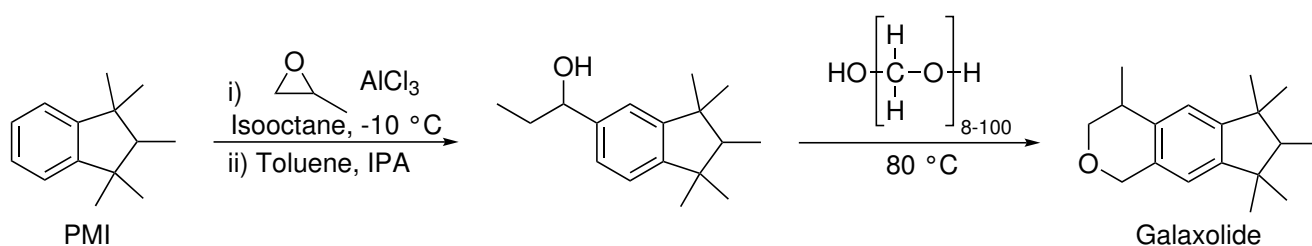


Figure 1.1: Commercially used fragrant compounds which are synthesised from THPMI. Tonnage data taken from European Chemicals Agency: Cashmeran,¹⁶ Sinfonide,¹⁷ Ambertonic,¹⁸ Nebulone,¹⁹ Operanide,²⁰ Trisamber,²¹ Amber Xtreme.²²

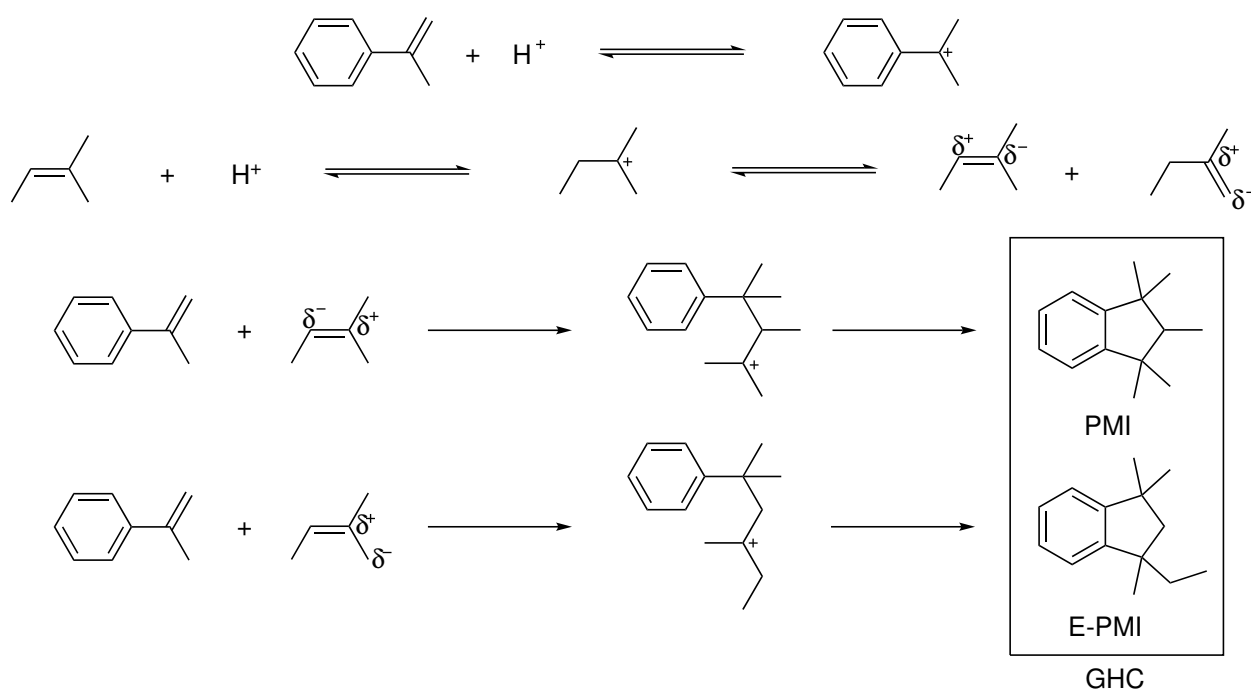


Scheme 1.2: The industrial synthesis of Galaxolide.

1.2.2 The industrial-scale synthesis of penthamethyl indane

Pentamethylindane is accessible through a variety of synthetic strategies. The most popular method is the acid catalysed cycloaddition reaction between α -methylstyrene and amylene at elevated room temperature. Acid catalysts for this reaction may include 70% sulfuric acid,²³ mixtures of concentrated sulfuric acid and acetic acid,^{24,25} phosphoric acid,²⁶ Amerbylst-15,²⁷ zeolite H-Y-mmm,²⁸ or a mixture of mineral acid, metal oxide (CeO_2 , Na_2MoO_4 , Na_2WO_4 or a combination thereof), and sulfolane.^{29,30} Currently, IFF use the first mentioned process to obtain a PMI yield of approximately 60%.²³ Other synthesis methods utilise Friedel-Crafts alkylation, either between cumyl chloride and amylene,³¹ or benzene and mesityloxide followed by Grignard reaction and cyclisation,³² or the cycloaddition of α -methylstyrene and t-amyl alcohol,³³ but fewer variations of these strategies have been patented. These reactions are typically performed in a batch or semi-batch reactor, but workers at IFF have recently demonstrated improved PMI yields in a flow microreactor.³⁴

The reaction mechanism for the reaction between α -methylstyrene and amylene is displayed in Scheme 1.3. It will be noted that two products, PMI and 1-ethyl-1,3,3-trimethylindane

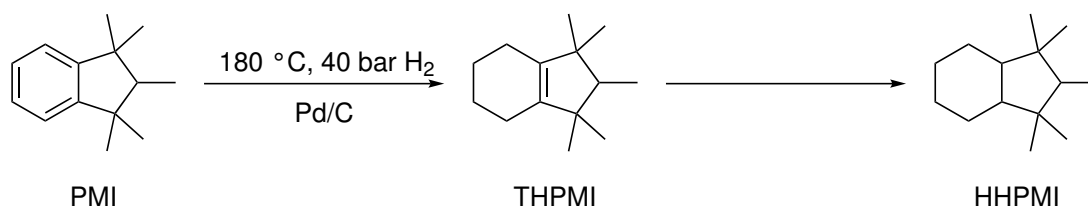


Scheme 1.3: Mechanism for the cycloaddition reaction.

(E-PMI), form during the reaction. Spoelstra *et al.*²⁵ reported the ratio of PMI to E-PMI is approximately 2 to 1 and independent of whether amylene or 2-methyl-1-butene were used and the catalyst ($\text{BF}_3 \cdot \text{Et}_2\text{O}$ or sulfuric acid/acetic acid mixture) employed. If other catalysts improve the selectivity to PMI, which is more thermodynamically stable,³⁴ is not known as these two products are treated as one and thus selectivities are not reported. Industrially, this mixture is referred to as galaxolide hydrocarbon, hereon listed as GHC, and contains approximately 92% PMI and 8% E-PMI.

1.2.3 The partial hydrogenation of pentamethyl indane to tetrahydropentamethyl indane

If the desired end product relates to Cashmeran, the GHC produced in the last step is reduced to form the corresponding alkyl-substituted cycloalkenes (Scheme 1.4). The THPMI used in the discovery of Cashmeran was probably synthesised using lithium reduction methods reported in the same era to obtain 1,2-di-*tert*-butyl-cyclohexene.³⁵ After the initial Birch reduction (described for PMI in other patents³⁶) to form a diene, a selective hydrogenation using Rh/C and molecular hydrogen furnished the cycloalkene in high yield. Performing a Birch reduction at the scale that would be required is not possible because it requires the use of condensed ammonia or volatile amines and a pyrophoric alkali metal at a cryogenic temperature.³⁷ Pfizer utilise this reaction to produce 1 kilogram of product and face considerable reaction engineering difficulties in doing so.³⁸ A more scalable method recently developed performs this reaction electrochemically,³⁹ but this still is probably limited to small scale synthesis of



Scheme 1.4: The partial reduction of PMI to THPMI under industrial conditions.

higher value pharmaceuticals and was, of course, not available 60 years ago. Therefore, an industrially viable process had to be developed.

Catalytic hydrogenation has been widely used in the chemical industry for a long time and in the 1960s a popular catalyst for this type of reaction was Raney nickel.⁴⁰ The hydrogenation of GHC to THPMI was initially performed in a batch reactor where the optimum conditions were found to be between 150–190 °C and 60–130 bar hydrogen pressure, which provided a THPMI yield of around 25%.⁴¹ This low yield coupled with the relatively high weight loadings of catalyst (approximately 5%) meant there was significant room for improvement. In the early 1990s, Raney nickel was replaced by a carbon-supported palladium catalyst and the yield of the process increased to approximately 63 wt.% THPMI under more mild conditions (100–150 °C and 30–70 bar hydrogen pressure).⁴² The current process employs a higher temperature of 170–180 °C and a hydrogen pressure of 40 bar to improve throughput, and early data shared by IFF indicated that the final yield is largely independent of pressure and temperature.⁴³ Moreover, further increases in pressure are not possible due to safety limits with the current industrial reactors. Regardless of catalyst used, GHC conversion is limited to around 90% conversion as above this level the yield of intermediate tetrahydroindanes (THI) begins to rapidly decrease (Figure 1.2). The major side-product of this reaction is the fully saturated compounds, hexahydropentamethylindane and hexahydrotrimethylethylindanes (HHPMI), which constitute ~25–60 wt.% of the post-reaction solution. This is undesirable as HHPMI cannot be readily functionalised for products required downstream and thus, it is converted back to GHC to minimise waste.

Owing to the economic importance of this process to IFF, they have sought to improve this partial reduction step in several ways that do not appear to have been deployed in industrial plants at this time. A recent IFF patent disclosed the development of circular economy methods comprised of flow hydrogenation and dehydrogenation processes.⁴⁴ The setup of this fixed-bed reactor is outlined in Figure 1.3. Briefly, GHC flows through the first reactor containing a Pd/C catalyst at a hydrogen pressure between 40–80 bar and temperature between 165–185 °C. This stream elutes into a distillation column that separates HHPMI from GHC and THI. The saturated compound is then fed into flow reactor 2 to be dehydrogenated in a stream of nitrogen to GHC at ~70% yield using a Pd/C catalyst at temperatures >300 °C. The GHC produced can then be recycled into the first reactor. Interestingly, HHPMI dehydrogenation can produce a 26% THI selectively at 10% conversion over a Pd–Ag/SiO₂ catalyst. Such low

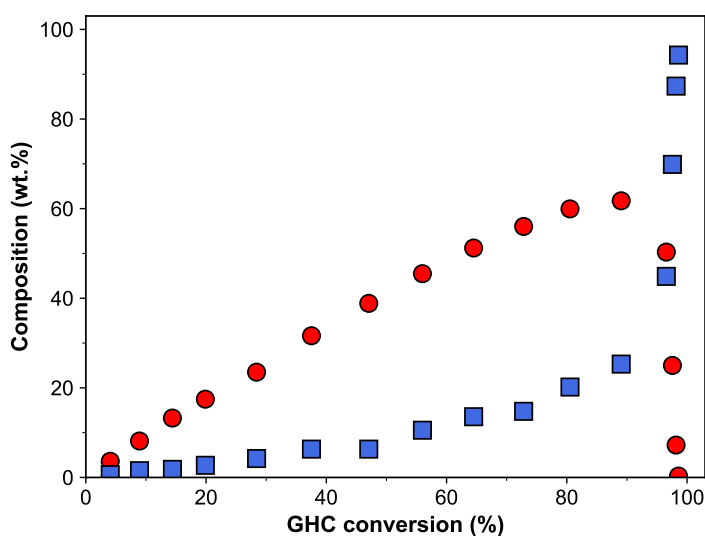


Figure 1.2: A composition *versus* conversion for the industrial scale reduction of GHC to THPMI and E-THPMI (■), and saturated products (■). Data taken from reference [43].

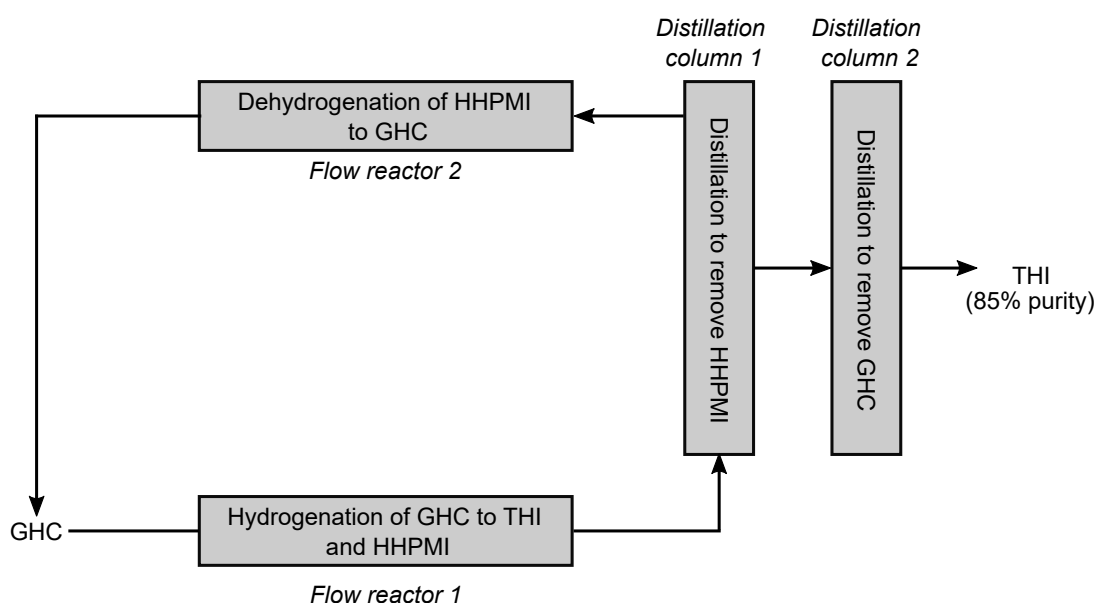


Figure 1.3: A process scheme for the circular economy method of producing THPMI. Figure adapted from [44].

THI yields are less economically favourable, though academically interesting, compared to the recycling of GHC. It is therefore not ready to be used at plant scale without significant improvements. Returning to the distillates from the initial separation, THI and GHC remain unseparated and are flowed into a second distillation column. The stream that leaves this column contains THI at 85% purity and the GHC distillate is returned to the start of the process.

The most recent patent application by IFF discloses information relating to the effect of various treatments and the addition of alkali/silver salts at a hydrogen pressure of 45 bar and temperature between 180–200 °C on THPMI selectivity.⁴⁵ Experimentally, this work differed

from industrial operation as a 33 wt.% PMI in decalin mixture was used *in lieu* of solventless operation. In all instances, the catalysts were prepared by incipient wetness impregnation with no activation step performed in most cases. Initially, a series of 5 wt.% palladium catalysts, supported on silica, alumina, titania, silica alumina, and carbon, were prepared and assessed for their activity; no selectivity was provided for this series. The Pd/C catalyst was found to be most active and used for further study. No characterisation data was provided, but the higher activity may be attributable to a higher palladium dispersion.

A possible promotional effect of acid washing the carbon support was also reported.⁴⁵ However, the authors did not perform the acid wash step themselves and instead purchased the material from the same manufacturer. Activated carbons are incredibly complex materials that are usually prepared by treating high carbon content raw materials, such as coal, wood, and agricultural waste (e.g. coconut shells, rice husk) at high temperatures or with chemically harsh reagents.⁴⁶ The end product is therefore subject to differences, even if the same precursor is used. Moreover, the two activated carbons used in the patent, Norit SX-1G and Norit SX2, are both described by the manufacturer as “acid washed, steam activated” carbons,⁴⁷ indicating both materials have been acid treated, so the effect may not be solely due to an acid treatment.

In addition, calcination of the support pre- or post- palladium deposition were shown to have an effect on activity and selectivity.⁴⁵ A catalyst prepared from calcined carbon was more selective than one that was not (Figure 1.4). Moreover, a second calcination step after palladium impregnation resulted in an even more selective catalyst, albeit with a lower activity. Rationalising the promotional effect of a calcination step on yield is not straightforward without characterisation data. Activation of activated carbons can be conducted by various methods. For example, the carbon used in this work is probably thermally activated, and said materials are prepared in two steps: (i) carbonisation of a carbon source (in this instance peat); (ii) pyrolysis of the product of the previous step in an oxidising atmosphere of air, steam, or carbon dioxide (steam for this carbon) between 500–1000 °C (temperature not known for Norit SX2). An acid wash is performed after this step to remove ash but low levels may remain. Therefore, the main effect of a calcination step may be attributable to the removal of phosphorous, sulfurous, or chlorine-containing compounds in the ash content^{48–50} or “amorphous carbon residue”^{51,52} that may negatively affect the catalyst performance. The lower activity of the catalyst calcined after deposition may be attributable to nanoparticle sintering under the conditions used. Lastly, the calcination effect is probably not attributable to a change in the pore structure as academic studies only note minor increments in pore volume and diameter at these temperatures.^{53,54}

The reaction temperature also appears to influence THI yield. Increasing the reaction temperature from 180 to 200 °C results in a 2% increment in intermediate yield. The role of temperature in the reduction of arenes is discussed at length in the Section 1.4.1.2, but briefly, it is possible that this increase in temperature promotes desorption of the intermediate (an endothermic process) or promotes a reaction pathway with a higher activation energy.

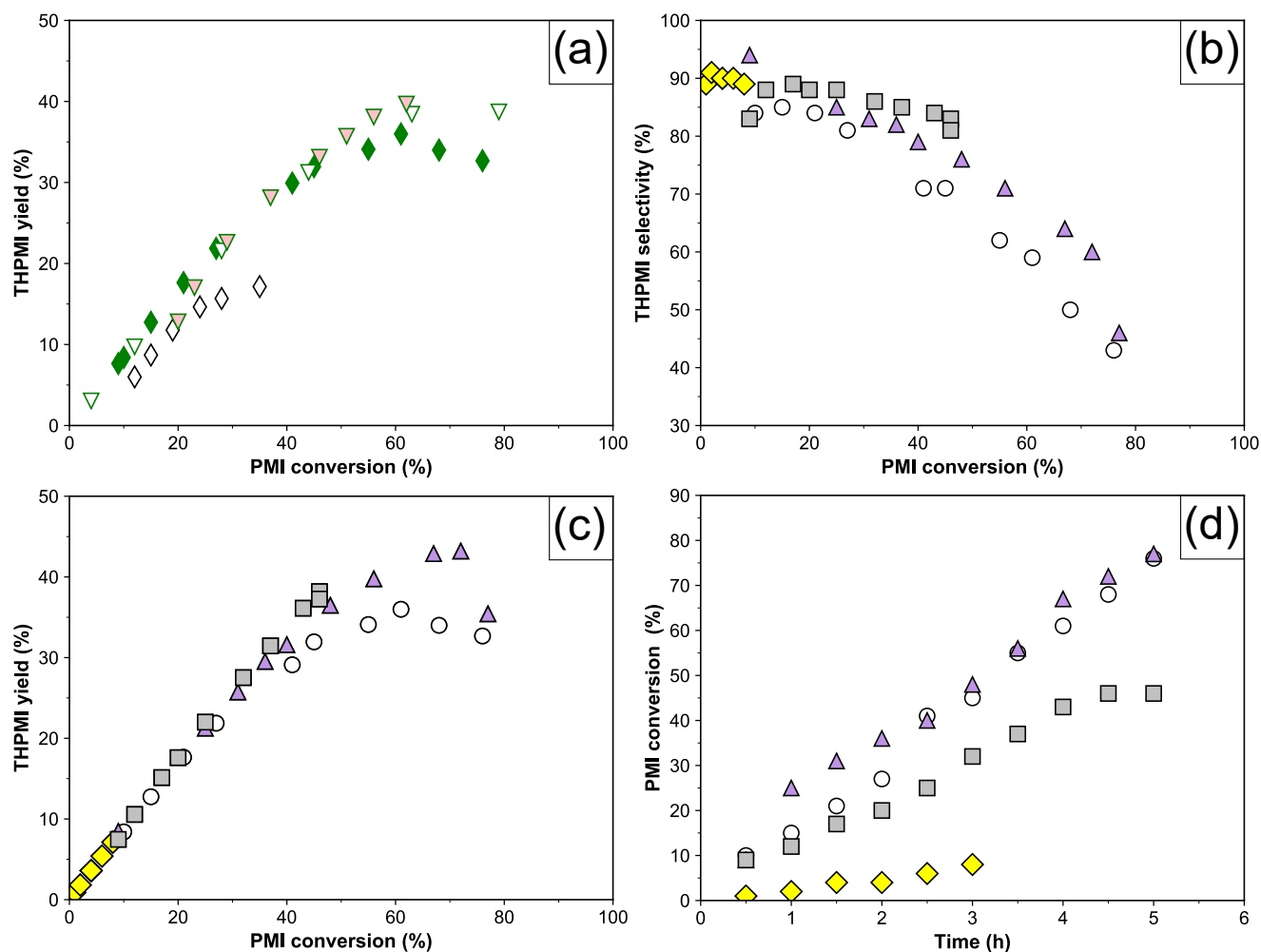


Figure 1.4: A summary of examples from a recent IFF patent using a 33 wt.% solution of PMI in decalin. **(a)** Effect of calcination on THPMI yield. Pd/(C not calcined) (\diamond) and Pd/(C calcined) (\blacklozenge) tested at 180 °C and 45 bar hydrogen. Pd/(Calcined C) (∇) and Calcined Pd/(Calcined C) (\blacktriangledown) tested at 200 °C and 45 bar hydrogen. **(b, c)** THPMI selectivity and yield of mono- and bimetallic catalysts supported on calcined carbon as function of conversion. **(d)** Activity of mono- and bimetallic calcined carbon-supported catalysts as a function of time. **(b–d)** tested at 180 °C and 45 bar hydrogen. Pd (\square) Pd-Na (\blacklozenge) Pd-K (\blacktriangle) Pd-Ag (\square).

The final part of this patent application disclosed the performance of 5 wt.% palladium-based bimetallic catalysts prepared by co-impregnation of the nitrate salts. The second metals were sodium, potassium and silver in molar ratios of 3, 6, and 6 to 1, respectively. Bimetallic catalysts are complex materials as the possible mixing and intimacy of the two components is dependent on the preparation method and consequently can result in various structures (Figure 1.5). Nevertheless, it is possible to discuss some literature examples of similar systems.

With the alkali metal promoters, the initial selectivity of these catalysts to THPMI was higher compared to the monometallic palladium catalyst. The effect of sodium addition on the rate was, however, detrimental. Meanwhile, potassium addition was reported to have a negligible effect on activity, and this catalyst provided a higher maximum yield of

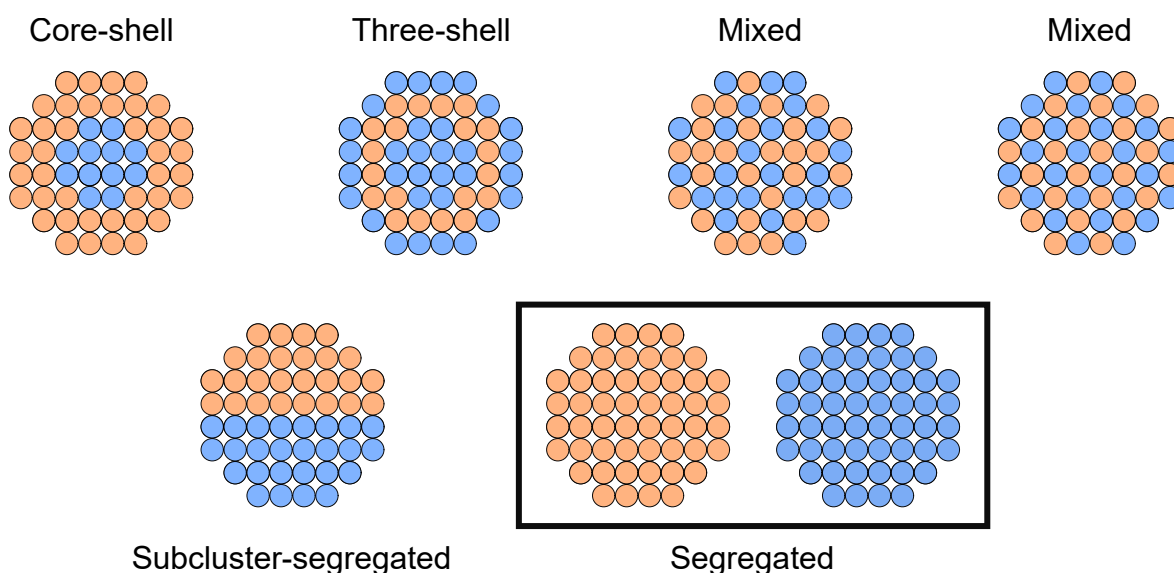


Figure 1.5: Schematic representation of possible bimetallic mixing patterns. Adapted from reference [55].

THPMI than the palladium on carbon catalyst. The use of alkali metals as promoters in hydrogenation reactions have been widely investigated, but to the extent of my knowledge, there are no reports of palladium-alkali metal catalysts for the reduction of benzene or other aromatic hydrocarbons. For example, Martin and co-workers discovered that doping 2.7 wt.% potassium in a 24.8 wt.% nickel on silica catalyst permitted trace amounts of cyclohexene to form in a system where it is not typically observed as a product.⁵⁶ They attributed this to electronic modification of nickel resulting in a weakening of the metal-adsorbate interaction. A similar explanation was put forward by Ronchin and Toniolo whilst studying the effect of hydroxide precipitating agent for ruthenium catalysts for use in the partial hydrogenation of benzene.⁵⁷⁻⁵⁹ Unfortunately, these workers work did not quantify the residual alkali metal content nor perform a comparison with a hydroxide free of group I or II elements such as ammonium hydroxide. The use of an alkali in the partial reduction of benzene appears to depend on whether it was used in the synthesis step as Struijk *et al.*⁶⁰ found no promotional effect when caesium chloride was added to the liquid phase.

The palladium-silver catalyst displayed a higher initial selectivity to the desired product than the monometallic palladium catalyst. However, the selectivity of this catalyst to THPMI at a higher conversion was not reported inside the patent. A possible cause of this absence is the decreasing activity of the catalyst over time and the seeming inactivity after 4 hours. Palladium catalysts alloyed with group 11 elements have been tested for benzene hydrogenation.⁶¹⁻⁶⁴ A rapid decrease in catalytic activity is observed as the relative coinage metal content increased in all studies. For instance, Leon and Vannice found that introduction of 1.07 wt.% copper in a 2.48% palladium on silica catalyst caused a near eight-fold decrease in the specific rate and six-fold decrease in turnover frequency based on surface palladium atoms.⁶⁴ They attributed the lower rate to be of geometric rather than electronic origin as analysis revealed an ensemble of three palladium atoms is needed to form an active site. Thus, the declining activity as a

function of time may be attributable to the evolution of the palladium-silver structure as the reaction proceeds. In other reactions where the addition of silver to palladium is beneficial, such as acetylene hydrogenation, silver is postulated, *inter alia*, to break up active ensembles, which changes the nature of surface and subsurface hydrogen species, or poisons specific sites.⁶⁵

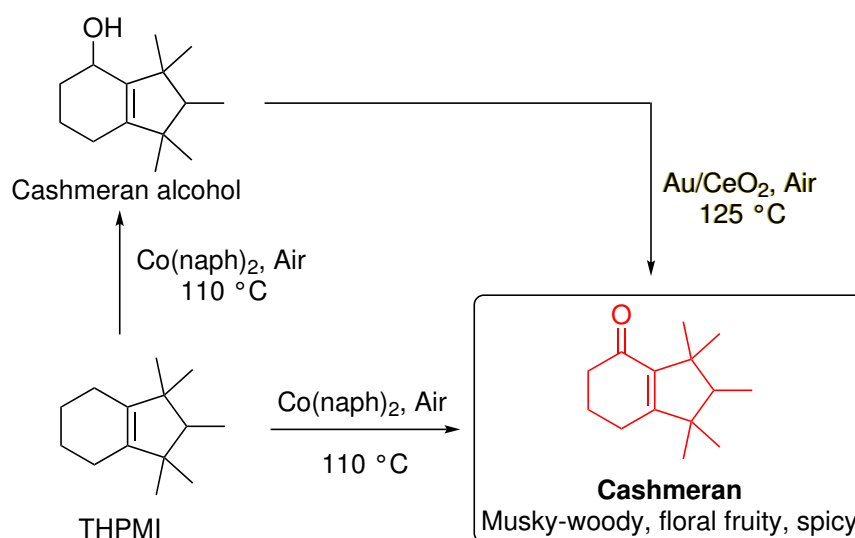
1.3 Products obtained from pentamethyl indane

1.3.1 Cashmeran

Cashmeran is a fragrant product manufactured at the kilotonne scale each year.¹⁶ Its unique olfactory properties have led to a surge in popularity in recent years,^{66,67} and therefore, improving the efficiency of the current manufacturing process is of utmost importance for IFF. There are many direct applications for Cashmeran, such as fine fragrances, personal care, fabric care, and home care. On account of its cost, the amount of Cashmeran found in perfumes rarely exceeds several per cent, though levels of 25% were used in *Dans Tes Bras* (Frédéric Malle, 2008) and *Duro* (Nasomatto, 2007).⁶⁷ The scent of Cashmeran is known to be complex, as its odour profile lies between that of woody and musky odourants. IFF themselves classify the compound as woody and amber, whilst their full olfactory description is *Diffusive, spicy, animalic odor with strong floral reinforcement. Powdery, velvet nuance. Long lasting. Aromatic, apple, earthy, amber woody, red fruit, pine [sic]*. This combination of odours is said to invoke the tactile sensation of touching cashmere which led to its name.

1.3.1.1 The Cashmeran process

Cashmeran was initially prepared by treating purified THPMI with superstoichiometric quantities of potassium dichromate in acetic acid at 100 °C in a batch reactor. In addition to Cashmeran, epoxy-Cashmeran was formed as a minor product and gave an overall product yield of around 94%.³⁶ This process was rapidly replaced with a new process that is still in use today.⁶⁸ The slurry obtained from the reduction of GHC is filtered and without further treatment, transferred to a separate batch reactor equipped with a gas addition tube. Cobalt naphthenate, an oxidation catalyst, is added and the reactor is heated to around 110 °C. A flow of air is then introduced to begin the reaction.^{68,69} The role of the catalyst for this reaction is to promote the selective oxidation pathway by controlling the decomposition of the hydroperoxide.⁶⁹ However, this decomposition leads to two oxidation products, *viz.*, Cashmeran and Cashmeran alcohol in approximately a 2 to 1 ratio. Selectivity to the epoxide in this process is low (*ca.* 2.5%), possibly due to the high reactivity of epoxides.⁶⁹ The allylic alcohol does not have the same olfactory properties as Cashmeran and requires oxidation to the ketone. A recently developed process selectively converts the alcohol to the ketone with 97–98% selectivity at high conversions using a Au/CeO₂ catalyst and air using the neat solution from



Scheme 1.5: The current industrial-scale synthesis of Cashmeran. For the $\text{Co}(\text{naph})_2$ pathway, see 68; for the Au/CeO_2 pathway see [70].

the previous step.⁷⁰ Filtration and distillation of this slurry yields pure Cashmeran at a *ca.* 50% yield,⁷⁰ which can be used directly in fragrance products.

1.3.2 Further products from the Cashmeran process

Cashmeran also serves as an intermediate to several other fragrant compounds as the ketone moiety affords new synthetic possibilities that are not attainable directly from hydrocarbons.^{67,71–75} A summary of the synthetic pathways of several compounds found in consumer products are presented in Scheme 1.6. Cyclisation of the ketone osmophore in Cashmeran or dihydrocashmeran with formamidine acetate forms Sinfonide and Ambertonic, respectively. The first mentioned molecule possess musky, ambery, and powdery notes whilst the second mentioned molecule has an ambery, musky, and woody odour.^{73,75} Hydrogenation of the $\text{C}=\text{C}$ double bond in Cashmeran changes not only the olfactory properties of the compounds but also the yield, which increases from 54% to 68%.⁷⁴ Despite this improvement, it may be preferable to obtain Ambertonic through Sinfonide: a 90% yield of the *cis*-isomer, which has more of a woody rather than ambery character (Figure 1.6), is achievable through this pathway compared to the 40% yield afforded from the dihydrocashmeran route.^{73–75}

The preference for the woody characteristics of the *cis*-isomer is probably due to the pre-existence of more potent amber fragrances, *viz.* Trisamber and Amber Xtreme, in the IFF portfolio.^{71,72} Trisamber was initially targeted as a synthetic substitute for Ambroxide,⁷⁶ an odorant obtained from the decomposition of sperm whale excrement product ambreine.⁷⁷ Its synthesis^{71,72,76} begins with the treatment of dihydrocashmeran with methanesulfonic acid and allyl alcohol to form an ether, followed by heating to promote a Claisen rearrangement, providing allyl-dihydrocashmeran. Subsequent reduction, with an appropriate reducing agent (e.g. Vitride), and cyclisation gives Trisamber in excellent yields. A few years after

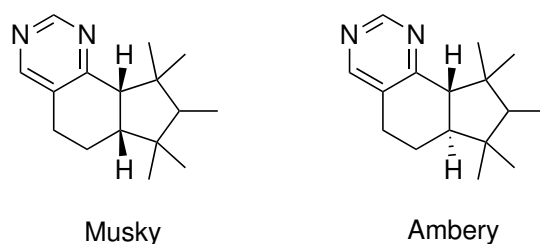
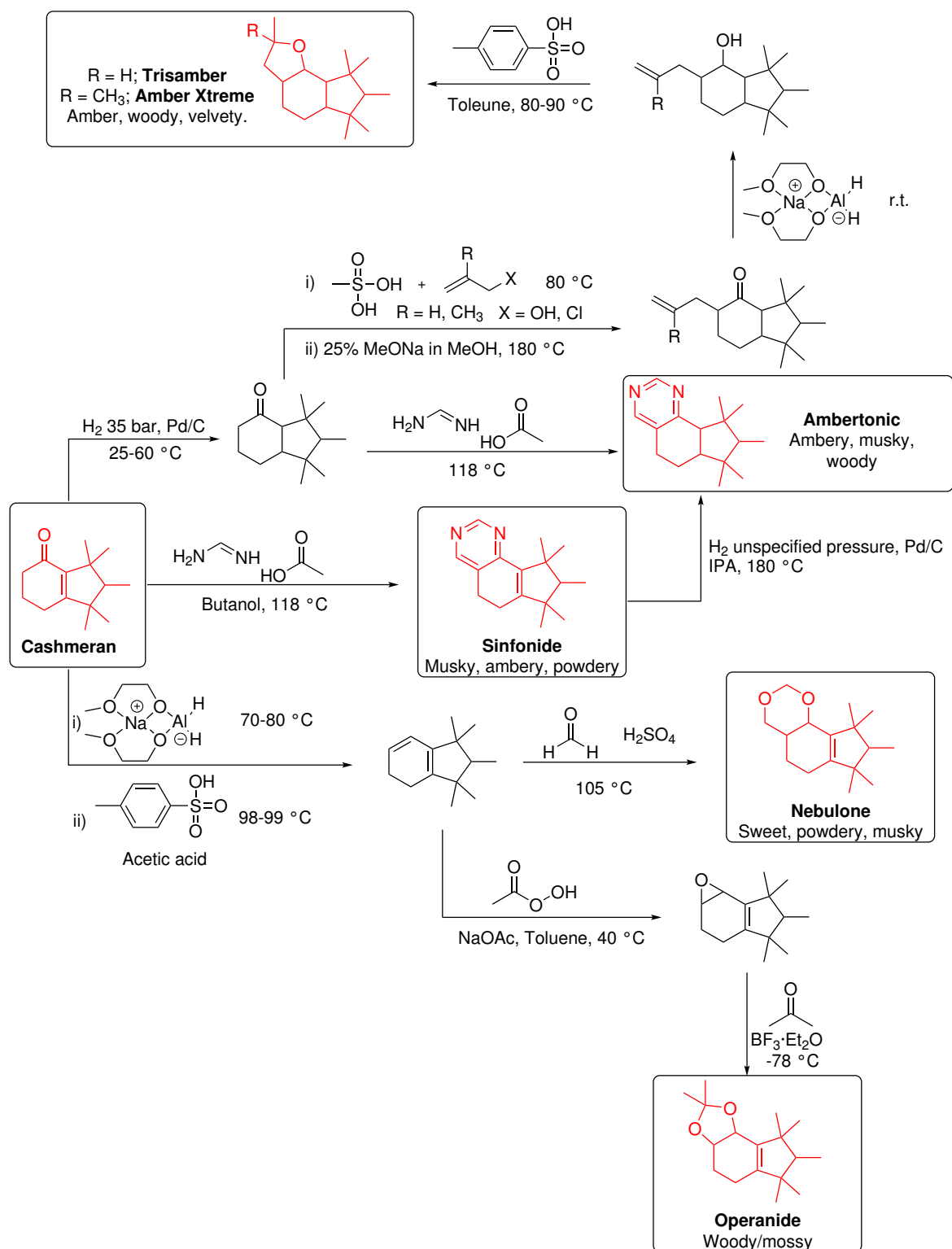


Figure 1.6: An example of the differing scent of enantiomers. Compound and olfactory information taken from [73] and [75].

commercialisation, Amber Xtreme was contemplated as a possible superior product owing to the incorporation of the additional methyl group,⁷⁶ which has been shown to enhance intensity and performance with respect to the parent compound. Using the same strategy, IFF workers used the same synthetic procedure described earlier in this paragraph to produce a 2–3 times more potent ambery, woody, and velvety odourant with better performance in fine fragrances.⁷⁶ As with Ambertonic, obtaining the *cis*-isomer is preferential,⁷⁶ but the relative quantities of each isomer from this synthesis is unclear. Synthetic strategies for unsaturated versions of Trisamber and Amber Xtreme are patented,⁷¹ but no further details on whether these compounds could then be used to produce the commercial compounds is provided. It is possible that this pathway is not feasible due to hydrogenolysis of the ether linkage or side reactions involving the C=C double bond, limiting process efficiency and with it the industrial viability.

Two Cashmeran ketal derivatives, Nebulone and Operanide, are also commercially manufactured.^{67,78,79} Both compounds are synthesised from dihydropentamethyl indane, which is synthetically accessible from THPMI or Cashmeran.^{41,80,81} The current industrial method for dihydropentamethyl indane synthesis firstly reduces Cashmeran to cashmeran alcohol using an appropriate hydride reagent (e.g. Vitral) followed by dehydration using *para*-toluenesulfonic acid. Curiously, the reduction step does not currently employ a catalyst. The selective reduction of the C=O moiety in α , β -unsaturated carbonyls has received significant attention from academic and industrial communities for several decades,^{82–84} as high yields of the saturated carbonyl are readily achieved.^{40,85} Of course, it would be more preferable to synthesise the diene directly from GHC but, as outlined above, the Birch reduction is impractical on a large scale, and electrochemical methods would require high capital expenditure.

Once the dihydropentamethyl indane has been obtained, the final stages of the syntheses can be performed. Nebulone is prepared using a Prins reaction,⁸⁶ between dihydropentamethyl indane and an excess of formaldehyde in the presence of sulfuric acid, and offers a powerful musk fragrance, with sweet, powdery, spicy and nitromusk notes.⁷⁸ Operanide is synthesised by selective epoxidation in the 4,5-position and subsequent transformation into the acetonide is achieved with acetone and $\text{BF}_3 \cdot \text{Et}_2\text{O}$. Its odour is described as woody/mossy.⁷⁹



Scheme 1.6: Examples of several products obtained from Cashmeran. Reactions taken from references [71–75].

1.4 The hydrogenation of aromatic compounds and cycloalkenes

The discussion of the partial reduction of GHC to THI in Section 1.2.3 served the purpose of introducing the reaction of interest in this work. What was lacking in this text was an explanation into what makes the process viable. The partial reduction of aromatics in general is difficult to realise as the cycloalkene intermediate is usually much more reactive than the original aromatic compound. Many studies have reported the presence of cycloolefins in reaction products but usually only in small quantities. That said, it has been noted that the addition of alkyl substituents increases the selectivity of the reaction, though there are but a few studies on such compounds. High yields of cyclohexene can be obtained from benzene but this transformation necessitates specific conditions and will be discussed separately. This section will explain how the monounsaturated intermediate forms by reviewing aromatic reduction, before discussing specific examples in which substantial quantities of cycloalkene intermediate are obtained.

1.4.1 Kinetic and mechanistic considerations

1.4.1.1 General overview

The hydrogenation of aromatics and alkenes is part of catalysis lore and has been widely studied since the advent of catalysis research.^a In fact, one of the first studies of catalytic hydrogenation alleged that benzene may be reduced to form cyclohexene over palladium black but not with platinum black as only cyclohexane forms.⁸⁹ The authors of this work never successfully isolated these products due to the limited separation methods of the time, meaning that this claim was based upon the observed gas contraction. Unfortunately, this result has largely been lost to history and the century of work that follows would suggest the authors were probably incorrect in their interpretation.

Benzene hydrogenation has typically been studied using a fixed-bed reactor. For benzene hydrogenation was an ideal model reaction, since it could be readily studied in the absence of a gas chromatograph and was an ideal means to study catalytic activity. In recent years, however, increasing legislation surrounding the use of benzene has limited its utilisation in catalytic study. The physical properties of benzene and other aromatic systems allows for their reactivity to be assessed in the liquid phase, either in flow or batch, or in static gas reactors also. Features of the reaction appear to have many similarities regardless of the reaction medium.

In almost all instances, the source of hydrogen is hydrogen gas (or its isotopes). However, there are two examples of cases where the authors purport that the reaction occurs through

^aSee references [87] and [88] for early overviews of European/American and Russian work, respectively.

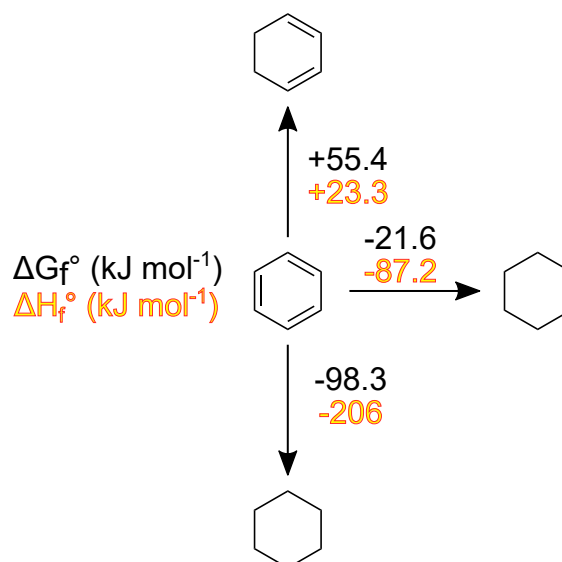


Figure 1.7: Gas phase thermodynamic data for the benzene-cyclohexadiene-cyclohexene-cyclohexane system using data reported by Janz.⁹³

a hydrogen transfer mechanism, involving the transfer of hydrogen from a donor to an acceptor. An early article reported the use of primary and secondary alcohols, which allegedly hydrogenated benzene using modified/unmodified Ni-Al catalysts.⁹⁰ However, recent work in our group suggests that in many of these examples, such chemistry may in fact be attributed to the in-situ generation of hydrogen being responsible for the observed chemistry.⁹¹ A more recent example proposes that ammonia borane can be used to hydrogenate silyl ether protected arenes over rhodium nanoparticles through a RhH₂ type complex, but did not rule out the possible role of in-situ generated hydrogen.⁹²

The hydrogenation of benzenes can lead to effectively two products: the monounsaturated cycloolefin and corresponding saturated compound. The thermodynamic viability of these reactions is most well established for the benzene system in the gas phase.⁹³ The formation of cyclohexadiene from benzene is endergonic and strongly adsorbed which may explain the why it is seldom observed as a product, while cyclohexene formation is initially favourable until around 110 °C at which point the reverse reaction becomes more energetically preferred. Cyclohexene hydrogenation remains thermodynamically feasible at higher temperatures at which the dehydrogenation of cyclohexane is most favoured. All hydrogenation steps in this system are exothermic, meaning that the reverse processes are endothermic. A summary of the thermochemistry of benzene is outlined in Figure 1.7. The introduction of substituents is only every considered from the viewpoint of the fully saturated products. Despite only small changes in the relative heats of hydrogenation,⁹⁴ the equilibrium constant decreases with increasing substituents.^{95,96}

1.4.1.2 Surface kinetics and mechanistic understanding

Insight into how a reaction proceeds on a molecular level can allow for the rational design of catalytic materials. In this instance, a *perfectly* selective catalyst for the partial reduction of an aromatic will not form any saturated product. This is achieved by forming the unstable intermediate and preferentially adsorbing the arene even in the presence of a significant excess of alkene. In other words, the ideal catalyst should cease to be active once four atoms of hydrogen are added *ortho* to one another in a regioselective manner. These are counsels of perfection⁹⁴ and understanding why this is so can be realised through consideration of the mechanistic details of aromatic hydrogenation.

But what constitutes an understanding of a reaction mechanism is a debate that has been ongoing for decades.⁹⁷⁻¹⁰⁰ Bond and Wells proposed that three pieces of information were required to gain some understanding of a reaction mechanism, which were: (i) the nature of the adsorbed species that form during the reaction (including inactive species); (ii) the interaction between these species which contribute significantly to the overall reaction (i.e. rate equations); and (iii) qualitative understanding of these interactions (i.e. which, if any, is the rate determining step).⁹⁷ When this information is available it is proposed that a mechanism can begin to be understood.

Indeed, one must also consider that no mechanism can ever be considered correct and only represents a working hypothesis which remains plausible only while there is no evidence that contradicts it. Therefore, any proposed mechanism must have a predictive (and thus falsifiable) ability. A consequence of this statement is that many mechanism statements may be equally well explained by experimental evidence, which can be readily observed by an inspection of the literature discussing the mechanism of aromatic and alkene hydrogenation.

The purpose of this section will be to provide an overview of proposed mechanisms for the reduction of aromatic hydrocarbons to the thermodynamically stable saturated product (conditions depending). It aims to answer, to the best of my ability, the requirements outlined above starting with the adsorption of reactants on the surface and the identification of active and inactive species. Finally, it leads on to a discussion on the kinetics of the reaction beginning with a brief overview of the power rate law formalism before considering the surface-based kinetic models along with experimental and theoretical evidence of the proposals.

1.4.1.2.1 Adsorption and identification of active species A heterogeneously catalysed reaction must be preceded by adsorption of at least one of the reactants. The mathematical description of this adsorption process is typically assumed to follow a Langmuir adsorption isotherm, which assumes that (i) all sites are uniform in energy and are unaffected by occupancy on neighbouring sites; (ii) the adsorbing molecule is immobile on the surface; (iii) each site may accommodate one adsorbed species and saturation is achieved at one monolayer coverage. From consideration of these propositions and assuming that the adsorption-desorption

process is at equilibrium for a molecule that does not dissociate at the surface, one obtains the Langmuir equation:

$$\theta = \frac{KP}{1 + KP} \quad (1.1)$$

where θ is the fractional surface coverage, K is the adsorption equilibrium constant, and P is pressure. This is a simplified view of adsorption on an ideal surface. Other, more complex isotherms that describe adsorption on non-ideal surfaces have also been proposed, such as the Freundlich and Temkin isotherms, and can account for experimental results which exhibit decreasing heats of adsorption with changing coverage. However, the advantage of the Langmuir isotherm is that multiple competing adsorbates can be included rather trivially, and kinetic expressions derived with its assumptions work well in most cases.¹⁰¹

As adsorption is a crucial prerequisite for catalysis, significant efforts have been expended to gain an understanding of the adsorbed state of various molecules. Classically these were performed using surface analytical vibrational techniques with single-crystal metal surfaces at low temperatures and ultra-high vacuum conditions, which are necessary for their successful operation. Catalytic reactions rarely utilise such conditions, particularly for hydrogenation reactions involving hydrocarbons. As such, surface species observed under these conditions are not necessarily the same as those that exist in the reaction environment on far more complex practical materials.¹⁰² For example, it is now accepted that the surface and adsorbate structure may change during a reaction, especially so at higher temperatures and pressures, and consequently, species that are unstable under high vacuum conditions may either be important or indeed the active species in a catalytic reaction.¹⁰³ Nevertheless, these studies are still very useful and worthy of discussion.

Over the past three decades, an array of techniques has been developed which permit molecular level studies of surfaces under more practical reaction conditions. One such technique with relevance to this work is sum-frequency generation (SFG). This is a surface sensitive optical vibrational spectroscopy that provides insight into the structure of adsorbates and reaction intermediates.¹⁰⁴ The simultaneous development of computational methods in this time can be used to complement the results from these studies and provide clear insight into the reaction.

The active adsorbed state in benzene hydrogenation over Pt catalysts has been identified using in-situ SFG^{105–107}. SFG spectra on Pt(111) and Pt(100) surfaces at high pressures (7.5, 10, 12.5, and 15 torr of benzene and 10, 50, 100, and 150 torr of hydrogen) and temperatures (310–440 K) indicated two adsorbed species were present. One of these species was attributed to a flat-lying species as a peak attributable to aromatic C-H stretching showed a small deviation (8 cm^{-1}) compared to that of gas-phase benzene. A wider spectral range was not reported in the manuscript, but separate studies utilising vibrational spectroscopies have observed small deviations between the free and adsorbed state at other characteristic frequencies.^{108,109} In addition, DFT studies suggest that the bond lengths and angles are largely unchanged from

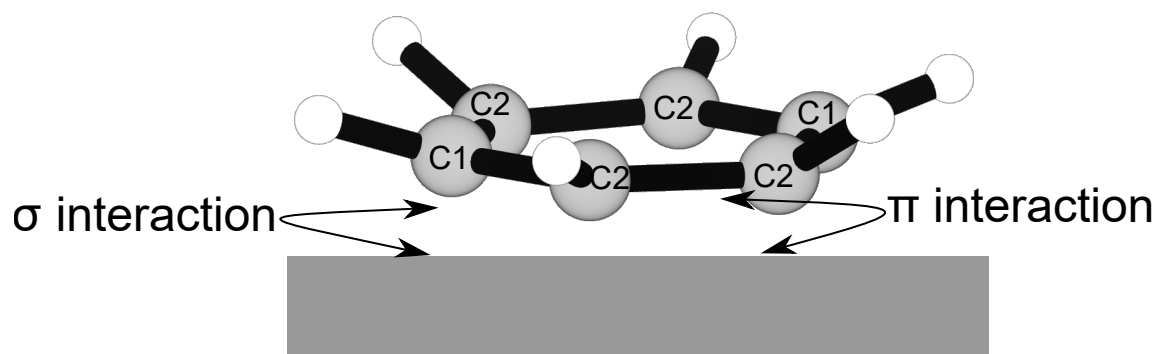


Figure 1.8: The diene- π complex of chemisorbed benzene.

the free molecule. The intensity of this peak in the SFG spectrum was shown to decrease as a function of temperature and eventually disappeared at *ca.* 400 K without a decrease in rate, suggesting it not the active species in the reaction. An earlier study by Masel and workers using high-resolution electron energy loss spectroscopy demonstrated that this species was unreactive when exposed to hydrogen, which supported this assertion.¹⁰⁹

The other species captured in the SFG spectrum was proposed to be a 3,6 di- σ 1,4-cyclohexadiene (diene- π) structure upon adsorption (Figure 1.8) based on previous studies.^{108,109} This species is much more strongly adsorbed on the surface and readily reacts with hydrogen.¹⁰⁹ The in-situ SFG spectra show intriguing temperature dependent behaviour depending on the platinum surface. For the Pt(111) surface, the $\nu(\text{C-C-H})$ and $\nu(\text{C-H})$ (vinylic) peaks increase with temperature. In contrast, new peaks appear on the Pt(110) surface and signals indicative of the diene- π benzene species do not rise. The new species is attributable to a π -allyl cyclohexene species and its formation will be considered more in the following section.

As for the active species on other metals, there are regrettably no in-situ studies to the extent of my knowledge. Numerous UHV studies for other surfaces, predominantly platinum group metals, have been reported, but more rarely in comparison to studies on platinum surfaces. Moreover, the structure of adsorbed benzene in these reports has been the subject of much debate. Some researchers conclude that benzene changes significantly upon adsorption and others claim the contrary. Thomas *et al.*¹⁰⁹ suggested that all authors were probably correct in their conclusions, and the alleged differences arose due to differing extents of surface coverage. The diene- π species is present at all coverages, while the non-distorted form is only observable at high coverage where it becomes the most abundant surface intermediate.

Benzene adsorption on other platinum group and iron triad surfaces at low benzene coverage are generally in good agreement with those studies outlined above.^{110–129} The chemisorbed state is, however, not thought to be identical on every metal due to differing extents of π -interaction induced rehybridisation. In addition, introducing substituents only has a minor effect on the strength of interaction,¹³⁰ so the following could be applicable

for the aromatics of interest in this work. It is generally believed that the adsorption on nickel is weaker than palladium which in turn is weaker than, in no specific order, ruthenium, rhodium, iridium, and platinum, based on both theoretical calculations and experimental measurements.^{118,120,129,131–142} For example, Liu *et al.*¹²⁹, who used surface enhanced Raman spectroscopy to probe this phenomena, observed an increasing blue shift of the M-C vibration and a decreasing red shift of the ring breadth to be in the order of rhodium, ruthenium, platinum (iridium was not investigated) indicating a stronger metal-adsorbate interaction. Platinum is also placed above rhodium in the hierarchy by Somorjai and co-workers through probing these two metals by low-energy electron diffraction.¹³² However, DFT methods usually rank the strength of adsorption on rhodium to be higher than platinum in contrast to experimental work.^{118,141,143–145} Iridium is often, but not always,^{137,138,141} considered to have the highest adsorption potential of platinum group and iron triad metal surfaces.^{135,136,140,146} The exact placing of ruthenium is not agreed, but it is thought to be at least as strong as platinum.^{141,147,148} With regards to iron and cobalt, these metals have undergone far less study.^{110–112,149} Chemisorption on Fe(110) is theoretically predicted to be as strong as on palladium.¹⁴⁹ On the cobalt surface,^{111,112} non-dissociative adsorption occurs at low coverages with small distortions to the aromatic system. Studies utilising osmium are limited and focus only on the Os(0001) surface,^{123–125} but Netzer *et al.* suggested the metal-adsorbate interaction may be stronger than Ir(111).¹²³

1.4.1.2.2 Aromatic hydrogenation Kinetic measurements on the hydrogenation of benzene are available for many elements of the periodic table, even radioactive technetium.^{150,151} No recent comprehensive kinetic measurements of the relative activities of each element are available, but a detailed account by Kubicka in 1968 of silica and alumina supported metals found the hydrogenation activity decreased in the order of Ru>Pt>> Tc ≈ Pd >> Re.¹⁵⁰ Even older specific rate measurements^b by Amano and Parravano in the 1950s agree that palladium is not very active in comparison with platinum and ruthenium, while noting that the latter is slightly more active than platinum.¹⁵² In addition, they reported rhodium to be more active still. Rhodium was also determined to be more active than iridium,¹⁵³ which has a similar activity to platinum.^{153–156} Iron, cobalt, and nickel are accepted to be less active than ruthenium, rhodium, iridium, and platinum,^{94,157,158} but there are conflicting reports on their placements relative to palladium.^{158–162} The only report of the activity of osmium finds it to be almost an order of magnitude lower than platinum and iridium.¹⁵⁵

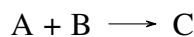
The effect of particle size in aromatic hydrogenation has long been debated. Bond summarises it as follows: ‘There is a general perception that the reaction is structure-insensitive, or almost so’. There are significant amounts of literature that supports this statement, but there are several deviations worthy of discussion. A recurrent theme in this regard is the importance of reduction temperature. For example, Aben *et al.* found that the turnover frequency (TOF)

^bChemisorption measurements were not widely used at this time.

over platinum on alumina was independent of dispersion, but correlated with a specific low temperature hydrogen desorption peak observed in temperature-programmed desorption (TPD) studies. The intensity of the low temperature peak variation was dependent on the reduction procedure¹⁶³ and more recent work indicated that this induces surface reconstruction, for which H₂-TPD is a suitable tool for its study.¹⁶⁴ Surface reconstruction was also attributed to be the origin of the moderate structure sensitivity observed by Flores *et al.*¹⁶⁵ when investigating the effect of pre-treatment conditions but no H₂-TPD were performed in this study. More recently, a series of studies on shape- and size-controlled nanoparticles afforded new insights into the structure sensitivity of this reaction. The formation of cyclohexene was observed in small quantities over the Pt(111) surface of single crystals^{105–107} and cuboctahedral nanoparticles,¹⁶⁶ which contain both the Pt(100) and Pt(111) planes. Conversely, when using Pt(100) single crystals^{105–107} and cubic nanoparticles,¹⁶⁶ which contain only the Pt(100) plane, did not produce cyclohexene, and lower overall TOFs were observed. Tetrahedral rhodium nanoparticles, rich in the (111) plane, supported on carbon catalysts provided similar results for the reduction of anthracene.¹⁶⁷ Monodisperse platinum supported on SBA-15—with particle sizes of 1.5±0.3 nm, 2.4±0.3 nm, 3.1±0.9 nm, 4.0±0.9 nm, and 5.2±0.9 nm—displayed a moderate structure sensitivity for benzene and toluene hydrogenation.¹⁶⁸ For benzene, the rate passed through a maximum value: particles 3.1 nm in diameter were three times more active than particles with a diameter of 1.5 nm. Toluene behaved similarly, except the rates over the 2.4 and 3.1 nm particles were approximately equal. The study of particles in this size range are useful as the greatest changes to the fraction of surface site types are expected within this region according to the classic statistical models of van Hardeveld and Hartog.¹⁶⁹ Additionally, this region also encompasses the gradual loss of metallic character.⁹⁴ The authors proposed that the observed structure sensitivity was probably caused by adsorption energy changes with particle size, although did not rule out the possible size dependence of the formation of dehydrogenated surface species, which poison the addition reaction (*vide infra*).¹⁶⁸

The activity of supported metal catalysts also depends on the underlying support in aspects not pertaining solely to dispersion effects. A significant enhancement in turnover frequencies are observed for acidic supports,^{170–179,179,180,180,181,181–187} such as silica-alumina and titania (with HCl impregnated titania displaying enhanced activity).¹⁷² Vannice and co-workers proposed that interfacial sites on acidic supports, which are not counted by hydrogen/oxygen/carbon monoxide chemisorption measurements, acted as additional active sites and were responsible for the TOF enhancement.^{170–178} More recent work, and in the original article that observed the higher activity on acidic supports,¹⁸² allege there is an electronic component to this effect,^{179–181,183–187} but there is controversy over whether a M^{δ+} is beneficial^{179–182} or not^{183–187} to hydrogenation activity. Moreover, Chou and Vannice argue that as the TOFs of silica and alumina supported catalysts, which show very different activities in nanoparticle electron-density dependent CO hydrogenation, are very similar, it is doubtful such an effect is present.¹⁷²

Many studies focussing on aromatic hydrogenation express kinetic data as a rate and as a function of the pressure/concentration of each component raised to a power, termed the “*order of reaction*”. For example, the following reaction:



may be expressed as:

$$\text{rate} = k P_A^a P_B^b P_C^c \quad (1.2)$$

where a , b , and c are the orders of reaction and can be positive, negative, or zero (including fractional). These values can provide some insight into the reaction mechanism. Aromatic hydrocarbons typically have an order of close to zero, whilst the order with respect to hydrogen is often between 0.5 and 1 (see Table 1.2), though these values increase with temperature. The fact that the order is zero indicates the aromatic compound is strongly adsorbed and the active sites have high fractional coverages, while also suggesting, but not confirming, the possibility of separate adsorption sites. Meanwhile, an order of 0.5 or 1 is usually taken to mean the addition of the first or second hydrogen atom, or hydrogen molecule, is the rate-determining step. More thought is needed for values approaching 3, or greater, as this implies the concurrent addition of six atoms or three hydrogen molecules which, although proposed by some, is generally rejected on statistical grounds.¹⁵⁸ The increase as a function of temperature is interpreted as a changing concentration of surface species.

A consequence of the changing of surface concentrations can also be observed when studying the rate of the reaction as a function of temperature. It is commonly observed in the gas phase that the rate of reaction increases exponentially as a function of temperature before passing through a maximum and decreasing rapidly at higher temperatures. The exponential region is described by the Arrhenius equation (Equation 1.3), which expresses the rate—or more correctly, the rate constant, k ,—as the product of a pre-exponential factor, A , and e raised to the power of the negative activation energy divided by the product of the gas constant, R , and the temperature, T .

$$\ln(k) = A \exp\left(\frac{-E_a}{RT}\right) \quad (1.3)$$

The *apparent* activation energies of a range of aromatics (benzene, toluene, the xylenes, tetralin) are strikingly similar, and are usually found in the region of $50 \pm 20 \text{ kJ mol}^{-1}$ (see Table 1.2) regardless of the phase used for the reaction. Note the modifier apparent is used to signify the activation energy is not “true”. That is to say the changing surface coverage results in the rate increasing less rapidly than it would in the absence of desorption. Thus, only when all reactants are tightly bound to the surface at increasing temperatures does the apparent activation energy equate to the *true* activation energy. The true activation energy can be calculated using the Temkin equation:⁹⁴

$$E_a^{app} = E_a^{true} + n_A \Delta H_A + n_H \Delta H_H \quad (1.4)$$

Table 1.2: Selected examples of the kinetics of aromatic hydrogenation over supported metal catalysts. $rate \propto P_H^x P_A^y$

| Substrate | Catalyst | E_a^{app} (kJ mol ⁻¹) | T (°C) | x | y | Reference |
|------------------|--|-------------------------------------|--------|------|------|-----------|
| Benzene | 5 wt.% Fe/C | 96.1 | 140 | 3.2 | -0.7 | [158] |
| | | | 200 | 4.0 | -0.3 | [158] |
| Benzene | 10 wt.% Co/SiO ₂ | 25.5 | 123 | 1 | 0.2 | [188] |
| | | | 179 | 1.7 | 0.5 | [188] |
| Benzene | 1.5 wt.% Ni/SiO ₂ | 49.2 | 135 | 0.9 | 0 | [189] |
| | | | 200 | 1.64 | 0.37 | [189] |
| Toluene | 1.5 wt.% Ni/SiO ₂ | 63.6 | 135 | 0.8 | 0 | [189] |
| | | | 200 | 1.6 | 0.35 | [189] |
| <i>o</i> -Xylene | 1.5 wt.% Ni/SiO ₂ | 73.4 | 135 | 0.8 | 0 | [189] |
| | | | 200 | 1.6 | 0.3 | [189] |
| <i>m</i> -Xylene | 1.5 wt.% Ni/SiO ₂ | 68.1 | 120 | 0.7 | 0 | [190] |
| <i>p</i> -Xylene | 1.5 wt.% Ni/SiO ₂ | 64.9 | 120 | 0.7 | 0 | [190] |
| Benzene | 0.4 wt.% Ru/SiO ₂ | 38 | 30 | 1.2 | 0 | [191] |
| | | | 127 | 2 | 0.2 | [191] |
| Benzene | 0.5 wt.% Pd/Al ₂ O ₃ | 51.8 | 140 | 1 | 0 | [171] |
| | | | 250 | 2.2 | 0.4 | [171] |
| Toluene | 0.5 wt.% Pd/Al ₂ O ₃ | 55.2 | 140 | 1.3 | 0 | [173] |
| <i>o</i> -Xylene | 0.5 wt.% Pd/Al ₂ O ₃ | 62.2 | 165 | 1.1 | 0 | [173] |
| <i>m</i> -Xylene | 0.5 wt.% Pd/Al ₂ O ₃ | 59.4 | 165 | 1.1 | 0 | [173] |
| Benzene | 0.24 wt.% Pt/SiO ₂ · Al ₂ O ₃ | 54.3 | 44 | 0.7 | 0.1 | [175] |
| | | | 83 | 0.6 | 0 | [175] |
| Toluene | 0.24 wt.% Pt/SiO ₂ · Al ₂ O ₃ | 46.0 | 60 | 0.9 | 0.1 | [175] |
| | | | 80 | 1.1 | 0 | [175] |
| Tetralin | 0.8 wt.% Pt/SiO ₂ · Al ₂ O ₃ | 45 | – | – | – | [185] |

where E_a^{app} is the experimentally measured activation energy, n_x is the reaction order for aromatic A or hydrogen H , and ΔH_x is the enthalpy of adsorption of the aromatic or hydrogen. “True” activation energies for the hydrogenation of aromatics are seldom, if ever reported, but are probably substantially higher. A simplified version of Equation 1.4 assumes n_x equates to unity, and E_a^{true} values are found to be in the region of 155–270 kJ mol⁻¹ as adsorption is exothermic.¹⁸⁹ Eventually, the adsorption terms dominate in the rate equation and this leads to the observed maximum and E_a^{app} is approximately equal to the heats of adsorption.^{101,158}

1.4.1.2.3 Side reactions A number of side reactions can occur in tandem with hydrogenation: hydrogen exchange, dehydrogenation, cracking, and hydrogenolysis.⁹⁴ Hydrogen exchange will not be detectable unless the reaction is performed with a hydrogen isotope, such as deuterium. The exchange process is believed to predominately follow a separate mechanism to addition.⁹⁴ The support for this hypothesis originates from (i) a strong particle size dependence on TOFs, indicating a structure sensitivity;^{94,192} (ii) differing kinetic parameters (exchange has a higher activation energy);^{94,193} (iii) exchange can occur on surfaces

which are inactive for addition.^{94,193} Dehydrogenation to form a strongly held carbonaceous overlayer is commonly observed in surface science studies during TPD experiments and reactions performed using ¹⁴C-labelled benzene show significant radioactivity of platinum, but not palladium, catalysts post-reaction.¹⁹⁴ However, possible carbonaceous deposits on metals under reaction conditions may be dependent on the catalyst as for other metals (e.g. ruthenium) there are reports both accommodating and contrary to this idea.^{60,195} Interestingly, the carbonaceous overlayer is considered by some to be the active centre in alkene hydrogenation.¹⁹² Cracking and hydrogenolysis may be related to the previous two points. Many studies ignore these reactions, and studies which do consider them report their absence or low level of formation.^{150,194,196}

1.4.1.2.4 The reaction at the molecular level A limited number of studies consider the reaction from direct consideration of the adsorbed species on the catalyst's surface. In principle, there are four mechanisms that can account for a surface catalysed bimolecular reaction (Figure 1.9):

- [1] A reaction which occurs by the interaction of two atoms or molecules chemisorbed at adjacent sites on the surface.
- [2] A reaction that happens through consequence of a collision between a molecule/atom on the surface and one in the liquid or gas phase.
- [3] A reaction between a molecule chemisorbed on the surface and the atoms of the underlying solid.
- [4] A reaction that takes place between a molecule/atom chemisorbed on the surface and one held in a van der Waals layer (i.e. physisorbed).

The general structure of the first three mechanisms were proposed by Langmuir shortly before he retired from the area of chemical kinetics. Unfortunately, a detailed account of the relevant history of these mechanisms and kinetics is not appropriate here, but the reader is directed to excellent accounts by Prins¹⁹⁷ and Laidler.¹⁹⁸⁻²⁰⁰ These ideas were later expanded upon by Hinshelwood and Rideal and these mechanisms are eponyms of their contributors, namely Langmuir-Hinshelwood (Mechanism 1) and Langmuir-Rideal (Mechanism 2). Mechanism 1 may also be referred to as Langmuir-Hinshelwood-Hougen-Watson as they extended this treatise to include reactant adsorption/product desorption as a rate limiting step.²⁰¹ Some refer to Mechanism 2 as the Eley-Rideal mechanism, but this is in part due to their repopularisation of this model. Their unique contribution is Mechanism 4: the "real" Eley-Rideal mechanism. Mechanism 3 is more commonly known as the Mars van Krevelen mechanism,²⁰² although the manner in which they re-expressed this mechanism in the context of total oxidation of hydrocarbons leaves much to be desired in the eyes of the kineticist.²⁰³

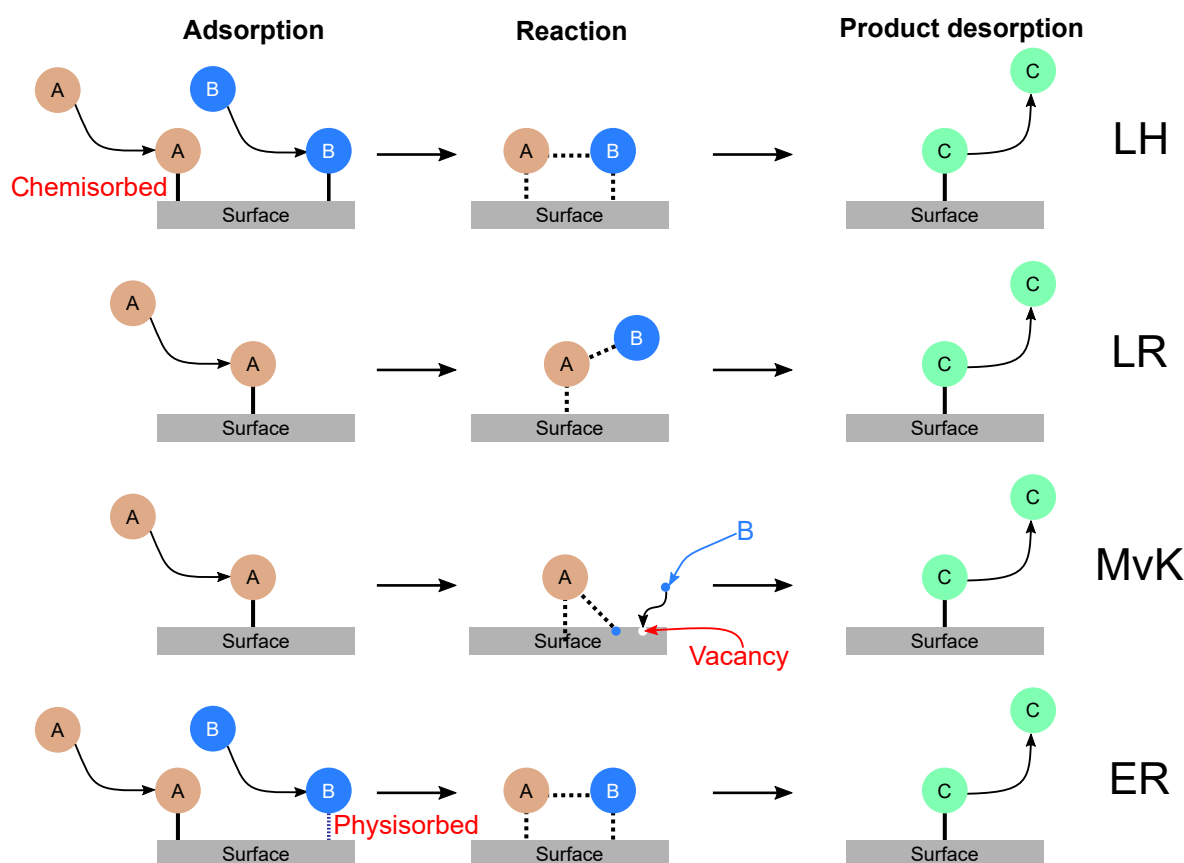


Figure 1.9: Surface mechanisms in heterogeneous catalysis. LH = Langmuir-Hinshelwood; LR = Langmuir-Rideal; MvK = Mars van Krevelen; ER = Eley-Rideal.

With the exception of the Mars van Krevelen mechanism, each of the mechanisms outlined above has been proposed to explain the hydrogenation of benzene. Most authors propose a Langmuir-Hinshelwood mechanism between an undissociated aromatic species and dissociated hydrogen. However, if reactants adsorb competitively or non-competitively, the number of surface species in the reaction, the rate determining step (if present), and how many reaction pathways significantly contribute to the rate are disputed. As discussed above, the possibility of many models giving similarly good fits can be the origin of the controversy and a universal model for all systems is not necessarily needed.

Support for competition between reactants is available from the orders of reaction. The negative order for benzene observed by Yoon *et al.*^{158,204} for supported iron catalysts implies competitive adsorption, but the order close to zero recorded over many other group 8–10 metal catalysts (Table 1.2) can be explained without it. Negative orders have also been reported on other metals, such as nickel.^{205–207} This observation is not universal, however.^{162,189,208} Keane and Patterson summarise this situation as “Such an apparent incongruity serves to illustrate the inherent complexity of these systems and the difficulties involved in drawing meaningful comparisons between reports that originate from different laboratories”.¹⁶² Thus, it is possible that the nature of competitive behaviour is unique to a reaction system, or a so far unidentified variable induces the competitive behaviour.

The surface reaction is most commonly considered to be a stepwise addition process involving atomic hydrogen.^{107,115,130,158,171,174,177,190,209,209–217} Fewer kinetic models propose sequential addition of hydrogen atom pairs^{205–207,218,219} or in some cases, all six hydrogen atoms at once.²²⁰ These mechanisms, despite providing good fits with the experimental data, are probably better explained by other proposals. Termolecular reactions are very difficult to justify using collision theory as the probability of a three-body collision is low. Even from a transition state theory perspective, it is difficult to preclude a two-step process with a rapid pre-equilibrium step and would be better explained by a series of elementary steps. Further evidence is the rate: a three-body collision would have a much lower pre-exponential factor owing to the large loss of entropy in the transition state, thus unless it were compensated by a lower activation energy it would be very slow. The same reasoning would therefore suggest the likelihood of a seven-body reaction to be near zero. A better explanation of the hydrogen orders of 3 or higher is to assume the addition steps prior to the rate-determining step are quasi-equilibrated.^{101,158}

The possibility of pairwise addition in toluene hydrogenation has also been assessed experimentally using the parahydrogen-induced polarization (PHIP) method.²²¹ PHIP effects are observable by nuclear magnetic resonance (NMR) spectroscopy, as the introduction of parahydrogen as a pair results in an anti-phase line shape and enhanced signal strength.²²² Hydrogenating toluene in a large excess of parahydrogen, to ensure the gas does not become enriched in orthohydrogen which displays no enhancement,²²³ over titania supported platinum, rhodium, and palladium catalysts does not show PHIP enhancement.²²¹ This suggests that the contribution of the pairwise route is negligible.

The manner in which hydrogen is added to the adsorbed aromatic controls what products form. A classical depiction of the reaction shows the pathway as benzene→cyclohexadiene→cyclohexene→cyclohexane. However, if the step- or pairwise addition of hydrogen atoms is considered, a complex reaction network may be conceived (Figure 1.10): atoms may be added in the *ortho*, *meta*, or *para* positions with respect to one another. Full path analysis is not possible with classic kinetic studies alone and supplemental theoretical methods are required. The full mechanistic pathway for benzene has been studied on the Ru(0001), Pd(111), and Pt(111) surfaces,^{118,130,147,216,224,225} with considerably more complex pathways for toluene and o-xylene hydrogenation (see Figure 5 & 6 in [217]) also probed on platinum catalysts.²¹⁷ The reaction over the Ru(0001) surface was computed to follow *ortho* addition to the ring, with 1,3-cyclohexadiene and cyclohexene expected as intermediates.¹⁴⁷ Whilst on the Pd(111) surface, *ortho* addition was energetically most favourable^{118,225} and one study calculated that this pathway accounted for over 90% of benzene conversion between 80 and 380 °C.²²⁵ Interestingly, this study also simulated the catalytic activities and found the results were in the same order of magnitude as those reported in literature.²²⁵ Early results for the Pt(111) surface indicated that the reaction proceeds *via* multiple radical species as a consequence of *meta* attack on the adsorbed species for the first three hydrogen additions.^{118,224} More

recent theoretical and combined experimental and theoretical work, however, indicates the net rate is greatest when proceeding through 1,3-dihydrobenzene (see Figure 1.10) and cyclohexene.^{130,216} This is in agreement to the work of Somorjai, as discussed previously, which shows that cyclohexene is both a product in the effluent stream and on the surface.^{105–107,166} It does not explain, however, why the formation of cyclohexene appears to have a higher activation energy than the formation of cyclohexane, an effect also observed on nickel.^{56,196} With regards to toluene and *o*-xylene, the lowest energy reaction routes proceed *via* hydrogen addition in the non-substituted positions for all steps due to steric hindrance.²¹⁷

Possible intermediates of the reaction can also be derived using experimental techniques. Two approaches have been utilised for this purpose: (i) use of radiolabelled compounds; (ii) use of substituted aromatics. The former method investigated the mechanism of benzene hydrogenation using a mixture of ¹⁴C-labelled benzene and cyclohexene at differential levels of conversion.^{226,227} The authors assumed stepwise addition and subsequently analysed the network map (Figure 1.10) on the basis of probability. If the addition is truly random, then the ratio of specific radioactivity of cyclohexene to cyclohexane should equal 0.4. However, all metal powders, *viz.* iron, nickel, ruthenium, rhodium, palladium, osmium, iridium, platinum and rhenium, displayed values between 0.01 and 0.27. Notably, some radioactive 1,3-cyclohexadiene was also observed, which is rarely observed in the reduction of aromatics.^{228,229} This was taken to mean that the direct hydrogenation route was preferable in all circumstances, which contrasts the results of the computational studies. The origin of this deviation is possibly attributable to the other surfaces present in bulk powder, which are not modelled in the work, are less selective. Alternatively, the mechanism may be sensitive to the catalyst preparation method or potential deactivation events. Another possible explanation is that the higher energy *meta* addition becomes more active at the higher temperatures used in this study, owing to its higher activation energy as modelled by Sabbe *et al.* in kinetic simulations.²¹⁶

Disubstituted aromatics have also been suggested to provide insight into the mechanism of aromatic reduction. The information gleaned from studying these compounds is, however, contested. The debate is centred around understanding the *cis* to *trans* ratio of the saturated product. Selectivity to the *trans* isomer is known to increase with metal dispersion, support acidity, bulk of substituent, temperature, and the inverse of pressure.^{190,218,230–239} However, only the *cis* isomer is expected if the reaction occurs in one sojourn on the surface, as the aromatic should lie flat on the surface with hydrogen attacking from below. Moreover, a desorption-readsorption process of an olefinic intermediate cannot account for the, in some cases well over 60%, selectivity to the *trans* isomer as the most sterically hindered cycloalkenes are expected based on the thermochemical principles outlined above.²³⁰

Several explanations to account for this observation have been forwarded: epimerisation, topside addition, isomerisation followed by either “rollover” of the adsorbed species or desorption and re-adsorption before hydrogenation. Each of these scenarios is presented

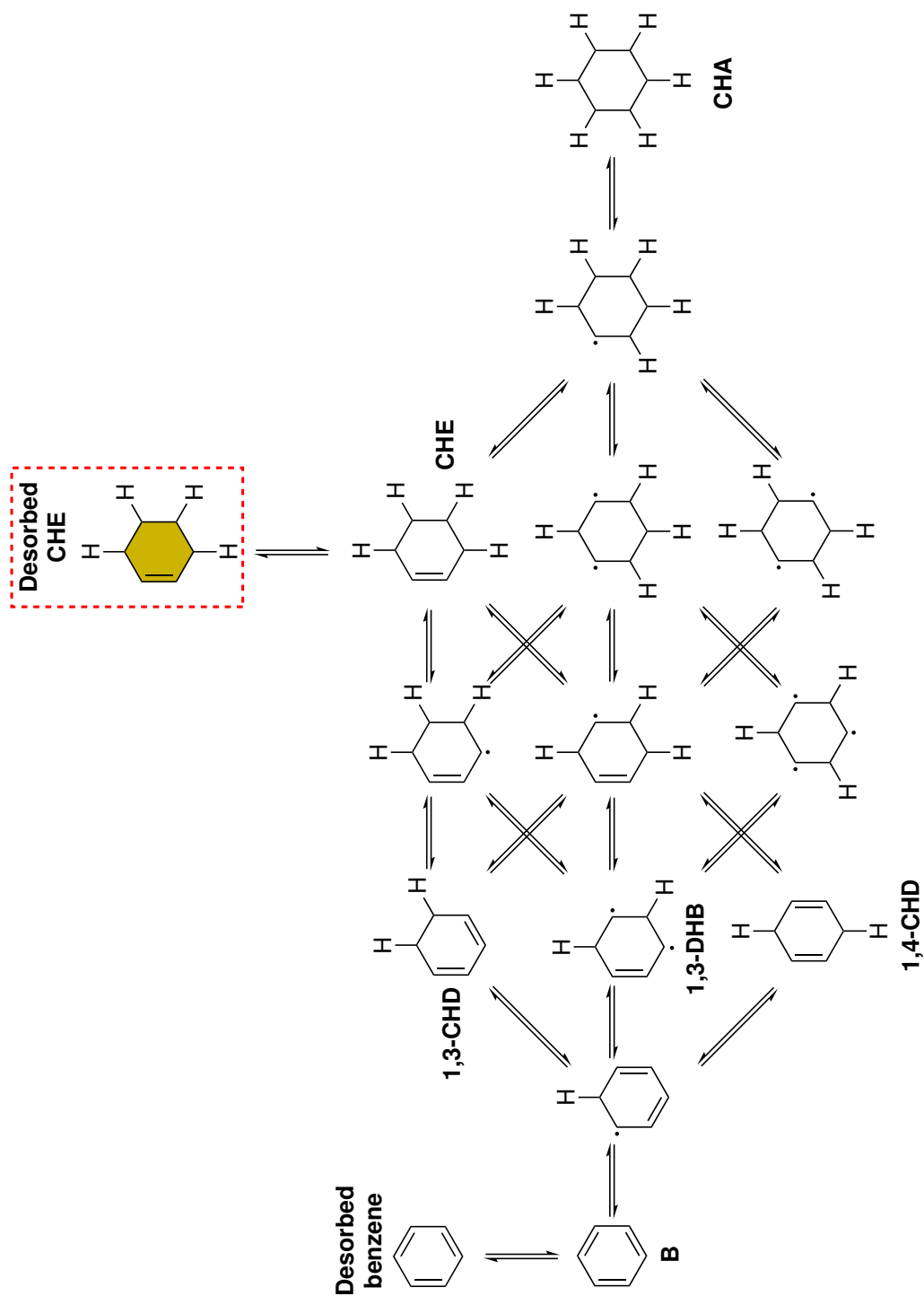


Figure 1.10: Reaction network of the hydrogenation of benzene to cyclohexane. Abbreviations: B = benzene; 1,3-CHD = 1,3-cyclohexadiene; 1,4-CHD = 1,4-cyclohexadiene; CHE = cyclohexene; CA = cyclohexane; 1,3-DHB = 1,3-dihydrobenzene. Figure adapted from [214].

in Figure 1.11. Epimerisation was observed to occur for mixtures containing each isomer of 1,2-dimethylcyclohexane over a nickel on silica under the same conditions used for the hydrogenation *o*-xylene.¹⁹⁰ However, the compositional change in the product stream could only account for at most 46% of the observed selectivity. Topside addition implies a reaction of the adsorbed intermediate alkene with a hydrogen molecule. A PHIP effect was observed in the NMR spectrum during the hydrogenation of cyclohexene, in both the reactant and saturated product, which indicates pairwise addition is possible, but its contribution to the overall reaction mechanism was estimated to be minimal (2%).²²¹

The flipping of the double bond on the surface by a so-called “roll-over” process, where a loosely bound intermediate turns over on the surface and is quickly attacked from the opposite side, or through desorption and re-adsorption on the opposite face has attracted much debate but a consensus is still lacking,^{218,233–237,237–240} as the kinetic behaviour of both processes leads to similar rate equations.²³⁷ Depending on the isomer, this requires an initial isomerisation reaction. The structure of cyclohexene under experimental conditions has been studied on platinum catalysts by SFG. These studies suggest that a dehydrogenated π -allyl species is present across a wide temperature range.^{241–243} In literature, this is one of the proposed mechanisms of isomerisation; the other being an addition-abstract process *via* an alkyl intermediate.⁹⁷ Subsequent “roll-over” or desorption and re-adsorption on the opposite face before hydrogenation can then account for the observed stereochemistry. This latter explanation is perhaps most well-received, but is unsatisfactory for some metals for some

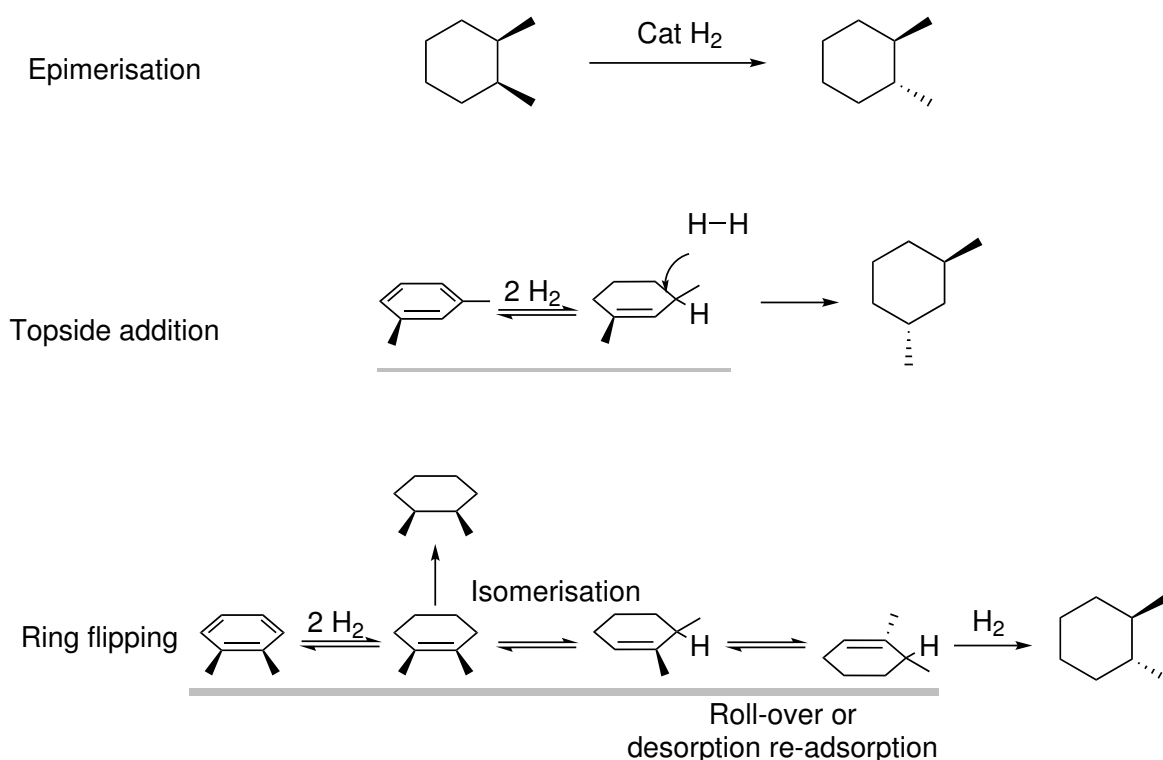


Figure 1.11: Possible mechanistic causes of differing *cis/trans* ratio observed during dialkyl-substituted aromatics hydrogenation.

metals, e.g. platinum.⁹⁴ The rate of hydrogenation over such metals is usually found to be much higher than the rate of isomerisation as determined by studies employing deuterium. Therefore, it is possible that the observed results are a consequence of the balancing of the rates of each proposed process, but a splitting of the variables for each catalyst system would probably require a Herculean effort.

On the basis of kinetic modelling, the rate determining step has been suggested to be the first,^{107,177,190,209} second,^{174,177} fourth,²¹⁰ fifth,²¹¹ or sixth^{158,209} step, and in some cases, absent.^{171,212} It is often argued that the first step must be rate-determining due to a breaking of the ring aromaticity, but orders of hydrogen above 0.5 do not readily reconcile with this proposal. Lin and Vannice suggested that the first step was indeed the rate determining step on all noble metals and the higher orders with respect to hydrogen were a consequence of the formation of inhibitory hydrogen-deficient surface species. This proposal was also used to rationalise an earlier observation for the hydrogenation of benzene over iron catalysts, which in some cases displayed the hydrogen reaction order to be greater than 3.^{101,158} However, reaction data for the xylenes suggested that such species were absent, yet the derived hydrogen reaction orders were still greater than the expected 0.5.¹⁷³ An alternative model forwarded by Vannice and associates, that could not be excluded from consideration, assumed that the second addition step was rate determining. Indeed, the in-situ SFG data discussed above indicates that the aromaticity is lost upon adsorption,^{105–107} so the addition of the first hydrogen atom may not be as demanding as once thought.

Computationally, the rate determining step appears to depend on the metal. Early DFT studies on the Ni(111) revealed that the first addition had the highest energy barrier.¹¹⁵ Whilst for Pd(111), the situation is more complex: at temperatures below 150 °C the addition of the second hydrogen atom is rate limiting in agreement with the work of Vannice. At higher temperatures, however, the third step was found to have the greatest influence on the rate. The shift was attributed to a change in concentration of surface species.²²⁵ For the reduction of benzene and toluene on Pt(111), the fifth step is usually found to be rate determining,^{213,214,216} though this possibly could shift to the sixth step for the former molecule at higher temperatures.²¹⁶

Finally, the Langmuir-Rideal and Eley-Rideal mechanisms have been proposed by several authors.²³⁷ The rare suggestion of this pathway is perhaps explained by the work of Mittendorfer and Hafner, who calculated that the activation energy of the Langmuir-Rideal mechanism was almost 200 kJ mol⁻¹ higher than for the Langmuir-Hinshelwood pathway.¹¹⁵ This translates, assuming equal pre-exponential factors, to a difference in rate of more than 20 orders of magnitude between 110–190 °C. Nevertheless, chemisorbed benzene was observed to react with gas phase hydrogen atoms on the Cu(111) surface.²⁴⁴ Moreover, others have suggested the mechanism may depend on temperature: at low temperatures a Langmuir-Rideal or Eley-Rideal mechanisms was followed,²⁴⁵ but higher temperatures led to the Langmuir-Hinshelwood mechanism dominating for nickel catalysts.²¹⁹ Theoretical studies by Rocha *et*

*al.*²⁴⁶ even indicated that chemisorbed hydrogen may react with gas phase benzene, but did not supplement this hypothesis with kinetic evidence.

1.4.2 The partial hydrogenation of aromatic compounds

As noted above, the principal focus of this project is to achieve the partial reduction of GHC to its corresponding cyclic alkenes. So far, this review has focussed on how the monounsaturated intermediate may form, namely, through *ortho* attack and ceasing to react further after two moles of hydrogen have been added to a substrate. Yet, few examples of such reactions have been given. This section will remedy this issue and discuss the limited work in which yields of cycloalkene intermediate are greater than 10%. Two topics will be covered: (i) substituted alkyl aromatics, and (ii) the partial reduction of benzene.

1.4.3 The partial reduction of alkyl-substituted benzenes

Aromatic compounds with two or three *tert*-butyl substituents have allowed for 65% yields of the corresponding cycloalkene to be obtained. A summary of the findings is listed in Table 1.3. It may be noted that rhodium catalysts afford greater selectivity than ruthenium, palladium, or platinum catalysts. Why selectivity varies between metals is uncertain. The work discussed so far would suggest the dominant pathway for reduction is through *ortho* attack leading to the most sterically hindered alkene, which is notably not observed for 1,2-*ditert*-butylbenzene (entries 1–4). These studies employed practical catalysts, which probably consist of multiple crystal planes and not one surface as with the model studies. A plane dependent selectivity has been established on platinum surfaces, so this may suggest a similar pattern of reactivity on other metal surfaces.

Table 1.3: Literature examples of conditions and catalysts needed to obtain tetrahydrobenzenes.

| Entry | Substrate | Catalyst | Solvent | P_{H_2} (bar) | T (°C) | Maximum alkene yield | Reference |
|-------|-------------------------------|---|---------------------|-----------------|--------|----------------------|-----------|
| 1 | 1,2- <i>t</i> -Butylbenzene | 5 wt.% Rh/C | EtOH | 1 | 25 | 30.1 (2,3-ene) | [35] |
| 2 | 1,2- <i>t</i> -Butylbenzene | 5 wt.% Rh/C | AcOH | 1 | 25 | 45.2 (2,3-ene) | [35] |
| 3 | 1,2- <i>t</i> -Butylbenzene | 5 wt.% Rh/C | EtOH | 1 | 25 | 5.7 (2,3-ene) | [35] |
| 4 | 1,2- <i>t</i> -Butylbenzene | 5 wt.% Pt/C | AcOH | 1 | 25 | 7.5 (2,3-ene) | [35] |
| 5 | 1,2- <i>t</i> -Butylbenzene | PtO ₂ | AcOH | 1 | 25 | 11.5 (2,3-ene) | [35] |
| 6 | 1,3,5- <i>t</i> -Butylbenzene | 5 wt.% Pt/C | n-Heptane | 1 | 25 | 49 | [247] |
| 7 | 1,3,5- <i>t</i> -Butylbenzene | 5 wt.% Rh/C | n-Heptane | 1 | 25 | 65 | [247] |
| 8 | 1,3,5- <i>t</i> -Butylbenzene | 5 wt.% Pd/C | n-Heptane | 1 | 25 | 12 | [247] |
| 9 | 1,4- <i>t</i> -Butylbenzene | 5 wt.% Rh/Al ₂ O ₃ | Cyclohexane | 0.34 | 25 | 22 (1,4-ene) | [232] |
| 10 | 1,4- <i>t</i> -Butylbenzene | 5 wt.% Rh/Al ₂ O ₃ | Cyclohexane | 0.84 | 25 | 30 (1,4-ene) | [232] |
| 11 | 1,4- <i>t</i> -Butylbenzene | 5 wt.% Rh/Al ₂ O ₃ | Cyclohexane | 0.97 | 25 | 35 (1,4-ene) | [232] |
| 12 | 1,4- <i>t</i> -Butylbenzene | 5 wt.% Rh/Al ₂ O ₃ | Cyclohexane | 7.7 | 25 | 16 (1,4-ene) | [232] |
| 13 | 1,4- <i>t</i> -Butylbenzene | 5 wt.% Rh/Al ₂ O ₃ | Cyclohexane | 68 | 25 | 9 (1,4-ene) | [232] |
| 14 | 1,4- <i>t</i> -Butylbenzene | 5 wt.% Rh/Al ₂ O ₃ | Cyclohexane | 150 | 25 | 3 (1,4-ene) | [232] |
| 15 | 1,3- <i>t</i> -Butylbenzene | 5 wt.% Rh/Al ₂ O ₃ | Cyclohexane | 0.84 | 25 | 1 (1,2-ene) | [232] |
| 16 | 1-Methoxyindane | 5 wt.% Rh/Al ₂ O ₃ | Hexane | 50 | 25 | 18 (3,7-ene) | [248] |
| 17 | 1-Methoxyindane | 5 wt.% Rh/C | Ethanol (with NaOH) | 50 | 25 | 18 (3,7-ene) | [248] |
| 18 | Indane | 32 wt.% Ni/Al ₂ O ₃ | n-Dodecane | 100 | 170 | 0.3 (3,7-ene) | [208] |
| 19 | Naphthalene | 0.6% Pt/Al ₂ O ₃ | Cyclohexane | 34 | 200 | 0 | [249] |
| 20 | Naphthalene | 5 wt.% Pt/C | Cyclohexane | 30 | 30 | 0 | [249] |
| 21 | Naphthalene | 5 wt.% Pt/C | Cyclohexane | 26 | 200 | 0 | [249] |

Table 1.3: Literature examples of conditions and catalysts needed to obtain tetrahydrobenzenes.

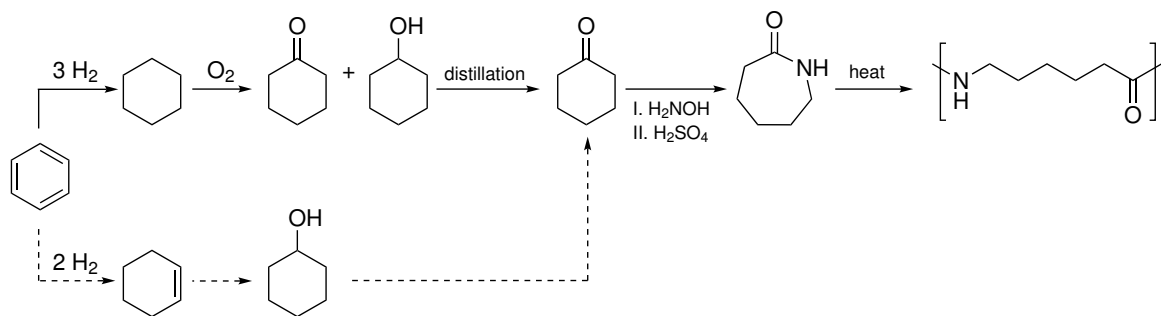
| Entry | Substrate | Catalyst | Solvent | P_{H_2} (bar) | T (°C) | Maximum alkene yield | Reference |
|-------|------------------------|-------------|--------------------------|-----------------|--------|--------------------------------|-----------------|
| 22 | Naphthalene | 5 wt.% Pt/C | Cyclohexane | 7 | 200 | 0 | [249] |
| 23 | Naphthalene | 5 wt.% Ru/C | Cyclohexane | 29 | 25 | 1.9 (2/3 1,9-ene 1/3 9,10-ene) | [249] |
| 24 | Naphthalene | 5 wt.% Ru/C | Cyclohexane | 25 | 200 | 0.2 | [249] |
| 25 | Naphthalene | 5 wt.% Ir/C | Cyclohexane | 28 | 60 | 0.3 (mostly 9,10-ene) | [249] |
| 26 | Naphthalene | 5 wt.% Ir/C | Cyclohexane | 26 | 200 | 0.4 (mostly 9,10-ene) | [249] |
| 27 | Naphthalene | 5 wt.% Pd/C | Cyclohexane | 29 | 38 | 0 | [249] |
| 28 | Naphthalene | 5 wt.% Pd/C | Cyclohexane | 33 | 200 | 0 | [249] |
| 29 | Naphthalene | 5 wt.% Pd/C | Cyclohexane | 7 | 200 | 0 | [249] |
| 30 | Naphthalene | 5 wt.% Rh/C | Cyclohexane | 33 | 25 | 0.8 (mostly 9,10-ene) | [249] |
| 31 | Naphthalene | 5 wt.% Rh/C | Cyclohexane | 23 | 200 | 0.7 (mostly 9,10-ene) | [249] |
| 32 | Naphthalene | 5 wt.% Rh/C | Cyclohexane | 30 | 25 | 1.2 (mostly 9,10-ene) | [249] |
| 33 | Pentamethyl tetralin | 5 wt.% Rh/C | None | 69 | 70 | 30 (unspecified) | [250] |
| 34 | <i>s</i> -Butylbenzene | Rh | [BMIM][BF ₄] | 40 | 75 | 14 | [251] |
| 35 | <i>o</i> -Xylene | Rh | [BMIM][BF ₄] | 40 | 75 | 5.3 (1,2-ene) 5.3 (2,3-ene) | [251] |
| 36 | <i>m</i> -Xylene | Rh | [BMIM][BF ₄] | 40 | 75 | 2.5 (1,3-ene) 2.5 (1,5-ene) | [251] |
| 37 | <i>p</i> -Xylene | Rh | [BMIM][BF ₄] | 40 | 75 | 4.1 (1,4-ene) | [251] |
| 38 | Toluene | Rh | [BMIM][BF ₄] | 40 | 75 | <1 (1-ene) | [251] |
| 39 | Ethylbenzene | Rh | [BMIM][BF ₄] | 40 | 75 | <1 (1-ene) | [251] |
| 40 | Propylbenzene | Rh | [BMIM][BF ₄] | 40 | 75 | 4.2 (1-ene) | [251] |
| 41 | Propylbenzene | Rh | [BMIM][BF ₄] | 40 | 75 | 30.9 (1-ene) | See SI in [251] |
| 42 | Propylbenzene | Rh | [BMIM][PF ₆] | 40 | 75 | 56.4 (1-ene) | See SI in [251] |

The nature of substituents also appears to be important. Increasing the number of substituents improves the yield, presumably due to a slower rate of addition at those locations. The difference in yield between the 1,3- and 1,4-isomers of di-*tert*-butylbenzene was attributed to the isomerisation of the 1,3- and 2,4-*tert*-butylcyclohexenes to the less sterically protected, and thus more reactive, *cis*-3,5-di-*tert*-butylcyclohexene. The effect was also present for 1,4-*tert*-butylcyclohexene, but the isomerisation to the more reactive 3,6 isomer—shown to be the origin of 80% of the saturated product in the low pressure region—was slower. 1-Methoxyindane (entries 16 and 17) displayed lower selectivity than the *tert*-butyl-substituted aromatics (entries 1–15), which is expected as there is less steric bulk.^{248,252} Compared with indane (entry 18), under vastly different conditions, a 60-fold improvement in intermediate yield is observed by introducing one substituent in the α position.²⁰⁸ The ring size does not appear to have a substantial effect on yield, as naphthalene provides similar quantities of octalins under similar conditions over a range of metals (entries 19–32).²⁴⁹ That said, the reduction of PMI to THPMI over palladium catalysts appears to yield twice as much tetrahydrobenzene than pentamethylnaphthalene produces over rhodium (entry 33),²⁵⁰ in contrast to what may be expected from the work on di- and tri-substituted *tert*-butylbenzenes (entries 1–8).

Pressure has been shown to strongly effect the yield of the monounsaturated intermediate during the reduction of 1,4-di-*tert*-butyl benzene by Siegel and co-workers (entries 9–14).^{231,232} In the region of 0.34 to 0.97 bar hydrogen, the maximum olefin yield increases with pressure. As pressure increases from 7.7 to 150 bar, the selectivity to the partially reduced product gradually decreases. The lower pressure region was controlled by the relative rate of isomerisation, while the higher pressure region was explained by an altered hydrogenation mechanism that promoted the deep hydrogenation of the arene.

Ionic liquids have been used in conjugation with ruthenium and rhodium catalysts to selectively reduce aromatic compounds to their corresponding tetrahydrobenzenes (entries 34–42). The promotional benefit of ionic liquids is thought to be caused by a surface poisoning effect.²⁵³ Evidence for this assertion are: (i) the more coordinating $[\text{PF}_6]^-$ ²⁵⁴ provides greater selectivity than $[\text{BF}_4]^-$; (ii) post-reaction analysis shows ionic liquids adsorb on the surface but do not induce electronic changes (as determined by X-ray photoelectron spectroscopy (XPS));²⁵³ and (iii) at low concentrations of ionic liquid ($\leq 3.5 \times 10^{-3} \text{ mol l}^{-1}$) the rate decreases non-linearly with increasing ionic liquid concentration, but the selectivity to cyclic alkenes remains constant;²⁵³ this suggests competition for surface sites.

As with the selective reduction of benzenes under more classical conditions, the introduction of bulky substituents results in higher quantities of the monoalkene intermediate.²⁵¹ Although, it is difficult to conclude which side group is most beneficial as full selectivity/yield conversion plots are not disclosed in the relevant publication. Interestingly, the total olefinic content obtained from *m*-xylene is greater than what is obtained from *p*-xylene,²⁵¹ in contrast with what would be expected from the work of Siegel and associates.^{231,232} This is possibly attributable to the ionic liquid retarding the rate of isomerisation, but no experiments were



Scheme 1.7: Standard industrial synthetic route for cyclohexanone (full arrows) and alternative synthesis of nylon 6 via cyclohexene (dashed arrows). Figure and caption reproduced with permission from [261].

performed to support this proposal. Benzene was also selectively reduced in this manner, but the yield was low and much greater yields are obtainable with the method discussed in the next section.²⁵⁵

1.4.3.1 The partial reduction of benzene

The partial reduction of benzene to cyclohexene is the most extensively studied reaction in this field and commercially, which operates at a scale of approximately 170,000 tons per year.²⁵⁶ The process attracts considerable interest as cyclohexene affords a more sustainable route for producing polyamides (Scheme 1.7). Much like the Cashmeran process, obtaining a high selectivity to the partial reduced intermediate is greatly challenging. Performing this reaction either solventless or solvated produces cyclohexene yields of at most a few percent. Several researchers have noted that the addition of small quantities of alcohols to a hydrocarbon solvent improves selectivity for cyclohexene approximately five-fold, but no such enhancement is observed for 1-methylcyclohexene in the partial reduction of toluene.²⁵⁷ Such low yields are not industrially feasible and in order to make the process viable a tetraphasic reactor is employed comprised of a gas (hydrogen), liquid (aqueous, containing added metal salts or organic compounds; and hydrocarbon; benzene, cyclohexene, cyclohexane), and solid (almost always ruthenium-based catalyst) at temperatures close to, or at, 150 °C under 50 bar hydrogen pressure. Almost all work in this area performed since the early 1980s has employed a reactor operating in this manner and industrial yields of cyclohexene are approximately 60%,^{258,259} though recent work has claimed a yield of 75.1% is possible.²⁶⁰

A number of studies have attempted to determine the optimum pressure for the reaction.^{262–266} Ning *et al.* found that the cyclohexene yield passes through a maximum in the region of 40–60 bar.²⁶⁵ Two factors operating concurrently were used to account for this behaviour. Firstly, it was proposed that the more selective stepwise addition process is preferred at higher pressures. The work discussed above indicates this reason is perhaps less probable, but the addition of the water phase complicates the issue. Secondly, at high hydrogen pressures the surface is purported to be saturated with hydrogen, and thus, fewer sites are available for benzene adsorption. Simultaneously, the hydrogenation of cyclohex-

ene becomes more facile when the surface is hydrogen rich. This could imply that: (i) the reactants competitively adsorb for surface sites, and that cyclohexene adsorbs more strongly than benzene; (ii) cyclohexene adsorbs on a separate site; and/or (iii) cyclohexene does not need to chemisorb to react. Each of these can probably be discounted. For (i), some kinetic data for a similar system hints at possible competition between benzene and hydrogen,²⁶⁶ but the adsorption enthalpy of benzene on the Ru(0001) surface was computed to be 30 kJ mol^{-1} higher than for cyclohexene.¹⁴⁷ Points (ii) and (iii) can be discarded on a probability basis. The difference in yield was also small, so could be caused by experimental error, but another explanation is that higher pressures result in a more hydrophobic surface, which reduces the catalysts interaction with water (*vide infra*). Meanwhile, other studies find pressure has no effect on yield, or it initially increases before plateauing.^{264,266} The former is ascribed to mass transfer effects²⁶⁴ whereas the latter was afforded no explanation.²⁶⁶

Temperature has also been found to impact the selectivity of the reaction.^{262–267} The selectivity/yield to cyclohexene initially increases as a function of temperature.^{262–267} Some workers then find it decreases at higher temperatures, whilst others do not,^{263,264} even if the same temperature region is explored.^{262,265–267} The initial increase was attributed to higher temperatures promoting the desorption of cyclohexene as it is an endothermic process.²⁶⁴ However, considering the work on platinum surfaces discussed above, an additional cause could involve a different mechanism. The maximum in selectivity as a function of temperature, which is not always observed, is stated to originate from increased cyclohexene solubility in water,²⁶⁷ catalyst decomposition, or agglomeration.²⁶¹ The solubility factor should affect all systems and initial studies revealed no relationship between particle size and cyclohexene selectivity.²⁶⁸

Despite long being recognised as important, the role of the water phase is still poorly understood. Some workers demonstrate that a stagnant water layer surrounding the particles imposes a mass transfer limitation.^{57,58,263,264,268} In turn, this allows for high cyclohexene yields to be obtained. Mass transfer limitations are not present in all instances, however, and instead attribute the enhancement to the six times lower solubility of cyclohexene in water compared with benzene at $150 \text{ }^\circ\text{C}$, or the nature of the catalyst itself.^{58,268,269} It has also been suggested that water improves yield through competitive adsorption and promoting the desorption of the cyclohexene, with the latter becoming more efficient in the presence of soluble metal salts. Early studies demonstrated that water is predominantly associatively adsorbed on ruthenium surfaces,^{270,271} although dissociative adsorption also occurs to some extent as evidenced by the $\text{H}_2\text{-D}_2\text{O}$ exchange reaction.²⁷²

Table 1.4: Selected examples of catalysts for the partial reduction of benzene.

| Entry | Catalyst | Benzene/Water (v/v) | Additives (concentration/volume) | P_{H_2} (bar) | T °C | Max C ₆ H ₁₀ yield (%) | Reference |
|-------|--|------------------------|-------------------------------------|--------------------|---------|---|-----------|
| 1 | Ru (unsupported) | 2.67 | ZnSO ₄ (0.16 M) | 50 | 150 | 16 ^a] | [264] |
| 2 | | 2.67 | ZnSO ₄ (0.16 M) | 50 | 150 | 46.1 ^b] | [264] |
| 3 | Ru (unsupported) | 1.67 | NiSO ₄ (0.16 M) | 35 | 150 | 11.6 | [60] |
| 4 | | 1.67 | MnSO ₄ (0.16 M) | 35 | 150 | 3.2 | [60] |
| 5 | | 1.67 | CrSO ₄ (0.16 M) | 35 | 150 | 5.1 | [60] |
| 6 | | 1.67 | ZnSO ₄ (0.16 M) | 35 | 150 | 26.3 | [60] |
| 7 | Ru/SiO ₂ (unknown loading) | 0.5 | ZnSO ₄ (0.6 M) | 60 | 130 | 25.6 | [265] |
| 8 | | 0.5 | ZnSO ₄ (0.6 M) | 60 | 140 | 39.4 | [265] |
| 9 | | 0.5 | ZnSO ₄ (0.6 M) | 60 | 160 | 37.6 | [265] |
| 10 | | 0.5 | ZnSO ₄ (0.6 M) | 40 | 140 | 21 | [265] |
| 11 | | 0.5 | ZnSO ₄ (0.6 M) | 70 | 141 | 38.7 | [265] |
| 12 | 2 wt.% Ru/La ₂ O ₃ | 0.5 | None | 20 | 150 | 15.3 | [266] |
| 13 | | 0.5 | None | 60 | 150 | 26.9 | [266] |
| 14 | | 0.5 | None | 90 | 150 | 27.7 | [266] |
| 15 | 1 wt.% Ru 1 wt.% La/SBA-15 | 0.5 | None | 40 | 140 | 7 | [273] |
| 16 | | 0.5 | CdSO ₄ (0.00156 M) | 40 | 140 | 28 | [273] |
| 17 | 1 wt.% Ru/La ₂ O ₃ | 0.5 | None | 20 | 100 | 0.8 | [274] |
| 18 | | 0.5 | NaN(CN) ₂ (0.006 M) | 20 | 100 | 5 | [274] |
| 19 | 5.8 wt.% Ru/Al ₂ O ₃ | 0.83 | None | 50 | 100 | 5 | [275] |
| 20 | | 1.2 | Ethyl acetate (9 mL) | 50 | 100 | 6.5 | [275] |
| 21 | | 1.2 | n-Methyl-2-pyrrolidone (9 mL) | 50 | 100 | 7.8 | [275] |
| 22 | | 1.3 | Ethylene glycol (9 mL) | 50 | 100 | 10.7 | [275] |
| 23 | | 0.8 | Monoethanolamine (500 ppm) | 50 | 100 | 15.5 | [275] |
| 24 | 1 wt.% Rh/Al ₂ O ₃ | 3 | HgCl ₂ (0.25 wt%) | 35 | 180 | 20.6 | [262] |
| 25 | 1.5 wt.% Ru/TiO ₂ | 0.33 | None | 50 | 150 | 23.8 | [260] |
| 26 | 1.5 wt.% Ru@TiO ₂ /TiO ₂ | 0.33 | None | 50 | 150 | 75.1 | [260] |
| 27 | 2 wt.% Ru/ZrO ₂ | 0.3 | None | 50 | 150 | 7.3 | [276] |
| 28 | 2 wt.% Ru@ZrO ₂ /ZrO ₂ | 0.33 | None | 50 | 150 | 21.5 | [276] |

^a First use.

^b Fourth use. Improve selectivity attributed to incorporation of iron from the reactor walls.

The aqueous phase usually contains soluble soluble metal salts or organic molecules, which are added to gain further improvements in selectivity. It is preferable to not use such compounds, since they can be corrosive and contribute to reactor fouling, but the selectivity gains by their addition generally redeem their negative attributes. The promotional effect of metal additives was as a serendipitous discovery, observed when the sodium hydroxide aqueous phase leached metal ions from the stainless steel autoclave walls and the bearings used for the impeller assembly.²⁷⁷ Metal ions in stainless steel—iron, chromium, nickel, manganese, copper, and lead—have all since been studied, amongst others, as additives for this reaction with varying degrees of success. However, the seminal work of Scholten and co-workers in the early 1990s lead to the prominent use of zinc sulfate as a reaction modifier.^{60,264} Organic additives on the other hand do not have a canonical molecule: reported compounds are all capable of forming hydrogen bonds and usually possess an alcohol or amine functional group but lactams and dicyanamide salts have also been used (entries 18, 20–23).

The promotional effect of additives is not fully understood. In their review, Foppa and Dupont summarised additives may (i) improve the hydrophilicity of the ruthenium surface (ii) promote the desorption of cyclohexene through physiochemical bonding (iii) poisoning or competing for sites on the surface (iv) electronic modification of the surface.²⁶¹ Similar reasoning is used when discussing the observed beneficial effect of chloride precursors.²⁶⁸ However, the nature of the physiochemical bond has come into question. In one study, Fan and co-workers investigated how ZnSO_4 and CdSO_4 benefited cyclohexene selectivity using gas phase DFT of hydrated and bare metal cations, which was supplemented by experimental methods.²⁷³ They concluded that CdSO_4 primarily modifies the surface whilst ZnSO_4 aids the desorption and hinders the re-adsorption of cyclohexene. An earlier study, however, considered the fully solvated Zn^{2+} and Cd^{2+} cations. They concluded that although metal cation- π and hydrogen bonded complexes are energetically feasible in the gas phase, when solvated the energy penalty is too high and are therefore implausible.²⁷⁸

A separate concern is the electronic state of ruthenium. It has been claimed that both electron-rich and electron-deficient ruthenium are key to obtaining high cyclohexene selectivity. The beneficial effect of electron-deficient ruthenium is ascribed to cyclohexene being weakly adsorbed and easily desorbed from the surface. However, many studies that purport the importance of a $\text{Ru}^{\delta+}$ species evidence its existence using the XPS Ru 3d region^{60,279–282} which overlaps with the C 1s region, and consequently renders accurate identification of Ru species problematic if not processed carefully.²⁸³ A solution to this problem is to use the less well studied Ru 3p region, which suffers from less interference from other elements and is suitable for quantitative and qualitative analysis.²⁸³ Indeed, studies which use the Ru 3p region have evidenced the existence of such a species,^{284–286} thus providing support for this hypothesis, which is also available from theoretical studies on several atom metal clusters.²⁸⁷

There are fewer studies claiming that electron-rich ruthenium improves selectivity to

cyclohexene. The logic in these instances is that the organic molecule containing N or O atoms donates a pair of electrons to a vacant d orbital, which enhances the electron density on ruthenium and promote the desorption of cyclohexene through electron repulsion.²⁸⁸ It is interesting to note that this article was submitted for publication five months before the same group later claimed the importance of the electron deficient species and utilised a catalyst composed of the same elements (RuCoB/Al₂O₃) under slightly different conditions.²⁸¹ A promotional effect such as this would probably be classified as a ligand effect, whose role is generally well understood in homogeneous catalysis, but much less well established in heterogeneous catalysis. Any effect would only be observed in the vicinity of the donor molecule and not the entire nanoparticle.

A puzzling aspect of almost all work in this area is the near sole use of ruthenium-based catalysts for this reaction. To put it into perspective, out of the hundreds of articles published for this reaction there is a single report of systems that do not, in part, contain ruthenium.²⁶² The same is true for toluene.²⁸⁹ Authors will often claim that ruthenium is the most selective for this reaction and is therefore used in their study but seldom cite any work where this is shown, with the superior performance of ruthenium being perhaps more attributable to lore rather than science. This belief could stem from work performed by Hartog and Zwietering in the early 1960s, which revealed small quantities of dimethyl cyclic olefins were achievable over carbon-supported rhodium ruthenium, and to a lesser extent Raney nickel, but not Pd/C or Pt/C under atmospheric hydrogen pressure between 0 and 60 °C.²⁹⁰ As discussed above, conditions clearly play a role, so the minimal work in other areas is disappointing. Maybe the lack of publications of work featuring the performance of other metals for this reaction is because they provide no selectivity: this we know to be false because of data available in patents.²⁹¹ Moreover, even if the performance of these catalysts is poor it still adds to the corpus of knowledge on the subject and may aid its development.

The only example for benzene hydrogenation is a Rh/Al₂O₃ catalyst poisoned with mercury.^{262,292} A cyclohexene yield of 20.6% was obtained in this instance which performs similarly to many ruthenium-based catalysts. The effect of mercury was ascribed to the same poisoning effect as described above. Surprisingly, for the partial hydrogenation of toluene, the Pt/Al₂O₃ and Pd/Al₂O₃ catalysts were reported to be inactive, but limited characterisation was conducted on these materials.²⁸⁹ Perhaps the strongest example of the ruthenium fixation in this area are two recent articles which claim to coat ruthenium nanoparticles in a porous shell of ZrO₂ and TiO₂.^{260,276} These shells are not caused by strong metal-support interaction effects and supposedly act to prevent benzene and cyclohexene adsorbing on the metal surface, thereby forcing the hydrogenation reactions to take place on the support using hydrogen, which can travel through these pores, that has spilled over. In these instances, the promotional effect of the metal oxide is attributed to a higher energy transition state for cyclohexene hydrogenation (and thus a slower rate).²⁶⁰ A separate article published at approximately the same time using very similar methodology by Yu *et al.* reasoned that the higher yields are due

to an enhancement of the hydrophilic effect described above when using the Ru@XO₂ (X=Ti, Si, or Zr) catalysts.²⁹³

1.5 Summary

This chapter has provided a foundation for the experimental work documented in this thesis. Initially, a brief introduction to the fragrances industry was provided, including a few examples of the difficulties it encounters. The reaction relevant to this work, namely, the partial reduction of GHC was introduced along with a background of relevant industrial processes. Then, a broader discussion of the reduction of the aromatic hydrocarbons followed with the aim of giving some insight into why and how the desired tetrahydroindanes may form. The final section outlined examples of instances where significant amounts of partially reduced products from benzene and other arenes were observed during experiments.

1.6 Thesis aims

The partial reduction of GHC to cyclic alkenes is an important step in the synthesis of the Cashmeran family of fragrances. In recent years, demand for these end stage products has soared significantly and this reaction now acts as a bottleneck for the process. To this end, the main aim of this thesis is two-fold, in that it is of a fundamental and an applied nature. On the one hand, the fundamental objective would be to gain an understanding of how the reaction mechanism depends on various experimental parameters, such as temperature and hydrogen pressure, or on the nature of the metal. On the other hand, this deeper understanding of the reaction should identify potential strategies that will allow for yield improvements without lowering reactor throughput at the industrial scale.

1.7 References

- [1] C. Wedekind, T. Seebach, F. Bettens and A. J. Paepke, *Proc. R. Soc. London. Ser. B Biol. Sci.*, 1995, **260**, 245–249.
- [2] M. McCoy, *DuPont's nutrition business will merge with IFF*, 2020, <https://cen.acs.org/business/mergers-&-acquisitions/DuPonts-nutrition-business-merge-IFF/98/i1>, accessed 2020-05-11.
- [3] *Smell Test Being Developed at Boston Hospitals Could Hold the Key to Early Covid-19 Detection*, 2020, [urlhttps://ir.iff.com/news-releases/news-release-details/smell-test-being-developed-boston-hospitals-could-hold-key-early](https://ir.iff.com/news-releases/news-release-details/smell-test-being-developed-boston-hospitals-could-hold-key-early), accessed 2020-06-10.

- [4] M. M. Bomgardner, *How perfumers walk the fine line between natural and synthetic*, 2019, <https://cen.acs.org/business/consumer-products/perfumers-walk-fine-line-between/97/i16>, last accessed 2020-05-18.
- [5] G. Ohloff, *Perfum. Flavor*, 1978, **3**, 11–22.
- [6] N. Neuner-Jehle and F. Etzweiler, in *Perfumes: Art, Science, and Technology*, ed. P. M. Müller and D. Lamparsky, Elsevier, London, 1991, ch. 6, pp. 153–212.
- [7] C. Nussbaumer, G. Fráter and P. Kraft, *Helv. Chim. Acta*, 1999, **82**, 1016–1024.
- [8] F. Etzweiler, D. Helmlinger, C. Nussbaumer and M. Pesaro, *Acetyl-tri- and tetramethyl octahydronaphthalenes and fragrances compositions containing the same*, US5214160, May 1993.
- [9] A. Stepanyuk and A. Kirschning, *Beilstein J. Org. Chem.*, 2019, **15**, 2590–2602.
- [10] K. A. D. Swift and P. Kraft, in *Advances in Flavours and Fragrances*, ed. K. A. D. Swift, Royal Society of Chemistry, Cambridge, 1st edn., 2002, ch. 15, pp. 138–146.
- [11] J. P. Barras, B. Bourdin and F. Schröder, *Chimia (Aarau)*, 2006, **60**, 574–579.
- [12] M. Gautschi, J. A. Bajgrowicz and P. Kraft, *Chimia (Aarau)*, 2001, **55**, 379–387.
- [13] European Chemicals Agency, *1-(1,2,3,4,5,6,7,8-octahydro-2,3,8,8-tetramethyl-2-naphthyl)ethan-1-one and 1-(1,2,3,4,6,7,8,8a-octahydro-2,3,8,8-tetramethyl-2-naphthyl)ethan-1-one and 1-(1,2,3,5,6,7,8,8a-octahydro-2,3,8,8-tetramethyl-2-naphthyl)ethan-1-one*, <https://echa.europa.eu/registration-dossier/-/registered-dossier/15069/1/2>, accessed 2020-05-11.
- [14] European Chemicals Agency, *(2R*,3S*)-2-acetyl-1,2,3,4,5,6,7,8-octahydro-2,3,8,8-tetramethylnaphthalene; reaction mass of: (1R*,2S*)-2-acetyl-1,2,3,4,5,6,7,8-octahydro-1,2,8,8-tetramethylnaphthalene*, <https://echa.europa.eu/registration-dossier/-/registered-dossier/9580/1/2>, accessed 2021-02-28.
- [15] G. Fráter, U. Müller and P. Kraft, *Helv. Chim. Acta*, 1999, **82**, 1656–1665.
- [16] European Chemicals Agency, *1,2,3,5,6,7-hexahydro-1,1,2,3,3-pentamethyl-4H-inden-4-one*, <https://echa.europa.eu/registration-dossier/-/registered-dossier/15957>, accessed 2020-05-11.
- [17] European Chemicals Agency, *7,7,8,9,9-pentamethyl-6,7,8,9-tetrahydro-5H-cyclopenta[h]quinazoline*, <https://echa.europa.eu/pl/substance-information/-/substanceinfo/100.227.675>, accessed 2021-04-06.

- [18] European Chemicals Agency, *7,7,8,9,9-pentamethyl-6,6a,7,8,9,9a-hexahydro-5H-cyclopenta[h]quinazoline*, <https://echa.europa.eu/pl/substance-information/-/substanceinfo/100.228.446>, accessed 2021-04-06.
- [19] European Chemicals Agency, *(4aR,8R,9bS)-7,7,8,9,9-pentamethyl-4,4a,5,6,7,8,9,9b-octahydroindeno[4,5-d][1,3]dioxine and (4aR,8S,9bS)-7,7,8,9,9-pentamethyl-4,4a,5,6,7,8,9,9b-octahydroindeno[4,5-d][1,3]dioxine*, <https://echa.europa.eu/pl/substance-information/-/substanceinfo/100.104.052>, accessed 2020-05-11.
- [20] European Chemicals Agency, *2,2,6,6,7,8,8-heptamethyl-4,5,6,7,8,8B-hexahydro-3AH-indeno[4,5-D][1,3]dioxole*, <https://echa.europa.eu/pl/substance-information/-/substanceinfo/100.104.541>, accessed 2020-05-13.
- [21] European Chemicals Agency, *2,6,6,7,8,8-hexamethyldecahydro-2H-indeno[4,5-b]furan*, <https://echa.europa.eu/substance-information/-/substanceinfo/100.103.656>, accessed 2021-04-06.
- [22] European Chemicals Agency, *Indeno(4,3 A-B) Furan Decahydro-2,2,7,7,8,9,9-Heptamethyl-*, <https://echa.europa.eu/pl/substance-information/-/substanceinfo/100.104.188>, accessed 2020-05-06.
- [23] R. A. Weiss, *1,1,2,3,3-pentamethyl-indan and preparation method thereof*, CN103772119A, May 2014.
- [24] G. Benz and E. H. Polak, *Production of poly alkyl indanes from styrene compounds*, US2851501, Sept. 1958.
- [25] D. B. Spoelstra, S. H. Weber and R. J. C. Kleipool, *Recl. des Trav. Chim. des Pays-Bas*, 1963, **82**, 1100–1106.
- [26] G. J. Ferber and P. J. Goddard, *Process for the production of indanes; process for the production of isochromans and indane precursors used in this process*, EP0061267A1, Mar. 1982.
- [27] M. A. Sprecker, S. Bright, M. H. Vock and F. L. Schmitt, *Flavoring with indane alkanols and tricyclic isochromans*, US4315951, Feb. 1982.
- [28] U. M. Dzhemilev, Katepov, B. Ivanovich, S. V. Bubennov, N. G. Grigorieva and M. R. Aglyullyl, *Method of producing homo- and co-oligomers of α -methylstyrene and isopentenes in the presence of hierarchical zeolite h-ymmm*, RU2735666C1, May 2020.
- [29] R. L. Cobb, *Acid catalyzed reactions of monovinyl aromatic compounds*, US4596896A, Jun. 1985.

- [30] R. L. Cobb, *Acid-sulfonance catalyzed production of cyclic alkylated compounds*, US5034562A, Jul. 1990.
- [31] E. Henkes, K. Halbritter, H. Mayr, W. Striepe and R. Pock, *Preparation of Indanes*, US4740646, Apr. 1988.
- [32] L. G. Heeringa and M. G. J. Beets, *Tricyclic isochromans and processes for making the same*, US3360530, Dec. 1967.
- [33] J. Stofberg and K. N. Nieuwland, *Process for preparing polyalkylindans*, US3278622A, Oct. 1966.
- [34] O. C. Okafor, S. Tadepalli, G. Tamy and A. Lawal, *Ind. Eng. Chem. Res.*, 2010, **49**, 5549–5560.
- [35] B. van de Graaf, H. van Bekkum and B. M. Wepster, *Recl. des Trav. Chim. des Pays-Bas*, 1968, **87**, 777–785.
- [36] J. B. Hall, *Indanone derivatives and processes for producing same*, US3773836, Nov. 1973.
- [37] P. W. Rabideau and Z. Marcinow, in *Organic Reactions*, 1992, vol. 42, pp. 1–334.
- [38] D. K. Joshi, J. W. Sutton, S. Carver and J. P. Blanchard, *Org. Process Res. Dev.*, 2005, **9**, 997–1002.
- [39] B. K. Peters, K. X. Rodriguez, S. H. Reisberg, S. B. Beil, D. P. Hickey, Y. Kawamata, M. Collins, J. Starr, L. Chen, S. Udyavara, K. Klunder, T. J. Gorey, S. L. Anderson, M. Neurock, S. D. Minter and P. S. Baran, *Science*, 2019, **363**, 838–845.
- [40] P. N. Rylander, *Hydrogenation Methods*, Academic Press, London, 1st edn., 1985.
- [41] J. B. Hall, *Hydrogenated indane derivatives and processes for producing the same*, US3751500, Aug. 1973.
- [42] B. Li, X. Lichun and G. Yuncui, *Method for preparing polymethyl substituted tetrahydroindane by selective hydrogenation of polymethyl substituted indane*, CN1117037A, Feb. 1996.
- [43] C. Lopez Cruz, *Private communication*, 2018.
- [44] S. Tadepalli, G. K. Tamy and A. P. Narula, *Circular economy methods of preparing unsaturated compounds*, US10435345B2, Oct. 2019.
- [45] Podkolzin, *Palladium catalysts supported on carbon for hydrogenation of aromatic hydrocarbons*, US20200001274A1, Jun. 2020.

- [46] M. Iwanow, T. Gärtner, V. Sieber and B. König, *Beilstein J. Org. Chem.*, 2020, **16**, 1188–1202.
- [47] Norit Corp, *Private communication*, 2021.
- [48] D. Vamvuka and E. Kakaras, *Fuel Process. Technol.*, 2011, **92**, 570–581.
- [49] S. V. Vassilev, C. G. Vassileva and D. Baxter, *Fuel*, 2014, **129**, 292–313.
- [50] S. V. Vassilev, C. G. Vassileva, Y.-C. Song, W.-Y. Li and J. Feng, *Fuel*, 2017, **208**, 377–409.
- [51] J. M. M. Tengco, Y. K. Lugo-José, J. R. Monnier and J. R. Regalbuto, *Catal. Today*, 2015, **246**, 9–14.
- [52] R. Banerjee and J. R. Regalbuto, *Appl. Catal. A Gen.*, 2020, **595**, 117504.
- [53] B. Li, X. Li, H. Wang and P. Wu, *J. Mol. Catal. A Chem.*, 2011, **345**, 81–89.
- [54] J. Zazo, A. Fraile, A. Rey, A. Bahamonde, J. Casas and J. Rodriguez, *Catal. Today*, 2009, **143**, 341–346.
- [55] R. Ferrando, J. Jellinek and R. L. Johnston, *Chem. Rev.*, 2008, **108**, 845–910.
- [56] H. Praliaud, J. A. Dalmon, C. Mirodatos and G. A. Martin, *J. Catal.*, 1986, **97**, 344–356.
- [57] L. Ronchin and L. Toniolo, *Catal. Today*, 1999, **48**, 255–264.
- [58] L. Ronchin and L. Toniolo, *Catal. Today*, 2001, **66**, 363–369.
- [59] L. Ronchin and L. Toniolo, *Appl. Catal. A Gen.*, 2001, **208**, 77–89.
- [60] J. Struijk, R. Moene, T. van der Kamp and J. J. F. Scholten, *Appl. Catal. A Gen.*, 1992, **89**, 77–102.
- [61] P. H. Emmett and N. Skau, *J. Am. Chem. Soc.*, 1943, **65**, 1029–1035.
- [62] G. Rienecker and S. Engels, *Zeitschrift fuer Anorg. und Allg. Chemie*, 1965, **336**, 259–269.
- [63] D. A. Cadenhead and N. G. Masse, *J. Phys. Chem.*, 1966, **70**, 3558–3566.
- [64] C. A. Leon and M. Albert Vannice, *Appl. Catal.*, 1991, **69**, 305–321.
- [65] A. Borodziński and G. C. Bond, 2008, **50**, 379–469.
- [66] I. Felker, G. Pupo, P. Kraft and B. List, *Angew. Chem. Int. Ed.*, 2015, **54**, 1960–1964.

- [67] N. Armanino, J. Charpentier, F. Flachsmann, A. Goeke, M. Liniger and P. Kraft, *Angew. Chem. Int. Ed.*, 2020, **59**, 16310–16344.
- [68] J. B. Hall and L. K. Lala, *Allylic oxidation of bicyclic hydrocarbons to alcohols and ketones*, US3847993A, Nov. 1974.
- [69] J. D. Macginley, *PhD Thesis*, Cardiff University, 2021.
- [70] O. Casanova Navarro, A. Corma Canós and S. Iborra Jornet, *Allylic oxidation method for the preparation of fragrances using metal-organic compounds and gold catalysts*, US8269048B2, Sep. 2012.
- [71] A. T. Levorse, A. P. Narula, E. Arruda and C. E. J. Beck, *Polyalkylbicyclic derivatives*, US6632788B2, Oct. 2003.
- [72] A. T. Levorse, A. P. S. Narula, E. M. Arruda and C. E. J. Beck, *Polyalkylbicyclic derivatives*, US7160852B2, Jan. 2007.
- [73] M. G. Monteleone, R. P. Belko, F. T. Schiet, P. D. Jones and A. T. Levorse, *Novel quinazoline compounds and their use in perfume compositions*, US20150218485A1, Feb. 2015.
- [74] R. P. Belko, F. T. Schiet, M. G. Monteleone, P. D. Jones, A. P. Narula and A. T. Levorse, *Novel quinazoline derivatives and their use in perfume compositions*, EP2851415B1, Apr. 2016.
- [75] R. P. Belko, P. D. Jones, A. T. Levorse, M. G. Monteleone, A. P. Narula and F. T. Schiet, *Novel pyrimidine derivatives and their use in perfume compositions*, EP2644688B1, Nov. 2017.
- [76] A. P. Narula, *Chem. Biodivers.*, 2014, **11**, 1629–1638.
- [77] C. Sell, in *The Chemistry of Fragrances*, ed. C. S. Sell, Royal Society of Chemistry, Cambridge, 2007, ch. 4, pp. 52–131.
- [78] R. P. Belko, M. A. Sprecker and C. E. J. Beck, *Methylene dioxy tetrahydroindane derivative*, US6303798, Oct. 2001.
- [79] M. Monteleone, R. Belko, M. Pawlak, C. Smith and M. Sprecker, *Acetonide fragrance compound*, US20050009729, Jan. 2005.
- [80] M. A. Sprecker, R. P. Belko and C. E. J. Beck, *Substituted tetrahydroindane derivatives and organoleptic uses of substituted tetrahydroindanes*, US20050009729, Feb. 1990.

- [81] M. A. Sprecker, R. A. Weiss, A. T. Levorse, H. H. Heinsohn, C. E. J. Beck and M. R. Hanna, *Carbon containing functional group substituted 4,5,6,7-tetrahydro-polyalkylated-4-indanes, isomers thereof, processes for preparing same and uses thereof*, US6271193B1, Aug. 2001.
- [82] P. Gallezot and D. Richard, *Catal. Rev.*, 1998, **40**, 81–126.
- [83] X. Wang, X. Liang, P. Geng and Q. Li, *ACS Catal.*, 2020, **10**, 2395–2412.
- [84] R. A. Farrar-Tobar, A. Dell'Acqua, S. Tin and J. G. de Vries, *Green Chem.*, 2020, **22**, 3323–3357.
- [85] M. B. Conway, *Hydrogenation of cinnamaldehyde to phenylpropanal over supported Pd catalysts*, Cardiff university technical report, 2017.
- [86] F. Doro, N. Akeroyd, F. Schiet and A. Narula, *Angew. Chem. Int. Ed.*, 2019, **131**, 7248–7253.
- [87] P. Sabatier and E. Reid, *Catalysis in organic chemistry*, D. Van Nostrand Company, New York, 1922.
- [88] V. N. Ipatieff, *Catalytic reactions at high pressures and temperatures*, The Macmillan Co., New York, 1936.
- [89] G. Lunge and J. Akunoff, *Zeitschrift für Anorg. Chemie*, 1900, **24**, 191–202.
- [90] B. T. Utelbaev, P. P. Zanozina and B. Z. Zhanabaev, *Izv. Vyss. Uchebnykh Zaved. Khimiya i Khimicheskaya Tekhnologiya*, 1986, **29**, 34–37.
- [91] M. Douthwaite.
- [92] C. Gelis, A. Heusler, Z. Nairoukh and F. Glorius, *Chem. Eur. J.*, 2020, **26**, 14090–14094.
- [93] G. J. Janz, *J. Chem. Phys.*, 1954, **22**, 751–752.
- [94] G. C. Bond, *Metal-catalysed reactions of hydrocarbons*, Springer, 2006.
- [95] A. Stanislaus and B. H. Cooper, *Catal. Rev.*, 1994, **36**, 75–123.
- [96] S. A. Ali, *Pet. Sci. Technol.*, 2007, **25**, 1293–1304.
- [97] G. C. Bond and P. B. Wells, *Adv. Catal.*, 1965, **15**, 91–226.
- [98] G. C. Bond, *Cat. Rev.*, 2008, **50**, 532–567.
- [99] S. L. Scott, *ACS Catal.*, 2019, **9**, 4706–4708.

- [100] G. J. Hutchings, *Faraday Discuss.*, 2021, **229**, 9–34.
- [101] M. A. Vannice, *Kinetics of Catalytic Reactions*, Springer US, Boston, MA, 2005.
- [102] G. Rupprechter, *Adv. Catal.*, 2007, **51**, 133–263.
- [103] G. A. Somorjai and Y. Li, *Introduction to surface chemistry and catalysis*, Wiley, New York, 2nd edn., 2010.
- [104] A. G. Lambert, P. B. Davies and D. J. Neivandt, *Appl. Spectrosc. Rev.*, 2005, **40**, 103–145.
- [105] K. M. Bratlie, L. D. Flores and G. A. Somorjai, *J. Phys. Chem. B*, 2006, **110**, 10051–10057.
- [106] K. M. Bratlie, M. O. Montano, L. D. Flores, M. Paajanen and G. A. Somorjai, *J. Am. Chem. Soc.*, 2006, **128**, 12810–12816.
- [107] K. M. Bratlie, C. J. Kliewer and G. A. Somorjai, *J. Phys. Chem. B*, 2006, **110**, 17925–17930.
- [108] V. H. Grassian and E. L. Muetterties, *J. Phys. Chem.*, 1987, **91**, 389–396.
- [109] F. S. Thomas, N. S. Chen, L. P. Ford and R. I. Masel, *Surf. Sci.*, 2001, **486**, 1–8.
- [110] M. Getzlaff, J. Bansmann and G. Schönhense, *Surf. Sci.*, 1995, **323**, 118–128.
- [111] K. Habermehl-Ćwirzeń, J. Katainen, J. Lahtinen and P. Hautojärvi, *Surf. Sci.*, 2002, **507-510**, 57–61.
- [112] K. Pussi, M. Lindroos, J. Katainen, K. Habermehl-Ćwirzeń, J. Lahtinen and A. Seitsonen, *Surf. Sci.*, 2004, **572**, 1–10.
- [113] C. Papp, T. Fuhrmann, B. Tränkenschuh, R. Denecke and H. P. Steinrück, *Phys. Rev. B Condens. Matter*, 2006, **73**, 1–9.
- [114] F. Mittendorfer and J. Hafner, *Surf. Sci.*, 2001, **472**, 133–153.
- [115] F. Mittendorfer and J. Hafner, *J. Phys. Chem. B*, 2002, **106**, 13299–13305.
- [116] W. Braun, G. Held, H. P. Steinrück, C. Stellwag and D. Menzel, *Surf. Sci.*, 2001, **475**, 18–36.
- [117] G. Held, W. Braun, H.-P. Steinrück, S. Yamagishi, S. J. Jenkins and D. A. King, *Phys. Rev. Lett.*, 2001, **87**, 216102.
- [118] C. Morin, D. Simon and P. Sautet, *J. Phys. Chem. B*, 2004, **108**, 5653–5665.

- [119] B. E. Koel, J. E. Crowell, C. M. Mate and G. A. Somorjai, *J. Phys. Chem.*, 1984, **88**, 1988–1996.
- [120] M.-J. Treanor, J. A. Garrido Torres, C. J. Bromley, H. A. Früchtl and R. Schaub, *J. Phys. Chem. C*, 2018, **122**, 11890–11904.
- [121] A. F. Lee, K. Wilson, R. M. Lambert, A. Goldoni, A. Baraldi and G. Paolucci, *J. Phys. Chem. B*, 2000, **104**, 11729–11733.
- [122] G. Hamm, T. Schmidt, J. Breitbach, D. Franke, C. Becker and K. Wandelt, *Surf. Sci.*, 2004, **562**, 170–182.
- [123] F. Netzer, H. Graen, H. Kuhlenbeck and M. Neumann, *Chem. Phys. Lett.*, 1987, **133**, 49–53.
- [124] H. Graen, M. Neuber, M. Neumann, G. Illing, H. J. Freund and F. P. Netzer, *Surf. Sci.*, 1989, **223**, 33–55.
- [125] H. Graen, M. Neumann, J. Wambach and H.-J. Freund, *Chem. Phys. Lett.*, 1990, **165**, 137–141.
- [126] C. Weststrate, J. Bakker, A. Gluhoi, W. Ludwig and B. Nieuwenhuys, *Surf. Sci.*, 2007, **601**, 748–756.
- [127] F. Netzer, E. Bertel and J. Matthew, *Surf. Sci.*, 1980, **92**, 43–52.
- [128] S. J. Jenkins, *Proc. Roy. Soc. A*, 2009, **465**, 2949–2976.
- [129] G.-K. Liu, B. Ren, D.-Y. Wu, S. Duan, J.-F. Li, J.-L. Yao, R.-A. Gu and Z.-Q. Tian, *J. Phys. Chem. B*, 2006, **110**, 17498–17506.
- [130] T. Bera, J. W. Thybaut and G. B. Marin, *Ind. Eng. Chem. Res.*, 2011, **50**, 12933–12945.
- [131] D. Lloyd, C. Quinn and N. Richardson, *Solid State Commun.*, 1977, **23**, 141–145.
- [132] H. Ohtani, M. A. Van Hove and G. A. Somorjai, *J. Phys. Chem.*, 1988, **92**, 3974–3982.
- [133] D. Graham and J. Howard, *J. Chem. Soc., Faraday Trans. 1*, 1984, **80**, 3365.
- [134] M. T. d. M. Cruz, J. W. d. M. Carneiro, D. A. G. Aranda and M. Bühl, *J. Phys. Chem. C*, 2007, **111**, 11068–11076.
- [135] S. J. Jenkins, *Proc. Roy. Soc. A*, 2009, **465**, 2949–2976.
- [136] X. Li, M. S. M. Wong and K. H. Lim, *Theor. Chem. Acc.*, 2010, **127**, 401–409.
- [137] W. Liu, J. Carrasco, B. Santra, A. Michaelides, M. Scheffler and A. Tkatchenko, *Phys. Rev. B*, 2012, **86**, 245405.

- [138] J. Carrasco, W. Liu, A. Michaelides and A. Tkatchenko, *J. Chem. Phys.*, 2014, **140**, 084704.
- [139] G. Canduela-Rodriguez, M. K. Sabbe, M. F. Reyniers, J.-F. Joly and G. B. Marin, *J. Phys. Chem. C*, 2014, **118**, 21483–21499.
- [140] J. B. Davis, S. L. Horswell, L. Piccolo and R. L. Johnston, *J. Organomet. Chem.*, 2015, **792**, 190–193.
- [141] K. G. Lakshmikanth, P. K. Ayishabi and R. Chatanathodi, *Comput. Mater. Sci.*, 2017, **137**, 10–19.
- [142] Y. He and S. Laursen, *Surf. Sci.*, 2019, **686**, 1–9.
- [143] H. Yildirim, T. Greber and A. Kara, *J. Phys. Chem. C*, 2013, **117**, 20572–20583.
- [144] J. Matos, H. Yildirim and A. Kara, *J. Phys. Chem. C*, 2015, **119**, 1886–1897.
- [145] Z. B. Ding, M. Tommasini and M. Maestri, *React. Chem. Eng.*, 2019, **4**, 410–417.
- [146] S. Yamagishi, S. J. Jenkins and D. A. King, *J. Phys. Chem. C*, 2008, **112**, 14417–14427.
- [147] C. Fan, Y. A. Zhu, X. G. Zhou and Z. P. Liu, *Catal. Today*, 2011, **160**, 234–241.
- [148] C. C. Chiu, A. Genest, A. Borgna and N. Rösch, *ACS Catal.*, 2014, **4**, 4178–4188.
- [149] A. J. R. Hensley, R. Zhang, Y. Wang and J. S. McEwen, *J. Phys. Chem. C*, 2013, **117**, 24317–24328.
- [150] H. Kubicka, *J. Catal.*, 1968, **12**, 223–237.
- [151] O. V. Pokrovskaya, Y. V. Voronin and G. N. Pirogova, *Bull. Acad. Sci. USSR Div. Chem. Sci.*, 1986, **35**, 623–624.
- [152] A. Amano and G. Parravano, *Adv. Catal.*, 1957, **9**, 716–726.
- [153] P. Mériaudeau, O. H. Ellestad, M. Dufaux and C. Naccache, *J. Catal.*, 1982, **75**, 243–250.
- [154] C. Bertizeau, G. Leclercq, R. Maurel, C. Bolivar, H. Charcosset, R. Frety and L. Tournayan, *J. Catal.*, 1976, **45**, 179–188.
- [155] M. G. Leclercq, R. Maurel, C. Bertizeau, D. Jaunay, H. Mendez, H. Charcosset, C. Bolivar, R. Frety and L. Tournayan, *Bull. des Sociétés Chim. Belges*, 1979, **88**, 577–597.
- [156] O. H. Ellestad and C. Naccache, in *Perspectives in Catalysis: Commemoration of Jons Jacob Berzelius*, ed. R. Larsson, CWK Gleerup, 1981, ch. 9, pp. 95–102.

- [157] W. Taylor, *J. Catal.*, 1967, **9**, 99–103.
- [158] J. Yoon and M. A. Vannice, *J. Catal.*, 1983, **82**, 457–468.
- [159] M. I. Phillips and P. H. Emmett, *J. Catal.*, 1986, **101**, 268–272.
- [160] P. C. Aben, J. C. Platteeuw and B. Stouthamer, *Recl. des Trav. Chim. des Pays-Bas*, 2010, **89**, 449–459.
- [161] J. Anderson and C. Kemball, *Adv. Catal.*, 1957, **9**, 51–64.
- [162] M. A. Keane and P. M. Patterson, *Ind. Eng. Chem. Res.*, 1999, **38**, 1295–1305.
- [163] P. C. Aben, H. van der Eijk and J. M. Oelderik, in *Proceedings of the Fifth International Congress in Catalysis Miami Beach, Florida*, ed. J. W. Hightower, Amsterdam: North-Holland, New York, 1973, vol. 4, pp. 717–728.
- [164] O. A. Yakovina and A. S. Lisitsyn, *Langmuir*, 2016, **32**, 12013–12021.
- [165] A. F. Flores, R. L. Burwell and J. B. Butt, *J. Chem. Soc. Faraday Trans.*, 1992, **88**, 1191.
- [166] K. M. Bratlie, H. Lee, K. Komvopoulos, P. Yang and G. A. Somorjai, *Nano Lett.*, 2007, **7**, 3097–3101.
- [167] K. H. Park, K. Jang, H. J. Kim and S. U. Son, *Angew. Chem. Int. Ed.*, 2007, **46**, 1152–1155.
- [168] V. V. Pushkarev, K. An, S. Alayoglu, S. K. Beaumont and G. A. Somorjai, *J. Catal.*, 2012, **292**, 64–72.
- [169] R. Van Hardeveld and F. Hartog, *Surf. Sci.*, 1969, **15**, 189–230.
- [170] M. Vannice and P. Chou, in *Proceedings of the Eighth International Congress on Catalyst Berlin Germany*, 1984, vol. V, pp. 99–111.
- [171] P. Chou and M. A. Vannice, *J. Catal.*, 1987, **107**, 140–153.
- [172] P. Chou and M. A. Vannice, *J. Catal.*, 1987, **107**, 129–139.
- [173] M. Vasiur Rahaman and M. A. Vannice, *J. Catal.*, 1991, **127**, 251–266.
- [174] M. Vasiur Rahaman and M. Albert Vannice, *J. Catal.*, 1991, **127**, 267–275.
- [175] S. Lin and M. Vannice, *J. Catal.*, 1993, **143**, 539–553.
- [176] S. Lin and M. Vannice, *J. Catal.*, 1993, **143**, 554–562.
- [177] S. Lin and M. Vannice, *J. Catal.*, 1993, **143**, 563–572.

- [178] D. Poondi and M. A. Vannice, *J. Catal.*, 1996, **161**, 742–751.
- [179] A. de Mallmann and D. Barthomeuf, *J. Chim. Phys.*, 1990, **87**, 535–538.
- [180] P. Reyes, I. Concha, M. König and J. Fierro, *Appl. Catal. A Gen.*, 1993, **103**, 5–16.
- [181] M. Williams, B. Fonfe, C. Woltz, A. Jentys, J. Vanveen and J. Lercher, *J. Catal.*, 2007, **251**, 497–506.
- [182] F. Figueras, R. Gomez and M. Primet, in *Adv. Chem.*, ed. W. M. Meier and J. B. Uytterhoeven, 1973, vol. 121, pp. 480–489.
- [183] L. Simon, J. van Ommen, A. Jentys and J. Lercher, *Catal. Today*, 2002, **73**, 105–112.
- [184] L. Simon, P. Kooyman, J. van Ommen and J. Lercher, *Appl. Catal. A Gen.*, 2003, **252**, 283–293.
- [185] O. Y. Gutiérrez, Y. Yu, R. Kolvenbach, G. L. Haller and J. A. Lercher, *Catal. Sci. Technol.*, 2013, **3**, 2365.
- [186] M. Luo, Q. Wang, G. Li, X. Zhang, L. Wang and T. Jiang, *Catal. Sci. Technol.*, 2014, **4**, 2081–2090.
- [187] M. Luo, Q. Wang, X. Zhang, L. Wang and B. Hu, *RSC Adv.*, 2015, **5**, 42468–42476.
- [188] W. F. Taylor and H. K. Staffin, *J. Phys. Chem.*, 1967, **71**, 3314–3319.
- [189] M. A. Keane and P. M. Patterson, *J. Chem. Soc. Faraday Trans.*, 1996, **92**, 1413.
- [190] M. A. Keane, *J. Catal.*, 1997, **166**, 347–355.
- [191] M. Schoenmaker-Stolk, J. Verwijs, J. Don and J. Scholten, *Appl. Catal.*, 1987, **29**, 73–90.
- [192] R. van Hardeveld and F. Hartog, 1972, **22**, 75–113.
- [193] A. Cinneide and J. Clarke, *J. Catal.*, 1972, **26**, 233–241.
- [194] J. M. Orozco and G. Webb, *Appl. Catal.*, 1983, **6**, 67–84.
- [195] H. Spod, M. Lucas and P. Claus, *Catalysts*, 2015, **5**, 1756–1769.
- [196] W. A. A. van Barneveld and V. Ponc, *Recl. des Trav. Chim. des Pays-Bas*, 1974, **93**, 243–246.
- [197] R. Prins, *Top. Catal.*, 2018, **61**, 714–721.
- [198] M. C. King and K. J. Laidler, *Arch. Hist. Exact Sci.*, 1984, **30**, 45–86.

- [199] K. J. Laidler, *Arch. Hist. Exact Sci.*, 1985, **32**, 43–75.
- [200] K. J. . Laidler, *Arch. Hist. Exact Sci.*, 1986, **35**, 345–374.
- [201] O. A. Hougen and K. M. Watson, *Chemical process principles Part 3*, J. Wiley; Chapman and Hall, New York; London, 1947.
- [202] P. Mars and D. van Krevelen, *Chem. Eng. Sci.*, 1954, **3**, 41–59.
- [203] M. A. Vannice, *Catal. Today*, 2007, **123**, 18–22.
- [204] K. J. Yoon, P. L. Walker, L. N. Mulay and M. A. Vannice, *Ind. Eng. Chem. Prod. Res. Dev.*, 1983, **22**, 519–526.
- [205] L. P. Lindfors, T. Salmi and S. Smeds, *Chem. Eng. Sci.*, 1993, **48**, 3813–3828.
- [206] L. P. Lindfors and T. Salmi, *Ind. Eng. Chem. Res.*, 1993, **32**, 34–42.
- [207] S. Toppinen, T.-K. Rantakylä, T. Salmi and J. Aittamaa, *Ind. Eng. Chem. Res.*, 1996, **35**, 1824–1833.
- [208] J. Deligny, L. Germanaud, J.-P. Dath and S. Brunet, *Catal. Letters*, 2018, **148**, 2548–2560.
- [209] K. H. V. Prasad, K. B. S. Prasad, M. M. Mallikarjunan and R. Vaidyeswaran, *J. Catal.*, 1983, **84**, 65–73.
- [210] J. W. Thybaut, M. Saeys and G. B. Marin, *Chem. Eng. J.*, 2002, **90**, 117–129.
- [211] S. Lu, W. W. Lonergan, J. P. Bosco, S. Wang, Y. Zhu, Y. Xie and J. G. Chen, *J. Catal.*, 2008, **259**, 260–268.
- [212] R. van Meerten and J. Coenen, *J. Catal.*, 1977, **46**, 13–24.
- [213] M. Saeys, J. W. Thybaut, M. Neurock and G. B. Marin, *Mol. Phys.*, 2004, **102**, 267–272.
- [214] M. Saeys, M. F. Reyniers, M. Neurock and G. B. Marin, *J. Phys. Chem. B*, 2005, **109**, 2064–2073.
- [215] M. Saeys, M. F. Reyniers, J. W. Thybaut, M. Neurock and G. B. Marin, *J. Catal.*, 2005, **236**, 129–138.
- [216] M. K. Sabbe, G. Canduela-Rodriguez, M. F. Reyniers and G. B. Marin, *J. Catal.*, 2015, **330**, 406–422.
- [217] T. Bera, J. W. Thybaut and G. B. Marin, *ACS Catal.*, 2012, **2**, 1305–1318.
- [218] H. Backman, A. K. Neyestanaki and D. Y. Murzin, *J. Catal.*, 2005, **233**, 109–118.

- [219] C. Mirodatos, J. Dalmon and G.A. Martin, *J. Catal.*, 1987, **105**, 405–415.
- [220] R.Badilla-Ohlbaum, H. Neuburg, W.F.Graydon and M. J. Phillips, *J. Catal.*, 1977, **47**, 273–279.
- [221] D. B. Burueva, O. G. Salnikov, K. V. Kovtunov, A. S. Romanov, L. M. Kovtunova, A. K. Khudorozhkov, A. V. Bukhtiyarov, I. P. Prosvirin, V. I. Bukhtiyarov and I. V. Koptuyug, *J. Phys. Chem. C*, 2016, **120**, 13541–13548.
- [222] S. B. Duckett and R. E. Mewis, *Acc. Chem. Res.*, 2012, **45**, 1247–1257.
- [223] M. Anand, A. M. Beale, M. Boronat, M. Bowker, A. L. Bugaev, V. I. Bukhtiyarov, C. R. A. Catlow, S. Chansai, M. Claeys, M. Conway, P. R. Davies, J. Edwards, J. El-Kadi, D. Eremin, N. Fischer, S. Guan, J. S. J. Hargreaves, C. Hess, G. J. Hutchings, F. Jameel, A. Reza Kamali, S. Kondrat, N. Lawes, D. Lennon, D. Li, P. Morgan, A. M. Oyarzún Aravena, C. Reece, R. Réocreux, P. W. Seavill, Y. Sekine, M. Shoji, I. Silverwood, M. Sinev, C. Smith, M. Stamatakis, L. Torrente Murciano, D. Uner, B. M. Weckhuysen, K. Whiston, M. Wolf, B. Yang and C. D. Zeinalipour-Yazdi, *Faraday Discuss.*, 2021, **229**, 378–421.
- [224] M. Saeys, M. F. Reyniers, M. Neurock and G. B. Marin, *J. Phys. Chem. B*, 2005, **109**, 2064–2073.
- [225] M. K. Sabbe, G. Canduela-Rodriguez, J. F. Joly, M. F. Reyniers and G. B. Marin, *Catal. Sci. Technol.*, 2017, **7**, 5267–5283.
- [226] Y. I. Derbentsev, Z. Paál and P. Tétényi, *Zeitschrift fur Phys. Chemie*, 1972, **80**, 51–62.
- [227] P. Tétényi and Z. Paál, *Zeitschrift fur Phys. Chemie*, 1972, **80**, 63–70.
- [228] P. Kluson, L. Cerveny and J. Had, *Catal. Letters*, 1994, **23**, 299–312.
- [229] A. Weilhard, G. Abarca, J. Viscardi, M. H. G. Pechtl, J. D. Scholten, F. Bernardi, D. L. Baptista and J. Dupont, *ChemCatChem*, 2017, **9**, 204–211.
- [230] S. Siegel, *Adv. Catal.*, 1966, **16**, 123–177.
- [231] S. Siegel and N. Garti, in *Catalysis in Organic Synthesis*, Academic Press, 1977, pp. 9–23.
- [232] S. Siegel, J. Outlaw Jr and N. Garti, *J. Catal.*, 1979, **58**, 370–382.
- [233] M. Viniegra, G. Córdoba and R. Gómez, *J. Mol. Catal.*, 1990, **58**, 107–114.
- [234] R. Gomez, G. Del Angel and V. Bertin, *React. Kinet. Catal. Lett.*, 1991, **44**, 517–522.

- [235] G. Del Angel, V. Bertin, A. Perez and R. Gomez, *React. Kinet. Catal. Lett.*, 1992, **48**, 259–264.
- [236] M. Viniegra, N. Martín, A. López-Gaona and G. Córdoba, *React. Kinet. Catal. Lett.*, 1993, **49**, 353–360.
- [237] D. Murzin, S. Smeds and T. Salmi, *React. Kinet. Catal. Lett.*, 1997, **60**, 57–64.
- [238] P. Reyes, M. E. König, G. Pecchi, I. Concha, M. López Granados and J. L. G. Fierro, *Catal. Letters*, 1997, **46**, 71–75.
- [239] A. Kalantar Neyestanaki, *J. Catal.*, 2003, **218**, 267–279.
- [240] R. L. Burwell, *Acc. Chem. Res.*, 1969, **2**, 289–296.
- [241] M. Yang, K. C. Chou and G. A. Somorjai, *J. Phys. Chem. B*, 2003, **107**, 5267–5272.
- [242] J. M. Krier, W. D. Michalak, L. R. Baker, K. An, K. Komvopoulos and G. A. Somorjai, *J. Phys. Chem. C*, 2012, **116**, 17540–17546.
- [243] J. M. Krier, K. Komvopoulos and G. A. Somorjai, *J. Phys. Chem. C*, 2016, **120**, 8246–8250.
- [244] M. Xi and B. E. Brent, *J. Vac. Sci. Technol. B Microelectron. Nanom. Struct.*, 1992, **10**, 2440.
- [245] J. P. G. Kehoe and J. B. Butt, *J. Appl. Chem. Biotechnol.*, 1972, **22**, 23–30.
- [246] A. Rocha, A. Rocha and V. T. da Silva, *Appl. Catal. A Gen.*, 2010, **379**, 54–60.
- [247] H. van Bekkum, H. M. A. Buurmans, G. van Minnen-Pathuis and B. M. Wepster, *Recl. des Trav. Chim. des Pays-Bas*, 2010, **88**, 779–794.
- [248] V. S. Ranade, G. Consiglio and R. Prins, *J. Org. Chem.*, 2000, **65**, 1132–1138.
- [249] A. W. Weitkamp, *J. Catal.*, 1966, **6**, 431–457.
- [250] J. B. Hall, L. K. Lala, M. G. J. Beets and T. W. I., *Bicyclic compounds and processes for making and using the same*, US3927083, Dec. 1975.
- [251] C. Zhao, H. Zhi Wang, N. Yan, C. xian Xiao, X. dong Mu, P. J. Dyson and Y. Kou, *J. Catal.*, 2007, **250**, 33–40.
- [252] V. S. Ranade, G. Consiglio and R. Prins, *J. Org. Chem.*, 1999, 8862–8867.
- [253] F. Schwab, M. Lucas and P. Claus, *Angew. Chem. Int. Ed. Engl.*, 2011, **50**, 10453–10456.

- [254] I. Krossing and I. Raabe, *Angew. Chem. Int. Ed.*, 2004, **43**, 2066–2090.
- [255] E. T. Silveira, A. P. Umpierre, L. M. Rossi, G. Machado, J. Morais, G. V. Soares, I. J. R. Baumvol, S. R. Teixeira, P. F. P. Fichtner and J. Dupont, *Chem. Eur. J.*, 2004, **10**, 3734–3740.
- [256] *Asahi Kasei Advisor Hajime Nagahara honored with Prize for Science and Technology*, 2018, <https://www.asahi-kasei.co.jp/asahi/en/news/2018/e180410.html>, <https://www.asahi-kasei.co.jp/asahi/en/news/2018/e180410.html>, accessed 2021-01-30.
- [257] J. Struijk and J. J. F. Scholten, *Appl. Catal. A Gen.*, 1992, **82**, 277–287.
- [258] O. Mitsui and Y. Fukuoka, *Process for producing a cycloolefin*, US4734536, Jul. 1987.
- [259] M. Konishi and H. Nagahara, *Process for producing cycloolefins*, US4734536, Mar. 1986.
- [260] X. Xue, J. Liu, D. Rao, S. Xu, W. Bing, B. Wang, S. He and M. Wei, *Catal. Sci. Technol.*, 2017, **7**, 650–657.
- [261] L. Foppa and J. Dupont, *Chem. Soc. Rev.*, 2015, **44**, 1886–1897.
- [262] E. Elemensov, P. Zanolina, B. Zhanabaev and B. Utelbaev, *Zhurnal Fiz. Khimii*, 1988, **62**, 2515–2517.
- [263] C. U. Odenbrand and S. T. Lundin, *J. Chem. Technol. Biotechnol.*, 1980, **30**, 677–687.
- [264] J. Struijk, M. D’Angremond, W. L.-d. Regt and J. Scholten, *Appl. Catal. A Gen.*, 1992, **83**, 263–295.
- [265] J. Ning, J. Xu, J. Liu and F. Lu, *Catal. Letters*, 2006, **109**, 175–180.
- [266] H. Spod, M. Lucas and P. Claus, *ChemCatChem*, 2016, **8**, 2659–2666.
- [267] J. Wang, Y. Wang, S. Xie, M. Qiao, H. Li and K. Fan, *Appl. Catal. A Gen.*, 2004, **272**, 29–36.
- [268] C. Milone, G. Neri, A. Donato, M. Musolino and L. Mercadante, *J. Catal.*, 1996, **159**, 253–258.
- [269] S.-C. Hu and Y.-W. Chen, *Ind. Eng. Chem. Res.*, 1997, **36**, 5153–5159.
- [270] J. A. Don and J. J. Scholten, *Faraday Discuss. Chem. Soc.*, 1981, **72**, 145–156.
- [271] T. E. Madey and J. T. Yates, *Chem. Phys. Lett.*, 1977, **51**, 77–83.
- [272] Y. Sawama, Y. Monguchi and H. Sajiki, *Synlett*, 2012, **23**, 959–972.

- [273] J.-L. Liu, Y. Zhu, J. Liu, Y. Pei, Z. H. Li, H. Li, H.-X. Li, M.-H. Qiao and K.-N. Fan, *J. Catal.*, 2009, **268**, 100–105.
- [274] F. Schwab, M. Lucas and P. Claus, *Green Chem.*, 2013, **15**, 646.
- [275] R. S. Suppino, R. Landers and A. J. G. Cobo, *Appl. Catal. A Gen.*, 2013, **452**, 9–16.
- [276] D. Rao, X. Xue, G. Cui, S. He, M. Xu, W. Bing, S. Shi and M. Wei, *Catal. Sci. Technol.*, 2018, **8**, 236–243.
- [277] M. M. Johnson and G. P. Nowack, *J. Catal.*, 1975, **38**, 518–521.
- [278] Z. H. Li, J. Liu, M. Qiao and K. N. Fan, *Mol. Phys.*, 2009, **107**, 1271–1282.
- [279] V. A. Mazzieri, P. C. L'Argentièrre, F. Coloma-Pascual and N. S. Fígoli, *Ind. Eng. Chem. Res.*, 2003, **42**, 2269–2272.
- [280] V. Mazzieri, F. Coloma-Pascual, A. Arcoya, P. L'Argentièrre and N. Fígoli, *Appl. Surf. Sci.*, 2003, **210**, 222–230.
- [281] G. Y. Fan, W. D. Jiang, J. B. Wang, R. X. Li, H. Chen and X. J. Li, *Catal. Commun.*, 2008, **10**, 98–102.
- [282] A. H. Gonçalves, J. C. S. Soares, L. R. R. de Araújo, F. M. Zotin, F. M. Mendes and A. B. Gaspar, *Mol. Catal.*, 2020, **483**, 110710.
- [283] D. J. Morgan, *Surf. Interface Anal.*, 2015, **47**, 1072–1079.
- [284] G. Zhou, R. Dou, H. Bi, S. Xie, Y. Pei, K. Fan, M. Qiao, B. Sun and B. Zong, *J. Catal.*, 2015, **332**, 119–126.
- [285] G. Zhou, Y. Dong and D. He, *Appl. Surf. Sci.*, 2018, **456**, 1004–1013.
- [286] L. Jiang and G. Zhou, *Appl. Surf. Sci.*, 2021, **535**, 1–11.
- [287] P. V. C. Azevedo, M. V. Dias, A. H. A. Gonçalves, L. E. P. Borges and A. B. Gaspar, *Mol. Catal.*, 2021, **499**, 111288.
- [288] G.-Y. Fan, R.-X. Li, X.-J. Li and H. Chen, *Catal. Commun.*, 2008, **9**, 1394–1397.
- [289] R. S. Suppino, R. Landers and A. J. G. Cobo, *Appl. Catal. A Gen.*, 2016, **525**, 41–49.
- [290] F. Hartog and P. Zwietering, *J. Catal.*, 1963, **2**, 79–81.
- [291] W. C. Drinkard, *Selective hydrogenation of aromatic hydrocarbons to cycloolefins*, US3767720, Oct. 1972.

- [292] E. Elemensov, P. Zanolina, B. Zhanabaev and B. Utelbaev, *Russ. J. Phys. Chem.*, 1988, **62**, 1304–1308.
- [293] X. L. Yu, Y. Li, S. M. Xin, P. Q. Yuan and W. K. Yuan, *Ind. Eng. Chem. Res.*, 2018, **57**, 1961–1967.

Chapter 2

Experimental

2.1 Materials

The chemicals used in the work presented in this thesis are listed in Table 2.1. Chemicals were used without further purification or treatment unless specified in following sections.

Table 2.1: List of chemicals used in production of this thesis.

| Chemical | Supplier | Purity |
|---|-------------------|----------------------------------|
| GHC | IFF | >98% ^a |
| THPMI (product mixture) | IFF | <i>ca.</i> 63% ^a |
| THPMI (distilled) | IFF | <i>ca.</i> 92% ^a |
| HHPMI (distilled) | IFF | <i>ca.</i> 95% ^a |
| Palladium chloride | Sigma Aldrich | 99.999% |
| Chloroplatinic acid | ACROS Organics | ACS Reagent |
| Ruthenium chloride hydrate | ACROS Organics | 35-40 wt.% Ru |
| Iridium chloride trihydrate | ACROS Organics | 53-56 wt.% Ir |
| Rhodium chloride hydrate | Sigma Aldrich | 38-40 wt.% Rh |
| Tetraammine palladium chloride | Alfa Aesar | 99.9% |
| 5 wt.% Pd/C (nominally 50 wt.% wet) | IFF | n.a. ^b |
| Graphene nanoplatelets (surface area 500 m) | Alfa Aesar | n.a. ^b |
| Octane | Sigma Aldrich | >98% |
| Acetone | Fisher Scientific | 99+% |
| Hexadecane | Sigma Aldrich | >99.8% |
| Hydrochloric acid | Sigma Aldrich | ACS Reagent 37% |
| 10% Hydrogen in Argon | BOC | Standard certified ($\pm 5\%$) |
| 5% Hydrogen in Argon | BOC | Standard certified ($\pm 5\%$) |
| 10% CO in Helium | BOC | Standard certified ($\pm 5\%$) |
| Helium | BOC | >99.99% |
| Argon | BOC | >99.99% |
| Nitrogen | BOC | >99.99% |

^a Determined by gas chromatography.

^b Not applicable.

2.2 Catalyst preparation

The impregnation method is a popular method to prepare a catalyst as it is readily scalable and simple to perform. This involves the wetting of a support with a solution containing a metal precursor, either with an excess of solvent or enough to fill only the pores, followed by drying and thermal activation. It should be stated that there is no single method and many laboratories will have their own approach to this procedure as the variables mentioned in the previous sentence can be varied *ad infinitum*. Controlling each of these steps when preparing one material is of utmost importance if the final catalyst is to be reproducible as batch-to-batch variability is long-standing issue in the field.¹

A method reported by Sankar *et al.*² attempted to improve the impregnation procedure by controlling important variables, such as the solvent volume, metal ion concentration, amount of support added, and impregnation and drying temperatures. Therefore, this method was used in this work to ensure that good reproducibility between batches of catalyst. Though it should be noted that these variables could be tailored to each metal precursor or support, no such study was performed during the course of this work.

2.2.1 Carbon-supported catalysts preparation

Catalysts used in studying the effect of metal were prepared using a modified impregnation method reported by Sankar *et al.*² A 100 mL round-bottom flask was charged with the amount of aqueous metal precursor solution (ruthenium chloride hydrate (4 mg mL⁻¹, rhodium chloride hydrate (5 mg mL⁻¹, palladium chloride (6 mg mL⁻¹ in 0.58 M HCl), iridium chloride hydrate (8 mg mL⁻¹, and chloroplatinic acid (10 mg mL⁻¹) necessary to prepare 1 g of a 5 wt.% catalyst. This was subsequently diluted, so that the total volume was 16 mL. The flask was immersed in an oil bath and the temperature was raised to 60 °C under agitation. Once at temperature, 0.95 g of the graphene nanoplatelets support was slowly added over a period of 8—10 minutes at which point the flask and the resulting slurry was stirred for a further 15 minutes before the temperature was raised to 95 °C for 16 h to dry. The obtained solid was then ground in a mortar with a pestle and transferred into an alumina calcination boat and heated in a tube furnace under a flow of 5% hydrogen in argon to 250 °C at a ramp rate of 5 °C min⁻¹ and held at this temperature for 2 h. These catalysts are denoted as “red. only”. A portion (500 mg) of the reduced only catalysts was then calcined under a flow of air at 250 °C for 4 h with a heating rate of 5 °C min⁻¹. These catalysts are denoted as “red. + calc.”.

2.3 Reactions

2.3.1 Hydrogenation reactions of aromatics

A 50 mL stainless steel high-pressure autoclave (PARR 5500 compact reactor with a 4836 controller box) equipped with an overhead stirrer, four-straight blade impeller, and liner (glass or PTFE) was used for reactions. In a typical reaction, the reactor was charged with 0.13 g catalyst and 16 g substrate. For experiments involving 5 wt.% Rh/GNP, this amount was lowered to 0.04 g of catalyst as preliminary experiments using the normal mass loading led to non-isothermal operation of the reactor. The reactor was then purged with nitrogen three times before being heated to the desired reaction temperature at a stirring rate of 1000 rpm. Once the set temperature was achieved, the reactor was pressurised with the requisite amount of hydrogen gas, which was maintained throughout the reaction using a high-pressure regulator and an open gas inlet tap. Periodically, samples were removed from the reactor using a sampling port; during this process the gas inlet tap was first closed before withdrawing a sample with the first part of the sample being discarded to ensure no residual chemicals from the previous sample were retained. This process lasted under 30 seconds and a small drop in pressure of several bar was noted. The gas inlet tap was subsequently opened to repressurise the reactor to the set pressure. At the end of a reaction, the stirring was stopped, and the reactor was cooled in an ice bath until the temperature decreased below 25 °C. Subsequently, the hydrogen gas was vented or collected in a gas bag and the reactor was opened.

2.3.1.1 Analysis and quantification

Reaction solutions were analysed by gas chromatography after filtration and dilution with acetone; the details for the gas chromatograph instrument are outlined in Section 2.4.1.1. Conversion was calculated by the following equation:

$$\text{Conversion} = \left(\frac{n(\text{Reactant}_0) - n(\text{Reactant}_t)}{n(\text{Reactant}_0)} \right) \times 100 \quad (2.1)$$

where $n(\text{Reactant}_0)$ is the number of moles of reactant at $t=0$ and $n(\text{Reactant}_t)$ is the number of moles of reactant at time t . The Reactant may be PMI or E-PMI as the conversion of these substrates is expressed separately. In addition, an overall conversion is also provided which may be expressed as the overall conversion of GHC, expressed by:

$$\text{Conversion} = \left(\frac{n(\text{PMI}_0) + n(\text{EPMI}_0) - (n(\text{PMI}_t) + n(\text{EPMI}_t))}{n(\text{PMI}_0) + n(\text{EPMI}_0)} \right) \times 100 \quad (2.2)$$

Selectivity is defined as:

$$\text{Selectivity} = \left(\frac{n(\text{Product}_t)}{n(\text{Reactant}_0) - n(\text{Reactant}_t)} \right) \times 100 \quad (2.3)$$

Where $n(\text{Product}_t)$ is the number of moles of product at time t . The product may be THPMI, E-THPMI, or HHPMI.

Yield is calculated by:

$$\text{Yield} = \frac{\text{Conversion} \times \text{Selectivity}}{100} \quad (2.4)$$

Turnover frequency, TOF, is calculated by:

$$\text{TOF} = \frac{\text{Reaction rate}}{\text{Number of sites}} \quad (2.5)$$

where the reaction rate is determined by the number of moles of substrate consumed over a period of time and number of sites is assumed to be related to the CO uptake during pulse chemisorption measurements (Section 2.5.5.4).

2.3.2 Isomerisation reactions

Isomerisation reactions were performed in a 50 mL glass Colaver reactor or the autoclave described above. The desired amount of catalyst was charged into the reactor and a 0.5 mol dm⁻³ purified THPMI in octane solution was added. This slurry was purged with nitrogen three times before exposing to pure hydrogen and stirred for several minutes to reduce the palladium catalyst. Subsequently, the reactor was vented and purged three times with nitrogen and then heated to the desired temperature.

2.3.2.1 Analysis and quantification

Reaction solutions were analysed by gas chromatography and nuclear magnetic resonance (NMR) spectroscopy after filtration. The gas chromatography quantification method outlined in Section 2.4.1.1 was also utilised for these experiments. NMR spectroscopy was used to detect the appearance of peaks in the vinyl region of the spectrum (4.5—6.5 ppm) (see Section 2.4.2 for details), though the concentration of products in the region were not quantified by this method.

2.4 Solution characterisation methods

2.4.1 Gas chromatography

Gas Chromatography is a separation technique comprised of two types: gas-liquid chromatography and gas-solid chromatography. The first mentioned chromatographic technique is widely used throughout science and is utilised in this work for the analysis of reaction mixtures whereas the latter is seldom used, except for the separation of low molecular weight gaseous species.³ The first mentioned technique is often referred to as only GC and a typical configuration for this instrument is shown in Figure 2.1. In a routine analysis, a sample is vapourised and injected onto a column and the separation of components depends on the interaction between the analyte and the stationary phase, which coats the inside of the column.

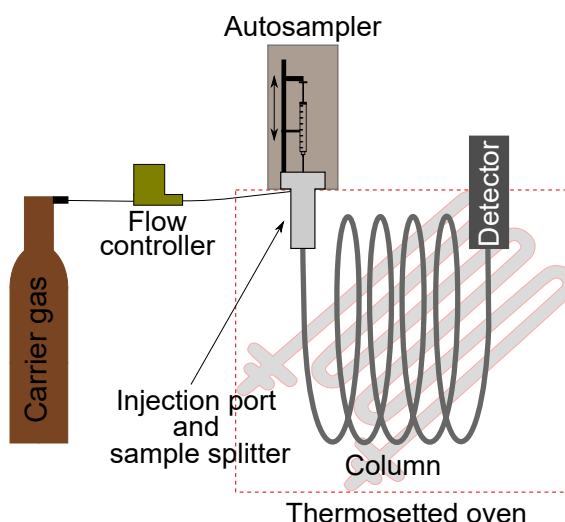


Figure 2.1: Instrument schematic for a GC instrument.

The analytes are moved along the column by a mobile phase, which for this method is a gas, to a suitable detector. During this time the conditions the column is exposed to (e.g. temperature) may change to improve separation efficiency.

The choice of instrumental setup is chosen so that optimum separation and, detector depending, response is maximised. Regarding the separation side, compounds must first be vapourised proportionally to their concentration in solution and without any decomposition. Subsequently, the sample is introduced onto the column, but the nature of this event depends on the type of column and the sample volume injected. Packed columns have diameters of tens of millimetres and are typically no more than 3 m in length. These contain packed, stationary phase-coated spheres and can tolerate direct injection. However, these have fallen out of favour in recent times for capillary columns, which can be longer than 60 m. But as their diameter is in the order of a few tenths of a millimetre, the vapourised sample must be split to ensure the column is not overloaded which would result in peak broadening and poorer separation. The sample is pushed along the column by the mobile phase carrier gas. The choice of gas can depend on the detector but common choices are hydrogen, helium, nitrogen, and argon, as these should be unreactive at these conditions. At the end of the column the effluent feeds into the detector.

The selection of detectors that are compatible with GC is vast, so the discussion is limited to the three types of detectors used in this work, namely, flame-ionisation, thermal-conductivity, and mass-spectrometry. A flame ionisation detector (FID) operates by directing the effluent from the column into an air-hydrogen flame which in turn pyrolyses organic molecules passing through. This generates ions and electrons which produces a small current ($\sim 10^{-12}$ A) that can be measured by a picoammeter. This is an incredibly sensitive detector and can detect as little as 1 picogram per second of material eluting from the column for hydrocarbons but this process leads to their destruction.³ The response of the flame is proportional to the number of reduced carbon atoms present in the flame which is why the

sensitivity is described in mass rather than concentration. Thus, this detector is highly suitable for the reaction mixtures used in this work, but if the products were noncombustible gasses such as CO₂, H₂O, etc., or compounds which contained very little carbon by weight (e.g. formaldehyde), then a different detector would be more appropriate.

The thermal-conductivity detector (TCD) is often referred to as the universal detector. It finds application not only in work involving chromatography but also in chemisorption and temperature-programmed experiments. The TCD works by comparing the thermal conductivity of the sample flow to that of a reference of pure carrier gas. Various configurations of TCD are possible, but twin detectors are usually used.³ Here a Wheatstone bridge circuit is employed with the carrier gas and sample gas flowing over separate arms and any differences in composition result in an out-of-balance signal which can be detected. The carrier gas can be an important choice with this detector. Helium and hydrogen both have thermal conductivities that are significantly higher than organic compounds, so small changes in effluent will result in large changes in thermal conductivity, but nitrogen and argon have thermal conductivities closer to organic compounds and will thus be less sensitive. Even with optimum gases the sensitivity is lower than other detectors by factors of 10⁴–10⁷.³ However it is advantageous as it is non-destructive and can be combined with other detectors and can be used for organic and inorganic species.

Mass spectrometers are instruments that ionise molecules and detect a mass-to-charge ratio (m/z). When a molecule loses an electron, the resulting cation is termed the molecular ion and is representative of the molecular weight of the original compound as the charge (z) is 1. An ionised molecule can fragment into smaller charged species which are a characteristic fingerprint of a molecule, possibly including multiply charged species for which $m \neq M_w$ and thence requires pondering of conceivable fragments. In recent decades this task has become more trivial as comparison to mass spectrometry computer databases is facile and aids in the elucidation of the structure of a fragment, provided that similar parent molecule is in the database. For molecules without a reference file, there have been recent efforts to predict their mass spectra using quantum or machine learning methods.^{4–7} The exact set-up of the mass spectrometer can vary markedly, but a common configuration involves electron or chemical ionisation, which operate by bombardment of the vapourised sample with electrons or (usually positive) ions, respectively. This results in the formation of charged species which are separated by a mass analyser, often quadrupole or ion trap analysers, before passing over a suitable transducer for detection.

2.4.1.1 Experimental

The products from the reactions of the hydrogenation of GHC and THPMI were analysed after separation from the catalyst by filtration with filter paper or PTFE syringe filters (0.45 μm) and diluted in acetone.

Liquid phase analysis

GC-FID Post-reaction solutions were analysed by GC-FID using an Agilent Technologies 7820A gas chromatograph equipped with an Agilent CP-Wax 52 CB column and flame ionisation detector. For quantification purposes, acetone solutions containing 2.5, 5, 10, 20, and 40 wt.% GHC, THPMI, and HHPMI were injected with 5 wt.% hexadecane acting as external standard. The relative response factors were calculated by the slope of a plot of A_{ISTD}/A_i versus m_{ISTD}/m_i , where A_x and m_x equate to the peak area and mass, respectively, of the internal standard *ISTD* or analyte *i*. Alternatively, this can be expressed as:⁸

$$\text{Response factor} = \frac{A_{ISTD}m_i}{A_im_{ISTD}} \quad (2.6)$$

This value equalled 1.14 for all analytes.

GC-MS Unknown product peaks for which no standard compounds were available were identified using GC-MS. Solutions were analysed using a Shimadzu 2010 Plus gas chromatograph equipped with an Agilent Technologies VF-WAXms column and QP2010 SE mass spectrometer. Mass spectra for all conceivable compounds were computed using the software associated with [6] in Ubuntu 20.04. These mass spectra were added to a database and the similarity of spectra was determined using the Stein and Scott dot product function⁹ in a Python script (see Supporting Information).

Gas phase analysis

GC-FID Gaseous products from the head space of the reactor were analysed using a Varian 450-GC equipped with a CP-Sil 5CB capillary column and flame ionisation detector. For quantification purposes, the detector response was evaluated by injecting known quantities of methane. The relative response factor of methane and other hydrocarbons produced was assumed to be equal as found by Dietz.¹⁰

2.4.2 Nuclear magnetic resonance spectroscopy

Nuclear magnetic resonance (NMR) spectroscopy is an analytical technique used to gain information on molecular structure and purity of atoms which have a nuclei with nuclear spin, *I*. This technique is nearly 80 years old and is used extensively to study solutions and solid materials. The work presented in this thesis uses only solution NMR spectroscopy and the discussion will focus on this topic. The basic operation involves exposing an appropriate nucleus to a magnetic field and pulsing a varied length radio wave at the sample. This causes alignment and perturbation of nuclear spins which after processing produces an NMR spectrum.

Many nuclei, such as ^1H , ^{13}C , ^{19}F , ^{27}Al , possess nuclear spin, I , which when exposed to a magnetic field will precess around the direction of the applied magnetic field at a characteristic frequency, referred to as the Larmor frequency. The Larmor frequency is determined by the magnetic field strength, B_0 , and the gyromagnetic ratio of the nucleus, γ —ultimately the “magnetic strength” of the nucleus—as expressed in Equation 2.7. When the sample is irradiated with a pulse of radio wave quanta orthogonal to the direction of the applied magnetic field (z axis), it generates an oscillating magnetic field in the xy axis tipping the magnetisation vector. This produces an oscillating magnetisation vector that generates a current that can be recorded to produce an exponentially decaying signal. The decaying signal is referred to as free induction decay and after Fourier transformation, produces an NMR spectrum. Most NMR spectra are produced by summation of n free induction decays with the improvement in the signal-to-noise ratio being proportional to \sqrt{n} . A schematic drawing of this process can be viewed in Figure 2.2.

$$\nu = \frac{\gamma B_0}{2\pi} \quad (2.7)$$

Inspection of Equation 2.7 does not imply that NMR may be used for characterisation purposes, in fact it suggests its sole purpose is an expensive detector of a specific element. The actual resonance frequency is highly dependent on the local chemical environment as the effective magnetic field, B_{eff} , felt by a nucleus slightly differs from that of the applied field several factors may cause changes to the electron cloud that shields the nucleus. The level of shielding is expressed as the magnetic shielding constant, σ . Thus, a more appropriate expression would be:

$$\nu = \frac{\gamma(1 - \sigma)B_0}{2\pi} = \frac{\gamma B_{eff}}{2\pi} \quad (2.8)$$

but this value is not what is plotted on an NMR spectrum. This absolute value is not particularly useful as it can be difficult to replicate between laboratories and even on the same piece of equipment on different days due to small instrumental changes. This is a result of the range

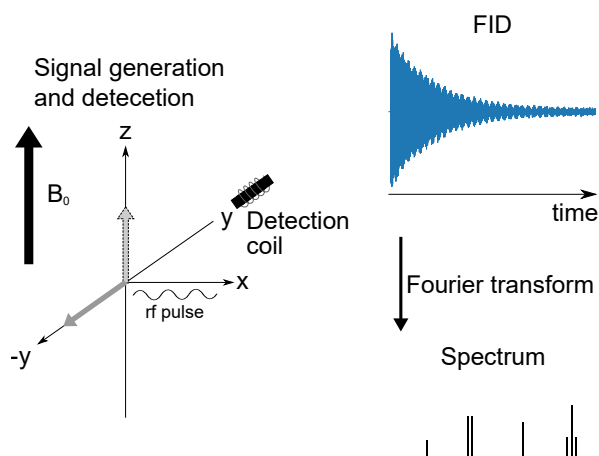


Figure 2.2: A visual representation of NMR spectroscopy.

of frequencies in the region of the resonance frequency are fairly small. Instead, it is more useful to reference the material to an internal standard, such as tetramethylsilane (TMS), to produce a chemical shift, defined as:

$$\delta(\text{ppm}) = \frac{\nu_{peak}(\text{Hz}) - \nu_{\text{TMS}}(\text{Hz})}{\text{Operating frequency (MHz)}} \quad (2.9)$$

The relative shifts are described as being downfield if the δ value is high or upfield if the δ value is low.

An observed chemical shift is dependent on how the electron cloud shielding the nucleus is altered. For example, in this work, NMR is used for the purposes of detecting isomerisation of alkenes. The chemical shift of alkenyl protons is downfield to alkyl protons as the π system generates an additional magnetic field which causes additional deshielding. Moreover, as the sp^2 hybridised carbon is more electronegative than a tetrahedral carbon atom, this causes greater bond polarisation and thus greater deshielding of neighbouring protons. Conversely, if the proton is attached to a carbon with an electron donor, there is increased shielding and thus an upfield shift.

2.4.2.1 Experimental

^1H NMR were recorded in CDCl_3 on a Bruker Avance 500 MHz spectrometer at 298 K with 128 scans. Chemical shifts of the analytes are reported in ppm and are referenced to the residual solvent peak for chloroform (7.26 ppm).

2.4.3 Viscosity

Viscosity is the measurement of a liquids resistance to flow.¹¹ Two types of viscosity exist: dynamic (or absolute, μ) and kinematic (ν). These two values may be interconverted if the density of the liquid, ρ , is known (Equation 2.10). Dynamic viscosity is the relationship between the stress and the shear rate given by Newton's Law of viscosity i.e. it is the force required to make a fluid flow at a certain rate. Kinematic viscosity is the ratio of dynamic viscosity to density that describes a fluid's resistance to flow when the only force acting upon it is gravity.

$$\nu = \frac{\mu}{\rho} \quad (2.10)$$

The measurement of viscosity can be made using a viscometer or rheometer. The former being suitable for measuring the viscosity of Newtonian fluids, which are fluids that have a viscosity is independent of the shear rate. One type of viscometer is the Ostwald viscometer (Figure 2.3). In this viscometer class the time taken for a known volume of liquid to pass through two graduation marks (point c and point d) in a capillary is recorded. This value is then multiplied by the viscometer constant (K_{vis}) that is unique to each viscometer to give the kinematic viscosity (Equation 2.11).

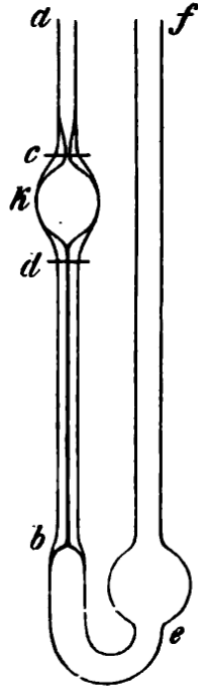


Figure 2.3: An Ostwald viscometer. Original drawing of Wilhelm Ostwald 1891.¹²

$$v = K_{vis}t \quad (2.11)$$

K_{vis} is calculated by measuring the time taken for a reference liquid of known viscosity (usually water) to pass between the two marks. From the Hagen-Poiseuille equation (Equation 2.12) it can be seen that the only parameters that will change between samples are the density and the time taken. Thus, Equation 2.12 can be rewritten as Equation 2.13.

$$V = \frac{\pi ghR^4}{8l\mu} \rho t \quad (2.12)$$

$$\mu = K_{vis} \rho t \quad (2.13)$$

Where g is gravity, h is height of liquid, R is the radius of the capillary, t is time taken for liquid to flow between graduation marks, l is the length of the capillary, and V is the volume of liquid.

It is important to note that equations 2.12 and 2.13 assume an ideal flow, but in reality, a pressure drop may occur at each capillary end. As a result, there is a deviation from ideal flow and in instances where the time taken for the liquid to flow is too rapid, the observed viscosity is lower than the actual value. The Hagenbach-Couette correction may be used to obtain the correct time for the flow; although, at long flow times this term approaches zero, so its contribution can be ignored. Manufacturers of viscometers provide a minimum time so that these corrections are not of concern to the experimenter.¹³

2.4.3.1 Experimental

Viscometry measurements were performed using an Ostwald-type PSL-Rheotek viscometer that was placed in a thermostatically controlled water bath. The correct volume of liquid was added to the viscometer and equilibrated at the desired temperature for 20 minutes. Subsequently, the liquid was drawn up past the two graduated marks and permitted to fall. When the meniscus reached the first of the graduation marks a stop clock was started; after it had reached the second graduation mark the time was stopped. This measurement was repeated three times and the average time was taken. The provided error is the standard deviation of the recorded values. The viscometer was calibrated using water from a Milli-Q® Direct 8 Purification System. All flow times were greater than the manufacture recommended minimum flow time. Data recorded during this work were modelled to an Arrhenius-type equation using the LINEST function in Microsoft Excel. Data processed from other sources was modelled by firstly determining the viscosity as a function of temperature at constant pressure. Subsequently, the experimental data was fitted to Equation 3.7 by minimising the residual sum of squares using the Nelder-Mead algorithm¹⁴ as implemented in the `scipy.optimize.minimize` library of SciPy version 1.4.1¹⁵ in Python 3.7.6.¹⁶ An example script is included in the external zip file.

2.4.4 Density-functional theory

Density-functional theory (DFT) is a quantum mechanical method that computes the electronic structure of chemical systems. It can be used to probe, for example, thermodynamic, kinetic, structural, and spectroscopic phenomena. The theoretical foundations of DFT are based on two theorems derived in the 1960s by Hohenburg and Kohn which offer a simpler solution to the Schrödinger equation of a many-bodied system.^{17,18}

The first theorem states that the ground-state energy of a system is a unique functional of the electron density.¹⁸ This means that the lowest energy of a system of electrons can be derived by considering the electron density as a function of three perpendicular coordinate axes, that is x, y, and z, without having to determine a wavefunction for a system. In other words, there is a one-to-one correlation between the electron density of a molecule and its wavefunction.

The second theorem states that the “true” electron density, which corresponds to the full solution of the Schrödinger equation, is the electron density that minimises the energy of the functional.¹⁸ This means that if the functional is known, then the Schrödinger equation can be solved exactly. Sadly, exact functionals are not known and significant efforts have been made to develop realistic approximations. As may be expected, there are many functionals to choose from when conducting DFT experiments. Fortunately, the performance of many functionals is evaluated in benchmarking studies by experienced computational chemists. This aids the neophyte in their attempts to gain insight into their chemical problem. The

purpose of performing DFT calculations in this work was to gain establish whether there was an equilibrium limitation and therefore knowledge of the thermochemistry of the compounds used in this study, which do not have experimental data available, was needed. Goerigk and Grimme reported a comprehensive benchmarking of density functionals for the calculation of main group thermochemistry.¹⁹ This report suggested that a range of functionals may be relevant to this study, which were: ω B97X-D,²⁰ PBE0-D3,^{21–23} and M06-D3.^{23,24}

2.4.4.1 Experimental

DFT calculations were submitted using WebMO and performed in Gaussian 09.²⁵ Structures were first optimised to a FUNC/cc-pVTZ²⁶ (where FUNC = PBE0-D3, ω B97X-D, or M06-D3) level of theory using the default PCM for cyclohexane. Vibrational frequency calculations performed to the same level of theory validated that the optimised geometries were at their local energy minima. Thermodynamic properties were calculated following the Thermochemistry in Gaussian white paper.²⁷

2.5 Catalyst characterisation techniques

2.5.1 Microwave plasma and inductively-coupled plasma atomic emission spectroscopy

Many of the techniques discussed in this section require precise knowledge of the mass of active component in the sample for the results to be meaningful. Knowledge of the amount of precursor and support used during the preparation is not enough, in fact a catalyst prepared by impregnation may only have 90% of the nominal and even less at higher weight loadings.²⁸ Therefore, the actual metal loading of a catalyst is required to quote results from techniques and experimental data to more than 1 significant figure. To determine the weight loading, the metal content of the catalyst is dissolved from the surface of the support typically with aqua regia and then analysed by microwave plasma atomic emission spectroscopy (MP-AES) or inductively-coupled plasma mass spectrometry (ICP-MS). These techniques are very sensitive, though it must be ensured that the metal of interest is fully digested from the surface in order to acquire accurate experimental data.

In MP-AES, a solution is pumped into a nebuliser where the resulting aerosol is introduced to the plasma region. Exposure to the plasma causes desolvation and the breakdown of particles and molecules into individual atoms whose electrons are excited to higher energy orbitals.²⁹ A drawing of this process is shown in Figure 2.4. This excited state is short-lived and the atom relaxes to the ground state accompanied by the release of a photon of a wavelength equal to the energy difference of the orbitals involved in the transition. Detection occurs by focussing the photons emitted with a series of mirrors onto a sensor that works

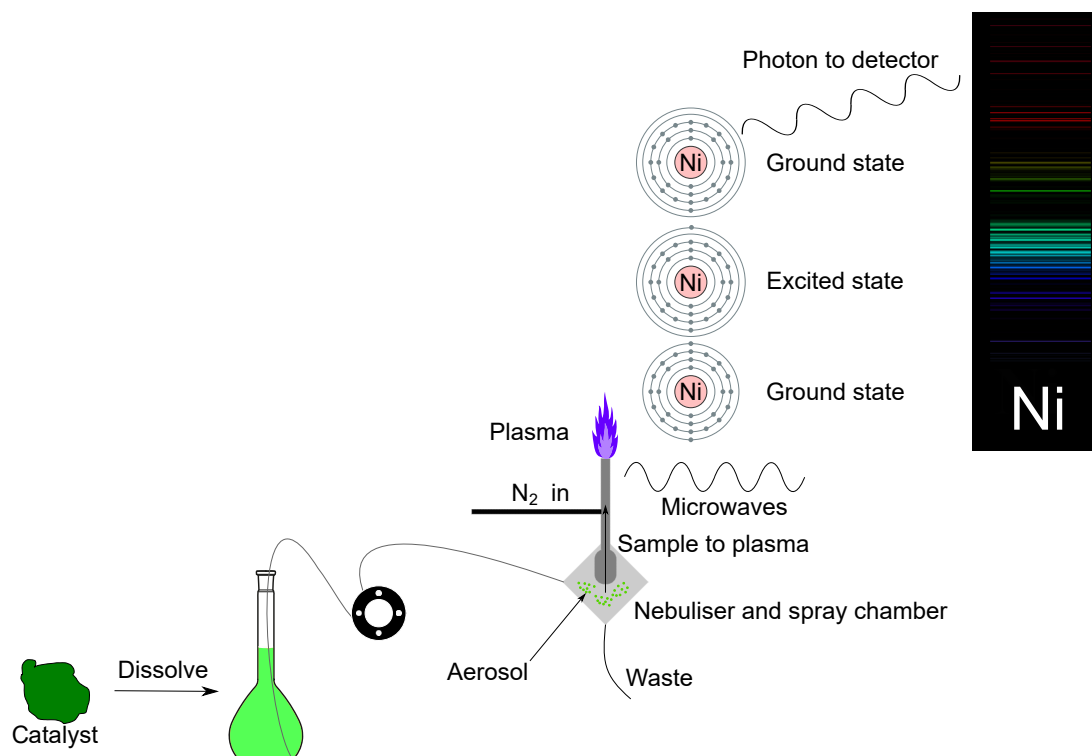


Figure 2.4: A drawing of MP-AES analysis for a nickel catalyst.

in a similar manner to a digital camera. The spectral lines observed are characteristic of its components as the electronic configuration of an element is unique, with the intensity being proportional to number of atoms that were excited.²⁹

This technique can detect over 70 elements, which includes almost all metals of interest to the catalytic scientist, at high levels of detection.³⁰ As multiple transitions are possible, multiple emission lines will occur and thence a different line can be selected if it conflicts with a different element in solution. Conversely, it may lead to detection of elements not present and enhance or depress spectral intensity and therefore provide inaccurate results.²⁹ Furthermore, a vacuum spectrometer is required for the analysis for several main group elements as their emission lines may be absorbed by components of the atmosphere.³⁰

The second mentioned technique, ICP-MS, operates similarly: a solution is vapourised and introduced to a plasma stream. However, in this technique, the ICP torch serves not only to atomise the sample but also to ionise it. The resulting stream of ions is then fed into a quadrupole mass spectrometer and the spectrum produced is used for quantification. In either technique the actual content is performed by comparing the recorded intensity to calibration solutions.

A significant advantage of ICP-MS over MP-AES is its significantly greater sensitivity (0.02–0.7 ppb) and wider element detection ability.³⁰ Moreover, unlike with atomic emission spectroscopies, the interpretation of data is much simpler, with each atom generating at most several peaks rather than the thousands possible for some elements. Unfortunately, this

method is not without several shortcomings, as multiple spectral interferences may occur during analysis runs. For example, different isotopes of elements of similar atomic mass may overlap in the mass spectrum, necessitating the use of less abundant and non-overlapping peaks. In catalytic materials, this problem may be encountered for those using bimetallic Ni-Fe catalysts as the peak for $^{58}\text{Ni}^+$ overlaps with the low abundance $^{58}\text{Fe}^+$ peak. Other interferences in ICP-MS include polyatomic ions that form in the high temperature Ar plasma. This latter problem can be fixed in two ways: (i) by using a much more expensive mass spectrometer,³⁰ and (ii) using an N_2 plasma source.³¹ The former is not ideal owing to the high cost, whilst the latter is a simple and effective option but such plasma sources are novel and not yet widely available.

2.5.1.1 Experimental

MP-AES Samples were analysed using an Agilent Technologies 4100 MP-AES. A known quantity of catalyst was added to an aqua regia solution (2 vol% in H_2O) and allowed to digest overnight. The liquid phase was subsequently filtered using a PTFE filter (0.45 μm , FisherBrand). Digested samples were manually introduced into a stream of nitrogen plasma using a peristaltic pump and a single pass spray chamber at a pressure of 120 kPa in the absence of any air injection. Calibration solutions using a reference material were used to make up a calibration at concentrations appropriate for the sample being analysed. Measurements were repeated three times with a wash step performed in between measurements. The value listed is equal to an average of these three measurements.

ICP-MS The following ICP-MS analysis was performed by Mr Simon Waller of Cardiff University Analytical Services. The digested samples were analysed using an Agilent Technologies 7900 ICP-MS equipped with a I-AS autosampler. A certified reference material (Perkin Elmer) was used to make up a calibration at concentrations of 0, 1, 10, 100, and 1000 $\mu\text{g l}^{-1}$, which were matrix matched to the sample being analysed. During analysis, an inline internal standard (terbium) was employed to correct for any instrumental drift or sample uptake variations. Samples are run in duplicate and values obtained are an average of 3–5 measurements made by the system.

2.5.2 Thermal-analytical techniques

Thermal-analytical techniques form the basis of several catalyst characterisation methods where a response is monitored as the temperature of the sample is controlled by a programme. The information gained from an experiment depends upon the conditions used during analysis and the detector employed. Whilst the qualitative analysis of the data is relatively straightforward, quantitative analysis is complex and not always possible. Three

techniques of this class will be discussed below, *viz.*, temperature-programmed reduction and temperature-programmed desorption, and thermogravimetric analysis.

2.5.2.1 Temperature-programmed reduction

Temperature-programmed reduction (TPR) is a technique that studies the reaction of materials with a reductive gas (usually hydrogen diluted in argon) as temperature is controlled as function of time. Reactivity is typically measured using a TCD either by itself or coupled with a mass spectrometer, but it is also possible to do gravimetrically which will be discussed separately in Section 2.5.2.3. To ensure the TCD signal is only affected by changes in the reductive gas, cold traps and molecular sieves are usually placed before the detector, but if coupled with another detectors (e.g. a mass spectrometer) it may be necessary to remove these items to ensure the other gases reach the detector unimpeded, which may add noise to the TCD signal.

Before the TPR experiment is performed, it is normal to perform a pretreatment—by heating the sample to approximately 120 °C under the flow of an inert gas such as He or Ar—to ensure any residual water or other physisorbed species from the surface of the catalyst. Once this has finished and the sample has cooled to the desired temperature, the TPR experiment can begin. Note that the term “desired temperature” was used as in some instances a sub-ambient starting temperature may be required to observe the reduction of readily reducible species (e.g. Pd²⁺ may occur at 200 K).²⁸

During the TPR experiment, careful deliberation over experimental parameters is required as a multitude of variables can affect both the qualitative and quantitative results. A careful study revealed that the maximum hydrogen consumption rate, T_M , was strongly dependent on the heating rate and gas concentration and weakly dependent on the flow rate or the amount of sample present, with the first two mentioned parameters causing T_M to shift by almost 50 °C.³² Consequently, if TPR is used to find suitable reduction conditions (see below), the relevant variables in the tube furnace must be matched to those used in the TPR experiment.

The most common use of TPR is to determine the temperature at which the precursor is reduced, the stoichiometry of the process, and the number of steps or species involved. From a qualitative perspective, this information may be determined by a comparison to the same catalyst in literature or by oxidising the reduced sample and repeating the TPR experiment which will only show the reduction of the metal oxide(s) rather than, for example, the chlorinated precursor. A qualitative understanding of the TPR profile is gained by integrating the area under peak curves whose area is calculated *via* calibration of a reference standard, such as silver oxide, or injection of a known quantity of gas, to yield a quantity of gas consumed during the reduction. With knowledge of metal loading, the stoichiometry of the reaction can be computed. The species involved in the reaction can be determined by coupling TPR equipment with an additional detector.

An additional use of TPR is to support the formation of bimetallic nanoparticles in the form of alloys. The premise of the argument is as follows: if the TPR profile of a catalyst shows only one peak, it suggests that the readily reducible component has catalysed the reduction of the other component as alloy formation has occurred, and on the contrary, the presence of two peaks implies two distinct metal phases and thus no alloy formation. These are not always true as in some instances there will be a single peak when there are two separate phases if hydrogen spillover is rapid enough.³³ Furthermore, alloy formation may occur during reduction due to species migration, so the TPR experiment on the freshly prepared catalyst will not be useful in this regard.

A different approach to assessing alloy formation using TPR is unique to palladium-based catalysts.^{28,34} When palladium is exposed to hydrogen gas at room temperature it will form palladium hydrides, but these are unstable at temperatures greater than around 60 °C, and decompose to produce hydrogen and in turn, a negative peak in the TPR profile. This phase is however very sensitive to alloying in bimetallic systems and the suppression of the intensity of this peak is taken to be an indicator of the extent of alloy formation.³⁵ If the alloy forms during the heating phase, then the hydrogen uptake of the sample should be recorded as the sample cools where no uptake peak will be observed if an alloy has formed. This method not only applies to metallic alloys, but also interstitial palladium compounds (e.g. Pd-C, Pd-B).^{36,37} This method is semi-quantitative in that it works for a series of catalysts of the same components. However, as this is a bulk phenomena, for particles with a diameter less than ~2.5 nm are unable to form this phase,³⁸ and thus will not show a negative hydride peak, so small palladium-rich particles will evade detection.

Finally, the gas used in TPR is typically hydrogen diluted in a gas of low thermal conductivity e.g. N₂ or Ar with a lower concentration leading to greater sensitivity as the composition derivative will be greatest. However, this may lead to situations where all the hydrogen is consumed (resulting in flat-topped peaks) and a significant change in reduction rate (at high concentrations the hydrogen gas is approximately constant). Therefore, hydrogen concentrations of 5 or 10% are usually used as a compromise. Carbon monoxide can also be used and affords several advantages as its product, carbon dioxide, is a poorer oxidant than water and is easier to dissipate away from the surface. This reductant has its own issues: coking can occur, especially at high temperatures, and its high toxicity limits application in laboratory furnaces.

2.5.2.1.1 Experimental Temperature-programmed reduction experiments were performed using either the Quantachrome Instruments ChemBET or Pulsar TPR /TPD Chemisorption Analyser both equipped with a TCD. A catalyst sample was heated under a flow of helium to 120 °C for 1 h with a ramp rate of 15 °C min⁻¹ before cooling to room temperature in the same gas flow. After cooling to room temperature, the carrier gas was changed to 10% hydrogen in argon and the sample temperature was ramped to 500 °C at a rate of 5 °C min⁻¹.

2.5.2.2 Temperature-programmed desorption

Temperature-programmed desorption (TPD) is a technique to study the desorption of molecules as the temperature of a sample is linearly ramped either under vacuum or in a flow of carrier gas. It is most commonly used in this area of research to characterise the acid/base properties of a catalyst and to determine the kinetic and thermodynamic values of adsorption/desorption and decomposition processes. Furthermore, it can also provide information on the number of desorption events, providing information about the number of adsorbed states on the surface.

The same equipment used in TPR can be used (Figure 2.5) to perform a TPD experiment. The steps to perform a TPD experiment are as follows: (i) sample pretreatment; (ii) adsorption of an excess of probe molecule at a defined temperature; (iii) removal of the weakly bound/physisorbed adsorbate by a flow of carrier gas; (iv) a linear temperature ramp. The gas in the effluent stream is detected with a TCD and the area under the peak is taken to be equal to gas adsorbed on the surface. Ideally, this should be coupled with detection by mass spectrometry but this is not always feasible.

Although the principal use of TPD is for investigating the acid/basic properties of a molecule, the primary interest of this work is to study the temperature programmed desorption of hydrogen to assess relative populations of hydrogen species present on a surface. The nature of these species has attracted significant attention since the 1930s but there remains no clear consensus on the matter. A simple overview is that hydrogen chemisorbed on metals will usually desorb below 300 °C with spillover hydrogen (if applicable) desorbing at higher temperatures. These forms will sometimes be designated “weakly” and “strongly” bound and probably exist in some form of dissociated state, but a separate form, described in older literature as “type C” hydrogen exists as an intermediate between the physisorbed and dissociated states with its desorption event often being missed owing to its relatively low adsorption enthalpy.³⁹

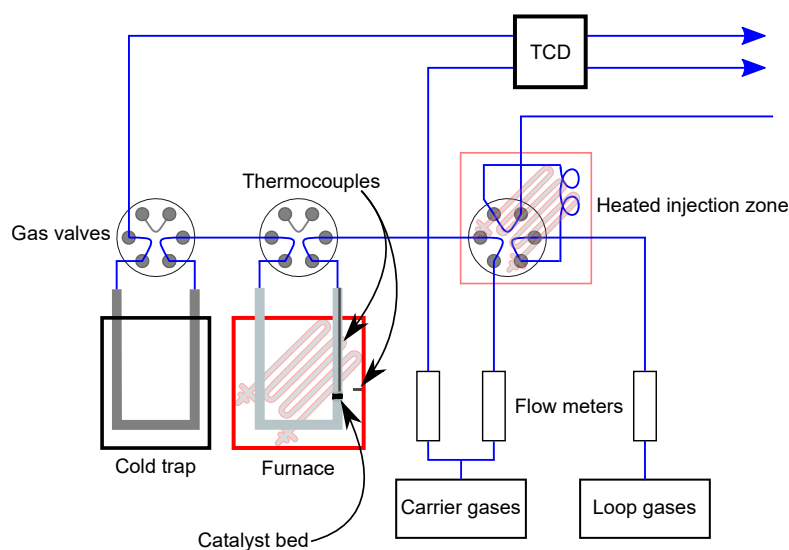


Figure 2.5: Apparatus for performing TPR, TPD, and pulse chemisorption experiments.

The application of H₂-TPD has been utilised by several groups to correlate a specific surface state with the activity of a catalyst series for a particular reaction. One pertinent study by Aben *et al.* investigated the activity of a series of Pt/Al₂O₃ catalysts after different reductive pretreatments for the hydrogenation of benzene at 50 °C in a microflow reactor. A linear relationship could not be found between the TOF and dispersion, yet when the TOF was plotted against the peak height of a low temperature hydrogen desorption peak (located between approximately –30—20 °C), such a correlation was found. Similar results can be found in kinetic modelling studies which often find the surface coverage of active hydrogen species to be lower than what would be expected of the total hydrogen surface coverage. However, work by Scholten and co-workers suggests that hydrogen interacts with metals typically used in hydrogenation reactions approximately equally from a thermodynamic perspective, though the relative proportions of each state was not considered. Moreover, the differences in catalytic behaviour were instead attributable to differing ways of interaction with the molecule being hydrogenated.³⁹

An additional use of H₂-TPD in the study of silica- and alumina-supported platinum nanoparticle reconstruction was outlined in recent publication by Yakovina and Lisitsyn.⁴⁰ It was found that the quantity desorbed and the relative populations of each hydrogen species was strongly dependent on the pretreatment for highly dispersed (D>94%, see supporting information of publication for details) alumina-supported platinum catalysts. However, for a silica-supported platinum catalyst of moderate dispersion (D=38), no such effects were observed. They reasoned that for ultrasmall particles, the reconstruction process was activated and led to increased surface coverages and greater Pt–H bond strengths caused by a stronger interaction of platinum with the support.

2.5.2.3 Thermogravimetric analysis

Thermogravimetric analysis (TGA) is a technique that records the mass of a sample as a function of temperature and/or time in a controlled atmosphere. The instrumentation of this method is displayed in Figure 2.6, an ultra-micro balance with a precision of *ca.* 0.01% is attached to a controlled heating chamber which allows gas to be flowed over the sample.⁴¹ The exit gas line can be coupled with another analysis technique, such as mass spectrometry or infrared spectroscopy, to aid the identification of gaseous products. In some instances, TGA is combined with differential thermal analysis (DTA), which records the temperature of a reference material and the sample of interest to provide information on the thermodynamics of the process. If the sample temperature is hotter than the reference cell during a mass change event, the event is exothermic; the reverse is true if the process is endothermic.⁴²

The setup discussed above, illustrated in Figure 2.6, permits the study of thermal stability and adsorption/desorption processes. The former is not only related to catalyst stability under defined conditions, but also provides information about the decomposition of precursor

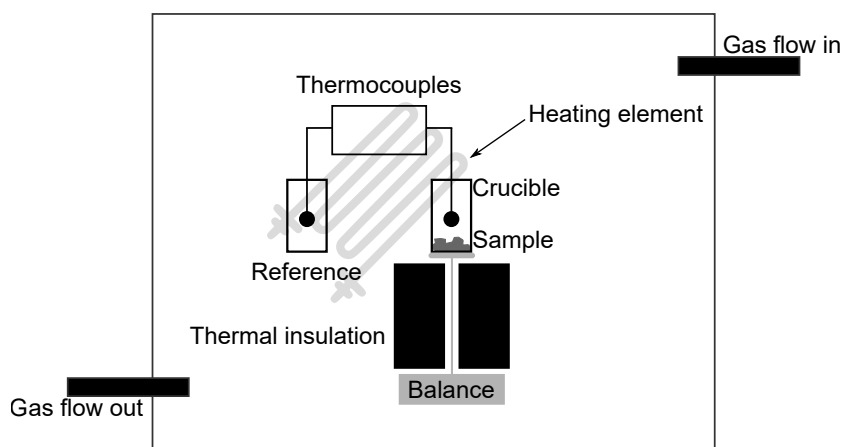


Figure 2.6: A TGA-DTA instrument schematic.

species, which may be useful when determining, for example, calcination conditions. For adsorption/desorption processes, information about poisons on the surface, coke formation, etc. can be obtained which may be useful to perform on the catalyst post-reaction.

2.5.2.3.1 Experimental Thermogravimetric analysis experiments were performed on a Perkin Elmer Pyris 1 TGA equipped with a PerkinElmer Clarus SQ 8 Mass Spectrometer. Samples were held at room temperature for 20 min under a flow of air at a rate of 20 ml min^{-1} to stabilise the mass spectrometer, before they were heated at rate of 5° min^{-1} to 250° C , at which point the temperature remained fixed for a further 2 h. These conditions were chosen to match the calcination procedure outlined above (Section 2.2.1).

2.5.3 X-ray characterisation

When a sample is irradiated by X-rays, several processes occur, *viz.*, scattering, diffraction, and absorption, of not just the surface layer, but the subsurface region. These phenomenon form the basis of X-ray characterisation techniques in catalysis, for which there are many methods available. This work has used just two of these X-ray techniques, X-ray diffraction (XRD) and X-ray photoelectron spectroscopy (XPS) which will be discussed below. That said, many X-ray techniques share a fundamental requirement of the use of monochromatic radiation, which is typically generated in two steps: (i) generation of X-rays and (ii) monochromatisation.

X-rays are generated in a Coolidge tube, which is an evacuated tube comprised of a metal filament (usually tungsten) cathode and an anode target made of a metal; for XRD this is often copper and for XPS this is often magnesium or aluminium. The filament is heated resulting in the emission of electrons that are then accelerated under an electric field towards the metal target. When electrons collide with atoms in the target, the energy is transferred to heat and X-ray radiation. The latter process being incredibly inefficient as less than 1% of the electrical power is converted to radiant power.

Some of the generated X-rays are emitted as a continuous spectrum of white radiation (or Bremsstrahlung) and if the voltage applied is high enough, superimposed on the continuous spectrum is the characteristic X-ray spectrum of the target which forms highly intense emission lines. These lines occur when an incoming electron has sufficient energy to eject an electron from a core electron shell which results in an electron from a higher shell filling the hole. This in turn results in the emission of an X-ray possessing an energy equal to the difference between the two levels. If the electron is emitted from the K shell and filled with an electron from the L shell, it is referred to as K_{α} radiation; if the vacancy is filled with an electron from the M shell it is referred to as K_{β} radiation, and so on. Moreover, as there are separate orbitals in each shell, an additional subscript is used to denote which orbital the electron came from. This is limited to where electron transitions are permitted i.e. the electron must originate from an orbital with a orbital quantum number ± 1 of the the orbital. For example, if the K (1s) electron of an atom is ejected it must be filled with an electron from a p orbital, as if a transition between an s or d orbital occurs $\Delta l \neq \pm 1$.⁴³ As there are two energy levels of p orbitals, $p_{1/2}$ and $p_{3/2}$, there are two X-ray photons emitted; if the transition is from an L shell the notation from the former level would be K_{α_2} whilst the latter would be K_{α_1} . The intensity of the K_{α_2} is about half of that of the K_{α_1} .

The generation of polychromatic radiation is problematic as having an X-ray of well-defined energy and wavelength is of crucial importance for the reasons outlined in the paragraphs below. In order to ensure the X-ray is as expected, the X-ray beam may pass through various components. Depending on the age of the instrument these may be limited to thin filters which reduce the intensity of the K_{β} line and Bremsstrahlung, but not the K_{α_2} component. Monochromators—single crystal of a material with an appropriate interplanar spacing— on the other hand are able to eliminate the K_{β} component and separate the K_{α_1} and K_{α_2} wavelengths if they are of different enough energy.

2.5.3.1 X-Ray powder diffraction

X-Ray powder diffraction (XRD) is an analytical technique that provides information on the bulk structure in a crystalline material and will reveal if a material is amorphous. The experimental procedure involves the generation of X-rays which are then filtered and focused with some other optics on a sample that is usually spinning. The detector is then rotated at a fixed distance whilst the X-ray source is fixed in position (or vice versa) and the intensity of the reflected X-rays is recorded. A set-up this configuration, known as the Bragg-Brentano geometry, is displayed in Figure 2.7.

The phenomenon of XRD is a consequence of the diffraction of X-ray radiation by the electron cloud of an atom in a periodic lattice. When a beam of X-rays impinges on a row of regularly spaced atoms with a spacing of d , at certain angles of incidence of θ , the waves are reflected and amplified whilst at others, or if there is no long range order, they are out of phase

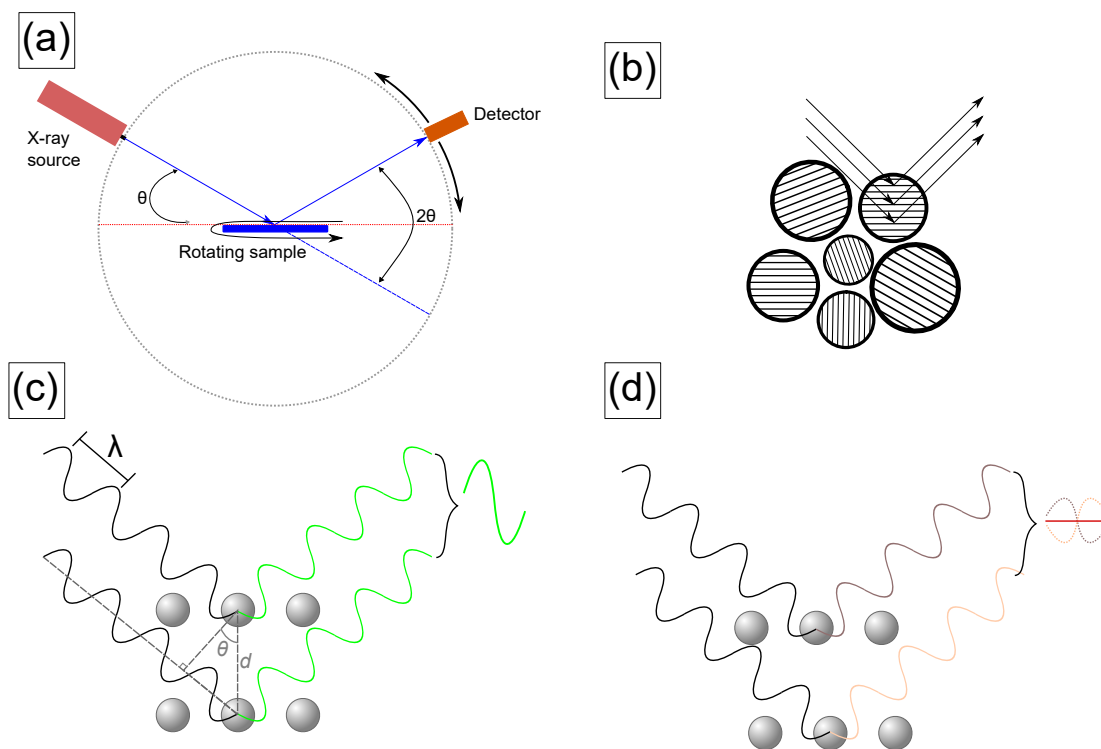


Figure 2.7: Diagrams relating to XRD. (a) A drawing of the Bragg-Brentano geometry used in XRD experiments. (b) An example of the small contribution of particles that contribute to Bragg's Law in a polycrystalline powder. Figure and caption adapted from reference [34]. (c) Constructive interference of an ordered crystal which satisfies Bragg's Law. (d) Destructive interference of an disordered crystal which does not satisfy Bragg's Law.

and produce deconstructive interference and cancel out (Figure 2.7c + d). The angles at which a material will display a diffraction peak is described by Bragg's Law (Equation 2.14).⁴⁴ As d is a fundamental property of a crystalline material, the identification of phases present in a sample is possible by comparing the experimental observed d values to a database.

$$n\lambda = 2d \sin(\theta) \quad (2.14)$$

Spinning is required because many catalytic samples come in the form of fine powders, and XRD experiments involve packing the powder onto a non-reflective sample holder. This means many crystals will be randomly orientated or have insufficient crystallites to provide a true average of the powder (Figure 2.7). To increase the likelihood of satisfying the Bragg condition, the sample is spun during the recording of the diffraction pattern as this allows the X-ray wave to interact with more of the sample which also improves the signal to noise ratio.

One final discussion point is necessary concerning the X-ray source. Each source has a characteristic wavelength which is important primarily as it changes the angles where diffraction is possible and secondary X-rays can be generated. Regarding the former, smaller wavelengths result a shifting of diffraction patterns to lower angles resulting in poorer resolution and d spacing accuracy. The latter is important as some of the sample will absorb X-ray photons during analysis, with electrons being ejected at a similar wavelength to the

incident beam. As described above, this process leads to the release of an X-ray, often referred to as X-ray fluorescence, at a different wavelength to the incident radiation. This is particularly a problem when using a copper source for analysis of samples rich in cobalt, iron, and manganese where the signal-to-noise ratio will be low. The solution to this problem is to use a different source, such as a cobalt, or a post-sample monochromator, such as graphite.

2.5.3.2 Experimental

XRD analysis was performed using a PANalytical X'Pert Pro diffractometer equipped with a nickel-filtered copper X-ray source ($\lambda=1.5406 \text{ \AA}$) working at 40 kV and 40 mA and analysed using a Bragg-Brentano geometry. Several programmes were used for obtaining the diffraction pattern depending on the information desired. The standard method was a broad scan in the 2θ angular range of $5\text{--}80^\circ$ using a step size of 0.0167° with a scan speed of $0.0418^\circ \text{ s}^{-1}$. For materials which primarily had Bragg peaks in the region of $30\text{--}50^\circ$, a separate experiment was performed where the angular range was narrowed to $30\text{--}50^\circ$ and the step size and scan speed were reduced to 0.00418° and $0.00354^\circ \text{ s}^{-1}$, respectively.

2.5.3.3 X-ray photoelectron spectroscopy

X-ray photoelectron spectroscopy (XPS) is an analytical technique used to probe the chemical and electronic state of the surface of materials to provide qualitative or quantitative data. For catalytic materials, a simplified view of an XPS experiment involves mounting a sample on a holder and transferring it to an ultrahigh vacuum analysis chamber, where the sample is subjected to X-rays that have passed through a monochromator. The detector measures the intensity and kinetic energy of electrons emitted when X-ray quanta are absorbed by atoms in the sample. Subsequent processing of the spectrum obtained reveals information about the surface of the sample.

The physical basis of XPS is the photoelectric effect which describes the process of the emission of an electron after an atom has absorbed a photon with sufficient energy (Figure 2.9). The kinetic energy of the ejected electron has a kinetic energy, E_k , equal to the energy of the

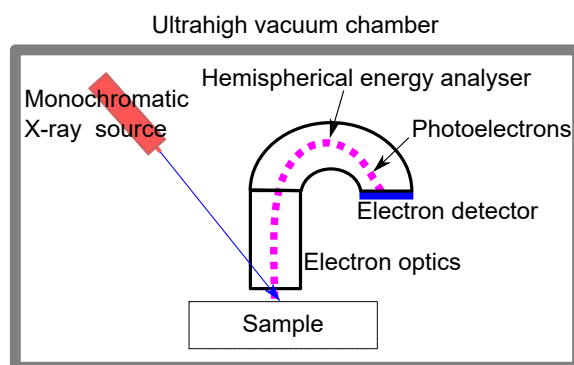


Figure 2.8: Instrument schematic for an XPS instrument.

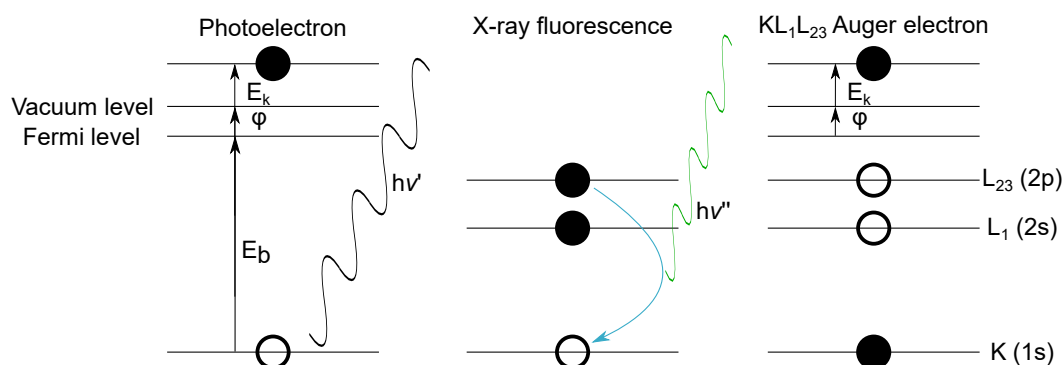


Figure 2.9: A visual representation of the photoemission process, X-ray fluorescence, and the Auger process. The positioning of the energy levels is arbitrary. Figure adapted from reference [34].

incident photon, $h\nu$, minus the sum of the binding energy of the electron, E_b , and the work function of the spectrometer ϕ :

$$E_k = h\nu - E_b - \phi \quad (2.15)$$

If the sample is conducting, then E_b can be calculated by Equation 2.15 as the Fermi level aligns with that of the spectrometer and the energy scale will be well defined. For materials that are insulators or poorly conducting this alignment does not happen and energy scale calibration is required. This is performed by assigning the C 1s peak, which is present in all materials exposed to air, to a value between 284.0–285.6 eV, which although has long been recognised as problematic, a universal solution is yet to be realised.^{45–50}

The photon source for laboratory XPS is usually Mg K α (1253.6 eV) or Al K α (1486.3 eV) X-ray radiation, though the use of shorter wavelengths has grown in popularity in recent years in a technique referred to as Hard XPS. This latter technique affords several advantages over conventional XPS such as information from the inner core levels (where binding energies are higher) and probe deeper into the sample.⁵¹

XPS is typically used to record the binding energies of core electrons, with the study of valence electrons being more suitable for ultraviolet photoelectron spectroscopy. Binding energies are element specific and slightly dependent on the atom's chemical state (bonding, oxidation state, etc.). A general rule is that a positive formal or partial charge on an atom will result in the binding energy increasing on account of an increased electronic interaction with any changes observed being described as chemical shifts. Indeed, the binding energy itself is dependent not only on the initial state, but on the electronic state that forms in the absence of the emitted electron.²⁸ The hole that forms when an electron is emitted affects not only the atom from where the electron originated but also the surrounding atoms. This requires electronic relaxation for stabilisation, but if the electron is not completely decoupled when this process occurs it must be included in kinetic energy of the photoelectron and therefore the binding energy.⁵²

In addition to peaks in the XP spectra arising from the photoelectric effect, additional electrons are detected from a process called Auger decay. The energy released during

fluorescence (*vide supra*) is taken up by another electron which is emitted from the atom (if of sufficient energy) to be detected at an element specific and X-ray independent wavelength. These Auger peaks may help allude the chemical state of a material in cases where the binding energy is misleading due to particle size effects or there is only a small shift between chemical states.⁵⁰

2.5.3.3.1 Surface sensitivity When assessing data obtained from XPS it is useful to understand the origin of the data, both what can be detected and how far into the surface the data originates. With regards to the former, the detection limit of XPS is said to be between 0.1–1 at.%; although, a recent study on 6000 binary systems using Al and Mg K α X-rays found that the detection limit could in fact vary by almost four orders of magnitude and be lower than 10 at.% for light elements in a heavy matrix to 0.01 at.% for heavy elements in a light matrix.⁵³ This behaviour occurs due to various types of peak interference.⁵³ From a catalytic perspective, the sensitivity will depend on metal loading, the support, and the depth distribution of the element of interest.

For the electron analyser to detect a photoelectron, it must first escape from the surface without losing energy during collisions with atoms in the solid. This distance is referred to as the inelastic mean free path of an electron and is dependent on the kinetic energy of the photoelectron, which is 1–2 nm when the kinetic energy is 15–1000 eV, and the probing depth is then taken to be 3 times these values meaning information from the outermost 6 nm is available.³⁴ However, depending on the material and instrument configuration, peak intensity may come from as little as the outermost 1 or as deep as 10 nm.⁵⁴

2.5.3.4 A brief overview regarding the quality of data

As with all techniques, XPS is not without its flaws. In recent years, a series of polemics about the practice of XPS have appeared in literature with some heated debate in *Chemistry World*. The problem arises from inexperienced users operating equipment and misinterpreting/misreporting data, with approximately 30% of published XPS being completely incorrect.⁵⁵ This has led to a group of eXPerts releasing a series of guides for inexperienced users/reviewers on good practices for XPS in attempts to improve data quality.^{49,50,54,56–61}

Let us use the example of a supported palladium catalyst in powdered form, where it can be mounted into a recess, to highlight some of these issues. The oxidation state of palladium may be of interest, however, exposure to air may lead to the oxidation state of the sample, whether “fresh” or “spent”, which may result in incorrect conclusions during analysis; it must be ensured that the surface is not tarnished by exposure to the atmosphere, and use of an inert atmosphere during mounting or an *in situ* treatment may be required before analysis.

Once placed in the instrument, XP spectra can be recorded. Great care is necessary in this step as oxidised palladium⁶² (and other metals in high valence states)⁵⁰ are known to reduce during the experiment, negating any effort expended in the previous step. A simple strategy to

see this effect is by scanning the palladium regions as the first and last spectra, but additional procedures may be required to capture the “true surface”.⁵⁰

Interpretation of XPS data is a task fraught with difficulty as the peak widths, positions, intensities, and backgrounds must be physically and chemically correct. The experimental data is fit using peaks based on mathematical functions or line shapes derived from model systems. The latter being more appropriate for catalytic materials due to their high complexity with a benefit of this approach being that it reduces the number of parameters required to fit the data as spectral properties such as line shape, spin-orbit coupling, and peak area and line width information are already determined.⁵⁰ The plausibility of fit is then assessed by mathematical methods such as the chi-squared method⁶³ or “uniqueness” plots, which plots the chi-squared value obtained against a fitting parameter that is varied; a horizontal line indicates that changes to the parameter do not contribute which suggests an inappropriate fit whilst a parabolic curve indicates a unique fit, but not necessarily a good or scientifically meaningful one.⁶⁴

2.5.3.4.1 Experimental

XPS was performed on a Thermo Scientific K-Alpha+ spectrometer equipped with a monochromatic Al K_α source (72 W). Survey spectra were recorded with a pass energy of 150 eV with a step size of 1 eV, whilst high-resolution scans utilised a pass energy of 40 eV with a step size of 0.1 eV. Sample charge compensation was controlled by the K-Alpha charge neutralisation system, which uses a combination of low energy electrons and argon ions. Data analysis was performed in CasaXPS using a Shirley background and Scofield sensitivity factors with an energy dependence of -0.6 . The binding energies are reported against the C 1s reference at 284.7 eV.

2.5.4 Textural property analysis

Catalyst supports are usually porous and have large surface areas as this affords some protection against the sintering of nanoparticles. It is of considerable interest to know the surface area, pore volume, and pore size distribution of both the “fresh” support and the prepared catalyst as these values may change during the preparation process. Examples of such changes may include a decrease in surface area, changes in physical structure, and pore volume. Possible explanations of these phenomena are the high heat treatment of the support, reactions of the support during the catalyst preparation, or pore blockage by the added metal. This latter point implies that some metal is effectively “lost” which is undesirable as catalytic metals are often expensive. In this section methods to determine textural properties of a solid, *viz.* adsorption behaviour, surface area, pore volume, and pore size distribution, will be considered.

Physisorption of an inert gas near its normal boiling point is a technique used to characterise textural properties of solid materials. The basic experimental procedure is as follows: a sample is outgassed to remove physisorbed species on the surface by using an elevated temperature and high vacuum. The sample is then cooled to a temperature near the normal boiling point of the adsorbate where an adsorption isotherm is recorded by measuring the amount of probe molecule removed from the gas phase (volumetrically) or directly (gravimetrically) which can work in static or dynamic systems. In the volumetric technique, a known quantity of gas is administered to a sample tube and the pressure difference is recorded at equilibrium. The adsorption isotherm is measured point-by-point with increasingly large volumes of gas before the reverse of this process is performed (desorption isotherm). The total pressure in the tube is usually kept low so the ideal gas law can be applied rather than the fugacity. This technique is the most widely used and is the method used in this thesis, so it will be the focus of the discussion, but as with chemisorption experiments (Section 2.5.5.4), the discussion is largely applicable to all techniques.

Support materials often have an array of compounds physisorbed to the surface which need to be removed before analysis. This is usually performed by an evacuation at an elevated temperature; for microporous materials (where the pore diameter, d_{pore} , < 2 nm) pressures of 10^{-5} bar are desirable to ensure an adequately clean surface. An alternative method for non-microporous materials involves exposing a sample to a flow of inert gas at a raised temperature which can be quicker than the vacuum method. Regardless of the outgassing method used, the conditions employed should not cause any structural changes to the sample and must be carefully controlled and recorded.

Then by exposing the sample to a gas below its critical temperature at a constant temperature, the amount of gas adsorbed is a function of pressure and recording the uptake produces an adsorption isotherm.⁶⁵ The shape of the resulting sorption isotherm of a material is dependent on the interaction between fluid-fluid, fluid-surface, geometry effects, and the states of components.⁶⁶ Isotherms are assessed and assigned to one of eight groups as recommended in the most recent IUPAC technical report on the subject (Figure 2.10), and this will form the basis of the discussion.⁶⁷

Type I isotherms are characteristic of microporous solids with relatively small external surface area and look similar to a Langmuir isotherm. Examples of materials which display this type of isotherm are activated carbons and zeolites. This isotherm is concave relative to P/P_0 and approaches a limiting value. This limiting factor is not due to the formation of a monolayer on the inner surface, but rather as a result of restricted access to the micropores. A steep uptake at low P/P_0 values occurs when there is a strong interaction between the adsorbate and the same component in the liquid phase. The division into Ia and Ib relate to the pore size and their distribution; the former is for materials that have mostly uniform pores less than approximately 1 nm whilst the latter are for materials with a wider pore size distribution that may include narrow mesopores ($d_{pore} < \sim 2.5$ nm).

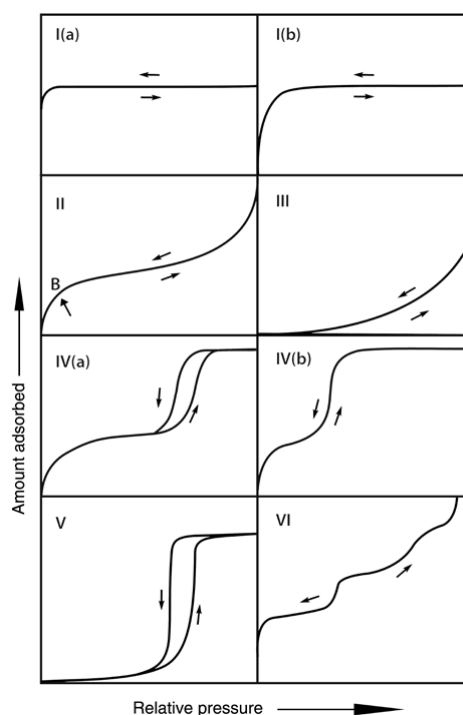


Figure 2.10: Classification of physisorption isotherms. Figure and caption reproduced from Thommes *et al.*⁶⁷

Type II isotherms are given by materials that are non-porous or macroporous (e.g. some silicas). This isotherm forms because monolayer-multilayer adsorption is unrestricted at high P/P_0 values. The transition from monolayer formation to multilayer adsorption can be indicated when a sharp knee (labelled “Point B” in Figure 2.10) is observed at the beginning of the middle almost linear section of an isotherm. Conversely, a less prominent “Point B” indicates significant overlap of monolayer-multilayer adsorption.

Type III isotherms are rarely observed under typical analysis conditions used for catalytic materials. It is reported that this isotherm will form if studying the adsorption of *n*-alkanes or benzene on silica.⁶⁸ It takes this shape when the interaction between the sample and adsorbate is weaker than the adsorbate and the same component in the liquid phase, with the adsorbed molecules clustering on the most favourable sites.

Type IV isotherms are typical of mesoporous materials such as MCM-41 or SBA-15. This shape originates by initially following the same profile as the Type II isotherm (usually a pronounced “Point B” is observed), before pore condensation occurs at higher P/P_0 values. As with the Type I isotherm, eventually these pores become full and the gas uptake will usually plateau. The difference between Type IVa and IVb is attributable to pore size: materials where d_{pore} is greater than 4 nm will display a Type IVa isotherm and vice versa.

Type V isotherms are often observed for the adsorption of water on hydrophobic materials. Initially, the adsorption profile is similar to Type III, however at higher P/P_0 values pore condensation or increased interaction between the surrounding liquid and adsorbate occurs.

Type VI isotherms are obtained when using argon or krypton on graphitised carbon blacks at liquid nitrogen temperatures (i.e. 77 K). It forms by the step-wise adsorption on a

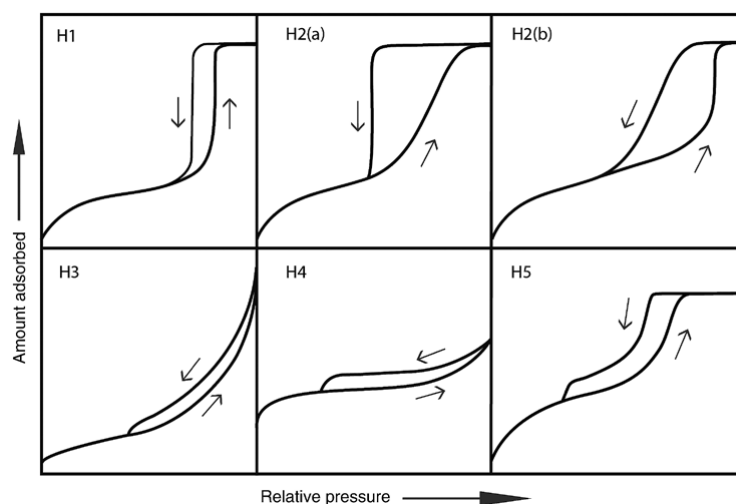


Figure 2.11: Classification of hysteresis loops. Figure and caption reproduced from Thommes *et al.*⁶⁷

uniform, non-porous surface and the sharpness of the steps depend upon the probe molecule, temperature, and homogeneity of the surface.

The nature of the hysteresis loop can be considerably complex as it is dependent on the pore size, pore shape, and adsorption conditions. Hysteresis loops occur because of capillary condensation as the condensation of a gas in a pore to a liquid is more readily achieved than its evaporation. As with physisorption isotherms, IUPAC has classified hysteresis loops into six groups (Figure 2.11). The classic example is the H1 hysteresis loop which represents the metastable adsorption branch with the desorption branch being associated with an equilibrium of the liquid-vapour transition. Other hysteresis loops are caused by more complex pore structures where effects such as pore blocking and cavitation can occur.⁶⁶ An important issue was raised by Schüth *et al.*⁶⁹ who stated that care should be taken to not overinterpret the sharp closure of hysteresis loops at a relative pressure of 0.42 for nitrogen physisorption measurements as this is an artifact of the stability of the meniscus of liquid nitrogen.

2.5.4.1 Data treatment procedures

2.5.4.1.1 The Brunauer-Emmett-Teller (BET) method The Brunauer-Emmett-Teller (BET) method⁷⁰ is widely used to determine for evaluating the surface area of materials. This method is an extension of Langmuir theory whereby molecules in the first layer act as sites for adsorption of the second layer and so on. It is then assumed that the uppermost layer is in dynamic equilibrium with the vapour meaning the number of layers covering a specific site will vary, but most importantly, the number of molecules in that layer is constant.⁷¹ This forms the basis of the theory and using the Langmuir equation as a starting point leads to derivation of the BET equation (Equation 2.16).

$$\frac{P}{v(P_0 - P)} = \frac{1}{v_m C} + \frac{C - 1}{v_m C} \left(\frac{P}{P_0} \right) \quad (2.16)$$

Where v is the volume of adsorbate adsorbed at the relative pressure, P/P_0 , v_m is the volume of an adsorbed monolayer, and C is the BET constant. A plot of $P/v(P_0 - P)$ against P/P_0 is usually plot between the relative pressure values of 0.05–0.35 which allows the BET surface area to be calculated. The gradient, s (Equation 2.17), and intercept, i (Equation 2.18), are then used to calculate the weight of the absorbed monolayer (Equation 2.19).

$$s = \frac{C - 1}{v_m C} \quad (2.17)$$

$$i = \frac{1}{v_m C} \quad (2.18)$$

$$v_m = \frac{1}{s + i} \quad (2.19)$$

The total surface area is then calculated as stated by Equation 2.20:

$$S_t = \frac{v_m N_A A_{cs}}{M_r} \quad (2.20)$$

Where S_t is the total surface area, N_A is Avogadro's number, A_{CS} is the cross-sectional area of the adsorbate. The specific surface area, S , is then be calculated by Equation 2.21:

$$S = \frac{S_t}{w} \quad (2.21)$$

Where w is mass of sample. The BET constant is calculated by:

$$C = \frac{s}{i} + 1 \quad (2.22)$$

The physical meaning of this constant was originally proposed to relate to net enthalpy of adsorption by the following equation:²⁸

$$C = \exp\left(\frac{H_1 - H_L}{RT}\right) \quad (2.23)$$

where H_a is the average heat of adsorption of the first layer and H_l is the enthalpy of liquefaction. subsequent layers. This is now viewed as an oversimplification and the BET constant should instead be used to provide insight into the shape of the isotherm in the low P/P_0 region. A C value of less than 2 indicates the isotherm is Type III or Type V and the BET method is unsuitable. If the BET constant is around 50, then it suggests "Point B" cannot readily be identified. To obtain a sharp "Pont B", a C value of approximately 80 must be obtained and the surface area is the adsorbate accessible surface area. Very high values of C ($> \sim 150$) indicate high-energy surface sites or the presence of micropores and the result should be treated with caution (*vide infra*).

The surface area this method provides a true probe accessible surface area for materials which display isotherms of Type II or Type IVa, but not for other isotherms. The difficulty in applying to Type IVb isotherms is because pore condensation can occur at low P/P_0 values.⁷² Its applicability to Type III isotherms is difficult to ascertain because of the rarity of isotherms

of this type and the fact that if the adsorbent is changed it is possible to obtain a Type II isotherm where the equation is valid.

For Type I isotherms, many of the assumptions made in the derivation of the equation are violated and thus cannot be used directly. Rouquerol *et al.*⁷³ have proposed that by carefully modifying the region used and ensuring that (i) C is positive, (ii) the gas uptake should continuously increase with $n(1 - P/P_0)$, and (iii) the P/P_0 value at which a monolayer is obtained is within the plotted region. The BET surface area obtained is an “apparent” value and its physical meaning relates to the adsorbate strongly interacting with the surface (the packing of the adsorbate and thus the cross-sectional area is therefore doubtful). Other methods have been proposed to calculate the surface area of Type I isotherms (e.g. Langmuir, Dubinin-Radushkevich, etc.), but the theoretical value of these is questionable.⁷⁴

2.5.4.1.2 Probe molecules and analysis conditions Up until this point there has been no mention of what is meant by adsorbate or the experimental condition employed. Indeed, the equations above indicate that the surface area above is strongly dependent on the choice of probe molecule. Many materials of catalytic interest have high surface areas ($> \sim 50 \text{ m}^2 \text{ g}^{-1}$) and nitrogen and argon are suitable for surface area analysis; for materials with much lower surface areas, the use of krypton is required. The most common probe molecule is nitrogen, used as its boiling point of 77 K, as both gaseous and liquid forms are cheap and widely available. Its surface area is assumed to be 16.2 \AA^2 which arises from its close-packed structure in the liquid state and this value is the standard value and was the former IUPAC standard probe.⁷⁵ However, this cross sectional area is dependent on the nature of the surface: apolar surfaces, such as graphite, tend to conform to the value, whilst on some polar surfaces, such as silica, this value may reduce by approximately 20%.⁷¹ The origin of this deviation lies in the quadrupole moment of nitrogen and the reorientation of the nitrogen molecule on the surface. The latest IUPAC recommendation is to use argon at liquid argon temperature (87 K) as it is not quadrupolar. At this temperature argon has a cross-sectional area of 14.2 \AA^2 and is generally less dependent on the surface chemistry of the sample and offers advantages in the analysis of micro- and mesopores and error reduction.⁶⁷ A major problem with this method is that liquid argon is less widely available.

2.5.4.1.3 Pore analysis Porous materials are often used in catalysis and knowledge of the pore volume, size, and distribution is of considerable interest. Pore volume for ideal Type I and Type IV isotherms can be calculated using the uptake at high P/P_0 values by applying the Gurvich rule which states that pores are filled with the adsorbate in the bulk liquid state. This rule cannot be applied for macroporous materials, as there is no near plateau at high relative pressures as larger pores are filled at higher relative pressures.

The calculation of pore size and pore size distribution are considerably more complex. For example, the pore packing in micropores is dependent on the pore size and shape and classical

methods do not correct for this, resulting in overestimation of the pore size.⁶⁶ For mesopores, the most popular analysis method involves using the Barret, Joyner, Halenda (BJH) method,⁷⁶ which is based upon the modified Kelvin equation which describes pore condensation. For a cylindrical pore the Kelvin equation is in the form of:⁷¹

$$\ln \frac{P}{P_0} = \frac{-2\gamma\bar{V}}{rRT} \cos \phi \quad (2.24)$$

where γ is the surface tension of the liquid, \bar{V} is the molar volume of the condensed liquid in a pore with a radius of r , and R and T are the gas constant and temperature, respectively.

The BJH method then makes some further assumptions about adsorbed films already present on pore walls which leads to the calculation of pore size, pore size distribution and pore volume using the desorption branch of the hysteresis loop; the adsorption branch of the loop can be used if corrections for the metastability are made and is required when pore blocking or percolation phenomena is observed in the hysteresis loop.⁷¹ The validity of the equation does not extend to narrow mesopores, $d_p \sim < 10$ nm, as pore radii of well-ordered mesoporous materials were shown to be underestimated by $\sim 25\%$. This deviation was partly ascribed to inhomogeneity in the fluid lacking a correction for the fluid-wall interaction.⁷⁷

More modern methods are based upon density-functional theory (DFT) and molecular simulations.⁶⁶ Theoretical techniques are the IUPAC recommended analysis method as the basis is on microscopic, rather than macroscopic, phenomena, under the proviso that a suitable model is chosen.⁶⁷ These methods take a geometrical model of a representative material and combine it with a model of the intermolecular forces in the system to provide a detailed explanation in the behaviour of the probe molecule in pores.⁷⁸ This provides a basis for calculating reliable information about the adsorption and desorption branches and is able to provide accurate pore information for materials with complex pore networks and independent of whether the adsorption or desorption branch is used. A large number of materials have been computed and thus many materials can use this method for property determination.

2.5.4.2 Experimental

Nitrogen physisorption was performed using a Micromeritics 3Flex for the industrial Pd/C catalyst in Chapter 4 and a Quantachrome Quadrasorb Evo or Quantachrome Surface area analyser in Chapter 5. Prior to analysis all samples were degassed for 16 h at 150 °C after which they were first cooled to room temperature before cooling to the analysis temperature (−196 °C). In Chapter 4, the adsorption branch was recorded from 1.76386×10^{-8} to 0.994582 P/P_0 whereas the desorption branch was recorded from 0.994582 to 0.0941492 P/P_0 . The isotherm was fitted with a NL-DFT model isotherm for a carbon material with infinite slits as implemented in the Micromeritics 3Flex software. In Chapter 5, adsorption branches were measured from a P/P_0 value of 0.004 or 0.05 to 0.99 and desorption branches were recorded

from 0.99 to 0.05. The Rouquerol BET method was used to analyse the apparent surface areas for all materials.^{70,73} Free space was measured post-analysis with helium.

2.5.5 Particle size and dispersion measurements

2.5.5.1 Electron microscopy

Electron microscopy is a group of characterisation methods that provide the opportunity to view a catalyst's structure in atomic detail in two or three dimensions with potentially a sub-Ångstrom spatial resolution.⁷⁹ This technique involves illuminating a sample with a beam of electrons and analysing the resulting wave with an appropriate detector. An array of techniques are built around this principle which are summarised in Figure 2.12.

Transmission (and high-resolution transmission) electron microscopy (TEM and HRTEM) are widely employed forms of electron microscopy used in catalysis. In these methods, high energy electrons are focused on a thin sample with the electrons that are not impeded by the sample being used to gather information about the specimen. The number of electrons that can pass through a sample are dependent on the density and the thickness of the sample which necessitates careful preparation of analysis samples. Preparation often involves disaggregation of a solid catalyst sample in a volatile solvent carefully pipetted onto a holey carbon film as this material does not strongly absorb or scatter electrons. In imaging mode, the transmitted

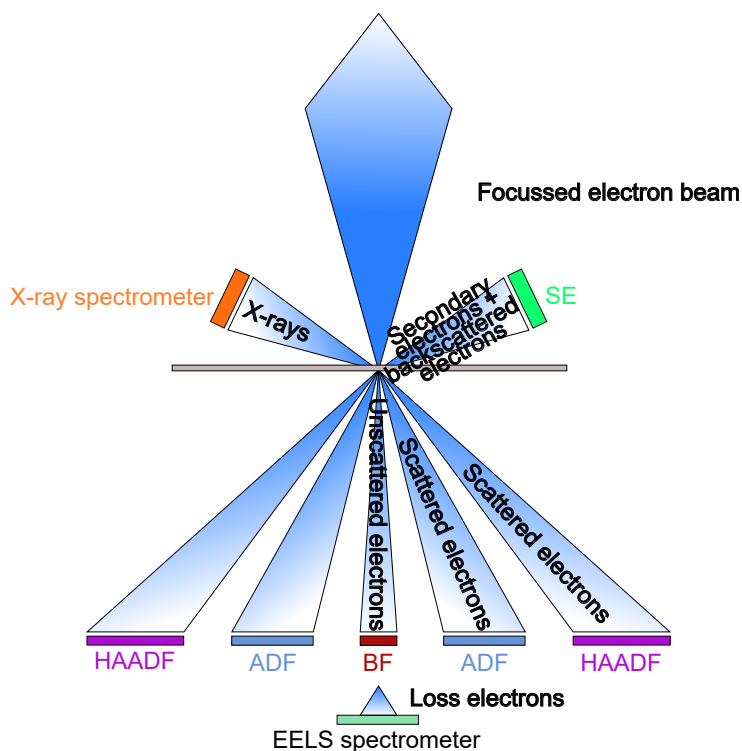


Figure 2.12: The interaction of an electron beam with a sample and a number of interactions are shown with relevant detectors; bright-field (BF), annular dark field (ADF), and high-angle-annular dark-field (HAADF). When the BF detector is not present, transmitted electrons can be analysed by electron energy-loss spectrometry (EELS). Image adapted from [79].

(unscattered) electrons can be used to form a two-dimensional bright-field image, whilst the diffracted electrons can be used to produce a dark-field image. For supported metal catalysts, the dark-field image is generally more useful as the metal nanoparticles will scatter the beam more than the support, appearing light in the image, and thus provide better contrast. However, image features are strongly dependent on focus and sample thickness and require careful interpretation.⁸⁰ In diffraction mode, information about the crystal orientation can be obtained over a very small area (c.f. XRD where a much larger area is probed).

Additionally, if the bright-field detector is removed, then the energy lost by electrons through inelastic scattering interactions with electrons in the sample can be recorded with an electron spectrometer, forming the basis of electron energy loss spectroscopy (EELS). EELS can be complementary to energy-dispersion X-ray spectroscopy (Section 2.5.5.2), because it is most sensitive for light elements and provides information *inter alia* on atomic and alloy composition, bonding and phase information, and oxidation state.⁸¹

Scanning electron microscopy (SEM) is another electron microscopy technique used in materials characterisation. Operationally, an electron beam is scanned point by point in raster mode that produces a signal at each point. This is then correlated to beam position to produce an image. Two types of electrons, backscattered (BSE) and secondary (SE), which arise from the elastic and inelastic scattering after interacting with the sample, respectively, are produced during the scan. The number of BSE that reach the detector is proportional to the atomic number with the depth probed limited by the incident beam energy, the atomic number/weight, and sample density. This can therefore provide information on a sample's composition.⁸² On the other hand, SE are characteristic of the very outer surface (approximately 0.5–1.5 nm for metals)⁸³ and are useful for obtaining information about the topography of a specimen.

A scanning transmission electron microscope combines the two modes of instrument, except that the electron beam is focused into a very fine point, and provides the high resolution of TEM with the region selectivity of SEM. An interesting application is STEM-HAADF (scanning transmission electron microscopy-high-angle annular dark-field imaging), which is highly dependent on atomic number (approximately Z^2) as detectors are placed at angles where electron scattering due to interactions with the nucleus occur (Rutherford scattering). Consequently, it provides exceptional resolution and permits for very small areas of a heavy element in a matrix of a light element to be detected which may not be observed in conventional TEM experiments.⁸⁴ This in turn produces a more accurate particle size distribution.⁸⁵ Moreover, this strong atomic number dependence allows the mixed metal or alloyed catalysts to be differentiated such as in PdPt/C catalyst.⁸⁶

2.5.5.1.1 Particle size distribution measurements with electron microscopy Electron microscopy is often used to obtain a particle size distribution of a catalyst specimen. However, a big issue is in the language used to describe a particle's size. Often a diameter is specified as it is convenient to describe a particle by a single number, yet nanoparticles are seldom

perfectly spherical, which begs the question of how to define diameter and how comparable is the value obtained from other techniques that will probably measure a different particle property and thus, yield a different diameter. In electron microscopy, the common procedure is to measure the diameter of ideally several hundred, if not thousands of particles, from various regions of the sample and dividing by the number of particles counted. Mathematically this is expressed as:

$$d_n = \frac{\sum n_i d_i}{\sum n_i} \quad (2.25)$$

which is known as a number average particle diameter. The range of particles is then usually also plotted as a histogram to show the particle size distribution of the catalyst. Early reports based upon theoretical models suggested that visual inspection of the distribution could provide insight into the particle growth mechanism: curves that tail towards small diameters imply growth by Oswald ripening whilst tailing towards large diameters suggests crystallite growth *via* coalescence,⁸⁷ however, more recent work based upon experimental methods that would allow differentiation between the two growth mechanisms saw only tailing to large particle diameters.⁸⁸

An average defined in this way is not ideal as often the activity has a relationship with metal surface area and a diameter alone is not as useful as a surface area. As the surface area of a sphere is given by $4\pi r^2$, the surface-weighted number diameter can be calculated as follows:

$$d_{sn} = \sqrt{\frac{\sum n_i d_i^2}{\sum n_i}} \quad (2.26)$$

however, in many other methods the average given is based upon the surface or volume of a particle independently of particle number. The derivations of the equations that follow can be found elsewhere.⁸⁹

In chemisorption experiments a surface-weighted diameter is obtained which is represented by:

$$d_s = \frac{\sum n_i d_i^3}{\sum n_i d_i^2} \quad (2.27)$$

which equates to the diameter of a sphere with the surface area as the particles under study. Therefore, to compare results from microscopy with chemisorption the average particle size must be defined in the same way.

Scherrer analysis of XRD peaks requires calculation of the volume-weighted diameter which is expressed as:

$$d_v = \frac{\sum n_i d_i^4}{\sum n_i d_i^3} \quad (2.28)$$

and provides the diameter of a sphere that has the same volume as the particles analysed.

However, great care needs to be taken when interconverting values as it must be ensured the value obtained from a particle count on a micrograph is statistically significant and

particles of all sizes are taken into account; in some instances, this is impossible depending on the technique employed as problems such as a lack of contrast or insufficient resolution may lead to the exclusion of a particle. Nevertheless, failure to do so will magnify unrepresentative sampling when comparing values to those obtained from a weighted average technique, such as chemisorption and X-ray line broadening analysis, as these methods have a much larger sampling size. For example, missing one 10 nm particle is the equal to ignoring one thousand 1 nm particles when calculated the volume-weighted particle size. Caveat operator!

2.5.5.2 Energy-dispersion X-ray spectroscopy

Energy-dispersive X-ray spectroscopy (EDX) is a supplementary technique of electron microscopy which provides information on the chemical composition of a sample. The electron beam of the microscope causes X-rays to be emitted from a sample (*vide supra*) which as previously mentioned are characteristic of a particular element. The sensitivity is dependent upon the detector used and the most common type of detector lacks resolving power for X-rays of similar energy, so its use for absolute element analysis is limited. It can be used for quantification of individual particles with correct calibration, although secondary fluorescence—indirect excitation, whereby characteristic radiation causes a separate element to emit an X-ray photon—may lead to misleading quantification data.³⁴

EDX analysis is performed by selecting a region of a TEM/SEM image to probe and then recording an X-ray spectrum. A digital image can then be generated of the relative concentration of an element superimposed with the image of the particle. It is helpful to analyse many particles and obtain a composition distribution when performing this analysis as the assumption of compositional uniformity, whether that be interparticle or at different regions of a material, has been shown to be incorrect by several studies, yet this is a task seldom carried out (see [2], [90], and [91] for examples).⁹² A recent article by Liu *et al.* outlined a correlative electron microscopy approach to solve this issue by using a TE microscope for structural characterisation and a SE microscope for compositional analysis: the separation of the two techniques allows the position of a particle to be resolved at a level SEM cannot achieve and affords the improved EDX ability of SEM which provides electrons with energies more suitable for excitation and less probable to inflict beam damage to a sample.⁹² Using this approach permits the composition distribution of catalyst as a function of particle size to be determined and related to its performance.

2.5.5.3 Experimental

2.5.5.3.1 TEM was performed on a Joel-JEM 2100 operating at 200 kV. Samples were dispersed in ethanol and deposited onto 300 mesh copper grids coated with holey carbon film. EDX analysis was performed inside the same instrument using an Oxford Instruments X-Max^N detector and the data were analysed using Oxford Aztec Point and ID software.

2.5.5.3.2 SEM was performed on a Tescan MAIA 3 field emission gun scanning electron microscope equipped with secondary and backscattered electron detection. EDX analysis was performed inside the same instrument using an Oxford Instruments X-Max^N80 detector and the data were analysed using Oxford Aztec Point and ID software.

2.5.5.4 Chemisorption of a reactive gas

Selective gas chemisorption is a surface-based method used for estimating the number of surface atoms, dispersion, and the surface-weighted average particle size and has been widely employed for around 60 years. The basic principle of gas chemisorption is simple: a catalyst is exposed to a known quantity of gaseous probe molecules, and by making certain assumptions the properties outlined in the first sentence of this paragraph can be calculated. This seemingly straightforward procedure is, however, a façade, as in some instances the results of chemisorption measurements demanded arduous efforts to rationalise.

Chemisorption measurements can be performed in static or dynamic systems. In the static method, the volume of gas adsorbed on a sample is measured as a function of pressure at a constant temperature to produce an adsorption isotherm from which a monolayer can be determined. This method may also utilise a microbalance to record gas uptake, but this can be problematic for hydrogen chemisorption measurements due to its low mass. A commonly used experimental method records the adsorption isotherm from low pressures to pressures that will ensure monolayer coverage. The resulting isotherm may display continued, albeit lower, uptake at higher pressures as the support will uptake the gas in accordance with Henry's Law. This contribution must be accounted for to obtain an accurate monolayer value, which can be achieved by a short evacuation period to remove the weakly adsorbed species, followed by a remeasuring of the isotherm. An example of the type of experimental data obtained from this technique is displayed in Figure 2.13a.

For flow methods, a panoply of techniques have been developed. The most popular technique, due to its inherent simplicity and widespread commercial availability, is known as the pulse-flow method. The first method of this kind involved injecting a large quantity of adsorbate into an inert carrier gas stream and flowed through a catalyst bed towards a detector; the quantity adsorbed is then given by the difference.⁹³ A later modification of this method involves pulsing smaller quantities of adsorbate, such that saturation takes multiple injections to achieve.⁹⁴ For a gas that adsorbs and does not decompose, the gas may be wholly adsorbed initially, but as the number of pulses increase, less gas is adsorbed and more makes it through to the detector. Eventually, the surface is saturated, so the gas passes over the sample and the detector records a constant value (Figure 2.13b). At this point, several more injections are made to provide an internal calibration. However, this assumption has two issues. Firstly, the saturated peak area recorded when analysing a sample may be lower than that of a blank tube as of a consequence of so-called "weak adsorption". In this instance, small amounts

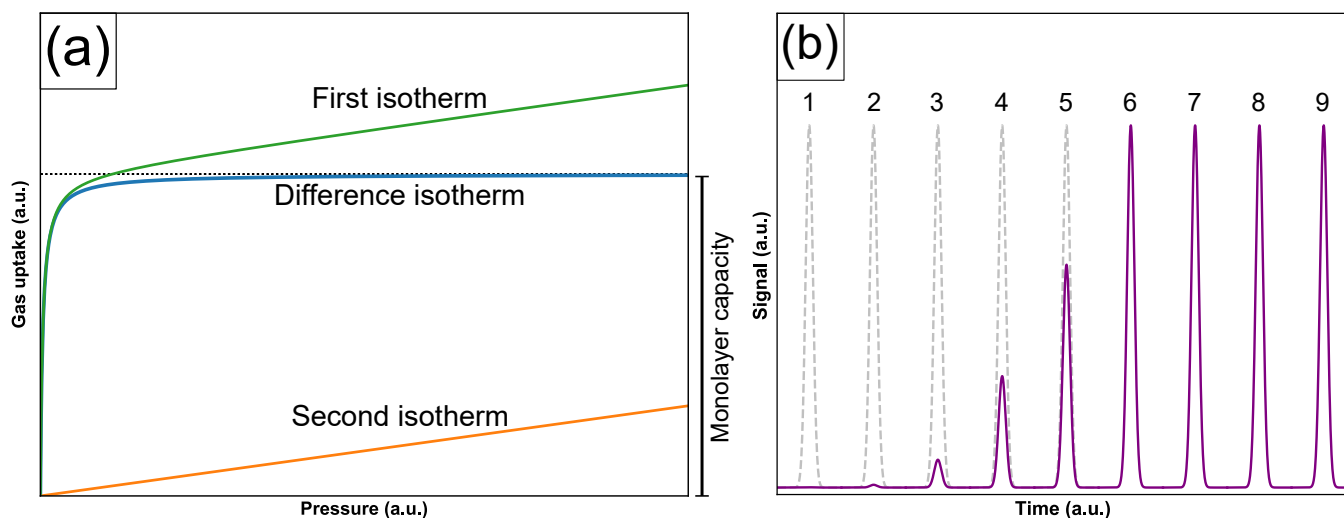


Figure 2.13: (a) An example adsorption isotherm for determining the surface area of a supported metal catalyst. The first isotherm is a combination of uptake on the support and metal surface, whilst the second isotherm is the uptake by the support after a short evacuation. (b) An example of data obtained when performing a pulse chemisorption experiment. Peaks 1–3 indicate the reactive gas is mostly adsorbed, peaks 4 and 5 show the surface approaching saturation and peaks 6–9 represent surface saturation. (b) is adapted from 71.

of desorption occurs in between pulse intervals that consequently causes a continuous small uptake. This effect can be probed by varying the time between injections but this is seldom done. A recent method based on the transient mass balance of the adsorptive purports to alleviate this issue but its impact and validity for a wide variety of catalysts remains to be seen.⁹⁵ The second issue relates to whether using the final peaks as internal calibration is valid, as any non-linearity in the TCD will result in error in the measurement of the quantity adsorbed. An issue shared by all pulse method concerns the interpretation of what has occurred when peak areas of several pulses are equal. Typically, it is assumed that this is equal to monolayer formation on the catalyst, but it may only mean that the flow path has achieved saturation and therefore will result in the surface area being underestimated.

Temperature-programmed desorption (TPD) has been employed by several authors to determine the metal surface area, but its use for this purpose is rare. A more detailed description is outlined in Section 2.5.2.2. The main assumption of this technique is that the quantity desorbed is assumed to be equal to what was adsorbed on the surface. However, as the temperature used in this method can be high, the probe molecule may react with the sample (e.g. CO reacting with Al_2O_3 to form CO_2)⁹⁶ which may result in quantification issues, since detection is solely made with a TCD in many cases. Furthermore, obtaining high quality data may require considerably more effort than other methods due to desorption-readsorption behaviour that results in broad peaks⁹⁷ and the amount desorbed can be sensitive to the saturation conditions.⁴⁰

Prior to recording the gas uptake of a catalyst, a pretreatment must be performed as metal nanoparticles exposed to air typically contain a thin oxide layer and possibly some other

contaminants, such as water or organic residues. This is achieved by heating the sample in a flow of hydrogen or oxygen to relatively high temperatures depending on their relative concentrations.⁹⁸ In some instances, it may be undesirable to remove these organic residues because the catalyst under evaluation is being assessed post-reaction and their removal may lead to misleading results. Furthermore, there are several other additional problems that may occur during pretreatment if the incorrect conditions are used, such as agglomeration or, depending on the support, the formation of intermetallic compounds (e.g. Pt-Al) or strong-metal support interaction effects (i.e. partial or complete encapsulation of the nanoparticles). Consequently, great care must be taken during this cleaning step. If an oxidative pretreatment has been used, the sample must first be reduced depending on the type of chemisorption experiment being performed. This specimen, or a catalyst that was reduced in the first instance, will require hydrogen on the surface to be removed. Experimentally this is carried out by flowing an inert gas over the sample at the elevated temperature for a period of time or subjecting the sample to vacuum.

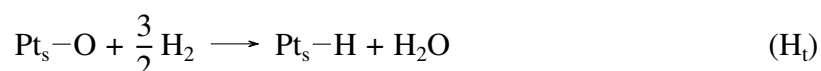
Samples are then cooled to an appropriate temperature and the adsorbate is introduced into the sample cell. Many molecules such as H₂ (and also D₂⁹⁹), CO, O₂, N₂O,^{100–102} NO,¹⁰³ and H₂S^{104–106} have been utilised in chemisorption experiments, however only the first three mentioned molecules are commonly employed. If low temperatures are used, the temperature must not be so low that it causes the condensation of carrier or analysis gas. For this reason, cooling to liquid nitrogen temperatures in the flow method will be hazardous. Initially, the unique issues associated with each gas will be considered before problems that all probe molecules share are discussed.

Hydrogen is often employed as the adsorptive gas as it readily dissociates over many metals of interest, although the coinage metals and ruthenium can pose issues due to a kinetically limited hydrogen adsorption and peculiar interaction with hydrogen at room temperature,¹⁰² respectively. Palladium requires special attention due to the possibility of forming a hydride; however, a monolayer can be achieved without the formation of palladium hydride if low partial pressures of hydrogen are used or the temperature is above the decomposition temperature of the hydride. Moreover, the β -hydride phase does not form until much higher pressures if deuterium is utilised in place of hydrogen at equivalent temperatures.¹⁰⁷ Particle size and carrier effects also influence the formation of this phase. Many studies have shown a decrease in the formation of this phase as dispersion increases (see references [38,108–110] for examples). Despite all these studies displaying a similar trend, the results revealed different hydrogen solubilities at equal dispersions. A recent combinatorial study that used electron microscopy and incoherent inelastic neutron scattering suggested this discrepancy was a result of hydrogen solubility and stability is dependent on particle size *and* agglomeration effects (particle shape, size, and morphology).¹¹¹ Supports strongly influence this latter point, and it was shown that it is more difficult to fully dehydrogenate palladium supported by porous carbon supports than non-porous carbon blacks.

Carbon monoxide is next frequently used and its application also has several unique issues. One unique problem with carbon monoxide is its ability to form highly volatile metal carbonyl species,¹¹² particularly with small nanoparticles of nickel, ruthenium, and rhodium.^{28,113} Moreover, the disproportionation of carbon monoxide to elemental carbon and carbon dioxide has been reported on small silica-supported palladium particles (but not larger ones) at room temperature.¹¹⁴ That said, carbon monoxide has two distinct advantages over hydrogen. Firstly, hydrogen physisorption on some supports (e.g. carbon) can be significant,⁹⁷ although on some supports (e.g. CeO₂) spillover of carbon monoxide and hydrogen can be so significant at room temperature it necessitates the use of cryogenic cooling baths, though this may not solve the problem entirely.¹¹⁵ Secondly, if using the pulse method, carbon monoxide may be used with hydrogen as a carrier gas.⁹⁸ This removes the need to clean the surface after the reduction step as carbon monoxide should readily displace hydrogen on the surfaces of nickel, palladium, platinum, rhodium, and iridium but not ruthenium.^{116,117} Furthermore, under the conditions employed for chemisorption experiments, these metals are practically inactive for Fisher-Tropsch and methanation reactions.

Oxygen is the final gas that has seen enough use to warrant discussion. By far the largest problem with oxygen chemisorption is the formation of subsurface oxides. Low temperatures can help to alleviate this problem, but this may result in incomplete coverage and with small particles may still be unsuccessful.²⁸ Moreover, as oxygen adsorption requires pairs of surface sites, complete coverage may not be possible due to the immobility of the oxide layer and thus, an accurate surface area cannot be obtained.

Multiple gases may be used in the form of a surface titration, most commonly with H₂ and O₂, although CO and O₂, H₂ and N₂O, alkenes and H₂, and H₂ and D₂ have also been employed but are less well developed.¹¹⁸ The hydrogen-oxygen titration has been extensively utilised since being reported by Benson and Boudart in 1965.¹¹⁹ The greatest advantage of this method is it is three times as sensitive as hydrogen or oxygen chemisorption experiments if the proposed reaction series is correct:



as the stoichiometric ratio of H_a:O_a:H_t is equal to 1:1:3. This ratio caused some significant debate at the time and later work revealed that these uptakes were probably affected by impurities in the platinum powder used.^{120,121} A careful study by O'Rear *et al.*¹²² showed that the titrated quantity should result in the titration ratio (R_t) being approximately equal to unity:

$$R_t = \frac{H_t}{2O_a + H_a}$$

The issue with stoichiometry has been an ongoing controversy since before the development of chemisorption techniques. Unfortunately, the debate over what stoichiometry values are correct is not limited to chemisorption as a whole and can be dependent on the variant used. Several reasons why stoichiometry issues arise were alluded to in earlier paragraphs, such as formation of bulk hydrides or oxides, but these do not explain the observed deviations completely.

Concerning hydrogen, recommended H/M_s values typically range from 1.0–1.2 for platinum, palladium, rhodium, and iridium, but deviations as high as 1.96, 1.98, and 2.72 for platinum, rhodium, and iridium, respectively have been reported.^{123,124} Several reasons have been forwarded for H/M_s values being greater than unity. Firstly, migration of H atoms to the support (i.e. hydrogen spillover) can lead to higher ratios, although under analysis conditions used in most chemisorption experiments this process is slow and its rate can be highly dependent on the nature of the support and on surface impurities, such as water and p-block elements. Secondly, X-ray absorption fine structure (EXAFS) analysis has revealed that multiple adsorption sites on corners and edges, leading to higher uptake, and the adsorption of hydrogen at the metal-support interface, resulting in the breaking of M–O bonds and weakening of the M–M bonds,^{125–130} are contributing factors.

Stoichiometry issues also arise for carbon monoxide as its adsorption can be associative, which can lead to linear (CO/M= 1), bridged (CO/M= 2), or capped (CO/M= 3) forms, or dissociative (CO/M= 2) (Figure 2.14). The relative contribution of each can be assessed by use of an ancillary technique, such as infrared spectroscopy, which can provide insight into the most appropriate stoichiometry factor for analysis. If performed, it must be done so under identical conditions to the chemisorption analysis as the relative ratio of each is dependent on the temperature, pressure, particle size, surface coverage, and matrix (if used). For many metals a CO/M value of 1–2 is typically assumed, with several studies suggesting that for palladium a value of approximately 2 should always be used.^{131–133}

With the assumption of a stoichiometric factor, properties of a nanoparticle can be calculated. Dispersion, *D*, otherwise known as fraction exposed, is defined as the fraction of total metal atoms, *N_{mt}*, which are located at the surface, *N_{ms}*. Knowledge of the number of atoms at the surfaces is calculated using the number of molecules adsorbed, *N_{aa}*, at the surface and the stoichiometry factor, *f*, of the adsorbate in the following manner:

$$D = \frac{N_{ms}}{N_{mt}} = \frac{N_{aa}}{f N_{mt}} \quad (2.29)$$

and may also be presented as a percentage. By very definition this value must be between 0 and 1 (or 0 and 100%). In order to obtain a surface area, the number of atoms present at a surface per unit area must be known. Usually, this value is obtained by assuming that specific numbers of low index planes are present at a surface depending on unit cell type. This work utilises metals which have a face-centred cubic or hexagonal-closest packed crystal structure; the former is typically assumed to have equal proportions of the (111), (100), and (110) planes

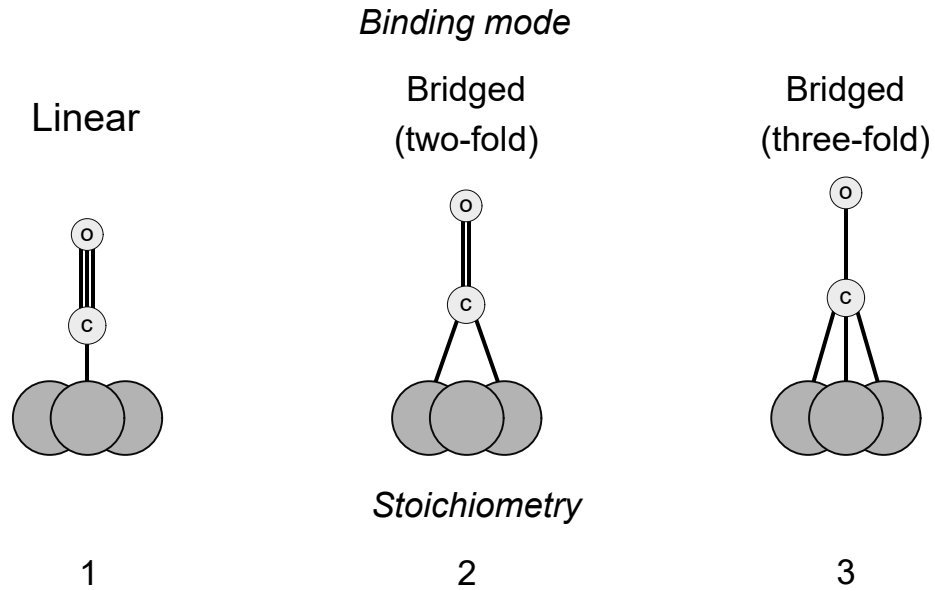


Figure 2.14: The binding modes of CO on a metal surface.

whilst the latter is assumed to be solely present as the (0001) plane. The specific surface area, S_{sp} , of a sample is then calculated by the product of this value, a_m , the dispersion, and the ratio of molecular weight to Avogadro's number as expressed in Equation 2.30.

$$S_{sp} = a_m \left(\frac{N_A}{Mw} \right) D \quad (2.30)$$

Using the surface area and assuming a particle shape allows the surface-weighted particle size, d_s , to be calculated. If a particle is assumed to be spherical or hemispherical in contact with a support, particle size can be calculated by:

$$d_s = \frac{6}{\rho S_{sp}} \quad (2.31)$$

Similarly, the particle size can be calculated from dispersion as Equation 2.31 calculates d_s using the surface area to volume ratio which may also be expressed as:

$$d_s = 6 \left(\frac{\sum n_i V_i}{\sum n_i A_i} \right) = 6 \left(\frac{v_m N_{mt}}{a_m N_{ms}} \right) = 6 \frac{v_m / a_m}{D} \quad (2.32)$$

where n_i is the number of particles of volume V_i and area A_i . This equation may also be used with the d_s value obtained from microscopy for comparative purposes.

However, the assumptions listed above may lead to discrepancies between the results of other characterisation techniques. If more knowledge of the shape of the particle is available, the number 6 in Equations 2.31 and 2.32 can be modified. If 2D microscopy images suggest that particles are spherical, several authors have suggested modifications to account for deviations in results depending on the nature of support. These ideas are most agreeable, but none have found widespread application. Borodziński and Bonarowska suggested using different equations for particle size depending on the measured dispersion, which offers the

Table 2.2: Assumed stoichiometry values for various probe molecules.

| Metal | H/M | CO/M |
|-----------|-----|------|
| Nickel | 1 | 2 |
| Ruthenium | 1 | 1 |
| Rhodium | 1 | 1 |
| Palladium | 1 | 2 |
| Iridium | 1 | 1 |
| Platinum | 1 | 1 |

advantage of not requiring an inherent assumption of particle shape or surface area.¹³⁴ More recently, the Le Valant group approached this problem using the H/M (where M = Pt, Pd, Rh, or Ir) and CO/Pt ratio in a polynomial expression based on perfect cuboctahedron clusters to determine surface area, dispersion, and particle size.^{135,136} In this instance, the assumption of a specific particle shape was made as it is representative of the number of surface atoms for a variety of very common particle shapes. Torrente-Murciano proposed introducing an interaction factor depending on the contact angle between the metal nanoparticle and the support, which was taken as an indication of interaction strength.¹³⁷ support.

Finally, and most crucially, the largest source of error in all calculations shown above is the user: failure to accurately determine the metal loading and using the nominal loading in its place provides a gross misrepresentation of the results. For example, catalysts prepared by impregnation typically have a metal content of approximately 90% of the nominal loading which decreases as metal content increases.²⁸ Other techniques may lead to better retention of the loaded metal nanoparticle but nevertheless, small variations in preparation may lead to false conclusions if not accounted for.

2.5.5.4.1 Experimental

Chemisorption measurements were performed using a Micromeritics Autochem II 2920 analyser equipped with a TCD. Before analysis, metal loadings of catalysts were determined by MP-AES. The sample (50–100 mg) was fixed between two pieces of quartz wool in a quartz u-tube. The sample was reduced under a flow of 10% H₂ in Ar for 1 hour at 200 °C. After this time, the temperature was kept constant but the gas was changed to Ar and the sample was purged under a flow of Ar for at least 1 hour before cooling to 35 °C. The analysis was performed with 10% CO in He with He as a carrier gas or 10% H₂ in Ar with Ar as a carrier gas. Pulses were introduced into the sample cell with a calibrated injection loop at a controlled temperature until peak area remained constant. Data was analysed in the traditional manner outlined in equations 2.29–2.32 with assumptions of values outlined in Tables 2.2 and 2.3.

Table 2.3: Metal properties used in the calculation of surface area and particle size. Data from table taken, or calculated, using reference [97].

| Metal | Molecular weight (g mol ⁻¹) | Density (g cm ⁻³) | Structure | a_m (Å ²) |
|-----------|---|-------------------------------|-----------|-------------------------|
| Ruthenium | 101.07 | 12.30 | hcp | 6.35 |
| Rhodium | 102.91 | 12.40 | fcc | 7.58 |
| Palladium | 106.42 | 12.02 | fcc | 7.93 |
| Iridium | 192.22 | 22.42 | fcc | 7.73 |
| Platinum | 195.08 | 21.45 | fcc | 8.07 |

2.5.5.5 Line broadening

The analysis of the breadth of Bragg reflections in a XRD pattern is a convenient method of determining particle size and possibly the particle size distribution and shape.^{138,139} Note that the use of the term particle size is a matter of convenience and a more scrupulous term would be “coherent diffraction domain size”, which can be defined as the regions of a crystalline material that scatter x-rays coherently but as this is verbose, particle size is used in its place.¹⁴⁰ The diffraction peaks of particles smaller than 100 nm begin to broaden as contributions that do not satisfy Bragg’s Law begin to scatter X-rays as there are an insufficient number of planes to cancel out this wave. This effect can be used to calculate particle sizes in the region of about 3–50 nm due to instrument capabilities of most laboratory instruments; nevertheless, detection of particle sizes as low as 1 nm are possible.¹⁴¹ If the instrument is assumed to be non-limiting, the upper limit of detection is about 12% of the extinction length (i.e. how deep the incident wave travels in a sample before its amplitude becomes zero).¹⁴²

The relationship between average particle size and peak width is described by the Scherrer equation:¹⁴³

$$\langle L \rangle = \frac{K_{Sch} \lambda}{\beta \cos \theta} \quad (2.33)$$

β is the line broadening due to particle size and is generally defined as the full width at half-maximum, $\beta_{1/2}$, or the integral breadth (i.e. the integrated intensity divided by the maximum intensity). K_{Sch} is the Scherrer constant and depends on how $\langle L \rangle$ and β are defined, the reflection being analysed, the particle shape, and on the size distribution however this value is usually taken to be 0.89, 0.9, 0.94, or unity. Because of this variation, the calculated particle size should be treated as a crude estimate only. $\langle L \rangle$ is the volume-weighted mean thickness of the particle in the direction perpendicular to the reflecting plane which is considered as the cube root of the volume of the crystallite.

The observed peak width is not solely attributable to the particle size of the material as it includes a term for the broadening that arises due to the instrument that must be corrected for. One such method is Warren’s correction expressed by:¹⁴³

$$\beta = (B^2 - b^2)^{0.5} \quad (2.34)$$

where B is the full width at half maxima (in radians) and b is the value for instrumental broadening, obtained by measuring the full width at half maximum of a diffraction peak for a well-defined crystalline material (e.g. silicon wafer) at an angle close to the reflection being analysed in order to minimise any geometric effects.¹⁴³ The preceding discussion assumes that the calculated β value is solely attributable to crystallite size: this is not strictly true, as the broadening observed in an XRD pattern may also be caused by strain and/or disorder in the peak being analysed. If such features are present, then a smaller particle size than actuality would result if Equation 2.33 were used.

2.5.5.5.1 Experimental Diffraction peaks were analysed using the Scherrer equation after background fitting and Rietveld refinement as implemented in PANalytical X'Pert HighScore Plus software. As with XRD, nickel-filtered Cu radiation was used as an X-ray source and a peak's full width at half-maximum was used for calculations assuming the Scherrer constant value of 0.9.

2.5.6 Volume and density measurements

The volume and density of catalysts were determined using a pycnometer (Figure 2.15). A pycnometer consists of two parts: a flask and a stopper with a fitted capillary. The total volume of the high-quality pycnometers is known to five significant figures and in some cases more, therefore allowing the density of any liquid at ambient temperature to be determined by recording its mass. This can be extended to determine the density of solids by using a combination of a solid and liquid of known density. The total mass of the flask, m_T , is given by the sum of the liquid reference, m_{ref} , and the mass of catalyst used, m_{cat} :

$$m_T = m_{ref} + m_{cat} \quad (2.35)$$

As the mass of liquid is known, its volume can be calculate by:

$$\rho = \frac{m}{V} \quad (2.36)$$

Where ρ is density, m is mass and V is volume. The volume of catalyst can then be determined by Equation 2.37.

$$V_{cat} = V_i - V_{ref} \quad (2.37)$$

Where V_{cat} is catalyst volume, V_i is the volume of the pycnometer when full of reference liquid and V_{ref} is the volume of reference liquid required to fill the pycnometer. If a catalyst is porous the water required to fill its pores must be accounted for in the above equation. Catalyst density can then calculated using Equation 2.36.

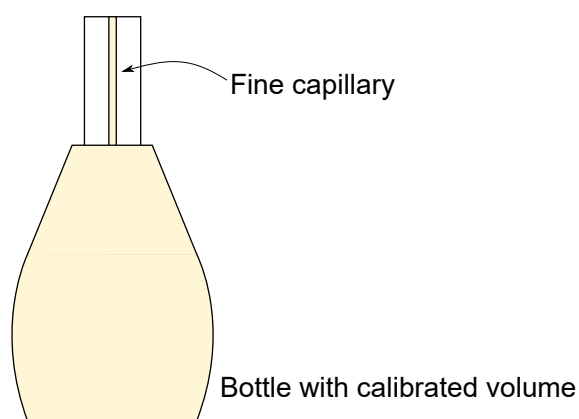


Figure 2.15: A typical pycnometer.

2.5.6.1 Experimental

Catalyst density Pycnometry measurements were performed using a Brand™ Blaubrand™ Borosilicate Glass Calibrated Density Bottle. A known mass of catalyst (approximately 1 g) was added into the flask, fitted with capillary stopper, and weighed. Deionised water was then added to the flask until it was full. The flask was re-weighed and its mass recorded. Data was processed according to the above procedure.

Liquid density Liquid densities were determined using a Brand™ Blaubrand™ Borosilicate Glass Calibrated Density Bottle. The bottle was filled with liquid until full and was placed in a beaker of water in a thermostated oven at a set temperature. The bottle was removed after 30 min, wiped clean, and weighed. This procedure was repeated three times and the density was calculated using Equation 2.36 using the average mass recorded. Density as a function of temperature was modelled to the equation proposed by Francis^{144,145} using the by minimising the residual sum of squares using the differential evolution algorithm¹⁴⁶ as implemented in the `scipy.optimize` library of SciPy version 1.4.1¹⁵ in Python 3.7.6.¹⁶ An example script is included in the external zip file.

2.6 References

- [1] S. L. Scott, T. B. Gunnoe, P. Fornasiero and C. M. Crudden, *ACS Catal.*, 2022, **12**, 3644–3650.
- [2] M. Sankar, Q. He, M. Morad, J. Pritchard, S. J. Freakley, J. K. Edwards, S. H. Taylor, D. J. Morgan, A. F. Carley, D. W. Knight, C. J. Kiely and G. J. Hutchings, *ACS Nano*, 2012, **6**, 6600–6613.
- [3] D. A. Skoog, J. F. Holler and S. R. Crouch, in *Princ. Instrum. Anal.*, Cengage Learning, 7th edn., 2016, ch. 27, pp. 720–745.

- [4] C. A. Bauer and S. Grimme, *J. Phys. Chem. A*, 2016, **120**, 3755–3766.
- [5] F. Allen, A. Pon, R. Greiner and D. Wishart, *Anal. Chem.*, 2016, **88**, 7689–7697.
- [6] J. N. Wei, D. Belanger, R. P. Adams and D. Sculley, *ACS Cent. Sci.*, 2019, **5**, 700–708.
- [7] H. Ji, H. Deng, H. Lu and Z. Zhang, *Anal. Chem.*, 2020, **92**, 8649–8653.
- [8] J.-Y. de Saint Laumer, E. Cicchetti, P. Merle, J. Egger and A. Chaintreau, *Anal. Chem.*, 2010, **82**, 6457–6462.
- [9] S. E. Stein and D. R. Scott, *J. Am. Soc. Mass Spectrom.*, 1994, **5**, 859–866.
- [10] W. A. Dietz, *J. Chromatogr. Sci.*, 1967, **5**, 68–71.
- [11] J. R. Partington, *An Advanced Treatise On Physical Chemistry Volume II*, Longmans Green and Co, 1951.
- [12] W. Ostwald, *Grundriss der allgemeinen Chemie*, W. Engelmann, Leipzig, 1899.
- [13] J. Wilke, H. Kryk, J. Hartmann and D. Wagner, *Theory and Praxis of Capillary Viscometry*, Schott-geräte gmbh technical report, 2000.
- [14] J. A. Nelder and R. Mead, *J. Comput.*, 1965, **7**, 308–313.
- [15] P. Virtanen, R. Gommers, T. E. Oliphant, M. Haberland, T. Reddy, D. Cournapeau, E. Burovski, P. Peterson, W. Weckesser, J. Bright, S. J. van der Walt, M. Brett, J. Wilson, K. J. Millman, N. Mayorov, A. R. J. Nelson, E. Jones, R. Kern, E. Larson, C. J. Carey, b. Polat, Y. Feng, E. W. Moore, J. VanderPlas, D. Laxalde, J. Perktold, R. Cimrman, I. Henriksen, E. A. Quintero, C. R. Harris, A. M. Archibald, A. H. Ribeiro, F. Pedregosa, P. van Mulbregt and SciPy 1.0 Contributors, *Nat. Methods*, 2020, **17**, 261–272.
- [16] G. Van Rossum and F. L. Drake, *Python 3 Reference Manual*, CreateSpace, Scotts Valley, CA, 2009.
- [17] P. Hohenberg and W. Kohn, *Phys. Rev.*, 1964, **136**, B864–B871.
- [18] D. S. Sholl and J. A. Steckel, *Density Functional Theory*, John Wiley & Sons, Inc., Hoboken, NJ, USA, 2009.
- [19] L. Goerigk and S. Grimme, *Phys. Chem. Chem. Phys.*, 2011, **13**, 6670.
- [20] J. Chai and M. Head-Gordon, *Phys. Chem. Chem. Phys.*, 2008, **10**, 6615.
- [21] C. Adamo and V. Barone, *J. Chem. Phys.*, 1999, **110**, 6158–6170.
- [22] M. Ernzerhof and G. E. Scuseria, *J. Chem. Phys.*, 1999, **110**, 5029–5036.

- [23] S. Grimme, J. Antony, S. Ehrlich and H. Krieg, *J. Chem. Phys.*, 2010, **132**, 154104.
- [24] Y. Zhao and D. G. Truhlar, *Theor. Chem. Acc.*, 2008, **119**, 525.
- [25] M. J. Frisch, G. W. Trucks, H. B. Schlegel, G. E. Scuseria, M. A. Robb, J. R. Cheeseman, G. Scalmani, V. Barone, B. Mennucci, G. A. Petersson, H. Nakatsuji, M. Caricato, X. Li, H. P. Hratchian, A. F. Izmaylov, J. Bloino, G. Zheng, J. L. Sonnenberg, M. Hada, M. Ehara, K. Toyota, R. Fukuda, J. Hasegawa, M. Ishida, T. Nakajima, Y. Honda, O. Kitao, H. Nakai, T. Vreven, J. A. Montgomery Jr., J. E. Peralta, F. Ogliaro, M. Bearpark, J. J. Heyd, E. Brothers, K. N. Kudin, V. N. Staroverov, R. Kobayashi, J. Normand, K. Raghavachari, A. Rendell, J. C. Burant, S. S. Iyengar, J. Tomasi, M. Cossi, N. Rega, J. M. Millam, M. Klene, J. E. Knox, J. B. Cross, V. Bakken, C. Adamo, J. Jaramillo, R. Gomperts, R. E. Stratmann, O. Yazyev, A. J. Austin, R. Cammi, C. Pomelli, J. W. Ochterski, R. L. Martin, K. Morokuma, V. G. Zakrzewski, G. A. Voth, P. Salvador, J. J. Dannenberg, S. Dapprich, A. D. Daniels, Ö. Farkas, J. B. Foresman, J. V. Ortiz, J. Cioslowski and D. J. Fox, *Gaussian 09 Revision D.01*.
- [26] T. H. Dunning, *J. Chem. Phys.*, 1989, **90**, 1007–1023.
- [27] J. W. Ochterski, *Thermochemistry in Gaussian*, 2000, <https://gaussian.com/thermo/>, accessed 2020-10-21.
- [28] G. C. Bond and V. Ponec, in *Stud. Surf. Sci. Catal.*, Elsevier, 1995, vol. 95, ch. 7, pp. 299–391.
- [29] G. Moore, in *Introd. to Inductively Coupled Plasma At. Emiss. Spectrom.*, 1989, ch. 1, pp. 1–17.
- [30] D. A. Skoog, J. F. Holler and S. R. Crouch, in *Princ. Instrum. Anal.*, Cengage Learning, 7th edn., 2017, ch. 10, pp. 231–252.
- [31] C. Neff, P. Becker, B. Hattendorf and D. Günther, *J. Anal. At. Spectrom.*, 2021, **36**, 1750–1757.
- [32] D. A. Monti and A. Baiker, *J. Catal.*, 1983, **83**, 323–335.
- [33] G. C. Bond and X. Yide, *J. Mol. Catal.*, 1984, **25**, 141–150.
- [34] J. W. Niemantsverdriet, *Spectroscopy in Catalysis*, Wiley, 2007.
- [35] S. B. Ziemecki, J. B. Michel and G. A. Jones, *React. Solids*, 1986, **2**, 187–202.
- [36] C. W. A. Chan, K. Y. Tam, J. Cookson, P. Bishop and S. C. Tsang, *Catal. Sci. Technol.*, 2011, **1**, 1584.

- [37] C. W. A. Chan, A. H. Mahadi, M. M.-J. Li, E. C. Corbos, C. Tang, G. Jones, W. C. H. Kuo, J. Cookson, C. M. Brown, P. T. Bishop and S. C. E. Tsang, *Nat. Commun.*, 2014, **5**, 5787.
- [38] M. Bonarowska, J. Pielaszek, W. Juszczyk and Z. Karpiński, *J. Catal.*, 2000, **195**, 304–315.
- [39] J. Konvalinka, P. Van Oeffelt and J. Scholten, *Appl. Catal.*, 1981, **1**, 141–158.
- [40] O. A. Yakovina and A. S. Lisitsyn, *Langmuir*, 2016, **32**, 12013–12021.
- [41] PerkinElmer Inc., 2009, 1–2.
- [42] A. Mekki-Berrada and A. Auroux, *Charact. Solid Mater. Heterog. Catal. From Struct. to Surf. React. Vol. 1&2*, 2012, **2**, 747–852.
- [43] M. Torres and J. Daz-Luque, *X-Ray Spectrosc.*, 2012.
- [44] P. W. H. Bragg and W. L. Bragg, *Proc. Roy. Soc. A*, 1913, **88**, 428–438.
- [45] B. V. Crist, *J. Electron Spectros. Relat. Phenomena*, 2019, **231**, 75–87.
- [46] G. Greczynski and L. Hultman, *ChemPhysChem*, 2017, **18**, 1507–1512.
- [47] G. Greczynski and L. Hultman, *Prog. Mater. Sci.*, 2020, **107**, 100591.
- [48] G. Greczynski and L. Hultman, *Angew. Chem. Int. Ed. Engl.*, 2020.
- [49] D. R. Baer, K. Artyushkova, H. Cohen, C. D. Easton, M. Engelhard, T. R. Gengenbach, G. Greczynski, P. Mack, D. J. Morgan and A. Roberts, *J. Vac. Sci. Technol. A*, 2020, **38**, 031204.
- [50] P. R. Davies and D. J. Morgan, *J. Vac. Sci. Technol. A*, 2020, **38**, 033204.
- [51] *Hard X-ray Photoelectron Spectroscopy (HAXPES)*, ed. J. Woicik, Springer International Publishing, Cham, 2016, vol. 59, p. 576.
- [52] F. S. Roberts, S. L. Anderson, A. C. Reber and S. N. Khanna, *J. Phys. Chem. C*, 2015, **119**, 6033–6046.
- [53] A. G. Shard, *Surf. Interface Anal.*, 2014, **46**, 175–185.
- [54] D. R. Baer, K. Artyushkova, C. Richard Brundle, J. E. Castle, M. H. Engelhard, K. J. Gaskell, J. T. Grant, R. T. Haasch, M. R. Linford, C. J. Powell, A. G. Shard, P. M. A. Sherwood and V. S. Smentkowski, *J. Vac. Sci. Technol. A*, 2019, **37**, 031401.

- [55] M. R. Linford, V. S. Smentkowski, J. T. Grant, C. R. Brundle, P. M. Sherwood, M. C. Biesinger, J. Terry, K. Artyushkova, A. Herrera-Gómez, S. Tougaard, W. Skinner, J.-J. Pireaux, C. F. McConville, C. D. Easton, T. R. Gengenbach, G. H. Major, P. Dietrich, A. Thissen, M. Engelhard, C. J. Powell, K. J. Gaskell and D. R. Baer, *Microsc. Microanal.*, 2020, **26**, 1–2.
- [56] D. Shah, D. I. Patel, T. Roychowdhury, G. B. Rayner, N. O’Toole, D. R. Baer and M. R. Linford, *J. Vac. Sci. Technol. B*, 2018, **36**, 062902.
- [57] W. E. S. Unger, *J. Vac. Sci. Technol. A*, 2020, **38**, 021201.
- [58] M. Suzuki, H. Nagao, Y. Harada, H. Shinotsuka, K. Watanabe, A. Sasaki, A. Matsuda, K. Kimoto and H. Yoshikawa, *J. Vac. Sci. Technol. A*, 2020, **38**, 023204.
- [59] C. J. Powell, *J. Vac. Sci. Technol. A*, 2020, **38**, 023209.
- [60] D. R. Baer, *J. Vac. Sci. Technol. A*, 2020, **38**, 031201.
- [61] A. Herrera-Gomez, *J. Vac. Sci. Technol. A*, 2020, **38**, 033211.
- [62] T. H. Fleisch and G. J. Mains, *J. Phys. Chem.*, 1986, **90**, 5317–5320.
- [63] P. M. Sherwood, *Surf. Interface Anal.*, 2019, **51**, 589–610.
- [64] B. Singh, A. Diwan, V. Jain, A. Herrera-Gomez, J. Terry and M. R. Linford, *Appl. Surf. Sci.*, 2016, **387**, 155–162.
- [65] A. V. Neimark, K. S. W. Sing and M. Thommes, *Handbook of heterogeneous catalysis*, 2008, 721–738.
- [66] K. A. Cychoz, R. Guillet-Nicolas, J. García-Martínez and M. Thommes, *Chem. Soc. Rev.*, 2017, **46**, 389–414.
- [67] M. Thommes, K. Kaneko, A. V. Neimark, J. P. Olivier, F. Rodriguez-Reinoso, J. Rouquerol and K. S. Sing, *Pure Appl. Chem.*, 2015, **87**, 1052–1069.
- [68] K. S. Sing, *Assessment of Surface Area by Gas Adsorption*, Elsevier Ltd., 2nd edn., 2013, pp. 237–268.
- [69] F. Schüth, M. D. Ward and J. M. Buriak, *Chem. Mater.*, 2018, **30**, 3599–3600.
- [70] S. Brunauer, P. H. Emmett and E. Teller, *J. Am. Chem. Soc.*, 1938, **60**, 309–319.
- [71] S. Lowell, J. E. Shields, M. A. Thomas and M. Thommes, *Characterization of Porous Solids and Powders: Surface Area, Pore Size and Density*, Springer Netherlands, Dordrecht, 2004, vol. 16.

- [72] F. J. Sotomayor, K. A. Cychosz and M. Thommes, *Acc. Mater. Surf. Res.*, 2018, **3**, 34–50.
- [73] J. Rouquerol, P. Llewellyn and F. Rouquerol, in *Stud. Surf. Sci. Catal.*, 2007, vol. 144, pp. 49–56.
- [74] K. S. Sing, *J. Porous Mater.*, 1995, **2**, 5–8.
- [75] K. S. W. Sing, D. H. Everett, R. A. W. Haul, L. Moscou, R. A. Pierotti, J. Rouquerol and T. Siemieniewska, *Pure Appl. Chem.*, 1985, **57**, 603–619.
- [76] E. P. Barrett, L. G. Joyner and P. P. Halenda, *J. Am. Chem. Soc.*, 1951, **73**, 373–380.
- [77] K. S. Sing, F. Rouquerol, J. Rouquerol and P. Llewellyn, in *Adsorpt. by Powders Porous Solids Princ. Methodol. Appl. Second Ed.*, Academic Press, 2013, vol. 270, ch. 8, pp. 269–302.
- [78] P. A. Monson, *Microporous Mesoporous Mater.*, 2012, **160**, 47–66.
- [79] J. M. Thomas, *Proc. Roy. Soc. A*, 2017, **473**, 20160714.
- [80] J. Riches and J. Drennan, in *Nanostructure Control of Materials*, Elsevier, 2006, pp. 57–75.
- [81] R. Egerton, in *Electron Energy-Loss Spectroscopy in the Electron Microscope*, 2011, ch. 5, pp. 293–397.
- [82] K. Kanaya and S. Okayama, *J. Phys. D: Appl. Phys.*, 1972, **5**, 43–58.
- [83] J. Piños, Š. Mikmeková and L. Frank, *J. Microsc.*, 2017, **266**, 335–342.
- [84] J. M. Thomas, P. A. Midgley, T. J. Yates, J. S. Barnard, R. Raja, I. Arslan and M. Weyland, *Angew. Chem. Int. Ed.*, 2004, **43**, 6745–6747.
- [85] B. Zhang, W. Zhang and D. S. Su, *ChemCatChem*, 2011, **3**, 965–968.
- [86] J. Liu, *J. Electron Microsc. (Tokyo)*, 2005, **54**, 251–278.
- [87] C. G. Granqvist and R. A. Buhrman, *J. Catal.*, 1976, **42**, 477–479.
- [88] A. K. Datye, Q. Xu, K. C. Kharas and J. M. McCarty, *Catal. Today*, 2006, **111**, 59–67.
- [89] ISO, *BSI Standards Publication Representation of results of particle size analysis Part 2 : Calculation of average particle sizes / diameters and moments from particle size*, 2014.
- [90] R. E. Lakis, Y. Cai, H. G. Stenger and C. E. Lyman, *J. Catal.*, 1995, **154**, 276–287.

- [91] A. A. Herzing, M. Watanabe, J. K. Edwards, M. Conte, Z.-R. Tang, G. J. Hutchings and C. J. Kiely, *Faraday Discuss.*, 2008, **138**, 337–351.
- [92] S. Liu, I. Gow, T. Davies, A. Barnes, M. Sankar, X. Gong, A. G. R. Howe, M. Dixon, G. J. Hutchings, C. J. Kiely and Q. He, *J. Mater. Chem. A*, 2020.
- [93] H. L. Gruber, *Anal. Chem.*, 1962, **34**, 1828–1831.
- [94] F. F. Roca, *J. Chromatogr. Sci.*, 1968, **6**, 161–164.
- [95] J. Friedland, B. Kreitz, H. Grimm, T. Turek and R. Güttel, *ChemCatChem*, 2020, **12**, 4373–4386.
- [96] C. Karakaya and O. Deutschmann, *Appl. Catal. A Gen.*, 2012, **445-446**, 221–230.
- [97] G. Bergeret and P. Gallezot, in *Handbook of heterogeneous catalysis*, Wiley-VCH Verlag GmbH & Co. KGaA, Weinheim, Germany, 2008, pp. 738–765.
- [98] J. J. F. Scholten, A. P. Pijpers and A. M. L. Hustings, *Catal. Rev.*, 1985, **27**, 151–206.
- [99] G. C. Bond, in *Metal-Catalysed Reactions of Hydrocarbons*, Springer US, 2005, pp. 93–152.
- [100] R. M. Dell, F. S. Stone and P. F. Tiley, *Trans. Faraday Soc.*, 1953, **49**, 195–201.
- [101] T. J. Osinga, B. G. Linsen and W. P. van Beek, *J. Catal.*, 1967, **7**, 277–279.
- [102] H. Berndt and U. Müller, *Appl. Catal. A Gen.*, 1999, **180**, 63–69.
- [103] T. Yamashita and A. Vannice, *J. Catal.*, 1996, **163**, 158–168.
- [104] J. R. Rostrup-Nielsen, *J. Catal.*, 1968, **11**, 220–227.
- [105] H. S. Bengaard, J. K. Nørskov, J. Sehested, B. S. Clausen, L. P. Nielsen, A. M. Molenbroek and J. R. Rostrup-Nielsen, *J. Catal.*, 2002, **209**, 365–384.
- [106] A. D. Hernandez, N. Kaisalo, P. Simell and M. Scarsella, *Appl. Catal. B Environ.*, 2019, **258**, 117977.
- [107] J. E. Benson, H. S. Hwang and M. Boudart, *J. Catal.*, 1973, **30**, 146–153.
- [108] M. Boudart and H. S. Hwang, *J. Catal.*, 1975, **39**, 44–52.
- [109] R. K. Nandi, R. Pitachi, S. S. Wong, J. B. Cohen, R. L. Burwell Jr. and J. B. Butt, *J. Catal.*, 1981, **70**, 298–307.
- [110] N. K. Nag, *J. Phys. Chem. B*, 2001, **105**, 5945–5949.

- [111] S. F. Parker, H. C. Walker, S. K. Callear, E. Grünewald, T. Petzold, D. Wolf, K. Möbus, J. Adam, S. D. Wieland, M. Jiménez-Ruiz and P. W. Albers, *Chem. Sci.*, 2019, **10**, 480–489.
- [112] A. A. Blanchard, *Chem. Rev.*, 1937, **21**, 3–38.
- [113] G. Bergeret, P. Gallezot, P. Gelin, Y. Ben Taarit, F. Lefebvre, C. Naccache and R. D. Shannon, *J. Catal.*, 1987, **104**, 279–287.
- [114] S. Ichikawa, H. Poppa and M. Boudart, *J. Catal.*, 1985, **91**, 1–10.
- [115] A. Holmgren, B. Andersson and D. Duprez, *Appl. Catal. B Environ.*, 1999, **22**, 215–230.
- [116] M. M. D. Baker and E. K. Rideal, *Trans. Faraday Soc.*, 1955, **51**, 1597–1601.
- [117] D. W. McKee, *J. Catal.*, 1967, **8**, 240–249.
- [118] G. C. Bond, *Metal-catalysed reactions of hydrocarbons*, Springer, 2006.
- [119] J. E. Benson and M. Boudart, *J. Catal.*, 1965, **4**, 704–710.
- [120] M. A. Vannice, J. E. Benson and M. Boudart, *J. Catal.*, 1970, **16**, 348–356.
- [121] D. O’Rear, D. Löffler and M. Boudart, *J. Catal.*, 1985, **94**, 225–229.
- [122] D. J. O’Rear, D. G. Löffler and M. Boudart, *J. Catal.*, 1990, **121**, 131–140.
- [123] B. J. Kip, F. B. M. Duivenvoorden, D. C. Koningsberger and R. Prins, *J. Catal.*, 1987, **105**, 26–38.
- [124] Y. Ji, A. M. Van Der Eerden, V. Koot, P. J. Kooyman, J. D. Meeldijk, B. M. Weckhuysen and D. C. Koningsberger, *J. Catal.*, 2005, **234**, 376–384.
- [125] M. Wallin, H. Grönbeck, A. L. Spetz, M. Eriksson and M. Skoglundh, *J. Phys. Chem. B*, 2005, **109**, 9581–9588.
- [126] M. Vaarkamp, B. L. Mojet, M. J. Kappers, J. T. Miller and D. C. Koningsberger, *J. Phys. Chem.*, 1995, **99**, 16067–16075.
- [127] M. Vaarkamp, J. T. Miller, F. S. Modica and D. C. Koningsberger, *J. Catal.*, 1996, **163**, 294–305.
- [128] C. Mager-Maury, G. Bonnard, C. Chizallet, P. Sautet and P. Raybaud, *ChemCatChem*, 2011, **3**, 200–207.
- [129] M. W. Small, S. I. Sanchez, N. S. Marinkovic, A. I. Frenkel and R. G. Nuzzo, *ACS Nano*, 2012, **6**, 5583–5595.

- [130] M. Carosso, E. Vottero, A. Lazzarini, S. Morandi, M. Manzoli, K. A. Lomachenko, M. J. Ruiz, R. Pellegrini, C. Lamberti, A. Piovano and E. Groppo, *ACS Catal.*, 2019, **9**, 7124–7136.
- [131] G. Fagherazzi, P. Canton, P. Riello, N. Pernicone, F. Pinna and M. Battagliarin, *Langmuir*, 2000, **16**, 4539–4546.
- [132] P. Canton, G. Fagherazzi, M. Battagliarin, F. Menegazzo, F. Pinna and N. Pernicone, *Langmuir*, 2002, **18**, 6530–6535.
- [133] P. Canton, F. Menegazzo, S. Polizzi, F. Pinna, N. Pernicone, P. Riello and G. Fagherazzi, *Catal. Letters*, 2003, **88**, 141–146.
- [134] A. Borodziński and M. Bonarowska, *Langmuir*, 1997, **13**, 5613–5620.
- [135] A. Le Valant, C. Comminges, F. Can, K. Thomas, M. Houalla and F. Epron, *J. Phys. Chem. C*, 2016, **120**, 26374–26385.
- [136] F. Drault, C. Comminges, F. Can, L. Pirault-Roy, F. Epron and A. Le Valant, *Materials (Basel)*, 2018, **11**, 819.
- [137] L. Torrente-Murciano, *J. Nanoparticle Res.*, 2016, **18**, 1–7.
- [138] B. E. Warren and B. L. Averbach, *J. Appl. Phys.*, 1950, **21**, 595–599.
- [139] W. L. Smith, *J. Appl. Crystallogr.*, 1976, **9**, 187–189.
- [140] J. S. Hargreaves, *Catal. Struct. React.*, 2016, **2**, 33–37.
- [141] K. O’Connell and J. R. Regalbuto, *Catal. Letters*, 2015, **145**, 777–783.
- [142] M. A. Miranda and J. M. Sasaki, *Acta Crystallogr. A: Found. Adv.*, 2018, **74**, 54–65.
- [143] H. P. Klug and L. E. Alexander, in *X-Ray Diffraction Procedures For Polycrystalline and Amorphous Materials*, John Wiley and Sons, Inc., New York, 1954, ch. 9, pp. 491–538.
- [144] A. Francis, *Ind. Eng. Chem.*, 1957, **49**, 1779–1786.
- [145] A. W. Francis, *Chem. Eng. Sci.*, 1959, **10**, 37–46.
- [146] R. Storm and K. Price, *J. Glob. Optim.*, 1997, **11**, 341–359.

Chapter 3

The characterisation of galaxolide hydrocarbon and the typical industrial product mixture

3.1 Introduction

Many research projects use starting materials and products that are widely available, extensively characterised, and have known physical properties (or use a solvent which is taken as representative of the solution). For GHC and the associated products of its hydrogenation, no such information was available as the compounds of interest are synthesised and used internally to manufacture consumer products. In particular, it should be noted that the product mixture is not purified in the production process and as a result, contains unreacted starting material and saturated products. Consequently, the industrial mixtures provided to carry out this work require sufficient characterisation and recording of physical properties, so that a deeper understanding of the reaction can be acquired and physical processes be better understood.

Herein the starting material, GHC, and a typical product mixture, taken from an industrial plant, are characterised using nuclear magnetic resonance (NMR) spectroscopy and gas chromatography-mass spectrometry (GC-MS). This analysis is performed to identify the various compounds relevant to this work, since reference materials for the compounds used in this work are not available commercially. Various physical properties of the aforementioned chemical mixtures are also reported. These are required to understand mass transfer processes that occur within the reaction and are outlined in the next chapter. The starting material is used to represent the state of the system at low levels of conversion whereas the product mixture is used to represent the reactor at the location of the yield maximum, where any mass transfer limitations may be detrimental to product yields. To understand the mass transfer process of liquid phase components, the density and viscosity of the neat solutions are needed.

As hydrogen must first dissolve before it can diffuse through solution, an understanding of its solubility in the hydrocarbons used in this work is needed, so this must be also be established.

3.2 Aims

- Characterise industrial materials to gain understanding of chemical composition.
- Record physical properties (density, viscosity, and hydrogen solubility) needed to understand liquid-phase mass transfer processes under reaction conditions.

3.3 Results and discussion

3.3.1 GC analysis

The gas chromatograph-total ion current chromatograms for the industrial starting material, GHC, and a typical industrial product mixture are displayed in Figure 3.1. The wax-type column used in these experiments was of the same type as was used for the general liquid phase analysis to allow for products to be identified based on their relative retention time on the column. The GC trace for GHC shows two prominent peaks with several small peaks visible. These two larger peaks are attributable to the two structural isomers of GHC, PMI and E-PMI, which exist in a ratio of 11 to 1 in favour of PMI as identified using GC-MS studies by reference to the National Institute of Science and Technology (NIST) database entry (Figure 3.2). The structure of E-PMI was identified using the method described below (Figure 3.3a). From an industrial perspective, these compounds are both considered to contribute to the yield of the process. The smaller peaks in this chromatogram could not be matched with a known compound in the NIST database, but the closest structural matches suggest they are side products from the acid catalysed cycloaddition reaction used to synthesise GHC (Section 1.2.2).

The industrial product mixture on the other hand displays a more complex GC trace with many peaks visible. The mass spectra of the peaks at 11 and 12 minutes were identical to those in the starting material. No plausible matches for other peaks were identified by searching the NIST 11 database available on the instrument. Internet searches for possible reaction intermediates in academic databases (Reaxys, SciFinder) did not return any results for the mass spectra of any of suspected compounds. Assignment of the structures based upon the fragments observed is difficult due to the ionisation method used in this study, electron impact, and the relatively high molecular weight of the possible compounds, meaning that many fragments are possible. For example, there are 91 conceivable fragments for PMI if only its immediate descendants are considered; if secondary fragments are formed this number

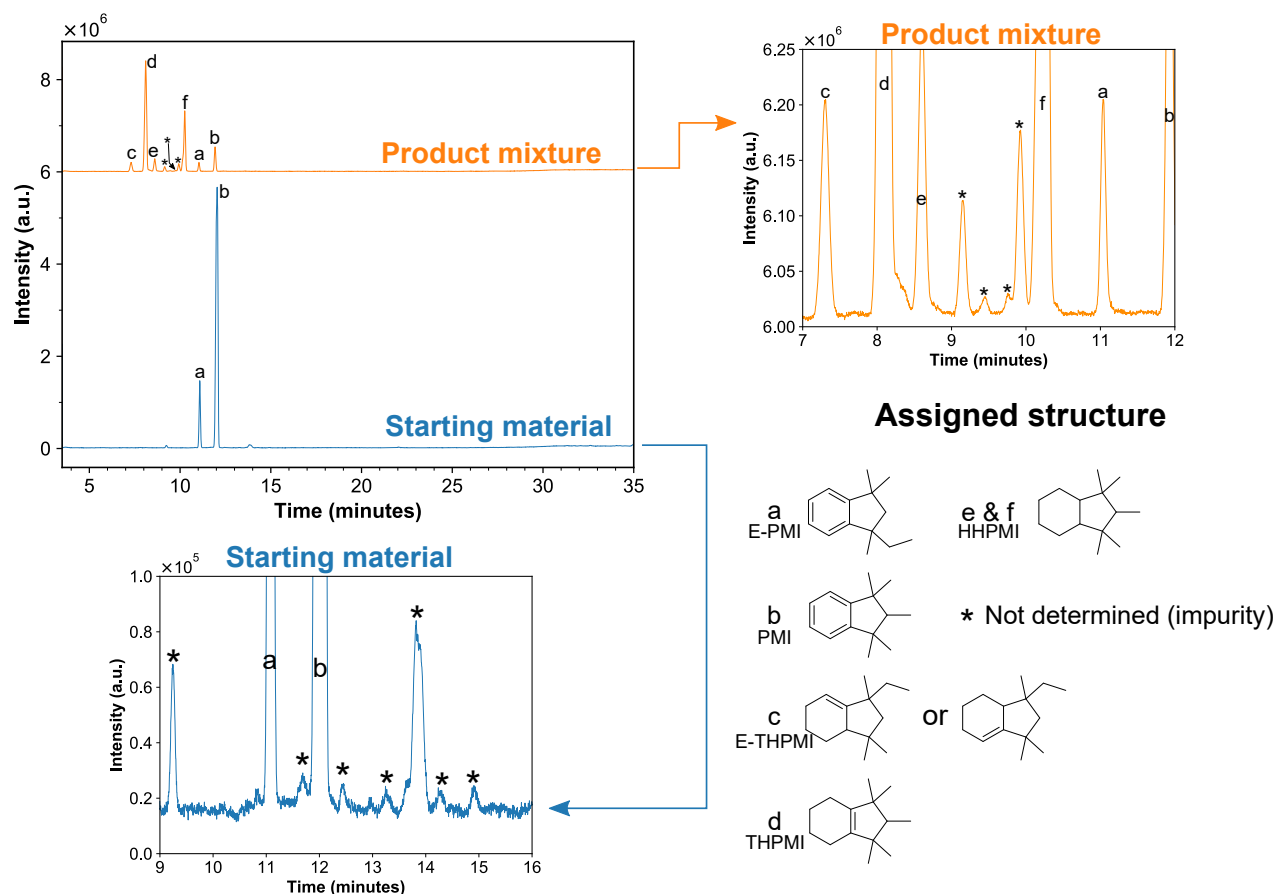


Figure 3.1: Total ion current chromatograms of the as received starting material, GHC, and a typical industrial product mixture, THPMI mixture.

increases into the hundreds.¹ Besides, even though a molecular species is feasible, it does not necessarily mean it will appear in the mass spectrum.

A possible solution to this issue is to use a machine learning approach. Here, a machine is trained to extract pertinent information from a mass spectral library to predict mass spectra for inputted molecules. For the purpose of this project, the program developed by Wei *et al.*², hereon referred to as NEIMS, will be used as a pretrained machine is freely downloadable, usable under an Apache license³ (i.e. without restriction), and provides better performance than other available methods.² To demonstrate this method was applicable to this work, the experimentally recorded and the NIST reference spectra of PMI were compared to the NEIMS simulated spectrum (Figure 3.2b and c). An excellent similarity score, calculated using Stein and Scott's dot-product function,⁴ was obtained for the experimentally recorded mass spectrum (83%) and NIST reference spectrum (85%). Moreover, the predicted base peak at 173 m/z is also found to be in agreement with the experimental data which indicates the most abundant fragment was correctly identified.

In an attempt to identify the structures of the unknown peaks, synthetic spectra were produced for all conceivable compounds for this reaction and added to a database. Next, the experimental spectrum for each peak was compared to the database and the level of

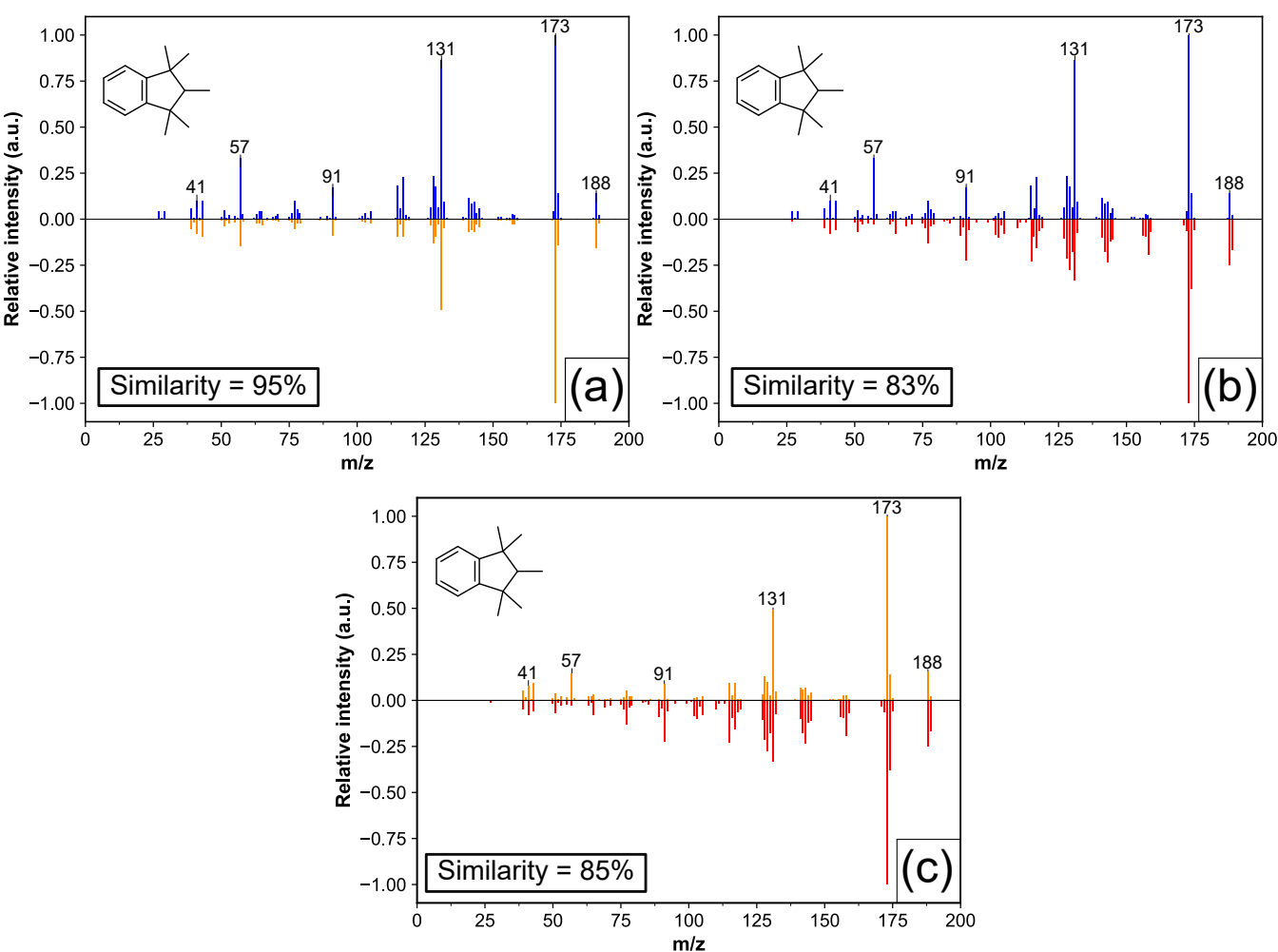


Figure 3.2: Electron impact (positive ionisation mode) mass spectra for PMI (peak b, Figure 3.1). (a) Experimental mass spectrum (■) plotted with the NIST reference spectrum (■) and NEIMS predicted mass spectrum (■); (b) experimental mass spectrum plotted with NEIMS spectrum; (c) NIST reference spectrum plotted with NEIMS spectrum. Similarity = $100 \times (\sum W_a W_b)^2 / (\sum W_a^2 \sum W_b^2)$ where W is equal to the product of the square root of peak intensity and m/z value and the subscript a and b are values of intensity and m/z in spectrum A and B .

similarity was assessed. For THPMI, only one structure gave a high similarity score, so this was assumed to be its structure (Figure 3.3b). Interestingly, a poor match is obtained for the tetrahydro-intermediate formed from E-PMI if the double bond is assumed to be in the same position as THPMI (Figure 3.3c). A good match score is achieved when the double bond is assumed to be in either of the positions adjacent to the two junction carbon atoms, though it is not possible to definitively determine which isomer forms due to the spectral similarities (Figure 3.3d and e). Simulated spectra for other isomers of this compound yielded low match scores. The saturated compounds should exhibit four peaks in a GC trace, yet only two peaks with a molecular ion peak at $m/z=194$ are observed (Figure 3.4). This observation is probably attributable to peak merging. As the column used in these experiments separates based on polarity, it would be anticipated that the two *cis* products would elute at similar times,

with the same being true for the *trans* products. Moreover, this explains why the similarity score is slightly lower for these compounds as the observed spectrum is the product of two compounds and offers an explanation on the absence of the cluster of peaks expected in the mass spectrum of E-THPMI around $m/z=160$. No other peaks could be readily identified as a possible reaction product and are probably formed from the reaction of impurities in the starting material.

The proposed structures assume that the charge on the molecular ion peak is equal to unity. This assumption is valid as all unknown peaks have a shorter retention time than GHC, which indicates they are not dimers, or heavier products, as these would be expected to elute at longer retention times.⁵ The formation of similar compounds has been reported to occur during benzene hydrogenation through a hydrodimerisation reaction between benzene and desorbed cyclohexene on acid sites on the catalyst surface.⁶⁻¹⁰ However, given that there is no evidence for the formation of these species, it can be assumed that no (or minimal) dimerisation occurs during the industrial process. Whether this is attributable to a catalytic property, a kinetic factor, or a thermodynamic limitation is not established.

Finally, one may note that although the m/z value of experimental peaks are in good agreement with the experimental spectra, the intensities differ vastly. This effect is probably due to the stochastic nature of the physical process or experimental issues as variability in the mass spectra of the same molecule spectral databases are common¹¹ and efforts to alleviate this issue are ongoing.¹² This is also why when considering the similarity score, the weighting to the intensity is less than that of the m/z value.

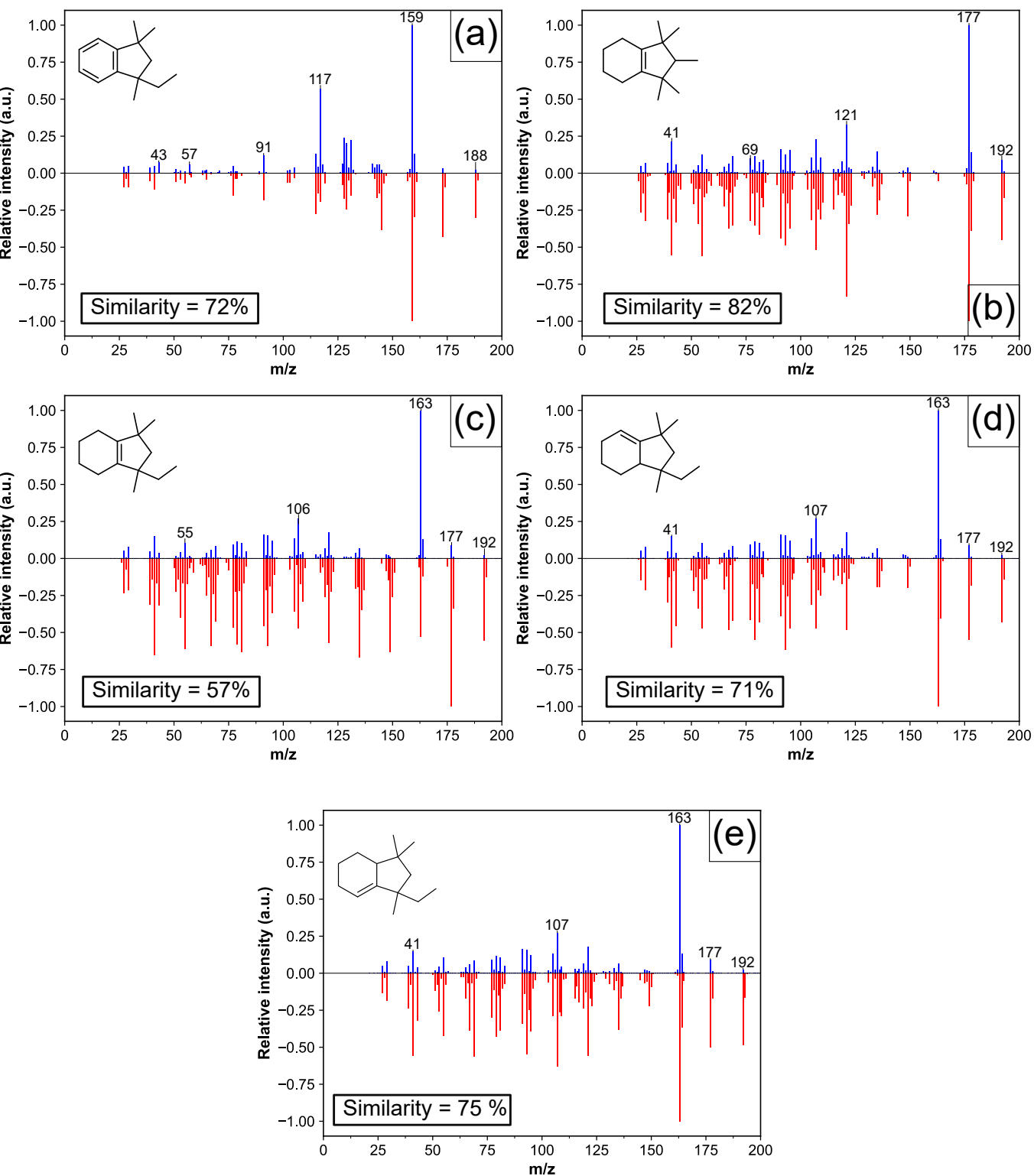


Figure 3.3: Electron impact (positive ionisation mode) mass spectra for **(a)** E-PMI (peak a, Figure 3.1); **(b)** THPMI (peak d, Figure 3.1); **(c-e)** isomers of E-THPMI (peak c, Figure 3.1). Experimental mass spectrum (■) plotted with NEIMS predicted mass spectrum (■). See caption of Figure 3.2 for similarity calculation.

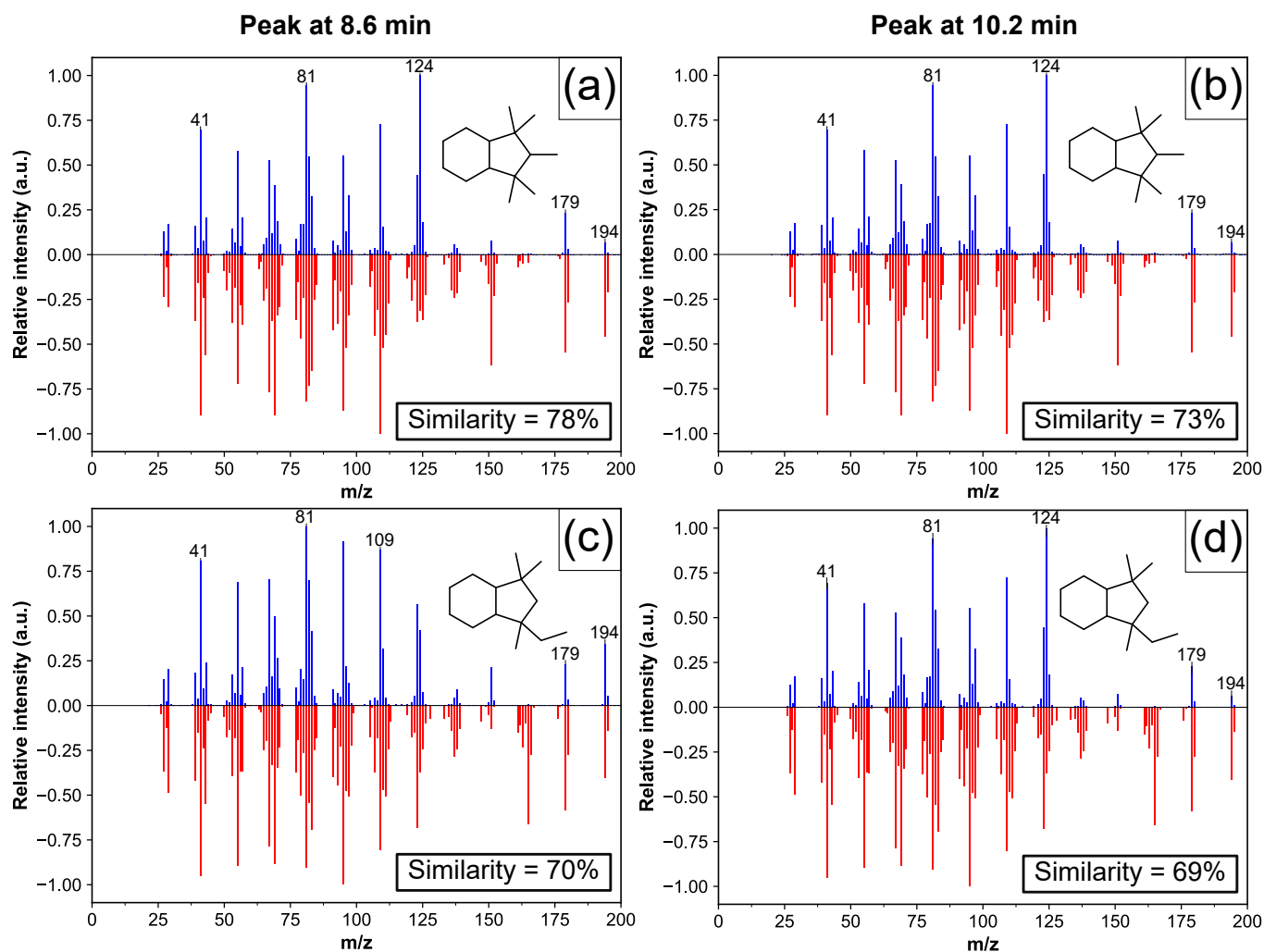


Figure 3.4: Electron impact (positive ionisation mode) mass spectra for HHPMI (peaks e and f, Figure 3.1). Experimental mass spectrum (■) plotted with NEIMS predicted mass spectrum (■). See caption of Figure 3.2 for similarity calculation.

3.3.2 NMR analysis

To further evidence the structural assignment of E-THPMI, where the double bond is located adjacent to and not between the two junction carbon atoms, the product mixture was analysed by ^1H NMR spectroscopy (Figure 3.5). This technique would be useful in this regard as tetrasubstituted alkenes would display no vinylic signals, which are commonly observed between $\delta_{\text{H}} = 4.5\text{--}6.5$ ppm,¹³ in a ^1H NMR spectrum. On the contrary, trisubstituted alkenes should exhibit one signal with a defined splitting pattern. However, the use of NMR methods in the characterisation of complex mixtures of varying analyte concentration is notoriously challenging and typically requires the use sophisticated experiments and skilful analysis.^{14,15} During their studies on the hydrogenation of a series of indanes, Ranade and Prins used the spectra of pure compounds or undertook the independent synthesis of the saturated product using reported procedures in literature as assignment of the ^1H NMR spectrum in isolation proved impossible.^{16,17} This issue is further complicated in this instance since this vinylic proton signal is (i) in low concentration and thus any signal would be of small intensity, and (ii) obfuscated by trace components which also resonate in the characteristic olefinic region. The latter point could be addressed by using a purified form of the proposed compound, but alas, this was not available. Alternatively, spectral prediction methods with a precision of 0.4 ppm for ^1H NMR are available,¹⁸ but no information on the splitting pattern is included. Moreover, the large number of signals within the error range predicted for this proton at 5.37 ppm (Figure 3.5b) render it difficult to conclusively identify this product using this method. The low intensity of all signals in the vinylic ^1H NMR region also reveals that the concentration of isomers of THPMI are small, if at all present. This agrees with the GC-MS data which found only low similarity scores for THPMI isomers.

One may consider using the ^{13}C nucleus for characterisation purposes instead. A variety of experiments are suitable for this purpose, such as standard ^{13}C NMR spectroscopy, which will provide information on all ^{13}C nuclei present, or the distortionless enhancement by polarisation transfer (DEPT) methods, which provide information on the substitution of the carbon atom. As with the ^1H NMR spectrum, however, the presence of similar carbon environments means structural assignment must depend on only the GC-MS data.

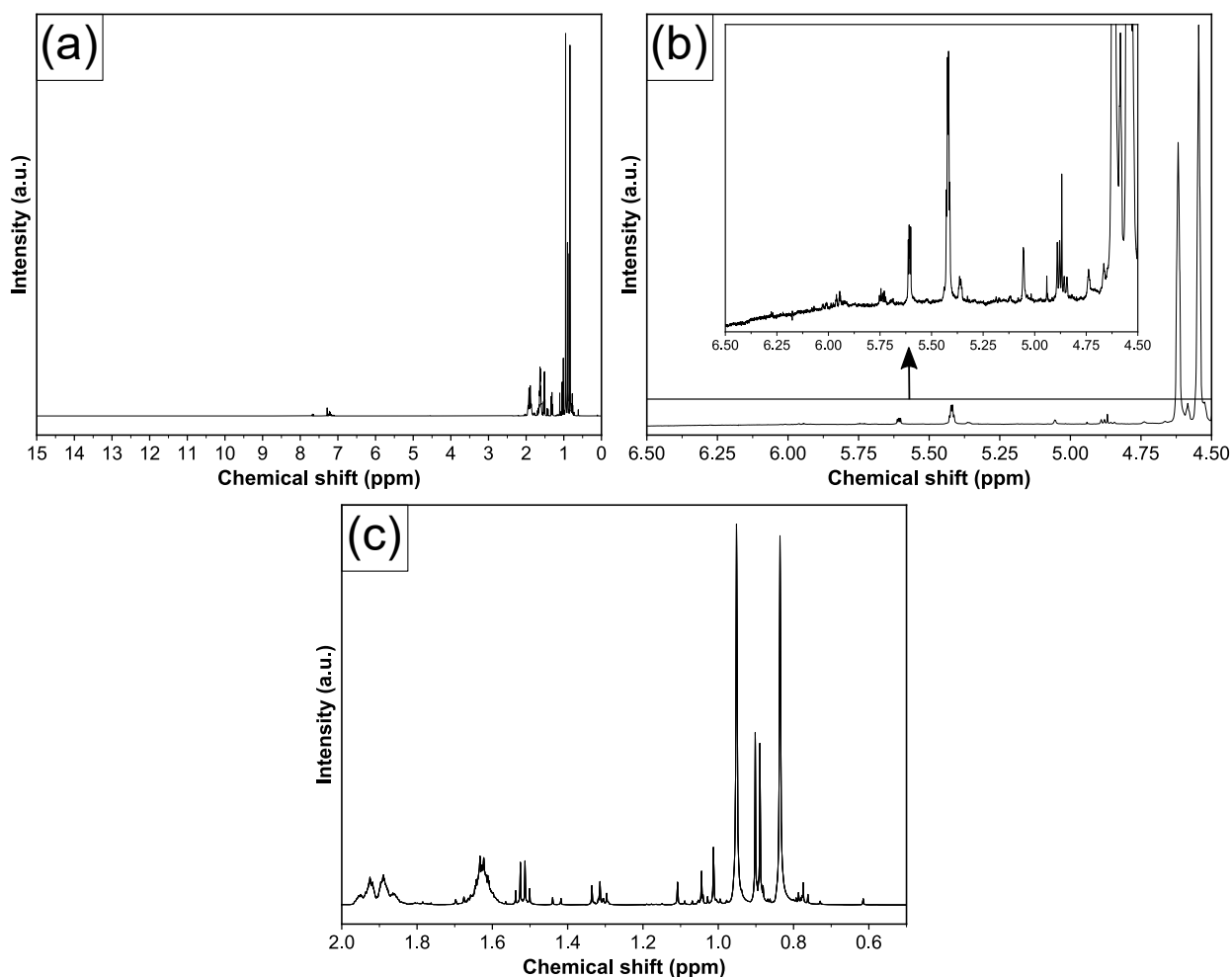


Figure 3.5: ¹H NMR spectrum of the THPMI product mixture. (a) Full spectrum; (b) vinylic region with inset of baseline; (c) alkane region.

3.3.3 Density measurements

Thermodynamic calculations of solution properties, such as hydrogen solubility, viscosity, and mass transfer coefficients, often requires a knowledge of the temperature dependence of liquid densities. Pressure also affects the density of liquids, but the compressibility of liquids is significantly smaller than that of gasses. The measurement of density is typically performed using a vibrating tube densimeter which can provide high accuracy (up to 0.0001 g/cm) of the effects of temperature and pressure but at a high cost. A cheaper alternative is the glass specific gravity densimeters, but these usually require large volumes of analyte. In addition to these techniques, simple equations based on correlations have been developed to estimate density.¹⁹ However, more accurate methods require specific thermodynamic properties of the compound to be known.¹⁹ Alternative methods based upon group contribution methods (i.e. only require structural knowledge) generally behave very well, though these can be subject to major failures and thus, *a posteriori* knowledge of density is desirable.^{19–21}

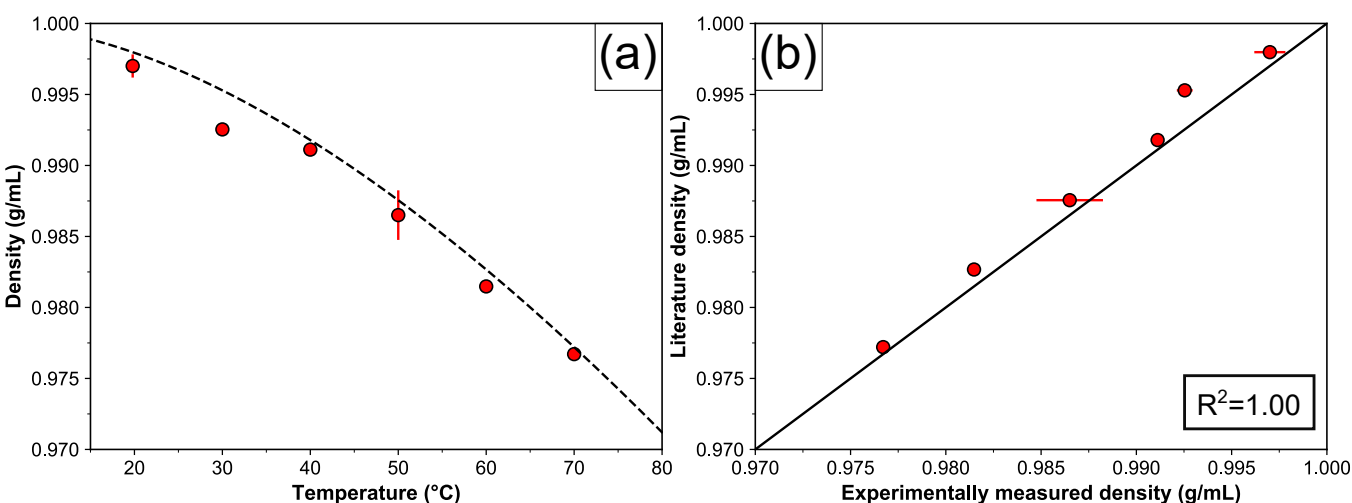


Figure 3.6: (a) A comparison of the experimentally measured density of water in this study (●) with values calculated using literature equation ρ (kg/m^3) = $(999.83952 + 16.945176 T - 7.9870401 \times 10^{-3} T^2 - 46.170461 \times 10^{-6} T^3 + 105.56302 \times 10^{-9} T^4 - 280.54253 \times 10^{-12} T^5) / (1 + 16.897850 \times 10^{-3} T)$ (----). (b) Parity plot of calculated values *versus* experimental values measured in this study. Line represents parity. Error bars represents standard deviation of recorded density.

A simple method was proposed that involved heating a pyrex density bottle in a thermostated oven in a moderate temperature region ($<100^\circ\text{C}$ for safety reasons) and recording the mass. As the thermal expansion coefficient of pyrex glass is in the order of $1 \times 10^{-6} \text{K}^{-1}$, the change in the calibrated flask volume should be within the measurement error. To test the suitability of this method, the density of water was recorded from room temperature to 70°C and compared with the values calculated using an equation derived by Kell,²² who fitted the equation to many available data sets (Figure 3.6a). The quality of measurement is also compared to literature value using a parity plot in Figure 3.6b. In both cases, it is clear this method is satisfactory for measuring the density of water and possibly other liquids in air at elevated temperatures.

As the purpose of the density measurements was to gain insight into thermodynamic properties of the reaction system at low and at high GHC conversions, density measurements were performed using the GHC starting material and the typical industrial product mixture (*vide supra*). The experimentally recorded densities for GHC and the industrial product mixture from room temperature to 100°C are displayed in Figure 3.7a. Given that this was outside the desired temperature region, the data was fitted to an expression proposed by Francis^{23,24} (Equation 3.1) to estimate the density under typical reaction conditions (i.e. $\geq 145^\circ\text{C}$).

$$\rho = A - BT - \frac{C}{E - T} \quad (3.1)$$

where ρ is the density at temperature T , A is a constant usually 0.06 greater than the liquid density at 20°C , B is the slope coefficient, C is an integer from 6–10, and E is a number approximately 34°C above the critical temperature for non-aromatic hydrocarbons and more still for aromatic hydrocarbons.

This equation was then regressed to experimental data using the differential evolution method, a global optimisation algorithm, as implemented in the SciPy (version 1.4.1) in Python 3.7.6. The results of the optimised curve fitting are displayed in Figure 3.7 along with associated parity plots. It is evident that the model fittings are excellent and near linear in the region of interest in agreement with literature density measurements on tetralin and decalin.^{25,26} The initial bounds for each data were set to broadly follow with the findings of Francis, such that the density was set to be between 0.85 and 1.2, the slope coefficient between 1×10^{-6} and 1×10^{-4} , C between 5 and 10, and parameter E set to ± 200 °C of the critical temperature estimated from using the Joback method (777 K for PMI and 773 K for THPMI). The C value was altered so that it equalled the closest integer, and the regression was repeated. The value for the E parameter was highly sensitive to the initial boundary conditions, even when the same seed value (1) was used. However, the change in this value results in near identical values for the other fitting parameters, with the effect of the E term causing an approximate 0.2% difference in the predicted value at 220 °C and therefore does not impact the predictive utility required from this fitting. If more data were to be acquired at higher temperatures, this should allow for a better solution to be derived but this was not attempted in this work for safety reasons.

As highlighted above, pressure may also influence the density of a liquid. The experimental procedure outlined above was not possible at high pressures, and as the equipment needed for such measurements was not available, literature data for tetralin²⁵ and decalin²⁶ were used as model compounds to assess potential pressure effects. These publications fitted the experimental data to the modified Tammann-Tait equation:

$$\rho(T, P) = \frac{\rho_0(T)}{1 - C \times \ln\left(\frac{B(T)+P}{B(T)+P_{ref}}\right)} \quad (3.2)$$

$$\rho_0(T) = A_0 + A_1 \times T + A_2 \times T^2 \quad (3.3)$$

$$B(T) = B_0 + B_1 \times T + B_2 \times T^2 \quad (3.4)$$

where A_0 , A_1 , and A_2 are fitting parameters for the reference density at a constant pressure, P_{ref} ; B_0 , B_1 , B_2 , are fitting parameters for the entire dataset,²⁶ such that prediction of densities at unrecorded temperatures and pressures is possible. These data are outlined in Table 3.1 and were used in conjunction with Equations 3.2–3.4 to probe the effect of pressure in the region of interest in this work, *viz.*, 145–210 °C and 15–85 bar. The relative change in density as pressure is increased from 15 to 85 bar between 145 and 210 °C is *ca.* 1% for each molecule, suggesting that the effect of pressure can be ignored if the compounds used in this work are assumed to behave similarly.

Table 3.1: Fitting parameters of the Tamman-Tait equation and relative density changes between 1.5 and 8.5 MPa for tetralin, *cis*-decalin, and *trans*-decalin.

| Liquid | A_0 | A_1 | A_2 | B_0 | B_1 | B_2 | C | P_{ref} | Density change (%) ^a | Reference |
|-----------------------|---------|----------|-------------------------|--------|----------|------------------------|---------|-----------|---------------------------------|-----------|
| Tetralin | 1191.20 | -0.70936 | -1.570×10^{-4} | 512.20 | -1.63032 | 1.376×10^{-4} | -0.2043 | 0.1 | 1.0 | [25] |
| <i>cis</i> -Decalin | 1243.0 | -1.456 | -1.03×10^{-3} | 507.6 | -1.961 | -2.04×10^{-4} | 0.074 | 15.0 | 1.0 | [26] |
| <i>trans</i> -Decalin | 1202.0 | -1.371 | -9.76×10^{-4} | 497.6 | -1.861 | -1.88×10^{-4} | 0.086 | 25.0 | 1.0 | [26] |

^a Calculated by $100 \times P_{8.5 \text{ MPa}} / P_{1.5 \text{ MPa}}$

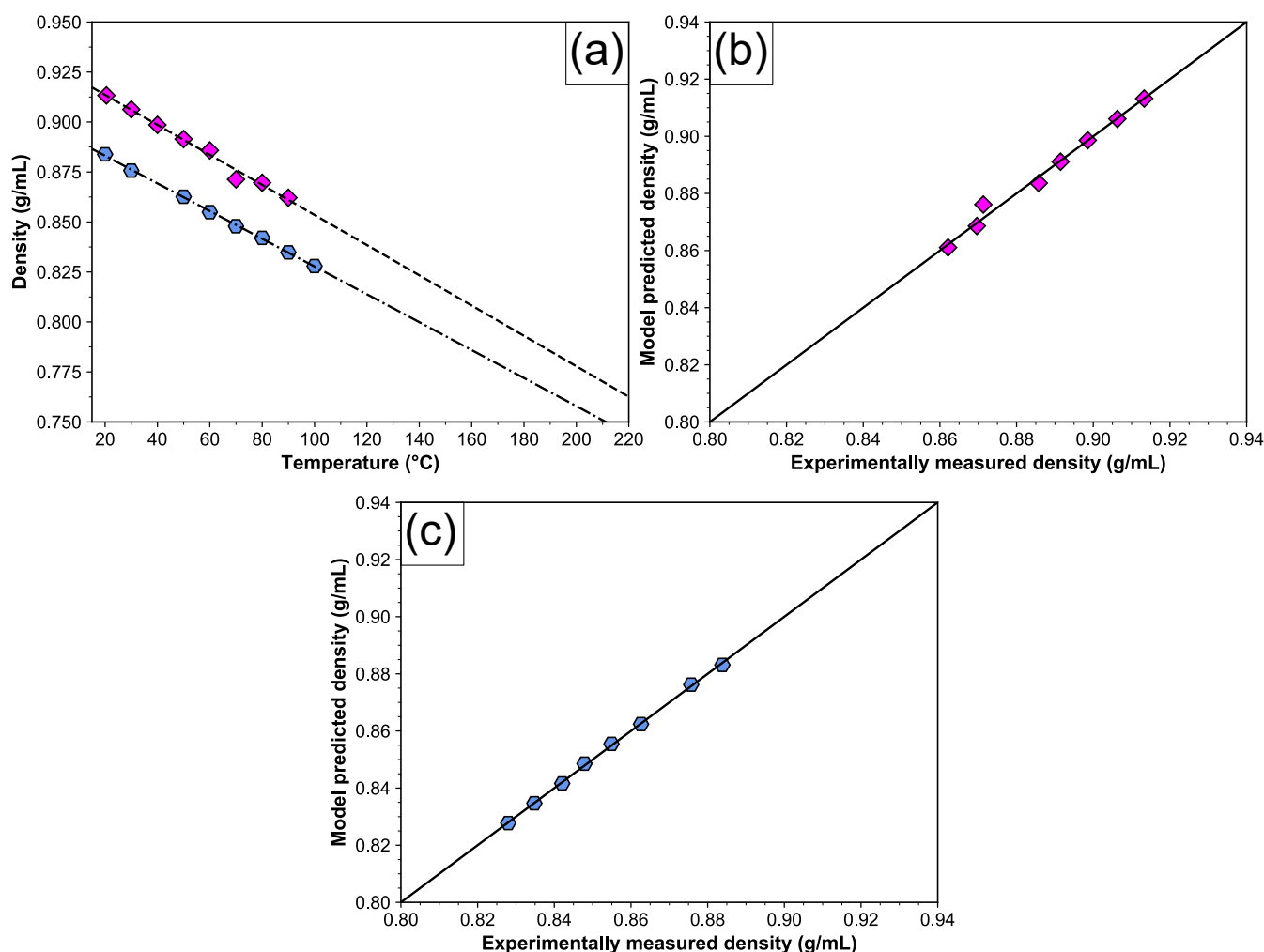


Figure 3.7: (a) Experimentally measured density of GHC (◆) and industrial product mixture (●) with model fittings using Equation 3.1 (---- = GHC, --- = THPMI). GHC fitting parameters: $A = 0.940 \text{ g/mL}$, $B = 7.31 \times 10^{-4}$, $C = 8$, $D = 710$; industrial product mixture fitting parameters: $A = 0.907 \text{ g/mL}$, $B = 6.74 \times 10^{-4}$, $C = 8$, $D = 726$. (b) Parity plot of model predicted values *versus* experimentally measured values for GHC. (c) Parity plot of model predicted values *versus* experimentally measured values for industrial product mixture. Black line on (b) and (c) represents parity. Error bars shown but generally too small to be seen.

3.3.4 Viscosity measurements

Many techniques used to estimate diffusion coefficients of a liquid, which are required when considering mass transfer processes in the following chapter, assume an inverse relationship with the viscosity of the solvent.¹⁹ As such, knowing the viscosity of a solution is necessary to understand mass transfer process in solution. The viscosity of GHC and a typical product mixture were recorded using an Oswald-type viscometer in the temperature region of 25–70 °C (Figure 3.8). To obtain information about the viscosity at temperatures used in future chapters, the dynamic viscosity data was fitted to an Arrhenius-type model, namely:

$$\ln \eta_L = A + \frac{B}{T} \quad (3.5)$$

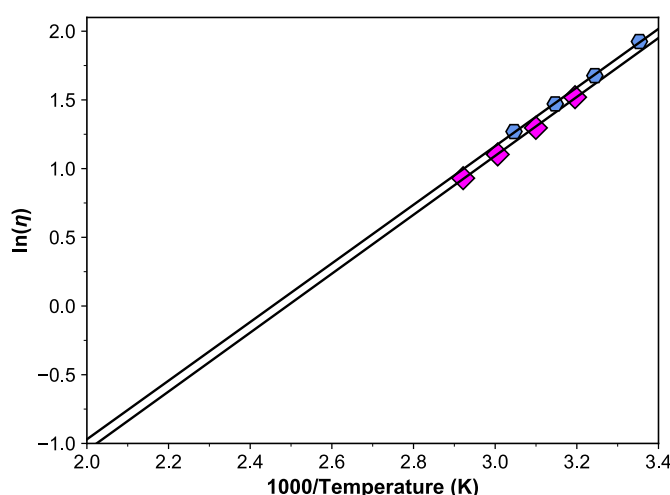


Figure 3.8: Dynamic viscosity data for GHC (◆) and industrial product mixture (●) recorded using an Oswald viscometer immersed in a water bath. Error bars shown but too small to be seen.

where η_L is the dynamic viscosity, A and B are constants, and T is temperature. The A and B values for GHC and the THPMI mixture are listed in Table 3.2 with the relevant graph presented in Figure 3.8.

Ewell and Eyring proposed that the physical meaning of these parameters can be interpreted using transition state theory.²⁷ This model purports that a liquid possesses a quasicrystalline structure which traps molecules in a “cage” of surrounding molecules.²⁸ Escape from this “cage” to an adjoining “hole” is possible if a molecule has an energy equal to B in Equation 3.5, which is also termed the free energy of activation divided by the gas constant. Further derivation consequently results in the A equating to the inverse of the molar volume of the liquid, V_m , multiplied by Avogadro’s number, N_A , and Planck’s constant, \hbar , (Equation 3.6).²⁸

$$\eta = \frac{N_A \hbar}{V_m} \exp\left(\frac{\Delta G^\ddagger}{RT}\right) \quad (3.6)$$

The ΔG^\ddagger value obtained is then related to the internal energy of vapourisation by the relation $\Delta G^\ddagger \approx 0.408\Delta U_{vap}$ which in turn can be approximated to the normal boiling point, T_b , using Trouton’s rule.²⁸ This states that the entropy of vapourisation of many liquids is roughly equal to 88 kJ/mol,²⁹ (see Table 3.3 for some examples) thus $\Delta G^\ddagger \approx 0.408\Delta U_{vap} \approx 3.8RT_b$. The T_b values calculated using this relation are presented for GHC, the industrial product mixture, and some other hydrocarbons in Table 3.3; for the hydrocarbons not measured directly in this study, viscosity values at various temperatures were taken from literature.³⁰ These values are of relevance for the mass transfer calculations as knowledge of the boiling point is required. Calculated values for benzene, tetralin, and *cis* and *trans* decalin were in good agreement with literature reported boiling points, however for methyl-substituted benzenes, *viz.* toluene and the xylenes, errors were greater than 25%. Although errors this large are not uncommon using this approximation procedure,²⁸ it is interesting that the failures are specific to methyl-

substituted benzenes and not all aromatic compounds. Several possible explanations of the deviations in this model have been forwarded:²⁷ (i) differing packing in the liquid phase; (ii) the flow process is not a unimolecular process and may involve a pair; or (iii) the transition state does not always proceed to products. These explanations however do not readily account for this variation being specific to alkylbenzenes.

As with density, the effect of pressure on viscosity must be considered. Viscosity data for tetralin, from 25 to 175 °C and 1 to 1200 bar,²⁵ and *cis*-decalin, between 1–1000 bar and 25–80 °C,³¹ were compiled to serve as model compounds as high pressures were not possible in the glass apparatus used for these measurements. These results indicated that the effect of pressure could lead to six-fold changes as pressure was increased from atmospheric to 1900 bar (Figure 3.9). As the pressures in this work were in the region of 15–85 bar, it is useful to understand the pressure dependence of viscosity in this region. The data was treated in a similar fashion to that which was used by Caudwell *et al.*²⁵ to make the prediction. But, to remain consistent with the analysis presented above, the temperature dependence of viscosity of both compounds was first calculated using Equation 3.5. Subsequently, the entire data set of each compound was fitted to the following equation:

$$\eta = A \exp\left(\frac{B}{T}\right) \left(\frac{p + E}{p_0 + E}\right)^D \quad (3.7)$$

where A and B are known *via* Equation 3.5, T is the temperature, p is pressure, and D and E are functions of temperature given by:

$$D = d_0 + d_1 \times T + d_2 \times T^2 \quad (3.8)$$

$$E = e_0 + e_1 \times T + e_2 \times T^2 \quad (3.9)$$

The fitting parameters of this procedure can be found in Table 3.2 and associated plots in Figure 3.9. This analysis reveals that at 145 °C, the lowest temperature used in this work, a viscosity change of 10% may be expected. As temperature is increased, however, the effect of pressure on viscosity reduces as a variation below *ca.* 5% is forecast. The 10% larger viscosity may at first seem high but recall that viscosity was logged for the purpose of mass transfer calculations which notoriously have high error margins.^{19,32} Therefore, the ambient pressure viscosity data recorded for GHC and the industrial product mixture is usable, but cannot be considered highly accurate in the pressure region of interest.

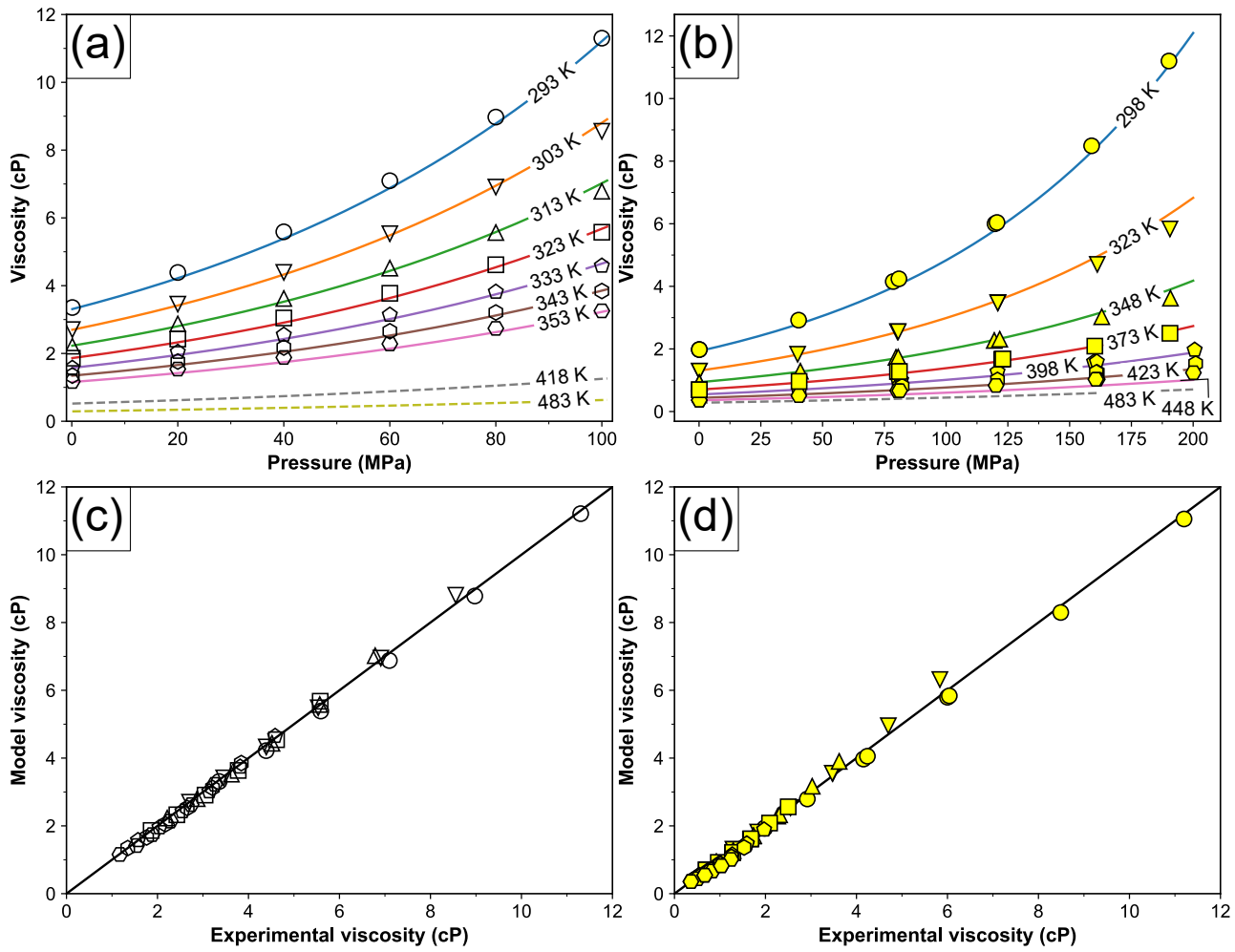


Figure 3.9: (a) Experimental viscosity data for decalin with model fittings using Equation 3.7 and Table 3.2. Dashed lines at 418 and 483 K are predicted viscosities. (b) Experimental viscosity data for tetralin with model fittings using Equation 3.7 and Table 3.2. Dashed line at 483 K are predicted viscosities. (c + d) Parity plots for model fittings for decalin (c) and tetralin (d). *Legend:* Decalin at 293 K (○), 303 K (▽), 313 K (△), 323 K (□), 333 K (◇), 343 K (⊙), and 353 K (⊚). Tetralin at 298 K (●), 323 K (▽), 348 K (△), 373 K (■), 398 K (◆), 423 K (⊙), and 448 K (⊚).

Table 3.2: Fitting parameters for the effect of pressure on a liquid’s viscosity obtained by fitting data in [25] and [31] to Equation 3.7.

| Fluid | A | B | d_0 | d_1 | d_2 | e_0 | e_1 | e_2 |
|---------------|---------|--------|--------|--------|------------|--------|--------|--------|
| GHC | -5.340 | 2144.3 | - | - | - | - | - | - |
| THPMI mixture | -5.238 | 2133.9 | - | - | - | - | - | - |
| Tetralin | -4.3853 | 1503.7 | 13.353 | 7.1989 | -0.0058511 | 7.1008 | 29.481 | 1.9097 |
| Decalin | -4.9848 | 1812.1 | 10.938 | 9.9479 | 0.0010955 | 6.2538 | 28.934 | 2.7790 |

Table 3.3: Table of enthalpies of vapourisation at normal boiling point, ΔH_{vap}^b , normal boiling points, T_b , entropies of vapourisation at normal boiling point, ΔS_{vap}^b , predicted boiling points using transition state theory, and the associated error. where ΔH_{vap}^b is the enthalpy of vapourisation at boiling point and T_b is the normal boiling point. Data taken .

| Compound | $\Delta H_{vap}^{T_b^a}$ (kJ mol ⁻¹) | Literature T_b^a (K) | $\Delta S_{vap}^{T_b^b}$ (JK ⁻¹ mol) | Predicted T_b (K) | Error ^c (%) | Joback T_b (K) | Error (%) |
|-----------------------|--|------------------------|---|---------------------|------------------------|------------------|-----------|
| Benzene | 30.72 | 353.23 | 86.96 | 319 | 9.5 | 359 | 1.6 |
| Toluene | 33.18 | 383.75 | 86.46 | 280 | 27 | 386 | 0.74 |
| <i>o</i> -Xylene | 36.24 | 417.55 | 86.79 | 308 | 26 | 414 | 0.74 |
| <i>m</i> -Xylene | 35.66 | 412.25 | 86.50 | 268 | 35 | 414 | 0.53 |
| <i>p</i> -Xylene | 35.67 | 411.45 | 86.69 | 284 | 31 | 414 | 0.69 |
| Tetralin | 43.9 | 480.35 | 91.4 | 399 | 16 | 476 | 0.92 |
| <i>cis</i> -Decalin | 41.0 | 468.95 | 87.4 | 479 | 2.3 | 458 | 2.1 |
| <i>trans</i> -Decalin | 40.2 | 460.45 | 87.3 | 418 | 9.1 | 459 | 0.29 |
| GHC | n.a. | n.a. | n.a. | 564 | 2.6 ^d | 549 | n.a. |
| THPMI mixture | n.a. | n.a. | n.a. | 562 | 2.0 ^d | 551 | n.a. |

^a Value taken from [30].

^b Calculated by $\Delta S_{vap}^b = \frac{\Delta H_{vap}^b}{T_b}$.

^c Calculated by $100 \times ((\text{Literature } T_b - \text{Predicted } T_b) / \text{Literature } T_b)$

^d Calculated by $100 \times ((\text{Joback } T_b - \text{Predicted } T_b) / \text{Joback } T_b)$

3.3.5 Hydrogen solubility measurements

The effect of pressure on gas solubility is described by Henry's Law as:

$$C = \frac{P_{gas}}{H} \quad (3.10)$$

where C is the concentration, P_{gas} is the pressure of the gas, and H is Henry's constant. The effect of temperature on H can be modelled with an Arrhenius-type equation:³³

$$H = H_0 \exp\left(\frac{-\Delta E}{RT}\right) \quad (3.11)$$

where H_0 is a pre-exponential factor, R is the gas constant, and T is temperature.

Hydrogen solubility data for many hydrocarbons has been reported in literature but not for GHC nor its components. It was desirable to record this property but unfortunately ongoing complications of the pandemic prevented its study (see Section 6.2.1). Instead, literature data for other hydrocarbons was examined to determine if it could provide insight for this system. The Henry's constants, expressed in the units $\text{bar dm}^3 \text{ mol}^{-1}$, of benzene, cyclohexane, m-xylene, tetralin, decalin, cumene, and mesitylene, expressed as the reciprocal of temperature are displayed in Figure 3.10a. It is evident that solvents with a higher molecular weight display greater Henry's constants. Coupled with the small r^2 value observed for this plot (0.569), it suggests using Henry's constants expressed in $\text{bar dm}^3 \text{ mol}^{-1}$ is not appropriate for estimating the solubility of hydrogen in the reaction under study in this thesis.

The greater Henry's constants are observed for solvent systems which, because of similar densities, have fewer moles of substance per unit volume. Therefore, it was proposed that a relationship may be established if the volume dependence is removed, that is to consider only the mole fraction of hydrogen present in solution. The Henry's constants, expressed in the

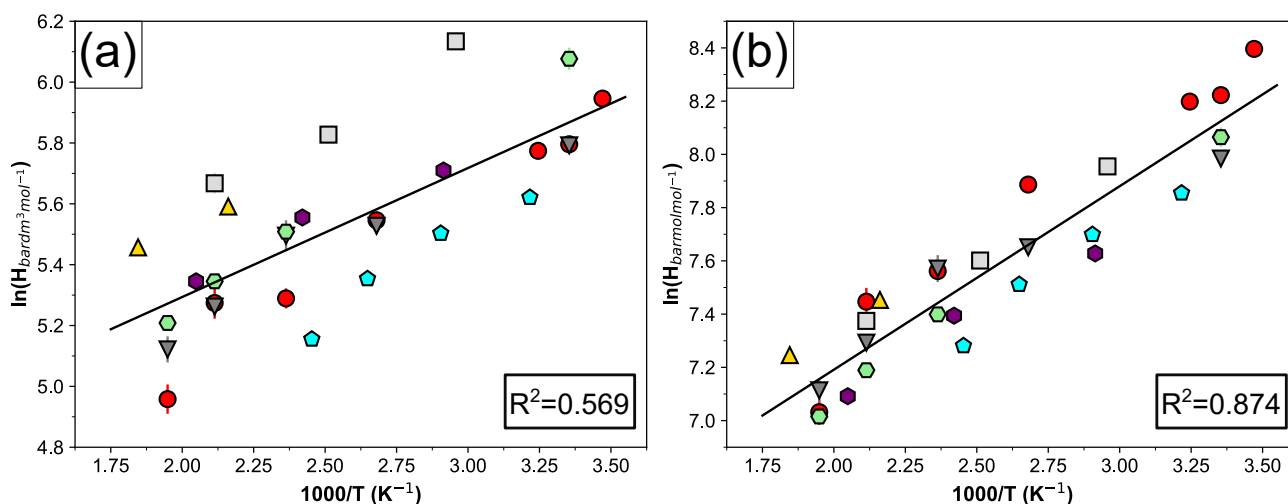


Figure 3.10: Effect of temperature on Henry's constant in units $\text{bar dm}^3 \text{ mol}^{-1}$ (a) and in units bar mol mol^{-1} (b). Legend: Benzene (●), cyclohexane (⬠), m-xylene (▲), tetralin (▼), decalin (◻), cumene (⬢), and mesitylene (⬡)

units bar mol mol^{-1} , for the hydrocarbons outlined above are presented in Figure 3.10b. In this instance a good correlation is observed ($r^2=0.87$), with deviations possibly attributable to errors in the experimental datasets. This means that the Henry's constant (in bar mol mol^{-1}) for monoaromatic or saturated hydrocarbon rings can be calculated by:

$$H_{\text{bar mol mol}^{-1}} = 5.8129 \pm 0.13576 + \frac{689.24 \pm 52.091}{T} \quad (3.12)$$

Once a Henry's constant is calculated using this equation, the mole fraction at the desired temperature can then be calculated using Equation 3.10. The mole fraction using this equation is then converted to a concentration by:

$$C_{H_2} = \frac{\rho x_{H_2}}{M_w x_{\text{GHC}}} \quad (3.13)$$

where ρ is the density at a temperature T (calculable using data outlined in Figure 3.7), x_{H_2} is the mole fraction of hydrogen, M_w is the molecular weight, which in this case was assumed to be 188 g mol^{-1} for GHC, and x_{GHC} is the mole fraction of GHC in solution.

3.4 Conclusions

In this chapter, the starting material, GHC, and a typical reaction product mixture, which contains aromatic, olefinic and saturated products, were characterised using NMR spectroscopy and GC-MS. As no database mass spectra existed for many of these commercially relevant molecules, synthetic spectra were generated using artificial intelligence methods. This allowed the identify of all major peaks in the gas chromatogram of each mixture to be established. Crucially, this analysis suggests that the double bond in the intermediate olefin obtained from E-PMI is not located between the two bridging carbon atoms as in THPMI, but adjacent to it. The implications of this difference are assessed in the following results chapter. Various physical properties were also recorded. The viscosity and density of these mixtures were also recorded and shown to behave similar to structurally similar bicyclic compounds. Finally, a facile method was proposed that allowed the hydrogen solubility to be determined under all experimental conditions. This method was based on an empirical relation where a strong correlation was observed when expressing the Henry's constant in terms of mole fraction solubility for multiple cyclic hydrocarbons instead of considering the usual volume dependence. The simplicity of this method could have applications for which no hydrogen solubility data is available.

3.5 References

- [1] F. Allen, A. Pon, R. Greiner and D. Wishart, *Anal. Chem.*, 2016, **88**, 7689–7697.
- [2] J. N. Wei, D. Belanger, R. P. Adams and D. Sculley, *ACS Cent. Sci.*, 2019, **5**, 700–708.

- [3] D. Belanger, *LICENSE*, <https://github.com/brain-research/deep-molecular-massspec/blob/master/LICENSE>.
- [4] S. E. Stein and D. R. Scott, *J. Am. Soc. Mass Spectrom.*, 1994, **5**, 859–866.
- [5] J. D. Macginley, *PhD Thesis*, Cardiff University, 2021.
- [6] L. H. Slaugh and J. A. Leonard, *J. Catal.*, 1969, **13**, 385–396.
- [7] J. Fahy, D. Trimm and D. Cookson, *Appl. Catal. A Gen.*, 2001, **211**, 259–268.
- [8] J. Qiu, K. Komura, Y. Kubota and Y. Sugi, *Chinese J. Catal.*, 2007, **28**, 246–250.
- [9] S. A. Kishore Kumar, M. John, S. M. Pai, S. Ghosh, B. L. Newalkar and K. K. Pant, *Mol. Catal.*, 2017, **442**, 27–38.
- [10] J. Huang, Z. Li, J. Yang, Z. Peng, Q. Liu and Z. Liu, *Ind. Eng. Chem. Res.*, 2021, **60**, 2326–2336.
- [11] S. Stein, *Anal. Chem.*, 2012, **84**, 7274–7282.
- [12] B. J. Place, *J. Am. Soc. Mass Spectrom.*, 2021, 0–8.
- [13] I. Fleming and D. Williams, *Spectroscopic Methods in Organic Chemistry*, Springer International Publishing, Cambridge, 2019.
- [14] P. Giraudeau, *Magn. Reson. Chem.*, 2014, **52**, 259–272.
- [15] P. Moutzouri, *PhD*, The University of Manchester, 2018.
- [16] V. S. Ranade, G. Consiglio and R. Prins, *J. Org. Chem.*, 1999, 8862–8867.
- [17] V. S. Ranade, G. Consiglio and R. Prins, *J. Org. Chem.*, 2000, **65**, 1132–1138.
- [18] E. Jonas and S. Kuhn, *J. Cheminform.*, 2019, **11**, 50.
- [19] B. E. Poling, J. M. Prausnitz and J. P. O’Connell, *The Properties of Gases and Liquids*, McGraw-Hill, 5th edn., 2000.
- [20] H. S. Elbro, A. Fredenslund and P. Rasmussen, *Ind. Eng. Chem. Res.*, 1991, **30**, 2576–2582.
- [21] E. C. Ihmels and J. Gmehling, *Ind. Eng. Chem. Res.*, 2003, **42**, 408–412.
- [22] G. S. Kell, *J. Chem. Eng. Data*, 1975, **20**, 97–105.
- [23] A. Francis, *Ind. Eng. Chem.*, 1957, **49**, 1779–1786.
- [24] A. W. Francis, *Chem. Eng. Sci.*, 1959, **10**, 37–46.

- [25] D. R. Caudwell, J. P. M. Trusler, V. Vesovic and W. A. Wakeham, *J. Chem. Eng. Data*, 2010, **55**, 5396–5396.
- [26] A. M. Chacón Valero, C. A. Alves, F. X. Feitosa and H. B. de Sant’Ana, *J. Chem. Eng. Data*, 2021, **66**, 1684–1693.
- [27] R. H. Ewell and H. Eyring, *J. Chem. Phys.*, 1937, **5**, 726–736.
- [28] R. B. Bird, W. E. Stewart and W. N. Lightfoot, *Transport Phenomena*, Wiley, 2nd edn., 2002, p. 914.
- [29] C. Krimizis-Tsatsoulis, *J. Chem. Thermodyn.*, 2021, **152**, 106256.
- [30] *CRC Handbook of Chemistry and Physics*, ed. W. M. Haynes, D. R. Lide and T. J. Bruno, CRC Press LLC, 97th edn., 2016.
- [31] M. Barrouhou, C. K. Zebérg-Mikkelsen, A. Baylaucq and C. Boned, *Int. J. Thermophys.*, 2003, **24**, 937–952.
- [32] G. W. Roberts, in *Catalysis in Organic Synthesis*, ed. P. N. Rylander and H. Greenfield, Academic Press, 1976, pp. 1–48.
- [33] B. Fillion and B. I. Morsi, *Ind. Eng. Chem. Res.*, 2000, **39**, 2157–2168.

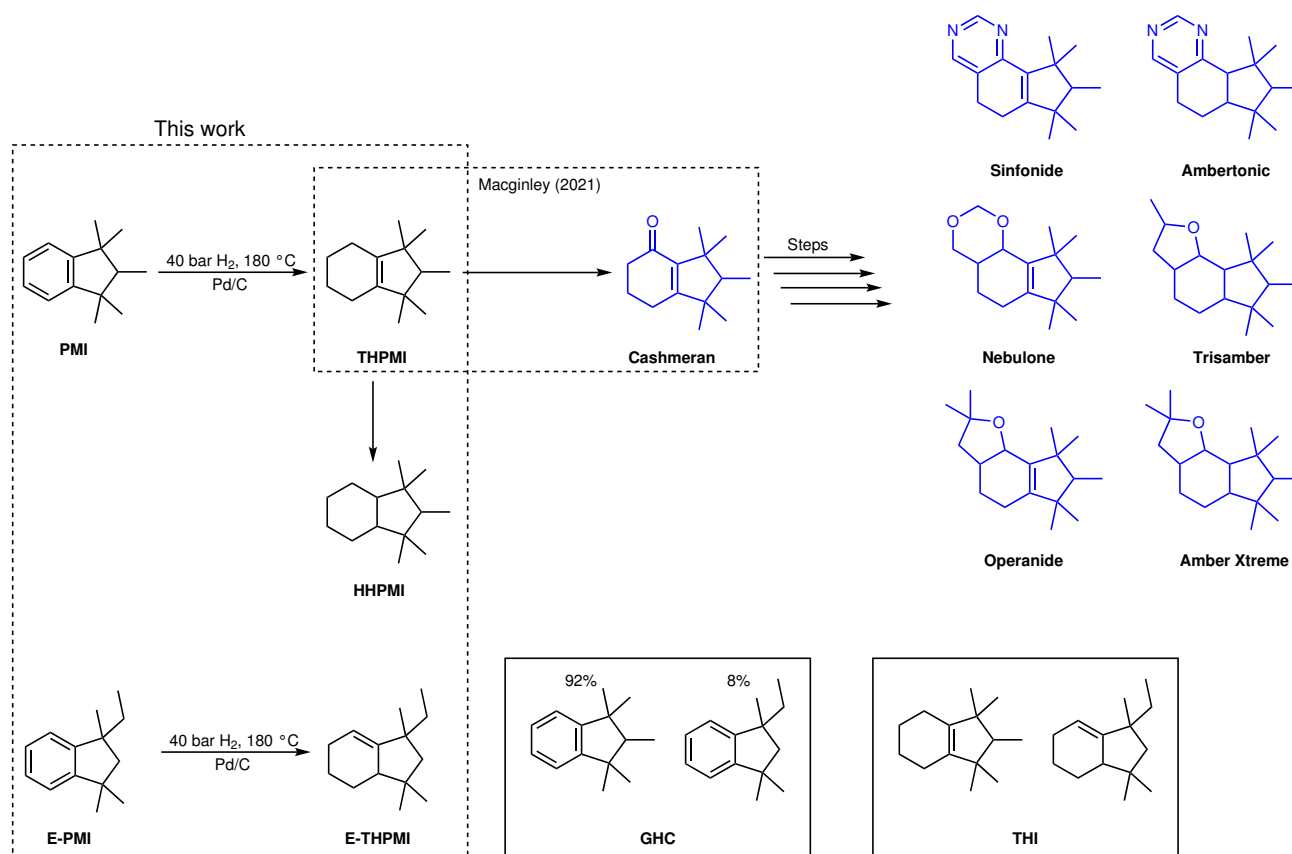
Chapter 4

The effect of some process variables in the partial reduction of galaxolide hydrocarbon to cyclic alkene intermediates

4.1 Introduction

THPMI, and its structural isomer E-THPMI, are important precursors in the synthesis of a family of fragrant molecules (Scheme 4.1). These compounds are currently produced industrially through the semi-batch reduction of GHC using molecular hydrogen over a 5 wt.% Pd/C at 180 °C and 40 bar hydrogen pressure. Under these conditions, a cycloalkene yield of 62 wt.% is achievable, though fluctuations of several wt.% are observed between batches. In recent years, however, the demand for downstream products has soared, resulting in a bottleneck at this stage of the process. Consequently, an improvement in the yield of the monounsaturated intermediates is greatly sought after.

Researchers at IFF have investigated a number of solutions for this issue. Tadepalli *et al.* reported a “circular economy” method for preparing a high yield of cyclic olefins (*ca.* 85%) using a series of plug flow reactors with continuous distillation.¹ However, the fiscal cost of deployment and operation of this technology deemed it commercially inviable. Aside from reactor engineering approaches, palladium-based bimetallic catalysts were investigated for the reduction of PMI diluted in decalin.² The most selective catalyst in this study, 5 wt.% Pd-0.8 wt.% Ag/C where the carbon was calcined prior to deposition, provided a selectivity to THPMI of 81% at 46% conversion. Unfortunately, the maximum yield for this catalyst was not disclosed, so despite demonstrating improved selectivity at a lower conversion, whether this performance resulted in a higher overall yield remains to be seen. Temperature effects have also been reported in the patent literature. Podkolzin *et al.* reported a small increment in



Scheme 4.1: Overview of commercial fragrances obtained from THPMI.

the maximum THPMI yield observed as temperature increased from 180 to 200 °C.² This is in contrast to data shared from industrial operations at the start of the project, which stated that experimental variables (temperature and pressure) have little to no effect on yield.³ It should also be considered that the patent for the current process employs a temperature 50 °C lower than the commercial process and reports roughly the same yield of 63 wt.% tetrahydroindane intermediates,⁴ though in these instances it is unknown whether the same Pd/C catalyst was used.

The lack of clarity regarding how the effects of temperature and hydrogen pressure influence reaction selectivity needs to be better understood, as in many hydrogenation reactions, such as the reduction of benzene to cyclohexene,⁵ alkynes to alkenes,⁶ and alkyl-substituted benzenes to the substituted cycloolefin⁷, these parameters are highly influential. Therefore, a systematic study was conducted to assess whether intermediate yields could be improved upon by modifying these parameters using the industrially used 5 wt.% Pd/C catalyst. Here, it is shown that a relative yield improvement of *ca.* 10% can be gained by utilising lower reaction temperatures and higher hydrogen pressures than what is currently used in the industrial process. This was determined using the design of experiments methodology. The origin of the cyclic alkene yield enhancement could not be attributed to a thermodynamic limitation, which was probed using density-functional (DFT) calculations, nor to mass transfer limitations,

which were shown to be absent under all conditions based on theoretical calculations and high apparent activation energies. Instead, the beneficial effect of temperature and pressure were reasoned to be a consequence of Langmuir-Hinshelwood kinetics. This was evidenced using literature DFT studies on the thermodynamics of adsorption of benzene and its intermediate hydrogenation products on the Pd(111) surface. The findings in this chapter could significantly reduce the amount of by-product generated during the production of a popular speciality chemical.

4.2 Aims

- Characterise the 5 wt.% Pd/C catalyst used during the industrial process by N₂ physisorption, X-ray diffraction, transmission electron microscopy, and CO chemisorption.
- Compare the performance of the laboratory scale reactor with the reactor that is used on the industrial scale.
- Assess whether the yield of cyclic olefins can be improved by altering the temperature and hydrogen pressure used during the reaction. If so, the origin of any beneficial conditions needs to be understood.
- Determine the equilibrium yield of THPMI under all conditions studied.
- Assess whether any reaction condition is limited by mass transfer effects.
- Determine the effect of hydrogen pressure on apparent activation energies.

4.3 Results and discussion

4.3.1 Characterisation of the fresh industrial Pd/C catalyst

The industrial catalyst was supplied with the label “Palladium on Carbon, 5 wt.% loading, nominally 50% water”. This description is “precise but vague”⁸ as it reveals only that palladium is supported on carbon and in paste form. The nominal loading provided is not necessarily equal to an actual loading and therefore any techniques that require such knowledge (e.g. chemisorption) to calculate a specific property will probably be wrong, unless this value is accurately determined. Moreover, the structure and trace impurity composition of carbon supports can vary markedly^{9,10} and how the metal nanoparticles are deposited on the surface affects whether they are on, or in, the support. Not all this information can be obtained through characterisation alone, but fundamental properties of the catalyst can be probed using an assortment of techniques.

4.3.1.1 Inductively coupled plasma mass spectrometry analysis

The elemental composition of the dried catalyst was analysed by inductively coupled plasma mass spectrometry (Table 4.1) after complete microwave digestion in aqua regia. A discrepancy of 20% was found to exist between the nominal and actual weight loadings of palladium. As the age of this catalyst is unknown, it is possible that the freshly prepared catalyst is much closer to this value and the formation of bulk palladium oxide, the thermodynamically stable phase of palladium at room temperature¹¹ and observed by X-ray diffraction (see below), is responsible for the large deviation. These results also indicate that impurities on the carbon are small as only low levels of other elements were detected in the catalyst's composition. It is unknown if these elements are an impurity or were deliberately added for selectivity reasons, but the very low levels suggest the former.

Table 4.1: ICP-MS characterisation of industrial 5 wt.% Pd/C after microwave digestion.

| Element | Composition (wt.%) ^a |
|---------|---------------------------------|
| Pd | 4.1 (4.16±0.26) ^b |
| Ir | 0.31 |
| Na | 0.019 |
| Br | 0.016 |
| Mg | 0.0082 |
| Al | 0.0072 |
| Fe | 0.0042 |

^a Semi-quantitative analysis.
Accuracy ±30%.

^b Quantified using analytical standards.

4.3.1.2 Textural property analysis

The textural properties of the 5 wt.% Pd/C catalyst employed in the industrial process and under investigation in this chapter were studied using N₂ adsorption-desorption measurements at 77 K (Figure 4.1). Unfortunately, it is not possible to compare the textural properties of the blank support with this catalyst owing to the commercial nature of the catalyst. The isotherm is a composite of the Type Ia and Type II isotherms with a H4 hysteresis loop. This means that the material is microporous, and as there is continued uptake until 0.99 P/P_0 , suggests it also possesses some meso- and macroporosity.¹² The pore size distribution obtained using the non-local density functional theory (NLDFT) method^a supports this assertion as it reveals the catalyst is largely comprised of micropores and small mesopores (Figure 4.2).

^aFor a carbon material with slits using nitrogen as a probe molecule as implemented in the Micromeritics 3Flex software

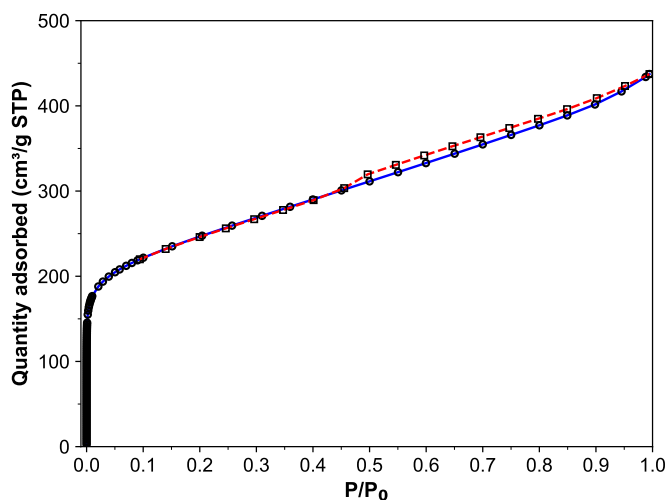


Figure 4.1: N₂ adsorption-desorption isotherm recorded at 77 K of Pd/C catalyst.

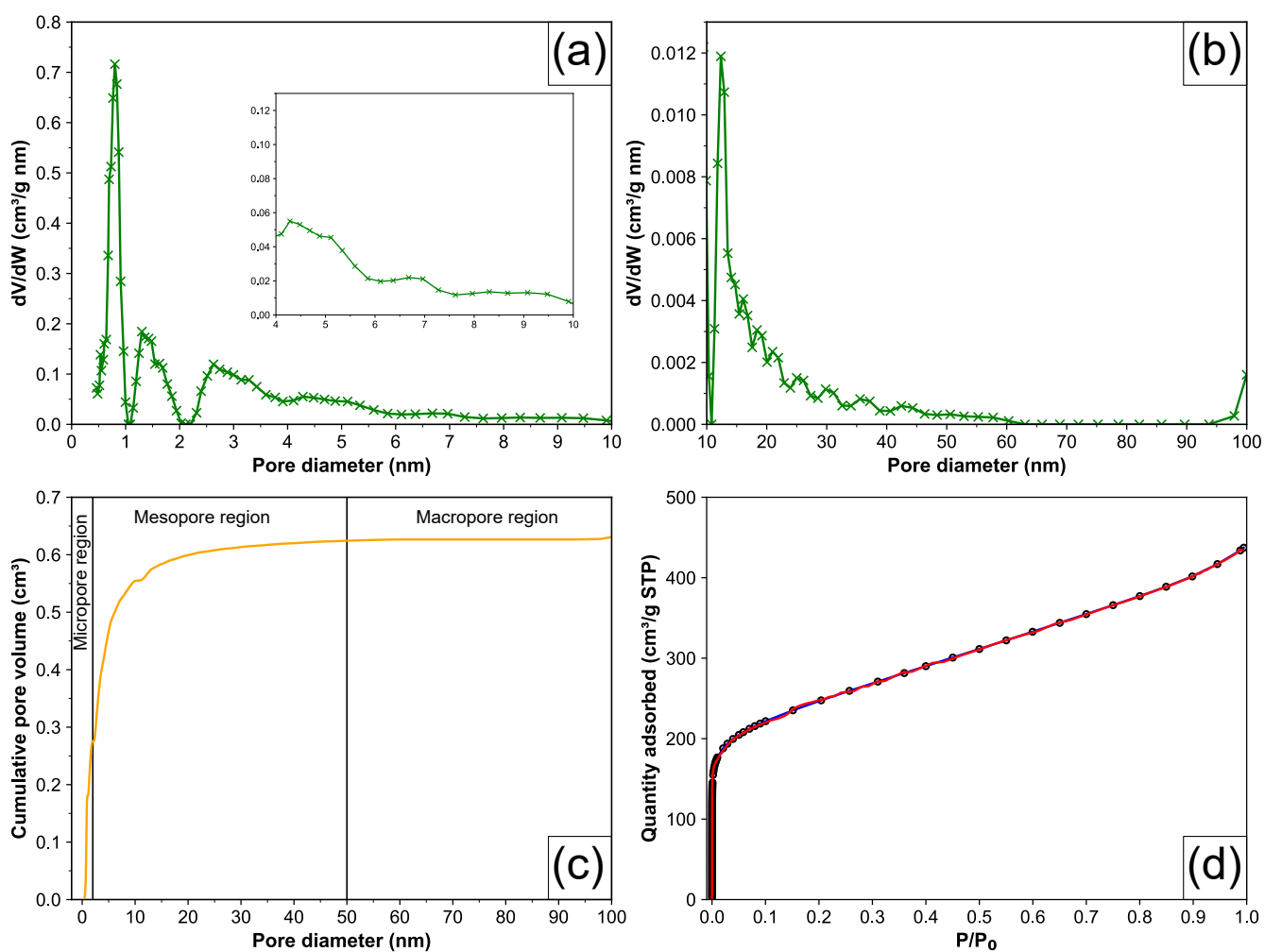


Figure 4.2: (a + b) NL-DFT pore size distributions for the IFF Pd/C catalyst. (c) Cumulative pore volume as a function of pore diameter. (d) NL-DFT model fitting where $\lambda=0.0316$ (—) overlaid on adsorption isotherm.

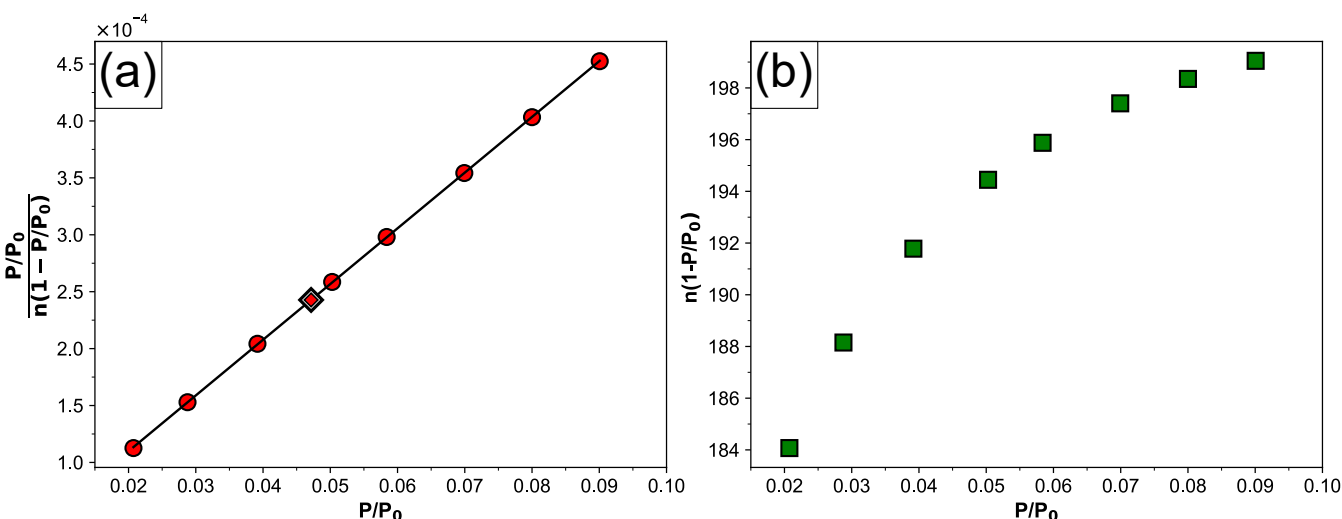


Figure 4.3: (a) BET plot for the industrial Pd/C catalyst. Surface area = 890 m². $C = 410$. (b) Rouquerol plot for the BET region. Legend: BET data point (●), uptake at monolayer volume, calculated by Equation 4.1 (◆), and Rouquerol plot data point (■).

As discussed in Section 2.5.4.1.1, the use of BET theory in the evaluation of the surface areas of microporous materials is problematic as the underlying assumptions in its derivation are no longer valid. Nevertheless, the method proposed by Rouquerol *et al.*¹³ permits a “material fingerprint”, or the “BET strong retention capacity” to be obtained.¹² This procedure has three requirements that allow for the objective evaluation of this value: (i) the C value must be positive, as negative values have no physical meaning. (ii) The BET equation must only be used in the pressure region where $n(1 - P/P_0)$ continuously increases with P/P_0 ; this is a so-called Rouquerol plot. (iii) The calculated monolayer value should be within the selected BET pressure range. Calculation of the P/P_0 value is obtained by setting n equal to n_m and rearranging the BET equation (Equation 2.16) to give:

$$P/P_0^m = 1/(\sqrt{C} + 1) \quad (4.1)$$

where P/P_0^m is the relative pressure at which the calculated monolayer capacity is formed.

These stipulations were met when using P/P_0 values between 0.0207307 and 0.0900671 and the resulting BET plot and Rouquerol plot are displayed in Figure 4.3. The apparent surface area of the material was calculated as 890 m² g⁻¹, with a C constant of 410. Again, the physical meaning of this value is not to be overinterpreted and is representative of the strong retention capacity, a value consisting of a contribution from the statistical monolayer on the non-microporous surface and the adsorbate that has filled the micropores.¹³

4.3.1.3 Particle size analysis

To gain information about the palladium particle size, the industrial catalyst was analysed by transmission electron microscopy (TEM), CO chemisorption, and X-ray diffraction (XRD).

Typical electron micrographs are displayed in Figure 4.4a–d and the associated particle size distribution is presented in Figure 4.4e. These data show that the palladium nanoparticles are mostly uniform in size, with a number average diameter of 2.6 nm and standard deviation of 0.9 nm based on a count of 119 particles. Analysis of the particle size distribution reveals a moderately skewed distribution towards larger particles. It should be noted that these images also contain several larger agglomerates, which do not have well-defined edges (Figure 4.4) due to varying contrast. As such, they were excluded from the count as differentiation between particles was not possible. Nevertheless, the particle size estimates from CO chemisorption and use of the Scherrer equation on the diffraction profile of several peaks are in close agreement to the calculated surface-weighted and volume-weighted particle sizes from the microscopy data (Table 4.2). As these methods both measure a much larger sample size than microscopy methods and are more heavily weighted towards larger diameter particles, it suggests that the particle size statistics presented in Figure 4.4 are representative in spite of the small particle count size.

Table 4.2: Number-average, surface-weighted, and volume-weighted particle sizes as determined by TEM, CO chemisorption, and XRD.

| Technique | Particle size (nm) | | | Dispersion (%) |
|------------------|--------------------|-----------|----------------|----------------|
| | d_n^a | d_s^b | d_v^c | |
| TEM | 2.6 ± 0.9 | 3.3 ± 1 | 3.6 ± 2 | 34 ± 1 |
| CO Chemisorption | – | 3.3 ± 0.2 | – | 34 ± 2 |
| XRD | – | – | 4 ^d | – |

^a Number average $d_n = \frac{\sum n_i d_i}{\sum n_i}$

^b Surface-weighted $d_s = \frac{\sum n_i d_i^3}{\sum n_i d_i^2}$

^c Volume-weighted $d_v = \frac{\sum n_i d_i^4}{\sum n_i d_i^3}$

^d Error of Scherrer analysis not possible as other reflections cannot be reliably fitted.

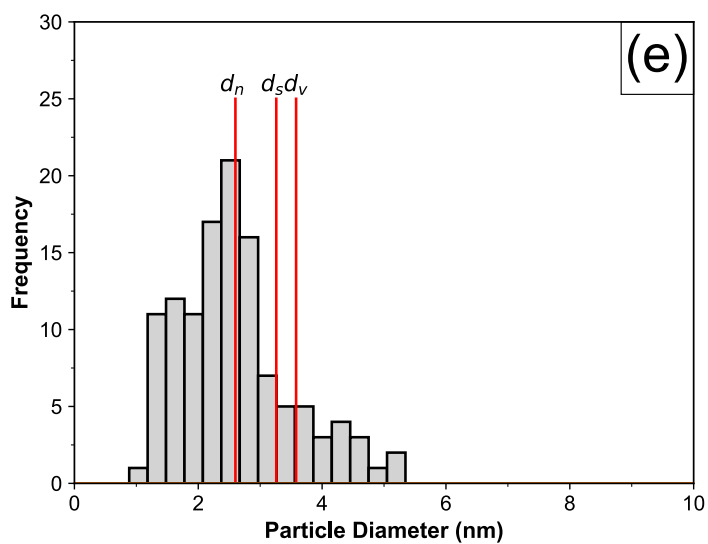
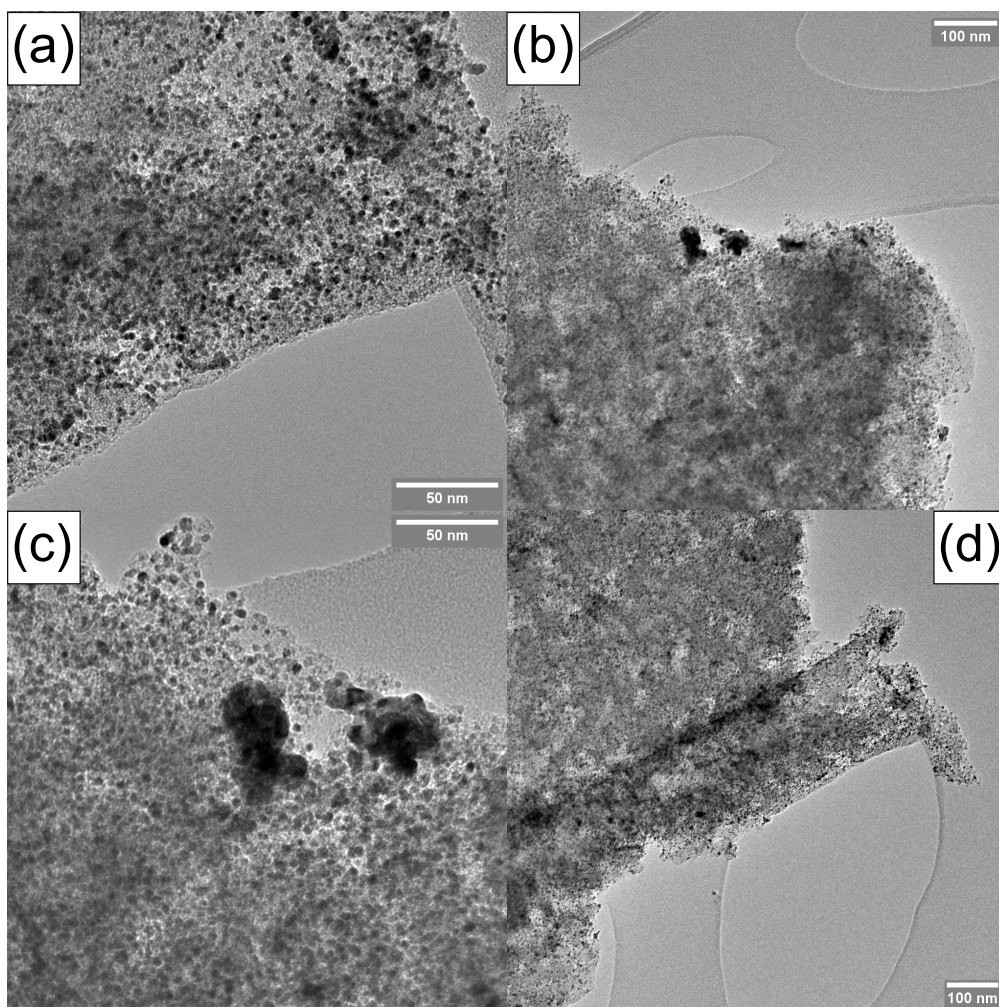


Figure 4.4: Particle size distribution of industrial 5 wt.% Pd/C catalyst. Histogram generated by counting 119 particles. Key: $d_n = \frac{\sum n_i d_i}{\sum n_i}$ (number average); $d_s = \frac{\sum n_i d_i^3}{\sum n_i d_i^2}$ (surface-weighted average); and $d_v = \frac{\sum n_i d_i^4}{\sum n_i d_i^3}$ (volume-weighted average).

4.3.1.4 X-Ray Diffraction

The bulk structure of the fresh catalyst was also evaluated by XRD. A broad peak centred at approximately $20^\circ 2\theta$ can be attributed to the C(002) plane on the carbon support. This peak indicates that the structural ordering of the carbon support is in between that of amorphous carbon and graphite and is usually referred to as turbostratic carbon.¹⁴ The downwards shift and broadening of this peak indicates increased lattice spacing caused by the rotation or translation of graphite layers with an insufficient cancellation effect.¹⁴ Several additional peaks arising from this material are present at 44 and $78^\circ 2\theta$, but cannot be readily separated from scattering contributions from palladium species present in the material. These diffraction peaks indicate that palladium is present in both metallic and oxide form. Scherrer analysis of the PdO(101) peak at $34^\circ 2\theta$ estimates a volume-average particle size of approximately 4 nm.

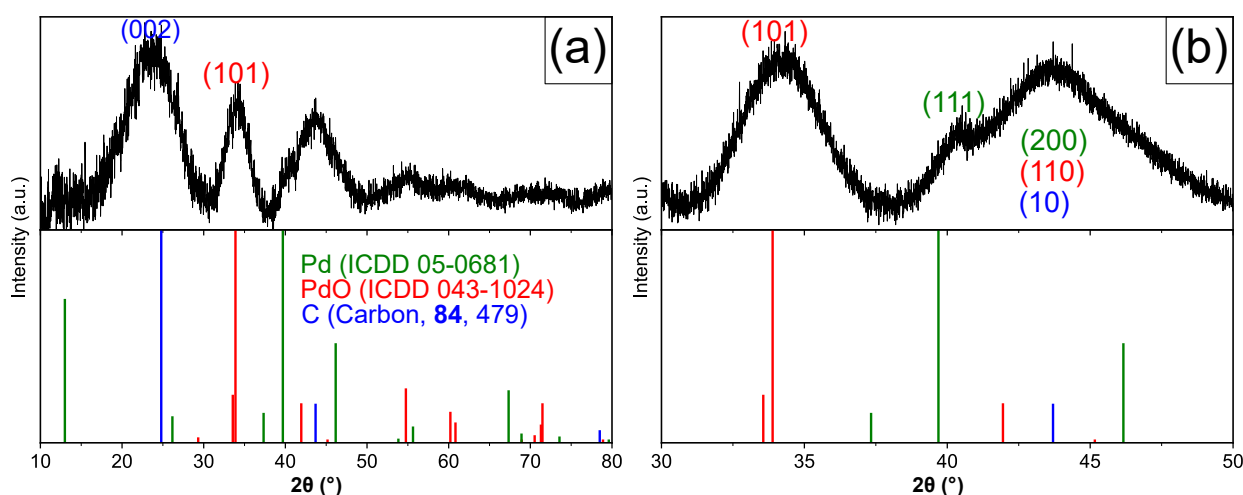


Figure 4.5: XRD pattern of IFF's Pd/C carbon catalyst. (a) Wide scan. (b) Narrow slow scan.

4.3.2 Process alignment

A reaction was performed under industrial conditions ($P_{H_2}=40$ bar, $T=180^\circ\text{C}$) to align the performance of the industrial catalyst in the 50 mL benchtop autoclave used in this work with the commercial scale batch reactor (Figure 4.6). The composition of PMI decreases linearly as a function of time until high degrees of conversion where it deviates. This suggests that the reaction rate is almost independent of its concentration over a wide concentration range and can be described as a zeroth order dependence. In contrast, E-PMI consumption appears to accelerate as a function of time. Previous studies have reported similar concentration dependence for both observations, however, these studies usually only report the kinetics of one aromatic compound at a time. Zero order behaviour for aromatic compounds is observed over many group 8–10 metals (see references [15–21] for examples), except iron which displays a negative reaction order for benzene.^{22,23} The former is attributed to a strong

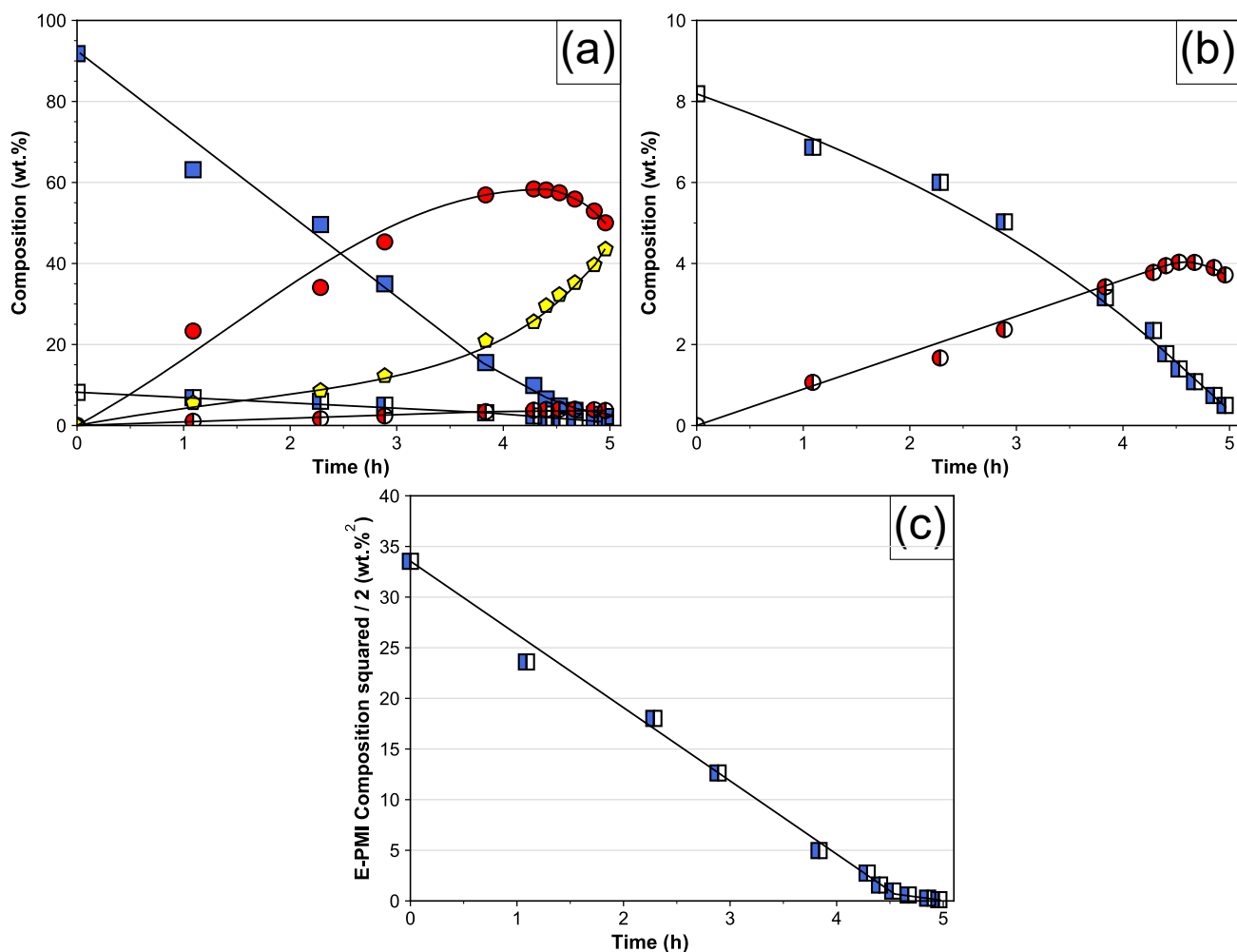


Figure 4.6: (a) Typical composition time profile for the reduction of GHC. (b) Magnified time profile for the reduction of E-PMI. (c) Negative first order kinetic plot for E-PMI composition. *Conditions:* 180 °C, 40 bar hydrogen pressure, 16 g GHC (solventless), 0.13 g 5 wt.% Pd/C. *Legend:* PMI (■), E-PMI (▣), THPMI (●), E-THPMI (◐), saturated products (◑). Lines serve as a guide only.

adsorption of the aromatic compound but does not give any insight into whether this is competitive or non-competitive, whereas the latter strongly infers surface competition.

It is improbable that E-PMI poisons the surface and only affects the adsorption of hydrogen and not PMI also. A more plausible hypothesis is that the surface equilibrium constant for PMI is greater than for E-PMI. Unfortunately, no successful kinetic modelling was performed in these studies, so absolute values of these constants can not be evaluated. However, Rader and Smith proposed a simple method to calculate the relative surface equilibrium constants of a competitive hydrogenation reaction.²⁴ If it is assumed that both reactions adsorb in a Langmuirian manner and follow the same reaction mechanism with the surface concentration of the intermediates ignored, the rate of hydrogenation of PMI is given by:

$$\frac{dC_{\text{PMI}}}{dt} = \text{rate} = \frac{k_{\text{PMI}} K'_{\text{PMI}} C_{\text{PMI}}}{(1 + K_{\text{PMI}} C_{\text{PMI}} + K_{\text{EPMI}} C_{\text{EPMI}})} f(\text{H}_2) \quad (4.2)$$

and the rate of hydrogenation of E-PMI can be calculated by:

$$\frac{dC_{\text{EPMI}}}{dt} = \text{rate} = \frac{k_{\text{EPMI}} K'_{\text{EPMI}} C_{\text{EPMI}}}{(1 + K_{\text{PMI}} C_{\text{PMI}} + K_{\text{EPMI}} C_{\text{EPMI}})} f(\text{H}_2) \quad (4.3)$$

where the subscript denotes the molecule being referred to, and k , K , C are the rate constant, surface equilibrium constant, and concentration, respectively. The K'_x and $f(\text{H}_2)$ terms are included for two reasons. The former term is used to not explicitly state a mechanism; in other words, the rate determining step is the same for each aromatic compound but not necessarily the chemisorbed aromatic species as use of K_{PMI} would indicate. Thus, this term is used and may instead represent a lumped quasi-equilibrated term for the surface equilibrium constants prior to the rate determining step (if present). The latter term is used to show the each reaction is equally dependent on hydrogen pressure and does not state the form of reactive hydrogen and whether its adsorption is competitive or non-competitive.

Dividing Equation 4.2 by Equation 4.3 and rearranging yields:

$$\frac{dC_{\text{PMI}}}{dC_{\text{EPMI}}} = \frac{K'_{\text{PMI}} k_{\text{PMI}} C_{\text{PMI}}}{K'_{\text{EPMI}} k_{\text{EPMI}} C_{\text{EPMI}}} \quad (4.4)$$

Grouping of terms and integrating between the limits of initial concentration, C^0 , and concentration at time t :

$$\int_{C_{\text{PMI}}^0}^{C_{\text{PMI}}^t} \frac{dC_{\text{PMI}}}{C_{\text{PMI}}} = \frac{K'_{\text{PMI}} k_{\text{PMI}}}{K'_{\text{EPMI}} k_{\text{EPMI}}} \int_{C_{\text{EPMI}}^0}^{C_{\text{EPMI}}^t} \frac{dC_{\text{EPMI}}}{C_{\text{EPMI}}} \quad (4.5)$$

gives:

$$\ln C_{\text{PMI}} = \frac{K'_{\text{PMI}} k_{\text{PMI}}}{K'_{\text{EPMI}} k_{\text{EPMI}}} \ln C_{\text{EPMI}} + \left(\ln C_{\text{PMI}}^0 - \frac{K'_{\text{PMI}} k_{\text{PMI}}}{K'_{\text{EPMI}} k_{\text{EPMI}}} \ln C_{\text{EPMI}}^0 \right) \quad (4.6)$$

after rearrangement. Consequently, a plot of $\ln C_{\text{PMI}}$ versus $\ln C_{\text{EPMI}}$ is of the form $y = mx + c$ and the gradient of the line is equal to $K'_{\text{PMI}} k_{\text{PMI}} / K'_{\text{EPMI}} k_{\text{EPMI}}$.

In the original publication the authors propose that by measuring the rate of reduction of the two components separately, the rate constants can become known.²⁴ However, pure components were not available in this work and the rate constants could not be assessed.²⁴ Nevertheless, the negative order behaviour displayed by E-PMI dictates that K_{PMI} must be greater than K_{EPMI} as k_{PMI} being higher than k_{EPMI} cannot account for the observed behaviour alone. If it is assumed that the rate constants are equal, this analysis indicates that the adsorption of PMI is several kJ mol^{-1} more favourable E-PMI. This agrees with what is expected intuitively, owing to the greater length of the hydrocarbon chain in E-PMI; whether this is of enthalpic or entropic origin is discussed in Section 4.3.3.3.

It should be noted that the log-log plot in Figure 4.7 appears to show a small deviation from linearity at lower concentrations of the aromatic compound. This effect could be noise in the experimental data but is observed consistently in repeat experiments. It is possible that at higher degrees of conversion, the competitive adsorption of the intermediate alkenes nullifies the assumptions made in the derivation of Equation 4.6. If only low conversion data

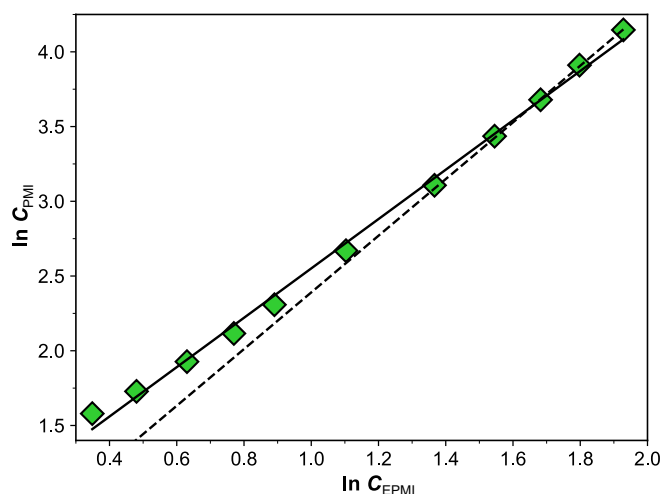


Figure 4.7: Plot of the natural logarithm of PMI concentration *versus* the natural logarithm of E-PMI concentration. All data points included linear regression (—), and only first four points considered (---).

is used, the m term increases to 1.87 ± 0.03 over multiple experiments which indicates the adsorption of PMI may be more preferable than the above analysis indicates.

The concentration of the cyclic alkenes increases with conversion of PMI and E-PMI before passing through a maximum after approximately 4.3 and 4.6 hours for THPMI and E-THPMI, respectively. The tetrahydroindane (THI) yield, which is the sum of the content of THPMI and E-THPMI and is of commercial importance, is equal to 62.1 wt.%. This value is in good agreement with the 62–65 wt.% achievable on a commercial scale and indicates good alignment between the laboratory reaction and industrial process. In addition, reaching the plateau also coincides with rapid increase in the concentration of the saturated products as the rate of hydrogenation of the intermediate becomes the dominant reaction.

Since the concentration of reactive intermediates in sequential reactions is dependent on the conversion of the starting material, it is often more useful to plot the yield of unstable intermediate against conversion.²⁵ Plots of intermediate selectivity *versus* conversion are also beneficial as they provide insight into the reaction mechanism. Examples of these plots are shown in Figure 4.8. The yield conversion plot (Figure 4.8a) reveals that the yield of the cycloalkene intermediate obtained from E-PMI is lower than what is obtained from PMI at an earlier level of conversion. This suggests that an improvement in process yield may be possible if the synthesis of GHC, as discussed in Section 1.2.2, is optimised to selectively produce more PMI.

In the early stages of the reduction of each aromatic substrate the selectivity is almost equal; inasmuch that if this is assumed to extend linearly to differential levels of conversion, the initial selectivity to the corresponding tetrahydroindane is marginally higher than 80%. For THPMI this selectivity appears to be roughly constant until >60% conversion of PMI. On the other hand, selectivity to E-THPMI decreases at a constant rate up to an E-PMI

conversion of 80%. In a sequential reaction, the initial selectivity is taken as an indicator of the specific properties of the catalyst and is termed the “*mechanistic*” selectivity.²⁶ These results indicate that the small change in substrate structure and resulting product does not impact the mechanistic selectivity. This is perhaps expected since the electronic effect of the substituents is probably similar, and in each case should provide enough bulk to facilitate the desorption of the cycloalkene intermediate *if* it forms. Moreover, this indicates that around 80% of the substrate hydrogenated proceeds *via* a pathway that produces a cycloolefin, which is in good agreement with the 90% calculated for the simulated reduction of benzene over the Pd(111) surface.²⁷ Whether this indicates that the 10% difference is attributable to a different reduction pathway that does not form THPMI or E-THPMI, or other surface planes being less selective is not clear with this data alone.

How the selectivity proceeds as a function of conversion potentially provides insight into the relative adsorption strength of the reactants if a procedure similar to that used in the competitive hydrogenation reactions is employed. If the rate constants are ignored for one moment, the relative surface coverage of two components is equal to:²⁶

$$\frac{\theta_A}{\theta_B} = \frac{C_A}{C_B} \exp\left(\frac{\delta\Delta G_a}{RT}\right) \quad (4.7)$$

where θ_x , C_x , $\delta\Delta G_a$, R , and T are the surface coverages, concentrations, differences in the free energies of adsorption, gas constant, and temperature, respectively of components A and B . This is termed a “*thermodynamic*” factor in selectivity. Thus, if the initial selectivity is observed to decrease rapidly, it may signify that the intermediate adsorbs more strongly on the surface. As discussed above, the introduction of an ethyl group in the α position to the aromatic ring disfavours its interaction with the surface. The double bond in E-THPMI being adjacent to the bridging carbons (Scheme 4.1) conveys that one carbon atom is without substitution. A consequence could be that this compound adsorbs on the surface preferably and is therefore easily hydrogenated.

If the rate constant is now examined, modelling data for *o*-xylene hydrogenation (and its intermediates) indicates that hydrogen addition occurs more readily at secondary, rather than tertiary carbons.²⁸ Thence, a kinetic factor may also be present in addition to a thermodynamic factor.

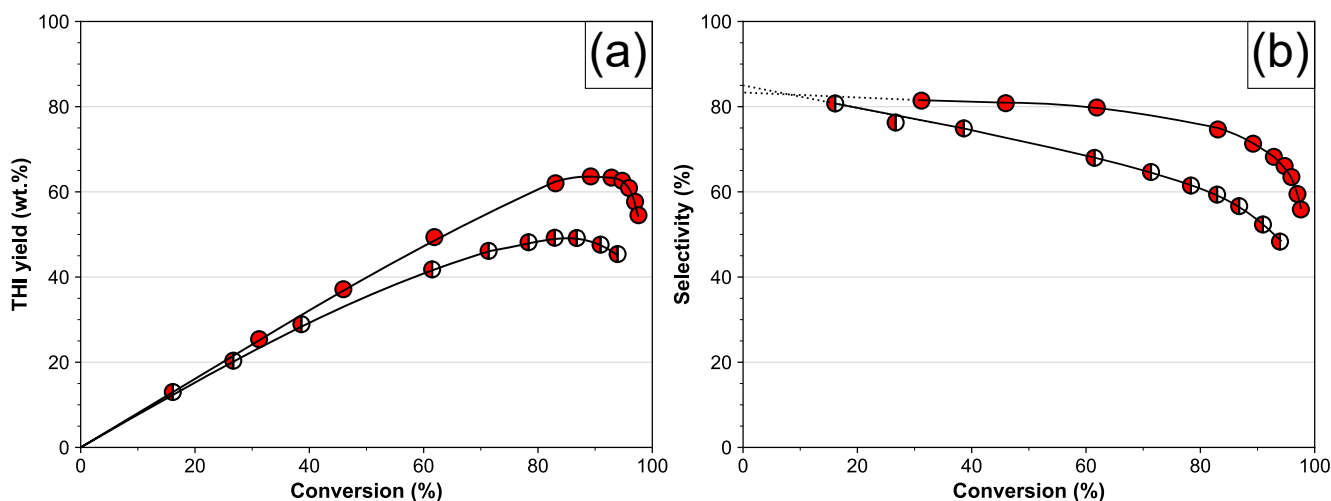


Figure 4.8: (a) Plot of tetrahydroindane yield *versus* PMI or E-PMI conversion. (b) Plot of tetrahydroindane selectivity *versus* PMI or E-PMI conversion. *Conditions:* 180 °C, 40 bar hydrogen pressure, 16 g GHC (solvent-less), 0.13 g 5 wt.% Pd/C. *Graph legend:* THPMI (●), E-THPMI (◐) Lines serve as a guide only. Dotted lines are linearly extrapolated using data to y intercept.

4.3.3 Effect of temperature and pressure

The effect of pressure was initially studied in the region of 20–60 bar hydrogen pressure at the current industrial temperature of 180 °C with the selectivity to tetrahydroindanes *versus* conversion and yield of tetrahydroindanes *versus* conversion plots of these experiments displayed in Figure 4.9. It is evident that the hydrogen pressure does affect the yield of THPMI and E-THPMI, with the maximum yield observed to increase with rising pressure until 40 bar after which its effect is less significant. The initial selectivity to THPMI and E-THPMI appear to be independent of pressure. Interestingly, the selectivity to E-THPMI at a low conversion at a hydrogen pressure of 20 bar and 180 °C is 98%.

Figure 4.10 shows the tetrahydroindane selectivity/yield *versus* conversion plots for reactions performed at 150–210 °C and 40 bar hydrogen pressure. In this instance, lower temperatures were found to be beneficial for THPMI yield with no limiting yield as a function of temperature observed in this region; once again, the initial selectivity was unchanged at all temperatures studied. This is significant as it suggests the current industrial reactors, which have a pressure limit of 40 bar, do not need to be upgraded (and thus does not require any capital expenditure) to gain an improvement in the desired product yield. However, it does contrast with the data reported in the patent by Podkolzin *et al.*, which stated that higher temperatures were beneficial.²

Since these experiments have demonstrated that by altering the temperature and hydrogen pressure of the reaction higher yields of the desired intermediates can be obtained, it indicates that the current process can be improved by “simply” altering a process variable. Further improvements in yield may be possible, but screening the effects of each variable under all

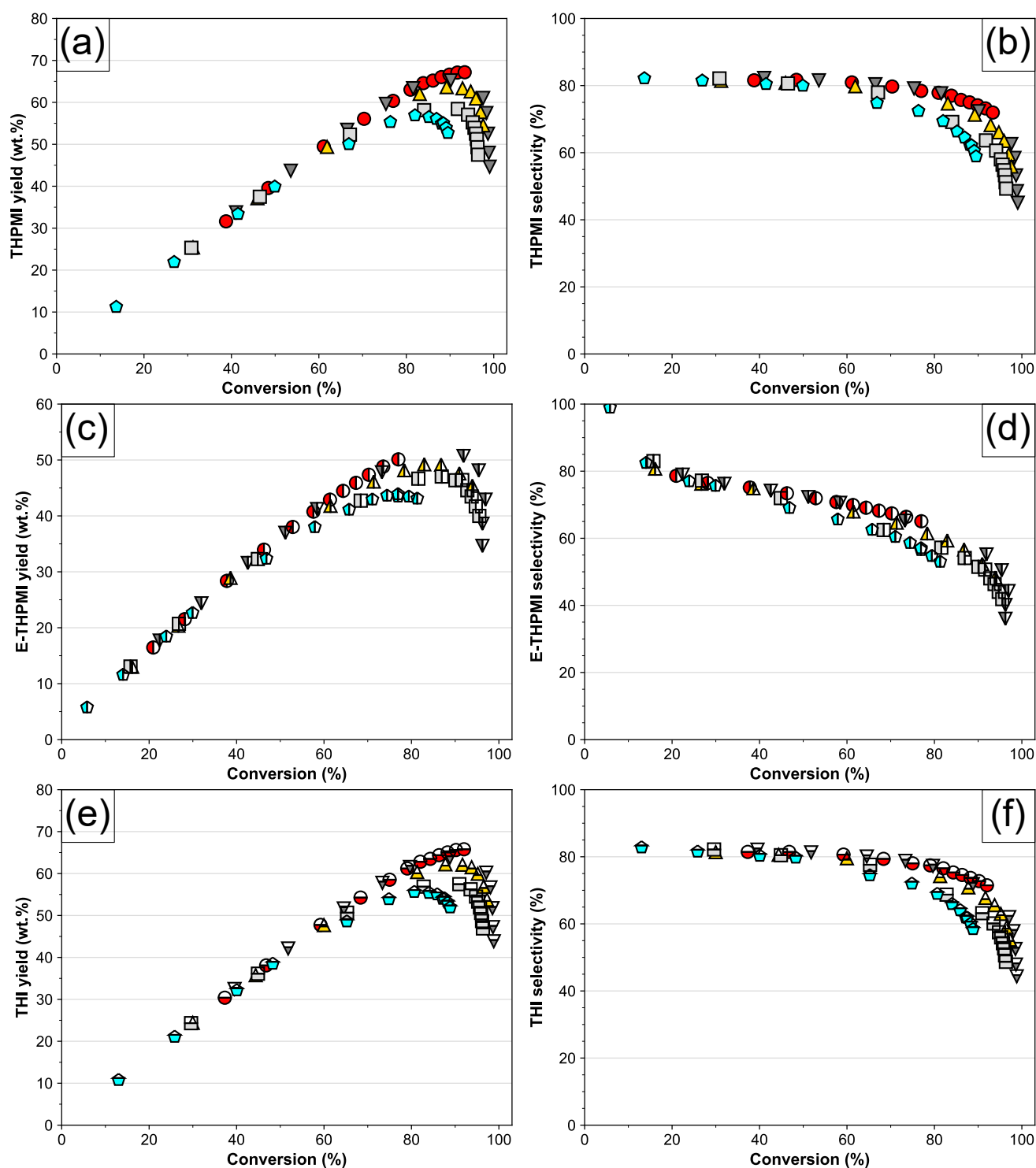


Figure 4.9: The effect of pressure on the yield of THPMI (a), E-THPMI (c), and THI (f). The effect of pressure on the selectivity to THPMI (b), E-THPMI (d), and THI (f). Legend: 20 bar (◐), 30 bar (◑), 40 bar (◒), 50 bar (◓), and 60 bar (●). Filled shapes represent THPMI (a + b), left-filled shapes represent E-THPMI (c + d), and bottom-filled shapes represent THI (e + f).

conditions is a laborious task. The design of experiments methodology is a solution to this issue. This procedure optimises the response of variables by using experimental designs

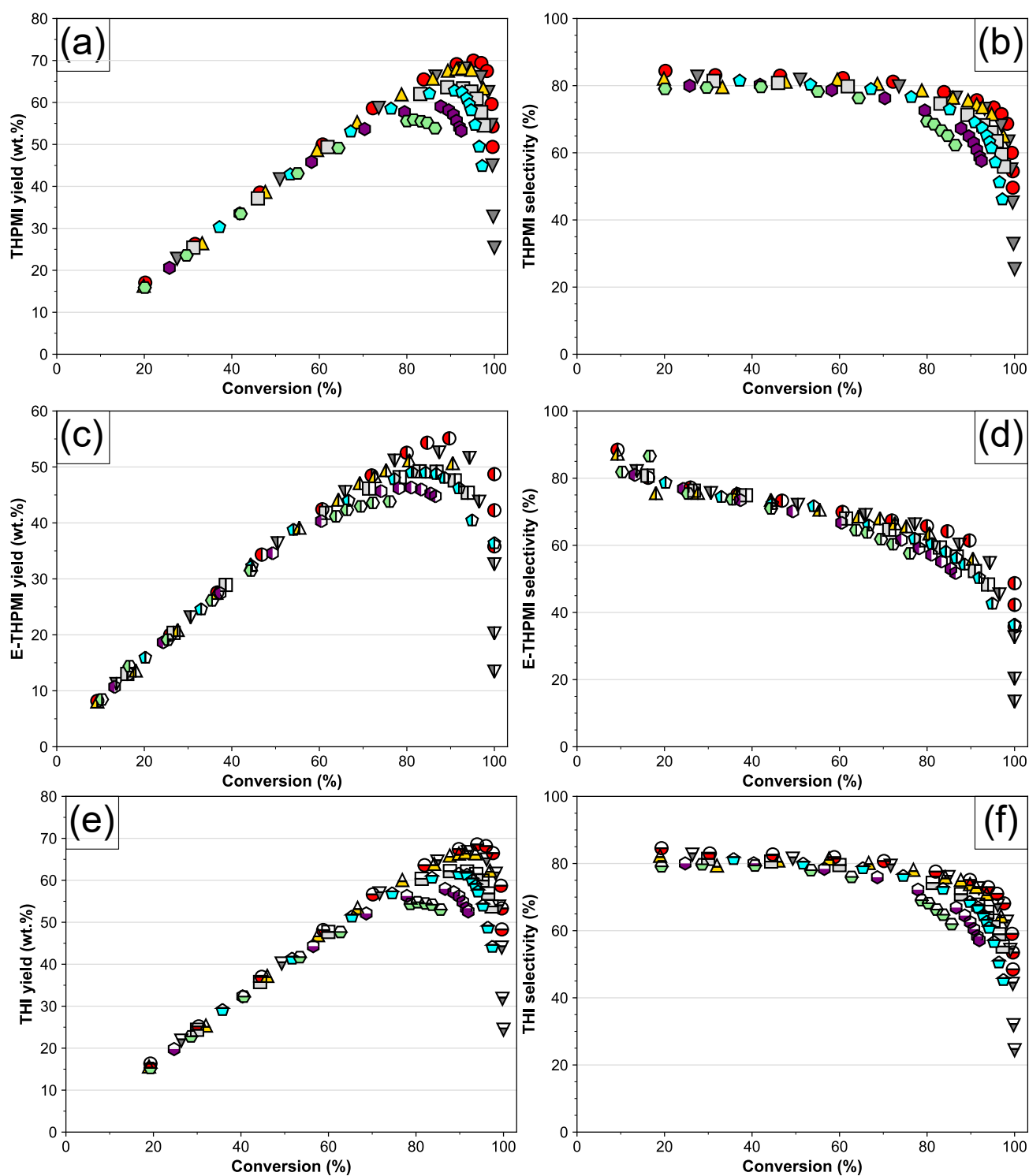


Figure 4.10: The effect of temperature on the yield of THPMI (a), E-THPMI (c), and THI (f). The effect of temperature on the selectivity of THPMI (b), E-THPMI (d), and THI (f). *Legend:* 150 °C (●), 160 °C(▲), 170 °C (▼), 180 °C (□), 190 °C (◐), 200 °C (◑), and 210 °C (◒). Filled shapes represent THPMI (a + b), left-filled shapes represent E-THPMI (c + d), and bottom-filled shapes represent THI (e + f).

that alleviate the need to perform experiments under every set of conditions using a tailored list of experiments in a randomised order. After the experiments are performed, the data

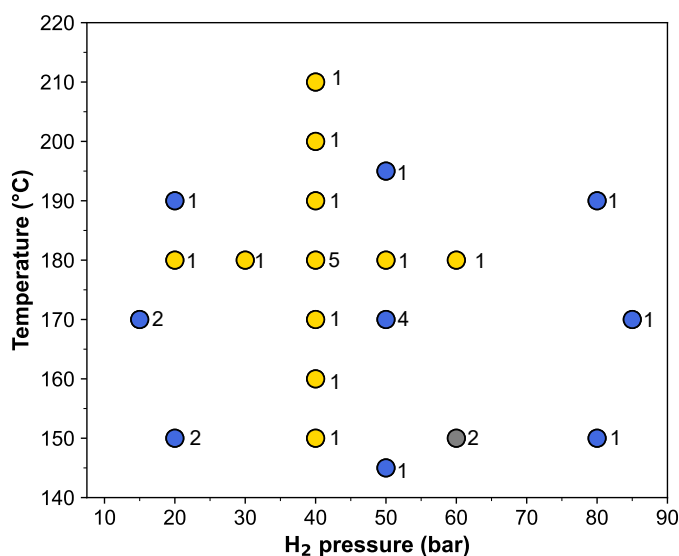


Figure 4.11: Experimental conditions used to generate contour plot. *Legend:* Initial study data (●), central-composite design point (●), and additional data point (●). Number denotes number of time an experiment was repeated.

is fitted to a quadratic model (Equation 4.8) which is used to generate a response surface for the entire experimental region. For the purpose of this work, a central composite design (Figure 4.11) was utilised over alternatives, such as Box–Behnken design, as this experimental design allows for more useful kinetic data to be extracted. The number written next to the circles denote the number of times an experiment has been repeated, some of which exceed the number recommended in the methodology.

$$Y = \beta + aT + bP + cT^2 + dP^2 + eTP \quad (4.8)$$

where Y is yield, β , a , b , c , d , and e are fitting parameters, and P and T are the pressure and temperature, respectively.

After the experiments were performed, the significance of each term in Equation 4.8 was analysed using ANOVA. Each term was found to be significant ($0.05 > P$) and was therefore used in the data fitting procedure. The contour plots are displayed in Figures 4.12–4.14, along with the corresponding parity plots and regression analyses. Summary plots of the data points that make up these figures are shown in Figures 4.15 and 4.16.

The contour plots generally concur with the initial data: higher pressures and lower temperatures favour improved yields of the desired olefinic intermediate. However, the contour plots also suggest some new information, namely, that the yield of the reactive intermediates is more sensitive to pressure changes at higher temperatures than at lower temperatures, and that they go through a maximum as a function of pressure. A similar surface response was observed by Spod *et al.*²⁹ in the partial hydrogenation of benzene, but the model was not verified in this instance, nor an explanation forwarded.

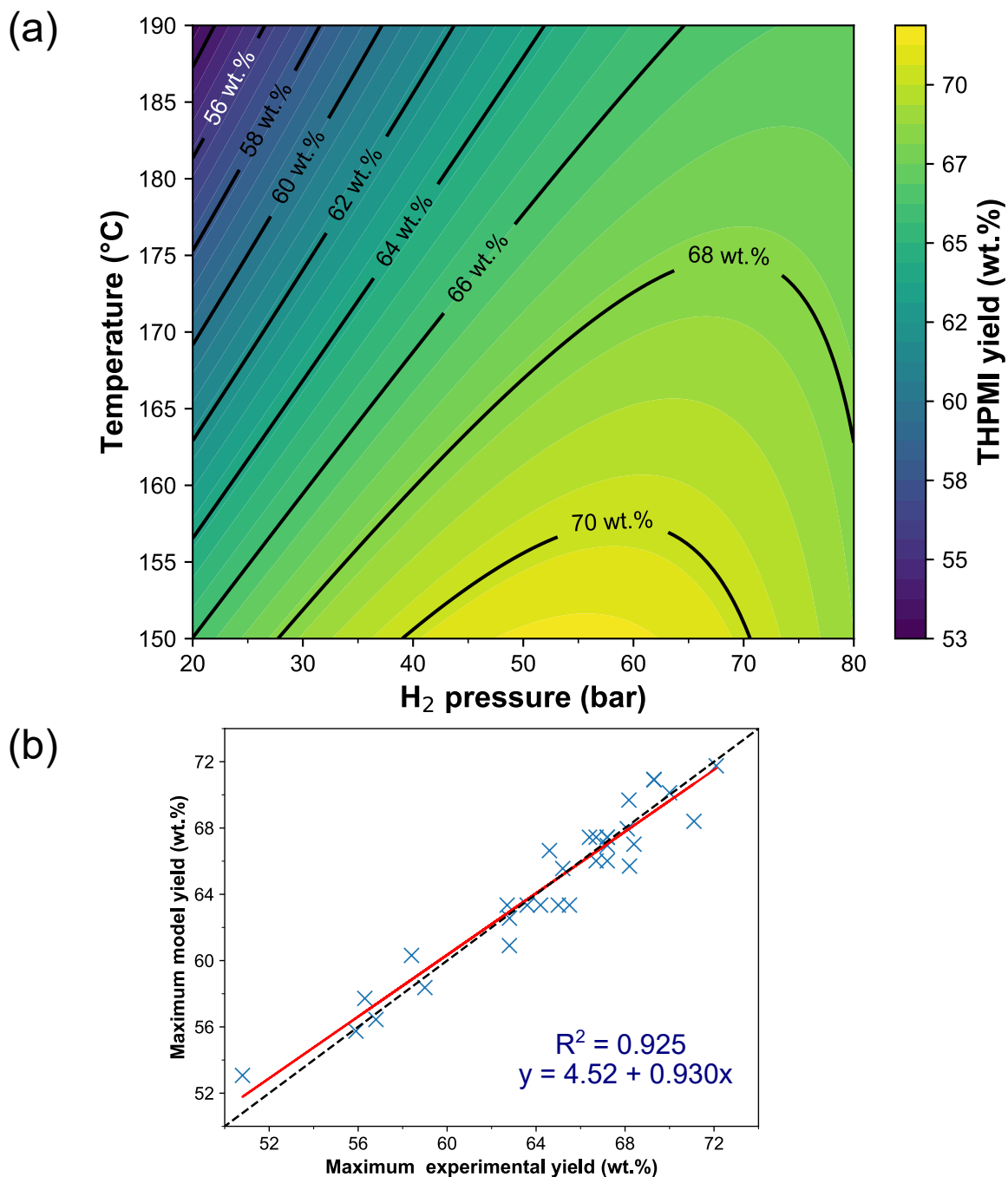


Figure 4.12: (a) Contour map of the maximum observed THPMI yield as a function of temperature and pressure. (b) Parity plot for model predicted yields and experimentally observed yields with regression analysis.

In an attempt to verify the model, several experiments in the predicted maximum region at 150 °C were performed but they did not result in improved yields of tetrahydroindanes. Moreover, work performed by our collaborators at IFF found that yield was independent of

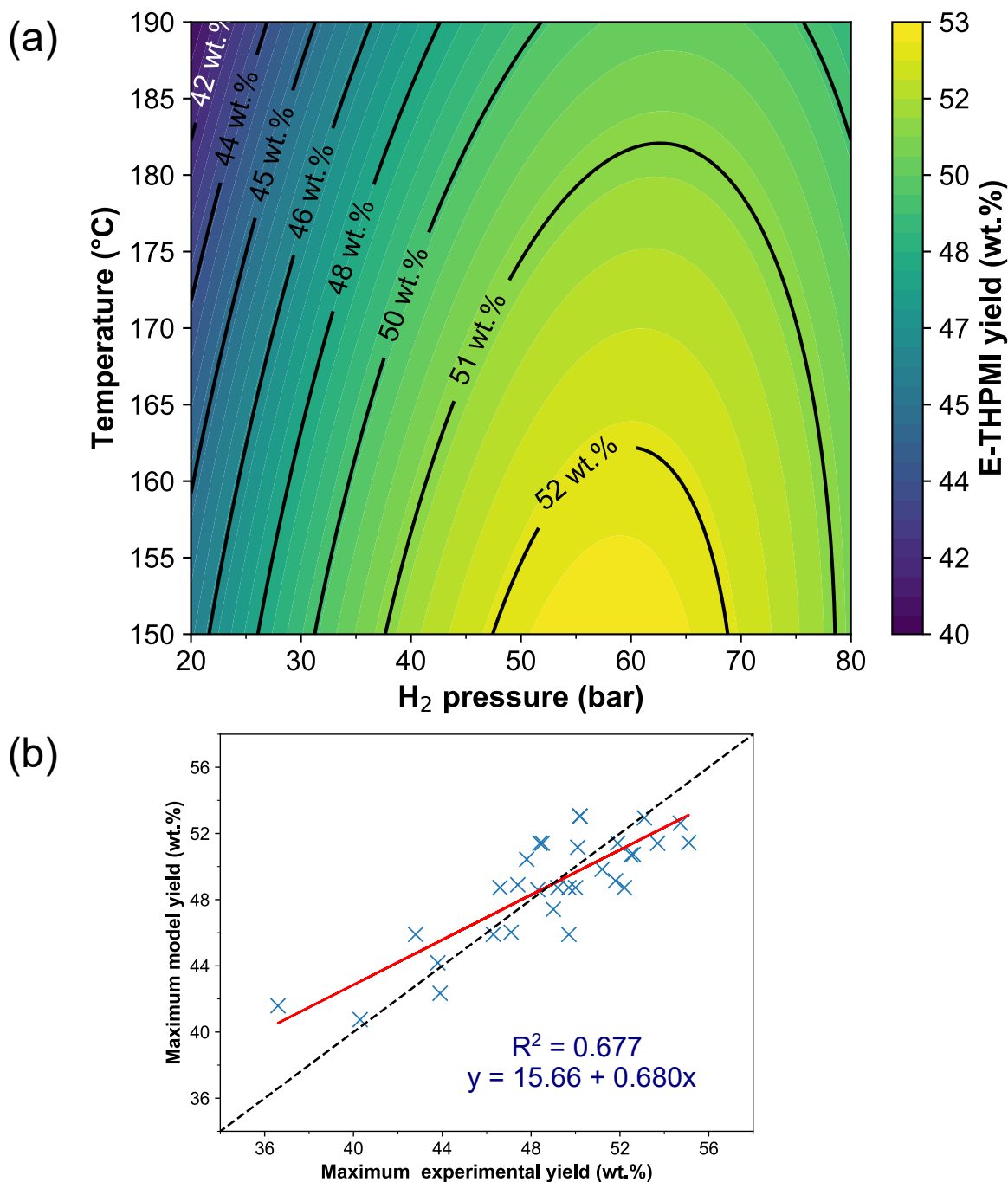


Figure 4.13: (a) Contour map of the maximum observed E-THPMI yield as a function of temperature and pressure. (b) Parity plot for model predicted yields and experimentally observed yields with regression analysis.

hydrogen pressure between 45 and 138 bar.³⁰ This indicates that although describing most experimental data well, a better model for the data may be available. However, the apparent failings of the quadratic model in this case may not be due to the model but the inputted data. For example, the data used in the modelling process assumes that the inputted yield was the maximum intermediate yield but this is not strictly true as the maximum observed

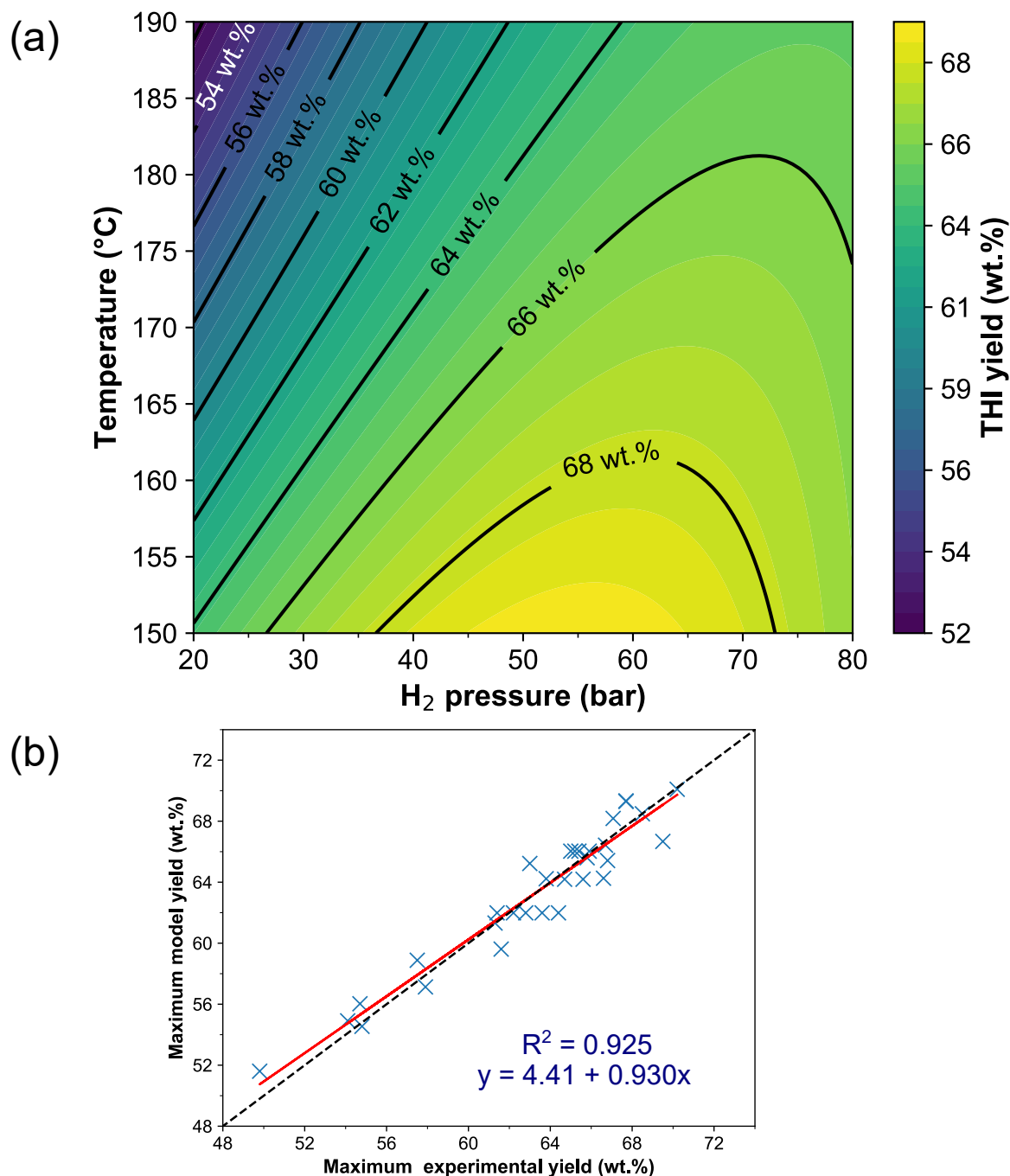


Figure 4.14: (a) Contour map of the maximum observed THI yield as a function of temperature and pressure. (b) Parity plot for model predicted yields and experimentally observed yields with regression analysis.

yield was used. Therefore, obtaining more experimental data in the maximum region will probably be preferable to using more complex models in the first instance, since this may lead to overfitting the data.

These data may also be used for analysing the kinetics of the reactions. Arrhenius plots for the rate of hydrogenation of PMI and E-PMI are presented in Figure 4.17. Typical Arrhenius

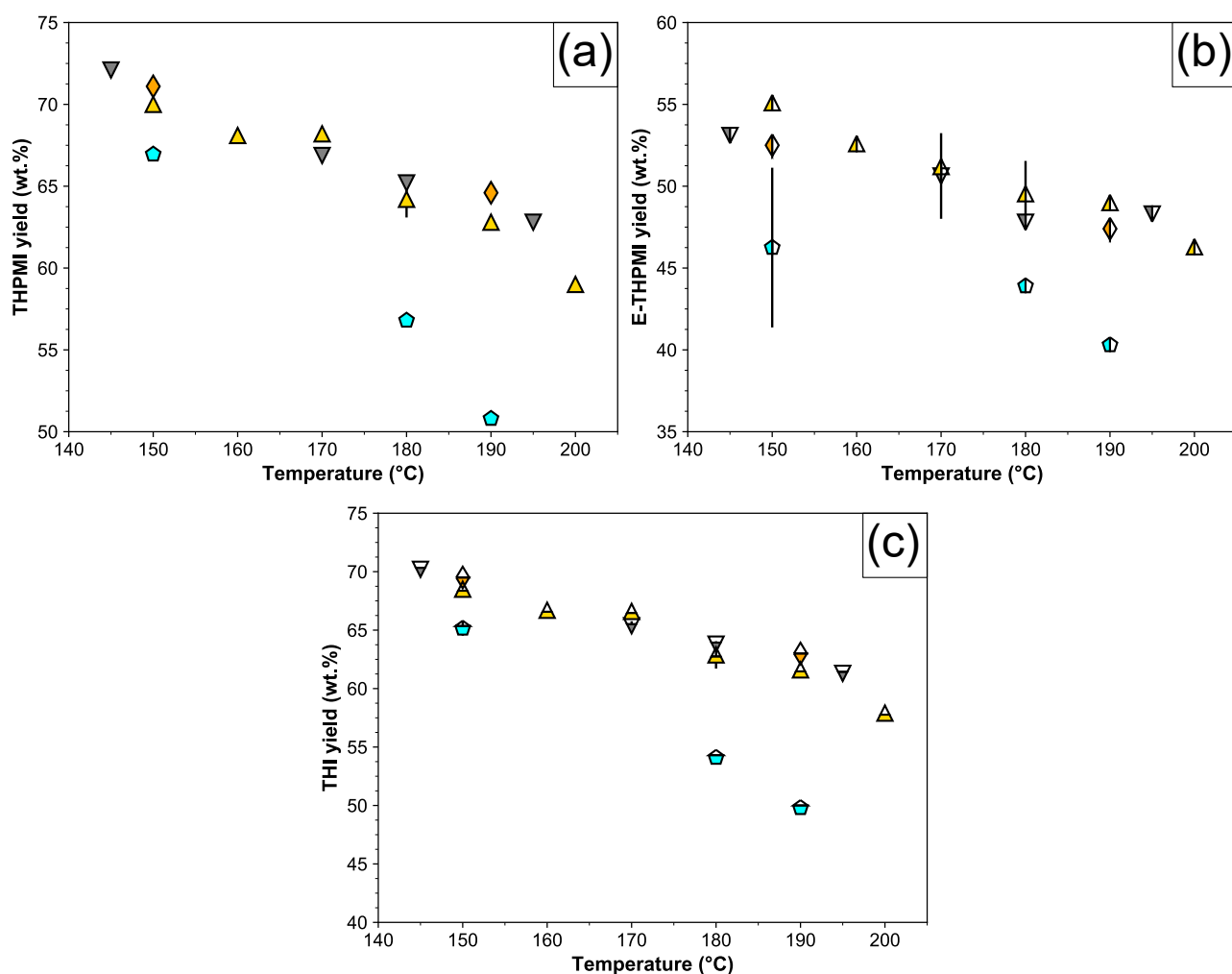


Figure 4.15: The effect of pressure on maximum of THPMI (a), E-THPMI (b), and THI (c). Legend: 20 bar (filled cyan pentagon), 40 bar (filled yellow triangle), 50 bar (filled grey inverted triangle), and 80 bar (filled orange diamond). Filled shapes represent THPMI (a), left-filled shapes represent E-THPMI (b), and bottom-filled shapes represent THI (c).

behaviour is observed as the rate increases exponentially with temperature. The apparent activation energies for each aromatic compound initially increases from 40 to 50 to 60 kJ mol⁻¹ as hydrogen pressure is raised from 20 to 40 to 50 bar, respectively. After 50 bar, increases in hydrogen pressure result in smaller changes to the apparent activation energies. No data is available for the tetrahydroindane intermediates as attempts to study the hydrogenation of this compound were unsuccessful and extraction of rates at high levels of conversions was found to be very sensitive to both the conditions used and the portion of the post-maximum data used.

The reaction orders with respect to the aromatic compounds and hydrogen are also possible with the design of experiments data (Figure 4.18). The integral method was used to determine the reaction order for PMI and E-PMI. At each temperature zero order and negative first order plots for PMI and E-PMI, respectively, gave the best fits. The reaction order for hydrogen was determined using log(TOF)-log(hydrogen pressure plots). Increasing the temperature resulted

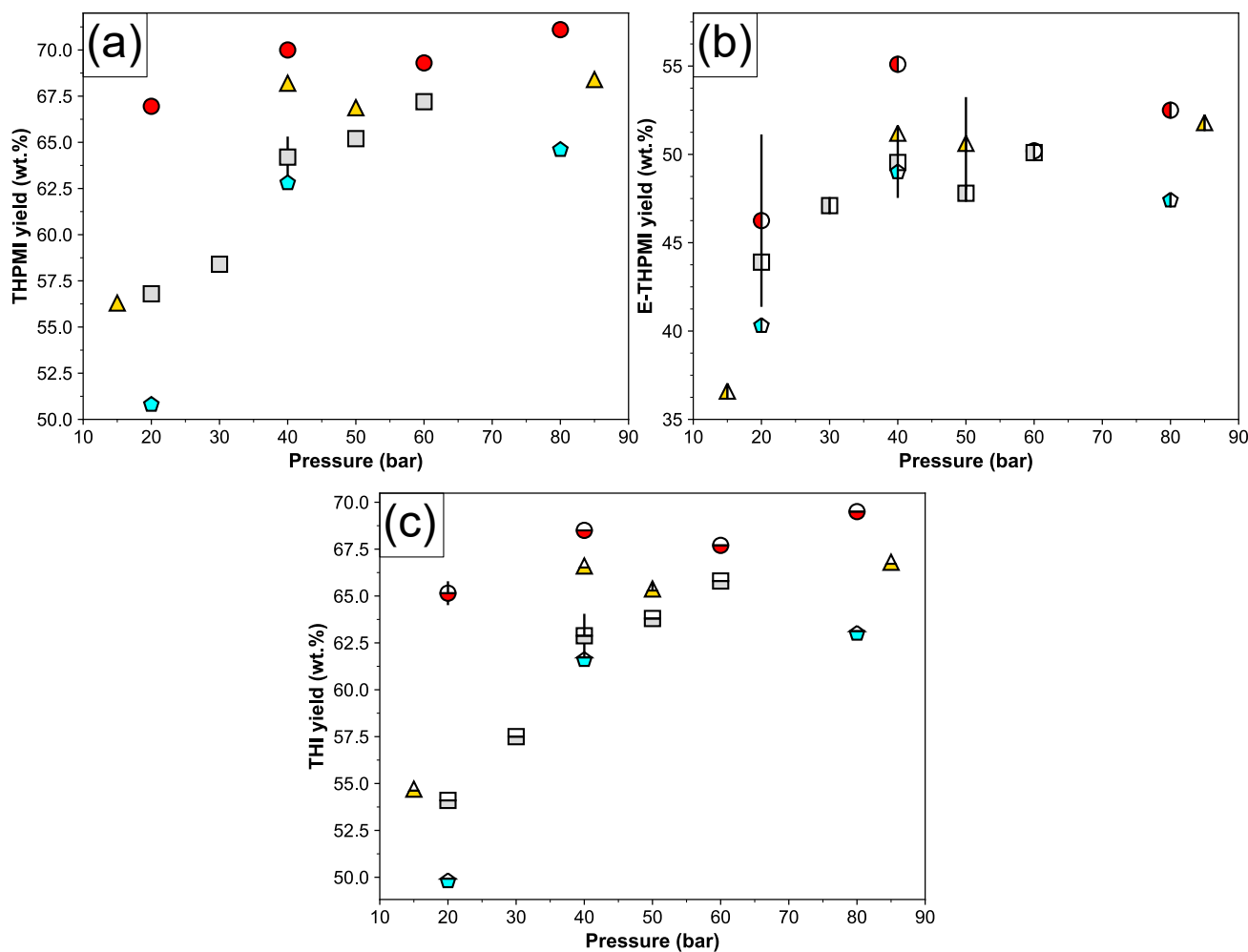


Figure 4.16: The effect of temperature on maximum of THPMI (a), E-THPMI (b), and THI (c). *Legend:* 150 °C (●), 170 °C (▼), 180 °C (□), and 190 °C (⬠). Filled shapes represent THPMI (a), left-filled shapes represent E-THPMI (b), and bottom-filled shapes represent THI (c).

in the hydrogen order increasing from about 0.6 ± 0.1 at 150 °C to near unity at 180 °C and above. As with temperature, the error associated with the effects of hydrogen pressure on the rate of hydrogenation of the intermediate olefins was too large to be used to probe the kinetic behaviour.

The effects of temperature and hydrogen pressure on the partial reduction of benzene and di-*tert*-butylbenzenes have been investigated previously.^{7,29,31–34} With regards to the effects of pressure, it has been reported that the yield of the cyclic olefin intermediate initially increases before passing through a maximum.^{7,31,34} Though not all authors report this, as others find cyclohexene yields are independent of pressure, due to mass transfer effects,³³ or increase as a function of pressure before plateauing.²⁹ This latter observation is in good agreement with the experimental data reported in this work, but in the original article the authors did not offer an explanation.²⁹

Temperature effects on the other hand are incongruous. Many workers agree that cyclo-

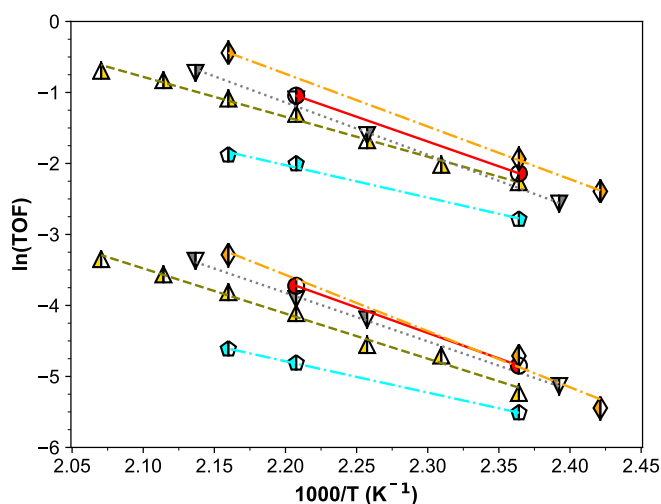


Figure 4.17: Arrhenius plots for PMI (right-filled shapes) and E-PMI (left-filled shapes). *Legend:* 20 bar (◐), 40 bar (△), 50 bar (▽), 60 bar (●) and 80 bar (◆).

Table 4.3: Arrhenius parameters for PMI and E-PMI obtained under different hydrogen pressures.

| Hydrogen pressure (bar) | PMI | | E-PMI | |
|-------------------------|-------------|-----------------------------------|-------------|-----------------------------------|
| | ln A | E_{app} (kJ mol ⁻¹) | ln A | E_{app} (kJ mol ⁻¹) |
| 20 | 8.02 ± 1.0 | 38.0 ± 3.7 | 4.94 ± 0.13 | 36.7 ± 0.13 |
| 40 | 11.9 ± 0.69 | 50.0 ± 2.5 | 10.7 ± 1.2 | 56.0 ± 4.8 |
| 50 | 16.0 ± 1.4 | 64.6 ± 5.2 | 10.9 ± 0.58 | 55.7 ± 2.1 |
| 60 ^a | 14.4 | 58.1 | 12.1 | 59.7 |
| 80 ^a | 15.4 | 60.8 | 11.8 | 58.0 |

^a Arrhenius parameters determined using two points.

hexene yield initially increases with temperature,^{29,31–35} but at higher temperatures different laboratories report different behaviour: some observe a continued increase in yield^{32,33} whilst others observed it passing through a maximum,^{29,31,34,35} even when the same temperature region is probed. In the temperature region explored in this work, the former behaviour is observed. The origin of the initial enhancement in these instances was attributed to higher temperatures promoting the desorption of the intermediate (as desorption is endothermic). This cannot account for the behaviour as the initial selectivity is virtually constant across all temperatures (Figures 4.10 and 4.9) which suggests that the quantity of alkene desorbed is constant. Alternatively, it has been forwarded that higher temperatures increase the solubility of cyclohexene in water³⁵ or lead to catalyst decomposition/agglomeration.⁵ The former explanation has no relevance to this work as the reaction medium is entirely hydrocarbon and an equal solubility of all components would be expected. Older work showed no particle size effects on the initial selectivity,³⁶ however Rioux *et al.*³⁷ demonstrated that cyclohexene hydrogenation is a structure sensitive reaction in the gas-phase over platinum catalysts at 448 K. In this instance, the rate of hydrogenation was observed to more than quadruple as

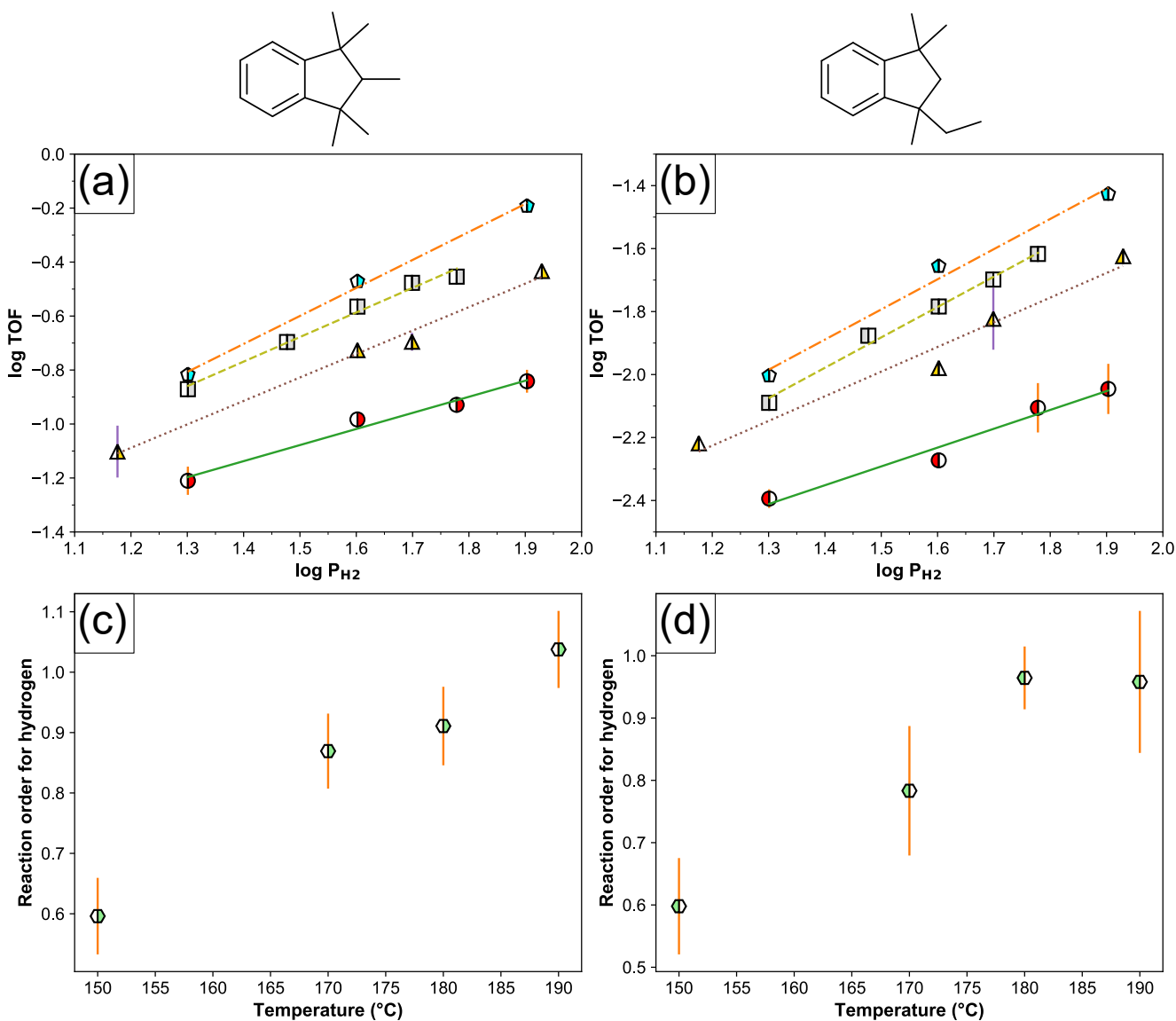


Figure 4.18: log TOF- $\log P_{H_2}$ plots the hydrogenation of PMI (a) and E-PMI (b) with a summary of the hydrogen reaction order as a function of temperature for PMI (c) and E-PMI (d).

particle size was increased from 1 to 4 nm and was attributed to a differing coverages of reactive hydrogen species.³⁷

As no obvious explanation to account for the observed behaviour is available in literature, several hypotheses to account for the behaviour were considered. These were categorised into two separate broad sections which will now be examined in turn. The areas considered were:

- [1] A physical effect
- [2] A catalytic effect.

4.3.3.1 Physical effects

4.3.3.1.1 Equilibrium limitations

The maximum attainable yield in a chemical reaction is dictated by thermodynamics. Catalytic

reactions are no different as despite following different reaction pathways, catalysts are substances that accelerate the rate at which a chemical system approaches equilibrium, without being consumed in the process. The equilibrium constant is dependent on temperature only as shown by the van't Hoff equation:

$$\frac{d}{dT} \ln K_{\text{eq}} = -\frac{\Delta_r H^\circ}{RT^2} \quad (4.9)$$

where T is temperature, K_{eq} is the equilibrium constant, $\Delta_r H^\circ$ is the standard enthalpy change of the reaction, and R is the gas constant.

However, to compute the equilibrium constant, thermochemical values must be known or the equilibrium position must be determined experimentally. No thermochemical values are reported for compounds in this work and the latter is not possible as the hydrogenation of the intermediate is probably favourable when its dehydrogenation is possible. Computational methods to probe the thermochemistry of reactions, which lack experimental values, are becoming ever more popular. A limiting factor in their application is, however, systematic errors leading to an over/underestimation of these values. Goerigk and Grimme recently thoroughly benchmarked a plethora of density functionals for the evaluation of general main group thermochemistry and their results indicate that the M06-D3,^{38,39} ω B97X-D,⁴⁰ and PBE0-D3^{39,41,42} methods may be applicable to the molecules of interest in this study.⁴³

To further verify that these functionals are suitable for this system, a small benchmarking study was performed on the benzene-cyclohexene-cyclohexane system. Both structure optimisation and frequency calculations were performed on optimised structures in cyclohexane using a cc-pVTZ basis set⁴⁴ combined with a M06-D3, ω B97X-D, and PBE0-D3 functional; the thermochemical values obtained from these calculations were then compared with literature data (Table 4.4). The computed standard reaction enthalpies and equilibrium constants for the benzene-cyclohexene-cyclohexane system are in reasonable agreement with the experimentally reported values for this system. The reaction enthalpy values calculated to the M06-D3/cc-pVTZ level of theory are most accurate with an average error of 7% whilst the PBE0-D3 method is least accurate with errors nearing 20%. Associated errors on the equilibrium constant increase considerably to several orders of magnitude for most reactions, not including the M06-D3 functional for the benzene to cyclohexene reaction. Small errors on reaction enthalpies and entropies can result in large errors on equilibrium constants owing to their exponential dependence.

The two best performing functionals, M06-D3 and ω B97X-D, were further benchmarked for the deep hydrogenation of indane to hexahydroindane (Table 4.4); no literature data was available for any partially hydrogenated intermediates. The relative error for the M06-D3 functional computed reaction enthalpy remains largely unchanged (7%), whereas the relative error for the ω B97X-D functional is now greater than 20%. Relative errors on the equilibrium constants for the indane-hexahydroindane system increase for both functionals with a smaller

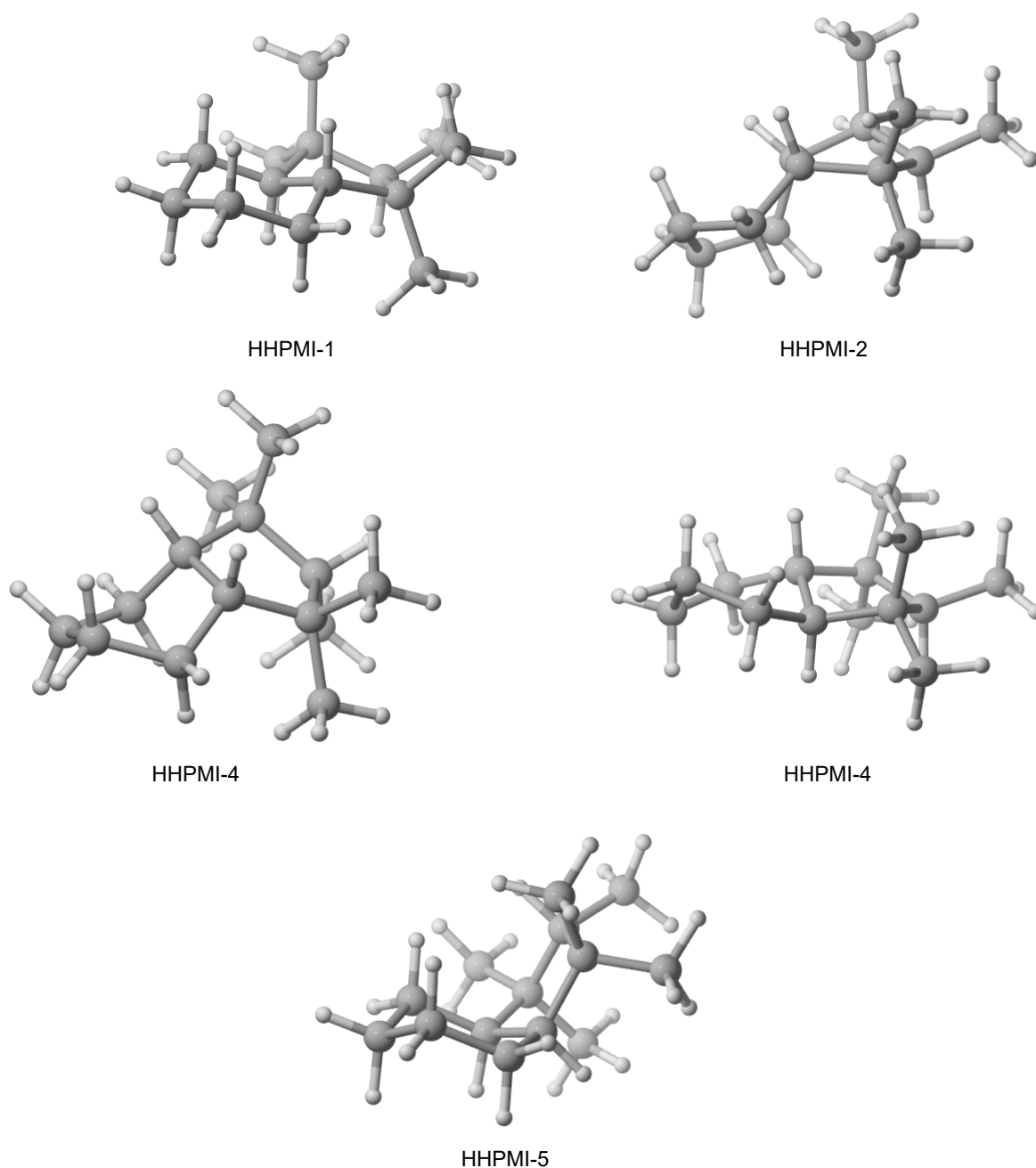


Figure 4.19: M06-D3/cc-pVTZ optimised structures of several HHPMI isomers.

errors found for the M06-D3 functional. In each case the error on the equilibrium constant was greater than for the reaction enthalpy.

As discussed above, knowledge of the equilibrium constant as a function of temperature is required. Figures 4.20 and 4.21 display the parity plots of the computed equilibrium constants *versus* the experimental equilibrium constants calculated using the integrated form of the van't Hoff equation (Equation 4.9) for the benzene-cyclohexene-cyclohexane and indane-hexahydroindane systems between 25 and 277 °C. The lines of best fit in these

plots are shown in solid black lines with the dashed line representing parity. Also shown in the plot is the linear regression analysis. The M06-D3 functional is once again best performing as a function of temperature owing to smaller errors on the equilibrium constant and reaction enthalpies. However, even for this best performing functional the relative error on the equilibrium constant is greater for the indane-hexahydroindane reaction than it is for benzene to cyclohexane. It is interesting to note that in general the results from the DFT calculations expect the hydrogenation reactions to be more energetically favourable at higher temperatures despite the higher predicted reaction enthalpies. Nevertheless, these data suggest that the results from the DFT calculations may indicate an “upper limit” on the equilibrium constants. Therefore, one may anticipate the true equilibrium constants for the PMI-THPMI-HHPMI system to fall below the computed values. This therefore suggests that M06-D3 and ω B97X-D functionals at this level of theory may provide a reasonable insight into the thermodynamics of the PMI-THPMI-HHPMI system.

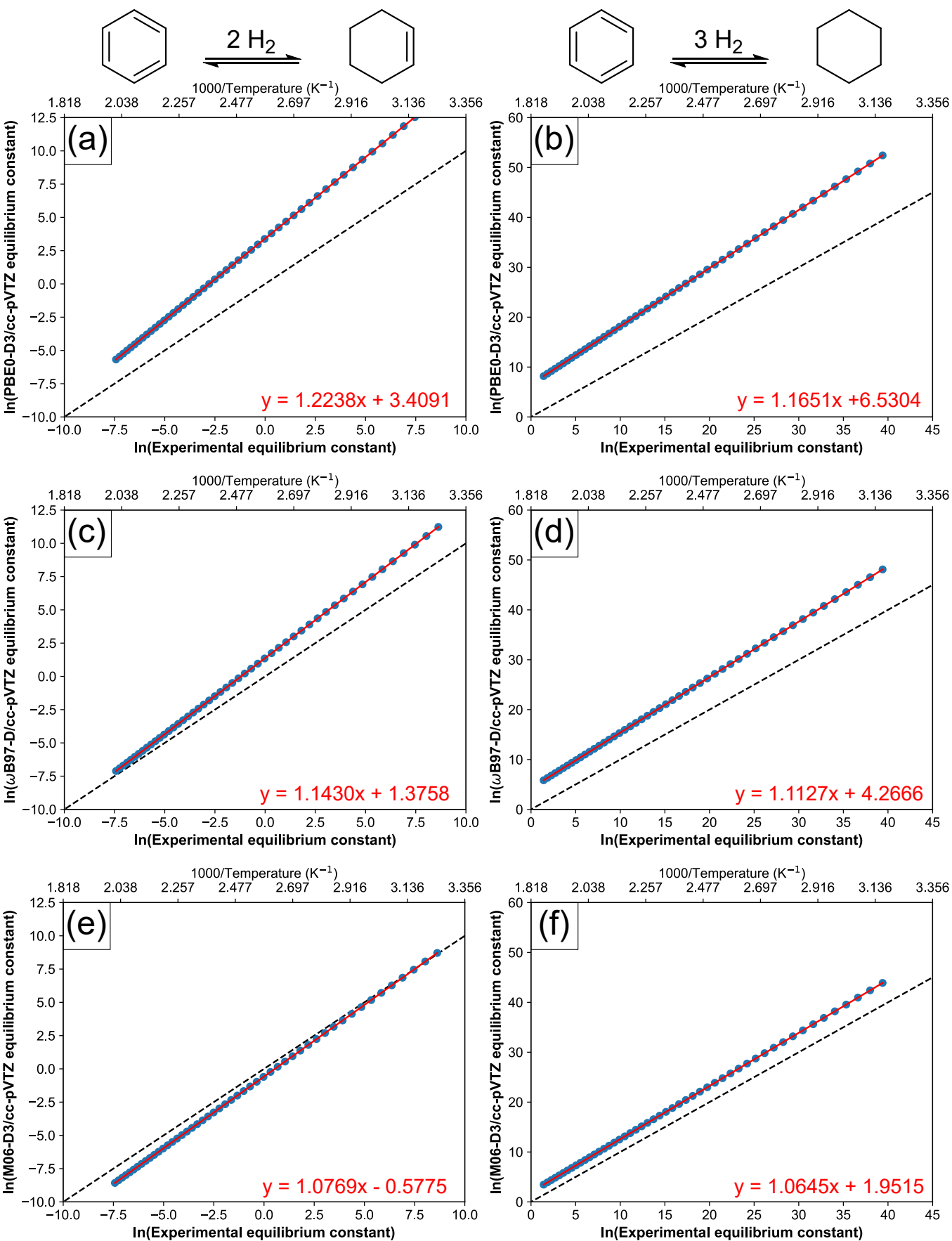


Figure 4.20: Parity plots for DFT calculated $\ln(K)$ (using PBE-D3 (a), ω B97X-D (b), M06-D3 (c) functionals with cc-pTVZ basis set) and experimentally calculated $\ln(K)$ for the benzene-cyclohexene system. Parity plots for DFT calculated $\ln(K)$ (using PBE-D3 (b), ω B97X-D (d), M06-D3 (e) functionals with cc-pTVZ basis set) and experimentally calculated $\ln(K)$ for the benzene-cyclohexane system.

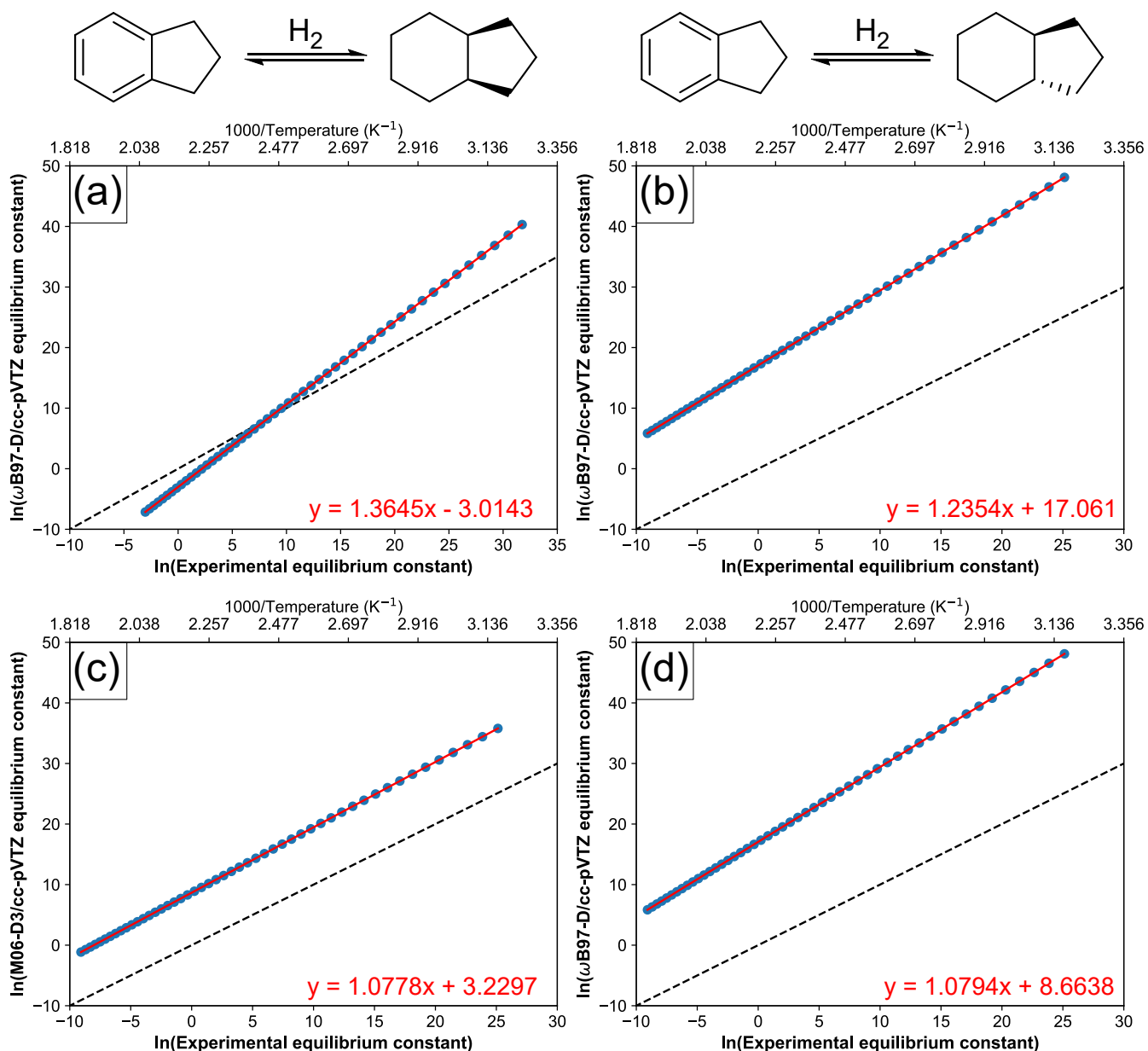


Figure 4.21: Parity plots for DFT calculated $\ln(K)$ (using PBE-D3 (a), ω B97X-D (b), M06-D3 (c) functionals with cc-pTVZ basis set) and experimentally calculated $\ln(K)$ for the benzene-cyclohexene system. Parity plots for DFT calculated $\ln(K)$ (using PBE-D3 (b), ω B97X-D (d), M06-D3 (e) functionals with cc-pTVZ basis set) and experimentally calculated $\ln(K)$ for the indane-hexahydroindane system.

Table 4.4: Thermochemical information for various aromatic or cyclic alkene hydrogenation reactions taken from literature or computed using DFT.

| Molecule | ΔH (kJ mol ⁻¹) | | | | $\ln K^a$ | | | |
|---------------------------------------|------------------------------------|-------------------------------|---------------------|---------------------|----------------------|-------------------------------|---------------------|-------------------|
| | PBE0-D3 ^b | ω -B97x-D ^b | M06-D3 ^b | Exp | PBE0-D3 ^b | ω -B97x-D ^b | M06-D3 ^b | Exp |
| Benzene→Cyclohexene | -106.3 | -99.2 | -93.5 | -86.8 ^c | 13.9 | 11.2 | 8.69 | 8.61 ^c |
| Benzene→Cyclohexane | -239.4 | -228.5 | -218.7 | -205.4 ^c | 52.4 | 48.1 | 43.8 | 39.4 ^c |
| Cyclohexene→Cyclohexane | -133.1 | -129.3 | -125.2 | -118.7 ^c | 38.4 | 45.3 | 37.9 | 30.9 ^c |
| PMI→THPMI | -111.9 | -105.7 | -100.2 | n.a. ^e | 16.1 | 13.2 | 10.8 | n.a. ^e |
| PMI→HHPMI-1 | n.d. ^d | -203.7 | -197.2 | n.a. ^e | n.d. ^d | 36.7 | 33.2 | n.a. ^e |
| PMI→HHPMI-2 | n.d. ^d | -173.6 | -166.6 | n.a. ^e | n.d. ^d | 24.4 | 22.1 | n.a. ^e |
| PMI→HHPMI-3 | n.d. ^d | -156.2 | -146.0 | n.a. ^e | n.d. ^d | 16.7 | 12.8 | n.a. ^e |
| PMI→HHPMI-4 | n.d. ^d | -172.8 | -166.2 | n.a. ^e | n.d. ^d | 24.6 | 21.8 | n.a. ^e |
| PMI→HHPMI-chair cis | n.d. ^d | -189.7 | -178.9 | n.a. ^e | n.d. ^d | 30.4 | 25.4 | n.a. ^e |
| THPMI→HHPMI-1 | n.d. ^d | -98.0 | -97.0 | n.a. ^e | n.d. ^d | 23.5 | 22.3 | n.a. ^e |
| Indane→ <i>cis</i> -Hexahydroindane | n.d. ^d | -228.5 | -199.7 | -185.0 ^f | n.d. ^d | 48.1 | 35.7 | 25.1 |
| Indane→ <i>trans</i> -Hexahydroindane | n.d. ^d | -256.7 | -202.7 | -188.1 ^f | n.d. ^d | 40.3 | 37.4 | 31.7 |

^a At 298.15 K and 1 bar pressure.^b Using a cc-pVTZ basis set.^c Calculated using data taken from [45–48].^d Not determined.^e Not available.^f Calculated using data taken from [48–51]

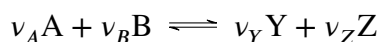
The above approach was subsequently used to probe the thermochemistry of the PMI-THPMI-HHPMI system (Table 4.4). The heat of hydrogenation is greatest when the saturated product is in the chair confirmation, in agreement with what is observed for cyclohexane. In contrast to the indane-hexahydroindane system, the M06-D3 functional calculates a 33 kJ mol⁻¹ higher enthalpy of formation for the *cis* isomer compared to the *trans* isomer. This discrepancy probably originates from unfavourable interactions between the methyl substituents on the five-membered ring and the cyclohexane skeleton.

Based upon the equilibrium constants, the partial reduction reaction is less favourable than the hydrogenation of benzene to cyclohexene (Table 4.4). Similarly, the equilibrium constants for the deep hydrogenation reactions are found to be in the order of PMI→HHPMI < indane→hexahydroindane < benzene→cyclohexane. This is expected as the equilibrium constant for the hydrogenation of benzene and its homologues is known to decrease as both the number of side chains and the number of carbon atoms in each side chain increases.^{52,53} With regards to the equilibrium constant of THPMI hydrogenation to HHPMI, the value is lower than the hydrogenation of cyclohexene to cyclohexane. This observation is also expected as the free energy for hydrogenation of alkenes decreases with substitution.⁵⁴

The natural logarithm of the equilibrium constant being less than unity at the temperatures used in this work does not mean that the reaction is thermodynamically impossible or even disfavoured. The free energy change of a reaction, ΔG , is defined by:

$$\Delta G_r = -RT \ln K + RT \ln Q \quad (4.10)$$

Where Q is the reaction quotient for the reaction:



and is equal to:

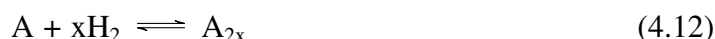
$$Q = \frac{P_Y^{\nu_Y} P_Z^{\nu_Z}}{P_A^{\nu_A} P_B^{\nu_B}} \quad (4.11)$$

where P is the pressure (or concentration) of molecule A , B , Y , or Z raised to its stoichiometric coefficient.

Equation 4.10 states that when $K > Q$, the reaction will proceed in the forward direction and vice versa, until chemical equilibrium, where $Q = K$, is established. In other words, this means that reactions that have positive ΔG° values (or $\ln K$ values less than unity) can be brought about by utilising higher pressures, ratios of reactants, or removing products as they form. Even if ΔG is positive, a reaction may proceed to a level of conversion that may be industrially useful or of academic interest.

The equilibrium conversion defines what the maximum possible conversion can be achieved at a certain temperature. In a heterophasic system, the mathematical complexity is greater than in a homogeneous system. Therefore, to simplify matters, the reaction is

assumed to take place in the gas phase. Aromatic compound A reacts with x (where $x = 1, 2,$ or 3) moles of hydrogen to form reduced product A_{2x} and may be expressed by:



In a semi-batch reactor operating isobarically, where consumed hydrogen is replenished, the pressure of A and A_{2x} can be expressed as functions of the conversion, X , of A:

$$P_A = P_{A0}(1 - X) \quad (4.13)$$

$$P_{A_{2x}} = P_{A0}(X) \quad (4.14)$$

$$P_{H_2} = P_{H_2,0} \quad (4.15)$$

As $Q = K$ at equilibrium, the concentrations of each reactant can be calculated as:

$$K = \frac{P_{A0}(X_e)}{P_{A0}(1 - X_e)P_{H_2}^x} \quad (4.16)$$

where X_e is the equilibrium conversion.

Rearranging Equation 4.16 so that it equals zero allows a solution be derived (Equation 4.17).

$$K(1 - X_e)P_{H_2}^x - X_e = 0 \quad (4.17)$$

This approach was used to calculate the equilibrium conversions for the reduction of indane to *cis*-hexahydroindane at different hydrogen pressures using literature thermochemical and equilibrium conversion values (Figure 4.22a + b). Upon comparison, it is evident that the calculated equilibrium conversions are in good agreement with the experimental data. The calculated equilibrium conversions using thermochemical properties obtained by DFT methods are higher than the experimental equilibrium conversions as anticipated considering the errors discussed above (Figure 4.22c + d). There is approximately a 50 °C shift between the experimental and computed equilibrium value when using the M06-D3 functional and greater values still are observed with the ω B97X-D functional.

Figure 4.23 displays the equilibrium conversions of PMI at different pressures with experimental THPMI yields also marked along with error regions of 50, 100, and 150 °C. No experimental yields are within 50 °C of the computed equilibrium yields. Moreover, if it is assumed that the experimental yields at constant pressure are the equilibrium conversions, then a plot of the natural logarithm of the equilibrium constant, calculated assuming the THPMI yield is the equilibrium conversion, against the reciprocal of temperature should yield the enthalpy of reaction. As discussed above, the reaction enthalpies calculated using the M06-D3 functional were shown to be of reasonable accuracy and equal to -100 kJ mol^{-1} . The gradient of the van't Hoff plots, presented in Figure 4.24, are significantly below this value and show linearity for the data at all hydrogen pressures. Consideration of this information suggests that the experimental yields of THPMI are probably not limited by thermodynamics.

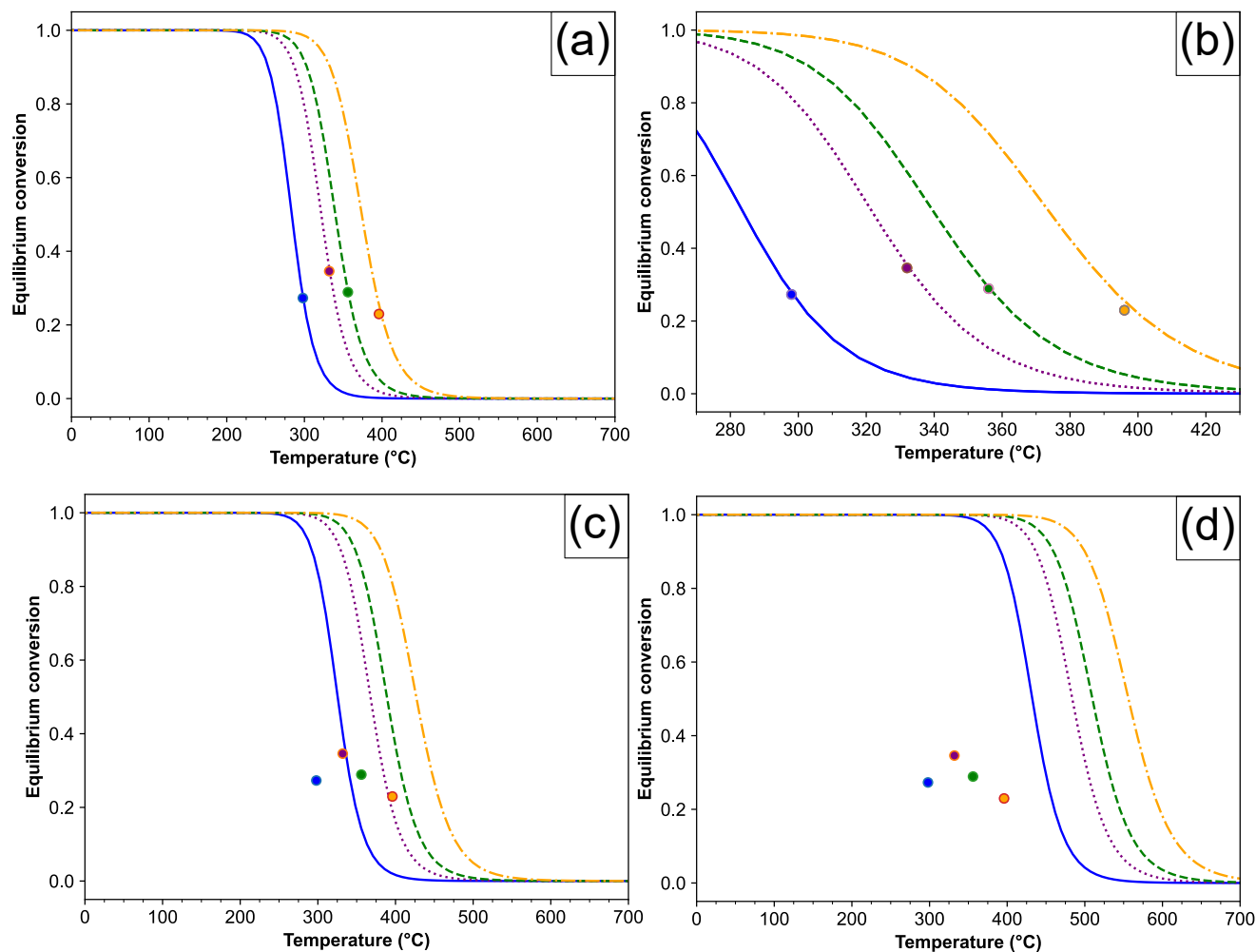


Figure 4.22: Calculated equilibrium conversions of indane to *cis*-indane as a function of temperature using data from reference [55] and Equation 4.17 for experimental data (a + b), M06-D3/cc-pVTZ level of theory (c), and ω B97X-D/cc-pVTZ level of theory. Legend: 4.6 atm H₂ pressure (—), 11 atm H₂ pressure (⋯), 16.6 atm H₂ pressure (---), and 30.4 atm H₂ pressure (-.-). Marker denotes experimental value, 4.6 atm H₂ pressure (●), 11 atm H₂ pressure (●), 16.6 atm H₂ pressure (●), and 30.4 atm H₂ pressure (●).

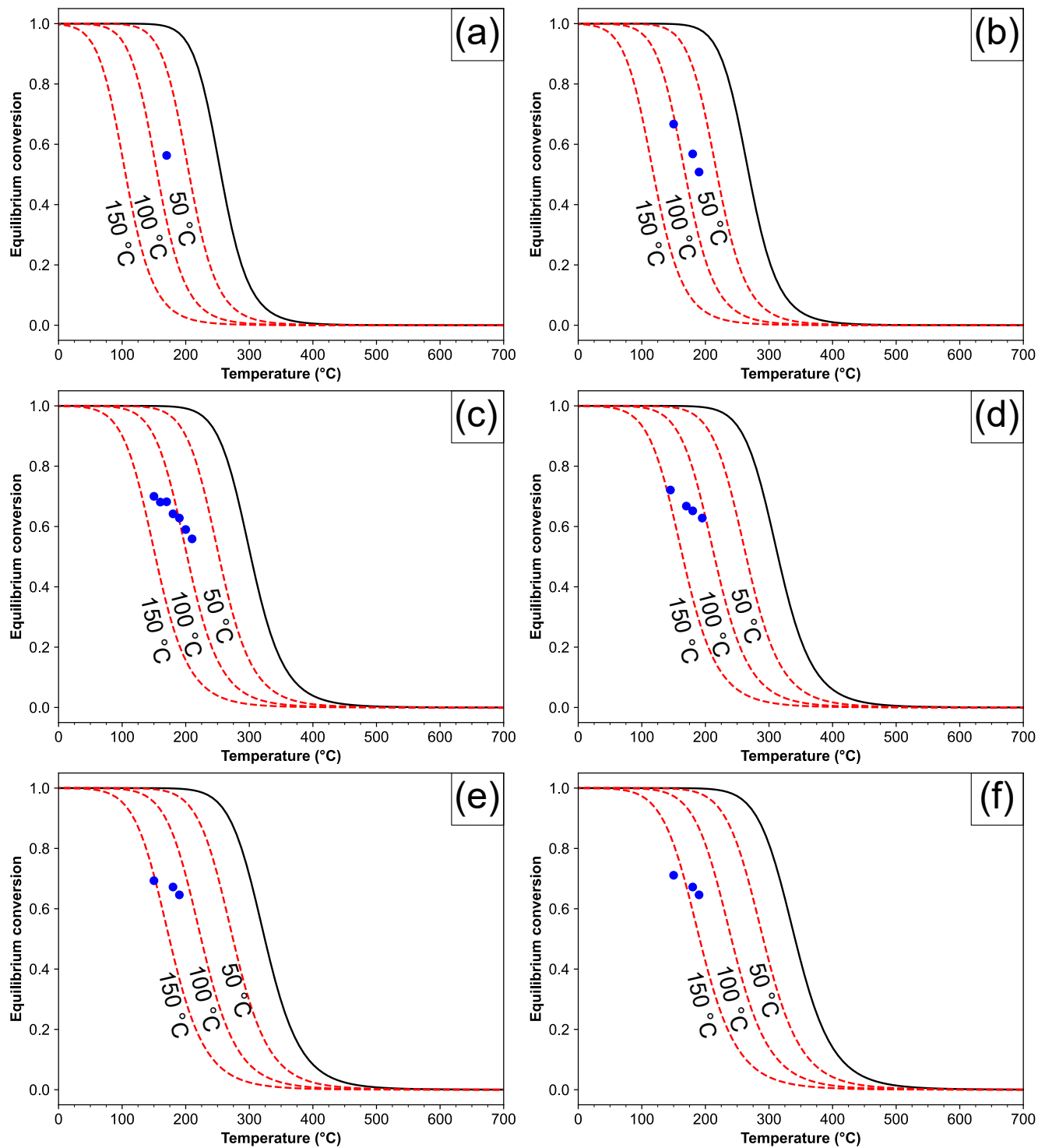


Figure 4.23: Equilibrium conversions for the reaction $\text{PMI} + 2 \text{H}_2 \rightleftharpoons \text{THPMI}$ (—) with temperature errors on K given as 50, 100, and 150 °C for maximum THPMI yields at 15 (a), 20 (b), 40 (c), 50 (d), 60 (e) and 80 bar (f) hydrogen pressure. Equilibrium conversion curves calculated using Equation 4.17. K is calculated using thermochemical values to a M06-D3/cc-pVTZ level of theory at 298 K and its variation with temperature calculated using the van't Hoff equation (Equation 4.30).

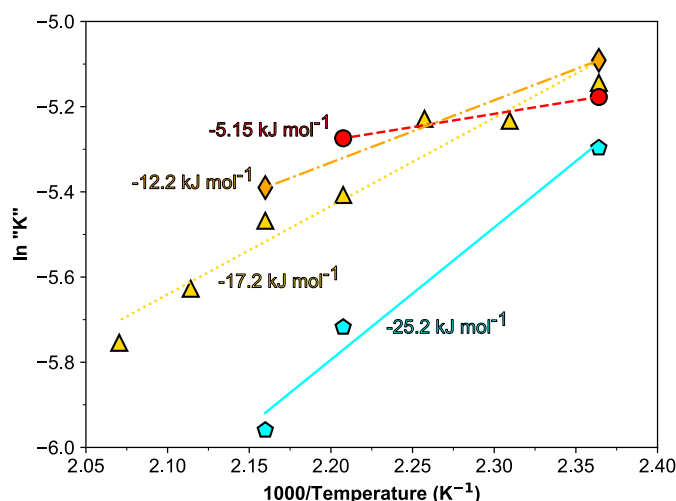


Figure 4.24: van't Hoff plot if the conversions of PMI to THPMI are assumed to be equilibrium conversions. "K" calculated using Equation 4.16. Legend: 20 bar H₂ pressure (◐), 40 bar H₂ pressure (◔), 60 bar H₂ pressure (●), and 80 bar H₂ pressure (◈). Number denotes enthalpy of reaction if K is the equilibrium conversion at temperature *T*.

4.3.3.1.2 Mass transfer limitations

The possibility of mass transfer effects lowering the THPMI yield were also investigated. The apparent activation energies for the reduction of PMI and E-PMI are greater than 20 kJ mol⁻¹ under all pressure regimes (Table 4.3), which suggests mass transfer limitations are not present at the start of the reaction; apparent activation energies below this are suspect, as rates which are controlled, or strongly influenced, by diffusion do not increase exponentially with temperature.⁵⁶ Nevertheless, the possibility of liquid-solid mass transfer was examined using the Carberry number, Ca. This number is the ratio of the experimental reaction rate and the rate of the reaction if it were under diffusion control and is written as:

$$Ca = \frac{r_{obs}}{6k_{ls} \left(\frac{W}{d_p \rho_p} \right) C_i} \quad (4.18)$$

where r_{obs} is the experimental rate, k_{ls} is the liquid-solid mass transfer coefficient, W is the catalyst weight, d_p is the catalyst particle diameter, ρ_p is the density of the catalyst, and C_i is the concentration of i in solution. The catalyst weight is a known quantity and C_i was determined using GC analysis. Experimental rates were determined by the differential between data points. Particle size information was provided by the manufacturer, and the density was determined using a density bottle and water accounting for the pore volume of the material. As many assumptions fall into this model, some degree of caution is used such that when $Ca < 0.05$ diffusion limitations are assumed to be absent.

The liquid solid mass transfer constant was calculated using the method outlined by Roberts:⁵⁷

$$\left(\frac{k_{ls} d_p}{D_{i,j}} \right)^2 = 16.0 + 4.84 \left(\frac{g d_p^3 (\rho_a - \rho_l)}{18 \mu D_{i,j}} \right) \quad (4.19)$$

where D_i is the diffusion coefficient for molecule i in solvent j , g is gravity (9.81 m s^{-2}), ρ_a is the apparent density of the catalyst, that is the density of the catalyst when its pores are filled with the reaction solvent, ρ_l and μ_l are the liquid density and viscosity, respectively.

The diffusion coefficient is a proportionality factor that relates the diffusional flux and the gradient in the concentration of the diffusing species; physically, it can be pictured as the mean statistical variance of the position of a species as a function of time.⁵⁸ Many researchers have proposed models that are heavily idealised as they assume that substrate i is diffusing in essential pure j . Despite this limitation, they still find application in many diffusion studies at higher concentrations.⁵⁹ Diffusion coefficients in this work were calculated using the widely used Wilke-Chang correlation:⁶⁰

$$D_{i,j} = \frac{7.4 \times 10^{-8} (\sqrt{\phi M_j}) T}{\mu_j V_i^{0.6}} \quad (4.20)$$

which is a modification of the Einstein-Stokes equation. The molecular weight and viscosity of solvent j are expressed by M_j and μ_j , respectively; T is temperature, and V_i is the molar volume of solute i at its normal boiling temperature. The ϕ term is the association factor of the solvent which for hydrocarbons equates to unity.

Many of these values were reported in Chapter 3 of this thesis. The molecular weight of the solvent was assumed to remain at 188 g mol^{-1} throughout the reaction as the action of square rooting the hydrogenation products results in negligible changes to this term. The molar volume at normal boiling point for hydrogen was taken from literature⁶¹ and was calculated for PMI and THPMI by extrapolating the liquid density to the boiling points reported in the previous chapter and then V_i is calculated by:

$$V_i = \frac{M_w}{\rho_{bp}} \quad (4.21)$$

where M_w is the molecular weight of compound i and ρ_{bp} is the density of the compound at its normal boiling point.

This treatment gives V_i values for PMI and THPMI to be 261 and $276 \text{ cm}^3 \text{ mol}^{-1}$, respectively. To verify these values, the additive method of Schroeder as outlined by Poling *et al.* was to compute values; predicted values using this method are typically within $\pm 4\%$.⁵⁹ Equation 4.22 outlines how this value is calculated: the number of atoms of an element, double and triple bonds in a molecule are counted and substituted into the appropriate place in the equation and seven is subtracted once if any rings present in the molecule. This method predicts V_i values for PMI and THPMI to be 252 and $266 \text{ cm}^3 \text{ mol}^{-1}$, respectively, in good agreement with the values disclosed in the first sentence of this paragraph.

$$V_i = 7 (N_C + N_H + N_O + N_N + N_{DB} + 2N_{TB}) \\ + 31.5N_{Br} + 24.5N_{Cl} + 10.5N_F + 38.5N_I + 21N_S - 7 * \quad (4.22)$$

With knowledge of all variables in hand, the Carberry numbers are now calculable using Equation 4.18. In all cases, computed Ca values were found to be between two and three orders of magnitude smaller than 0.05, thus satisfying the criteria for the absence of external mass transfer resistances.

The porous nature of the catalyst means the hydrogenation may occur inside the catalyst, which could also be the rate limiting. As with the Carberry number, the high apparent activation energies at various pressures suggests such a limitation is not present as reactions limited by pore diffusion have experimental activation energies approximately half the diffusion-free value.⁵⁶ It is also possible to evaluate whether a reaction is controlled by pore diffusion, referred to as the Weisz-Prater criterion,⁶² using the following equation:

$$\Phi = \left(\frac{n+1}{2} \right) l_p^2 D_{i,eff} \left(\frac{R_{obs} \rho_p}{W} \right) \frac{1}{C_i} \quad (4.23)$$

where Φ is the Weisz-Prater criterion, n is the reaction order, l_p is the critical dimension of the catalyst particle, which for a sphere is equal to a third of the radius of a particle; C_i is assumed to be equal to the concentration of i in the bulk as external mass transfer limitations are absent.

The value obtained from the above equation is dependent on reaction order, however, as a broad generalisation it can be stated that a value less than 0.3 indicates that the impact of pore diffusion is negligible, a value greater than 6 implies that it is significant.⁶³ In-between values are highly dependent upon the reaction order. For instance, a zero-order reaction requires Φ greater than 6 for pore diffusion effects to be significant. For liquid phase reactions, however, this value is difficult to calculate as the effective diffusion is hard to determine as the entire system needs to be considered. Moreover, in this instance the molecular diameter between the methyl groups on opposite sides of the ring begins to approach the average pore diameter of the catalyst which may hinder its diffusion. If $D_{i,eff}$ is crudely approximated to equal the bulk diffusivity of PMI, THPMI, and hydrogen, then Φ values are roughly three orders of magnitude lower than 0.3, suggesting that internal diffusion limitations are absent.

4.3.3.2 Examination of possible catalytic effects

The origin of a kinetic effect may lie in several places. Firstly, it is necessary to exclude any possible effects that may be due to changes in the catalyst's structure during the reaction. Where possible, catalysts were collected after filtration at the end of a reaction, washed with ethanol and dried under vacuum at 40 °C. Post-reaction catalysts were examined by XRD (Figure 4.25) and the particle sizes determined using the Scherrer equation are outlined in Table 4.5. Although the turbostatic structure of the support appears to become deformed after the reaction, the particle size of palladium is in good agreement with the freshly reduced catalyst. This suggests that the bulk structure of palladium remains unchanged as the pressure and temperature are varied.

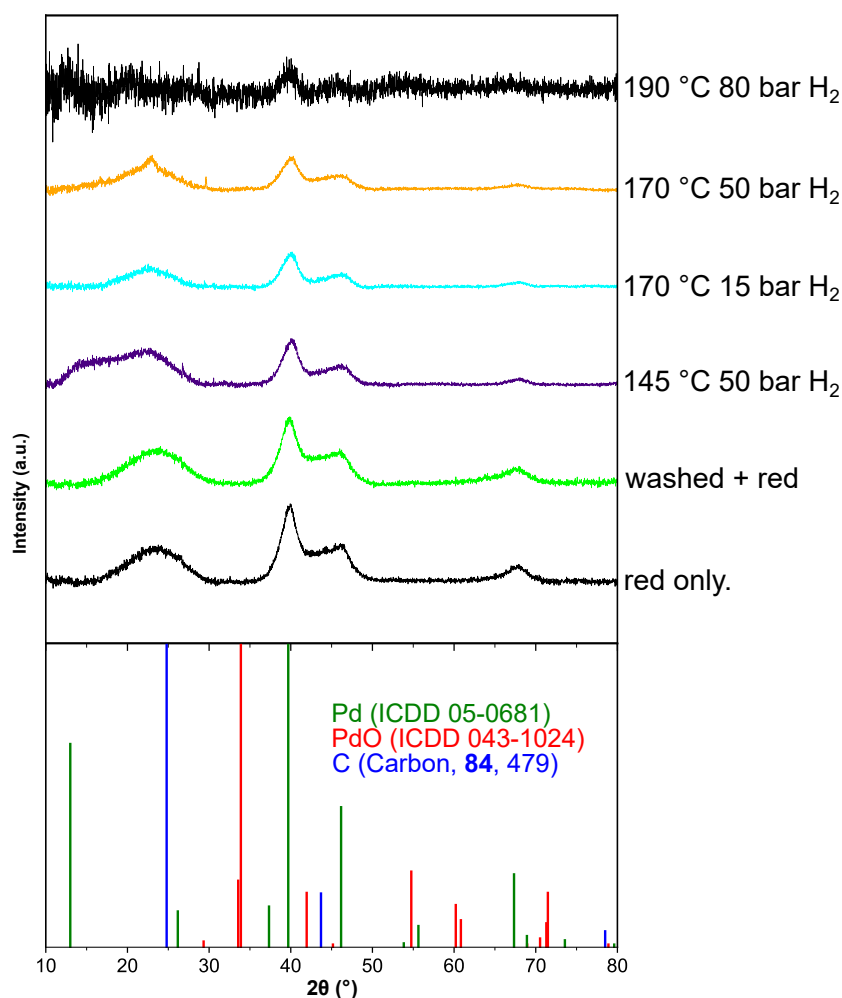


Figure 4.25: XRD patterns of post-reaction catalysts under stated conditions. Reduced only and a catalyst washed using ethanol after reduction also shown to highlight reduction and washing procedure does not impart changes.

That being said, X-ray diffraction is not surface sensitive and gaining an understanding of changes in surface area post-reaction is important. A reaction was performed at 170 °C and 50 bar hydrogen pressure at double the usual scale but with the same substrate to catalyst ratio to ensure sufficient catalyst was available for characterisation. After the above washing procedure, CO chemisorption revealed the palladium surface area had to decreased from 6.2 ± 0.31 to $4.0 \text{ m}^2 \text{ g}^{-1}_{\text{sample}}$. As the particle size estimated from XRD remains unchanged post-reaction, the decrease may be attributable to the formation of coke on the surface. What effect this may have on selectivity is unclear. Its possible formation must first be established by additional methods, such as TGA, before understanding how its formation depends on experimental parameters, which could go on to alter the reaction selectivity.

Table 4.5: Palladium particle sizes of post-reaction catalysts determined using the Scherrer equation.

| Miller index | P_{H_2} (bar) | T (°C) | Particle size (nm) |
|--------------|-----------------|-----------|--------------------|
| 111 | 50 | 145 | 3 |
| | 15 | 170 | 3 |
| | 50 | 170 | 4 |
| | 80 | 190 | 4 |
| | Red. only | Red. only | 4 |
| 220 | 50 | 145 | 2 |
| | 15 | 170 | 3 |
| | 50 | 170 | 3 |
| | 80 | 190 | n.d ^a |
| | Red. only | Red. only | 2 |

^a Not determined due to no observable peak.

Additional kinetic explanations require consideration of the reaction of the surface mechanism. Most commonly, hydrogenation reactions of unsaturated hydrocarbons are assumed to follow Langmuir-Hinshelwood kinetics. The competitive nature of adsorption for unsaturated molecules and hydrogen is disputed. Evidence for competitive behaviour originates from negative reaction orders for aromatic compounds sometimes observed during kinetic studies.²² DFT calculations support this as benzene and hydrogen adsorption has highly favourable adsorption energies in the three-fold hollow fcc position.^{27,64,65} Moreover, Gonzo and Boudart demonstrated that the reaction rate for the hydrogenation of cyclohexene could be inhibited by aromatic solvents, such as benzene, toluene, or xylene, but not by polar or non-polar solvents, such as methanol, n-heptane, or ethyl acetate, suggesting competitive behaviour of these compounds and stronger adsorption of the aromatic.⁶⁶ The aforementioned DFT studies supported this observation as benzene was calculated to more strongly adsorb than cyclohexene by at least 15 kJ mol⁻¹.²⁷ Finally, the nature of the reactive hydrogen species for each reaction is generally considered to be a weakly adsorbed species, but whether this species is the same in each reaction is unclear. For example, the rate of benzene aromatic hydrogenation has been shown to correlate with the height of a peak observed at low temperatures in H₂-TPD,⁶⁷ but no such study is available for cyclohexene to the extent of my knowledge.

If the hydrocarbon molecules are assumed to compete for surface sites, then the results can be rationalised considering their relative strengths of adsorption. A van't Hoff plot for the surface equilibrium constants of benzene and cyclohexene using the computed thermodynamic adsorption properties by Sabbe *et al.* is displayed in Figure 4.26.²⁷ The slope of the line for benzene is steeper than it is for cyclohexene as the adsorption of the former compound is more exothermic. As a result, the adsorption potential for benzene weakens more than for cyclohexene as the temperature is raised (Equation 4.7). In other words, the surface coverage of benzene decreases more rapidly than that of cyclohexene as a function of temperature.

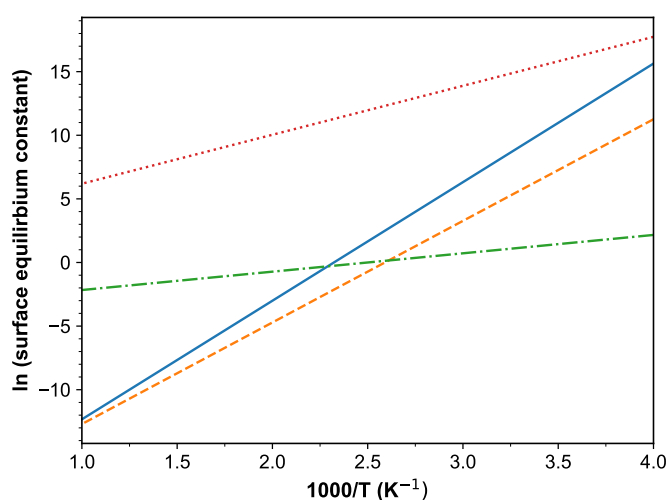


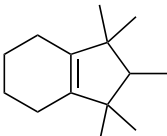
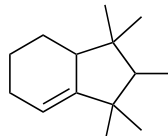
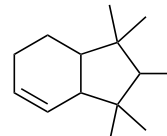
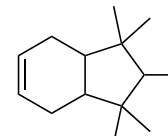
Figure 4.26: Natural logarithm of surface equilibrium constants of benzene and cyclohexene (obtained from DFT calculations) and monodehydrogenated phenyl species (extracted from kinetic rate expressions) as a function of the reciprocal of temperature. *Legend:* Benzene (—), cyclohexene (---), hydrogen-deficient phenyl species (-.-), and $\text{C}_6\text{H}_{10\text{ads}} \rightleftharpoons \text{c-C}_6\text{H}_{9\text{ads}} + \text{H}_{\text{ads}}$ (.....).

Although this reasoning explains the temperature effect, it cannot account for the effect of pressure on intermediate yield. The lower selectivity to E-THPMI compared to THPMI was attributed to the double bond in the first mentioned compound being located in a less sterically hindered position (Scheme 4.1), and was thus more reactive. If the double bond in THPMI were to isomerise to a sterically less hindered position, which is energetically feasible (Table 4.6), it could explain the decrease in yield of THPMI. This is not to say that isomerisation does not occur in E-THPMI also, as its yield too displays a hydrogen pressure dependence.

Such behaviour was observed by Siegel and co-workers,⁷ who estimated that the isomerisation of 1,3- and 2,4-di-*tert*-butylcyclohexene to less sterically hindered cyclic alkenes was the origin of 80% of the saturated product in some cases at low hydrogen pressures (<1 bar) using a Rh/Al₂O₃ catalyst. The mechanism for the isomerisation of alkenes has been long debated and is generally thought to depend on the metal catalyst involved.⁶⁸ For instance, isomerisation on palladium surfaces is thought to predominantly proceed *via* a π -allyl intermediate.⁶⁸ This is the alternative to the classical Horiuti-Polanyi reversible stepwise addition process⁶⁹ of hydrogen, which is more commonly observed on platinum.⁶⁸ It is also possible both pathways occur simultaneously,⁷⁰ with the relative rate dependent on the reaction system.

Regardless of the underlying mechanism, isomerisation followed by desorption and re-adsorption on the opposite face (or roll-over) would lead to the generation of the *trans* isomer. Figure 4.27 displays *trans/cis* ratio as a function of PMI conversion at 150 to 190 °C at different pressures. The *trans/cis* ratio at 150 °C is almost independent of pressure. At 170, 180, and 190 °C the *trans/cis* ratio diverges at lower conversions when lower pressures of hydrogen are used, before approaching a constant value at high conversion.

Table 4.6: Relative free energies of THPMI isomers calculated to a ω B97X-D/cc-pVTZ level of theory.

| |  |  |  |  |
|--|---|--|---|---|
| | THPMI | THPMI-2 | THPMI-3 | THPMI-4 |
| Relative free energy (kJ mol ⁻¹) | 0 | +0.25 | +0.39 | +0.34 |
| Equilibrium proportion | 25% | 25% | 25% | 25% |

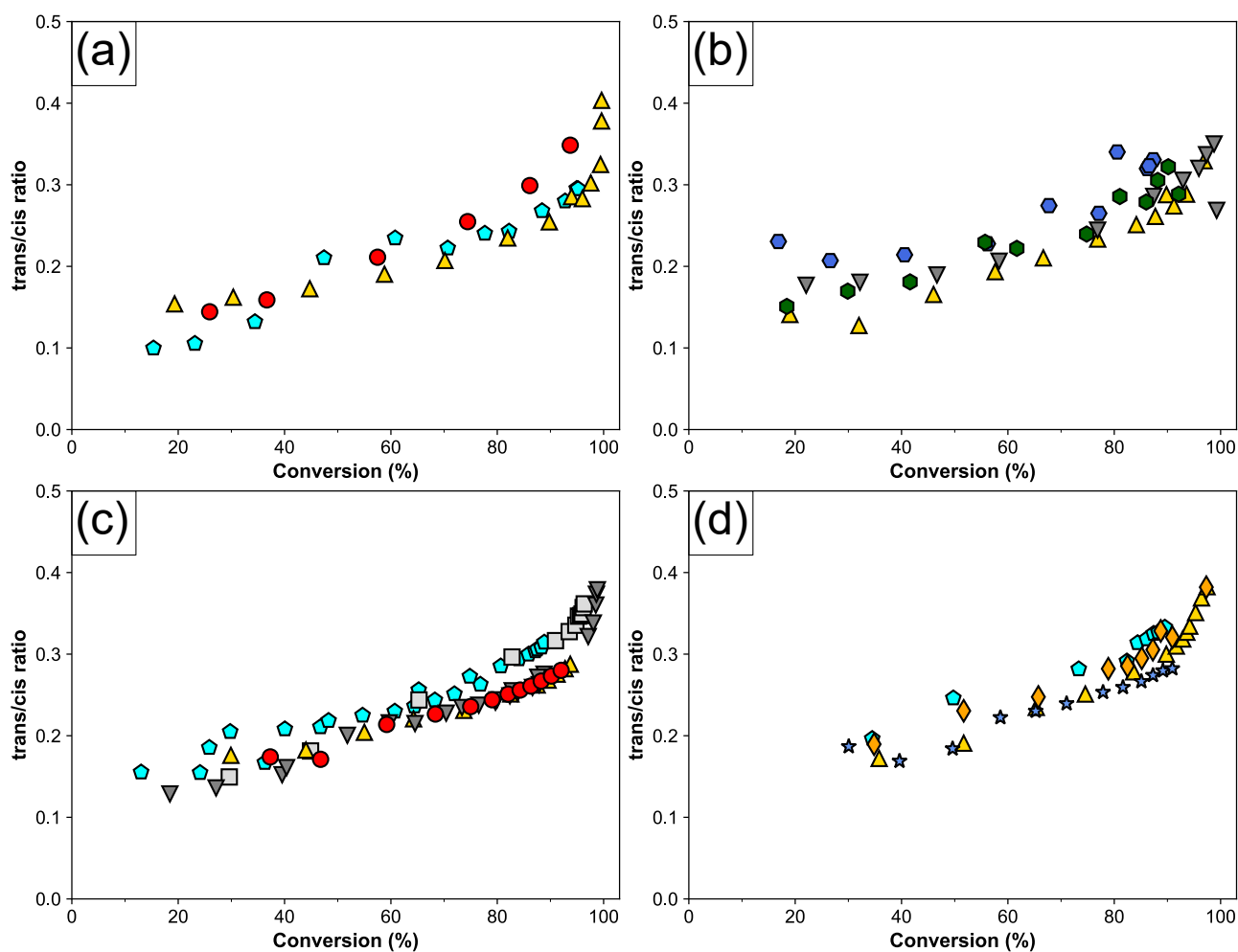


Figure 4.27: *Trans/cis* ratios at different pressures at 150 (a), 170 (b), 180 (c), and 190 °C (d). *Legend:* 15 bar (◈), 20 bar (◈), 40 bar (△), 50 bar (▽), 55 bar (☆), 60 bar (●), 80 bar (◇), and 85 bar (◈).

If the π -allyl mechanism is considered dominant in this instance, the pressure effect can be understood by considering the surface concentration of such species. If cyclohexene is used as a model, its adsorption is expressed by:



where S is a surface site, K_1 is the equilibrium constant for the process, and $\text{C}_6\text{H}_{10}\text{-S}$ is the surface cyclohexene complex. The dehydrogenation of this surface species to form the π -allyl species is expressed as:



where K_2 is the equilibrium constant for the process and H-S is a surface bound hydrogen atom. Rearranging and combining Equations 4.24 and 4.25, leads to the surface coverage of the π -allyl species, if S is the same site, as:

$$\theta_{\text{C}_6\text{H}_9} = \frac{K_1 K_2 C_{\text{C}_6\text{H}_{10}}}{\left(\sqrt{K_H P_{\text{H}_2}}\right) \left(1 + K_1 C_{\text{C}_6\text{H}_{10}} + \frac{K_1 K_2 C_{\text{C}_6\text{H}_{10}}}{\sqrt{K_H P_{\text{H}_2}}}\right)} \quad (4.26)$$

This equation computes that the surface species of the π -allylic species decreases as the inverse of the square root of pressure. In other words, there is an initial strong decline in the surface fraction of this species with increasing pressures before it begins to plateau, which agrees with what is observed in the experimental yields.

The thermodynamics of the surface reaction to form such a species has been studied computationally. Early studies by Koel *et al.* on platinum surfaces predicted that the dehydrogenation of cyclohexene to the allylic C_6H_9 species was highly exothermic ($\Delta H_r = -134 \text{ kJ mol}^{-1}$) using a quasi-empirical valence bond approach.⁷¹ More recently work by Sabbe *et al.* calculated that the enthalpy of formation of the π -allyl species was $-18.1 \text{ kJ mol}^{-1}$ at medium hydrogen coverages on Pt(111)⁷² and -32 kJ mol^{-1} on Pd(111).²⁷ Despite being mildly exothermic, the dehydrogenation of cyclohexene to the π -allyl species is still thermodynamically favoured until $>1000 \text{ }^\circ\text{C}$. This is not in contradiction to the experimental results as the surface coverage of hydrogen lowers as a function of temperature, thereby favouring its formation.

In an attempt to observe the isomerisation reaction, a purified THPMI mixture, containing 92% THPMI,^b was diluted in octane and combined with the reduced industrial Pd/C catalyst before heating to $70 \text{ }^\circ\text{C}$ under a nitrogen atmosphere. As a control, an octane solution containing 1-methylcyclohexene was exposed to the same conditions. The composition of the THPMI solution remained unchanged after 4 h, whereas 1-methylcyclohexene was shown to isomerise to 3- and/or 4-methylcyclohexenes.^c The 1-methylcyclohexene experiment suggests

^bOnly a very small quantity of this compound was available.

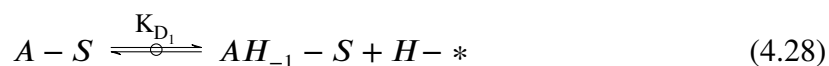
^cThese isomers could not be separated on the column used in these experiments.

that hydrogen is not required for the isomerisation reaction over palladium. The lack of isomerisation observed for THPMI may be due to a higher activation energy of reaction or alternatively an activated adsorption process.

The isomerisation experiment was repeated at 90 °C with 70 times the catalyst mass and extended to six hours. No isomerisation products were detected by ¹H NMR. Gas chromatography analysis indicated that dehydrogenation of THPMI to PMI had occurred as well as its hydrogenation to HHPMI in ratios that differ from the improbable termolecular disproportionation reaction. Moreover, the concentration of E-PMI was approximately constant whilst E-THPMI decreased in concentration. This suggests a transfer hydrogenation reaction has occurred. Interestingly, more *trans*-HHPMI formed than *cis*-HHPMI which requires an isomerisation process to account for its formation. As E-THPMI lacks the steric protection THPMI has, this may indicate that THPMI isomers are rapidly hydrogenated using *in-situ* generated hydrogen.

The isomerisation reaction alone cannot account for the rise in the hydrogen reaction order with temperature. Vannice and associates have previously invoked the formation of hydrogen-deficient aromatic species chemisorbed on the surface during the hydrogenation of benzene,^{15,17,18,22,23,73-76} but not toluene and the xylenes on palladium catalysts.^{16,77} This process is distinctly different to the addition process and is usually described as a hydrogen exchange reaction, more commonly studied in the presence of deuterium gas. For example, H₂-D₂ exchange reactions involving benzene and alkyl-substituted benzenes (including substitution of the alkyl substituents) are observed, which cannot be explained by a Horvut-Polanyi reversible stepwise addition process due to differing dependencies on *inter alia* particle size, hydrogen pressure, and temperature.^{68,78,79} Moreover, although a tilted species has been observed using surface science⁸⁰⁻⁸² and density-functional methods,^{83,84,84} this species is considered to be chemisorbed and is instead a result of energy minimisation on the surface.

The formation of such species on the surface can be written as:



where *A* and *AH*₋₁ represent an aromatic compound and partially dehydrogenated compound, and *S* and * are adsorption sites. The surface coverage for the dehydrogenated species is expressed as:¹⁵

$$\theta_{AH_{-1}-S} = \frac{K_{D_1}}{K_{H_2}^{0.5} C_{H_2}^{0.5}} \theta_{A-S} \quad (4.29)$$

Thus, the concentration of such species is inversely proportional to the square root of hydrogen pressure.

Thermodynamic adsorption parameters for mono-dehydrogenated species (extracted from kinetic rate expressions fitted to experimental data) are shown in Figure 4.26 with those for

benzene and cyclohexene discussed above. The adsorption of the singular dehydrogenated species is only slightly exothermic and thus the surface equilibrium constant only changes mildly with temperature. As the adsorption of cyclohexene is weaker than that of benzene, the dehydrogenated species would inhibit the binding of cyclohexene more than benzene if a single adsorption site for unsaturated compounds is assumed. Consequently, this would mean that the presence of such species, favoured by lower hydrogen pressures and higher temperatures, would actually be *beneficial* for selectivity to the partially reduced product, which is in contrast to what is observed experimentally. Therefore, it does not seem probable that these species exist in a high concentration on the surface, in agreement with the kinetic modelling of toluene and the xylenes over palladium catalysts by Vannice and Rahaman.^{16,77}

Several additional explanations for the increase in hydrogen reaction order with rising temperature are: (i) the rate-determining step changes at higher temperatures and (ii) the hydrogen coverage changes as temperature is increased. The first explanation was observed by Sabbe *et al.* in *ab initio* kinetic modelling where the rate-determining step shifted from the second addition to the third addition above 425 K on the Pd(111) surface,²⁷ but no such calculations were performed in the current project. The second explanation was invoked by Chou and Vannice during the hydrogenation of benzene and was supported by their kinetic models. No kinetic modelling was accomplished in this work and would need to be performed to evidence this hypothesis.

4.3.3.3 The effect of temperature and pressure on the relative surface equilibrium constant

Figure 4.28 shows the effect of temperature and hydrogen pressure on the $K'_{\text{PMI}} k_{\text{PMI}} / K'_{\text{EPMI}} k_{\text{EPMI}}$ term outlined in Equation 4.4 using the initial investigation data; if the other data outlined is used instead, the results do not change. This term remains constant at approximately 1.87 if the above data procedure is utilised. If E-PMI hydrogenation were to have a different dependence on hydrogen pressure, a deviation as a function of pressure would be expected. As this is not observed, this supports the assumption that PMI and E-PMI react with, and depend equally upon, the same reactive hydrogen species.

Given that the surface equilibrium constants and rate constants depend on temperature, the fact that no temperature effects are observed is quite interesting. Assuming once again that k_{PMI} and k_{EPMI} are equal, a plot of the relative equilibrium constant *versus* the reciprocal of temperature allows the relative enthalpy, $\delta\Delta H$, and entropy of adsorption, $\delta\Delta S$, to be evaluated according to a modified van't Hoff equation (Equation 4.30).

$$\ln \frac{K_{\text{PMI}}}{K_{\text{EPMI}}} = \frac{-\delta\Delta H}{RT} + \frac{\delta\Delta S}{R} \quad (4.30)$$

As a line of best fit through this data has a very small gradient, it indicates the heats of adsorption of each compound are almost equal. Bera *et al.* found that the heats of adsorption

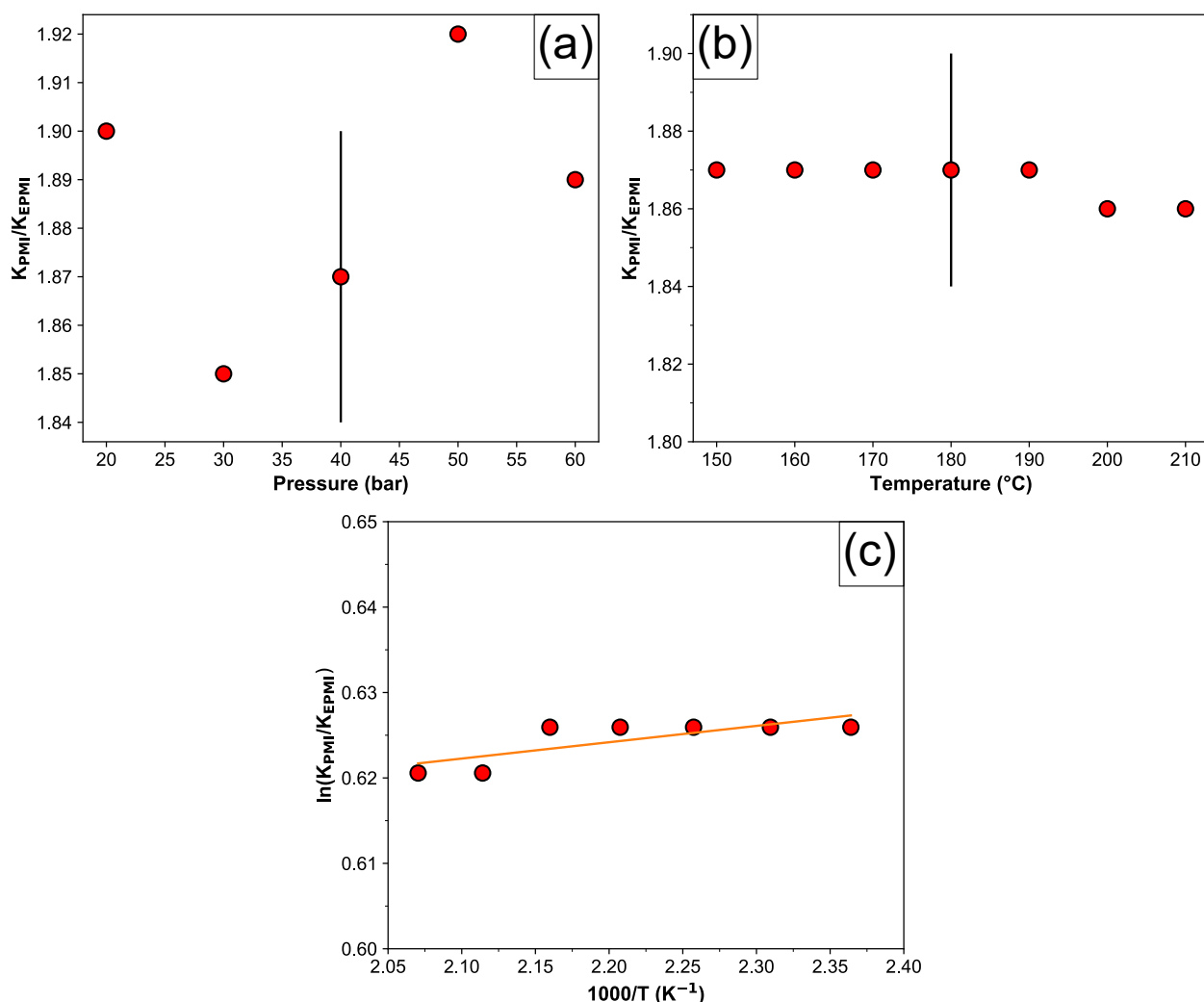


Figure 4.28: Plots of K_{PMI}/K_{EPMI} versus pressure (a) and temperature (b). (c) Modified van't Hoff plot for K_{PMI}/K_{EPMI} .

of benzene, toluene, and *o*-xylene on platinum on ZSM-5 were approximately equal to 55 kJ mol^{-1} .²⁸ Moreover, Singh and Vannice found the adsorption heat for benzene on a palladium on alumina catalysts equals 46 kJ mol^{-1} .⁷⁵ Shim *et al.* obtained similar heats of adsorption for toluene and *o*-xylene (45.2 and 46.5 kJ mol^{-1} , respectively), but did record a lower value for benzene (37.3 kJ mol^{-1}).⁸⁵ However, the chemisorption enthalpies of these substrates was calculated to increase from with number of substituents over nickel supported on silica and zeolite KY, with the adsorption of benzene also found to be roughly 20 kJ mol^{-1} higher than the platinum catalysts.²⁰ In this example, the decreasing surface equilibrium constants with increasing substitution was due to the loss of entropy upon adsorption.²⁰ Consequently, this suggests that loss of entropy upon adsorption, possibly relating to the ethyl chain, is responsible for the kinetic behaviour of E-PMI.

4.3.4 Apparent activation energies and compensation

A sympathetic relationship is commonly observed between the natural logarithm of the Arrhenius factor (A_{app}) and the experimentally observed activation energy (E_{app}), termed “compensation” or “compensation effect”, and is described by:

$$\ln A_{app} = mE_{app} + c \quad (4.31)$$

where m is equal to:

$$m = (T_i R)^{-1}$$

with R being the gas constant and T_i the isokinetic temperature (i.e. the temperature at which all reactions proceed at the same rate).⁸⁶ The experimentally determined activation energies and the logarithm of Arrhenius factors are presented in Figure 4.29. It is evident that there exists a linear relationship for these values, with the exception of a small deviation for the experiments conducted at 50 bar hydrogen pressure (though the error range on these values conforms to the relationship). The absence of overlap between the data can be ascribed to the inhibiting effect of PMI on the rate of E-PMI hydrogenation. This results in the $\ln A_{app}$ term, ultimately the rate at infinite temperature, being lower than the value that would be obtained if it were hydrogenated alone. The isokinetic temperature for PMI and E-PMI equate to 387 ± 14 K and 385 ± 51 K, respectively, though it should be noted that this prediction was not verified experimentally. That said, criteria outlined by Bond *et al.*,⁸⁶ namely that (i) the highest value of E_{app} is more than 50% greater than the lowest, (ii) the reported values are outside the statistically error ranges, and (iii) E_{app} varies rationally with the experimental variable, are satisfied.

The physical origin of the T_i term is contested. One explanation forwarded by Larsson states its origin lies in the “selective energy transfer at the active site” and that one function of

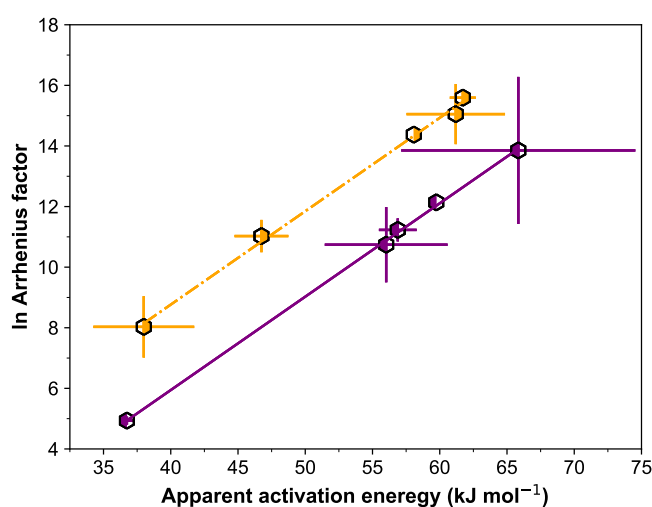


Figure 4.29: Compensation plot for PMI and E-PMI hydrogenation from the apparent kinetic values presented in Table 4.3.

the catalyst is “to supply energy into that vibrational mode of the reactant that most effectively takes the system to the activated state”.⁸⁷⁻⁸⁹ The system is then treated as a “coupled, damped, oscillation system of classical physics”⁸⁷⁻⁸⁹ and derives the following equation:

$$T_i = N_A \hbar c R^{-1} (\nu^2 - \omega^2) \omega^{-1} (\pm 0.5\pi - \arctan[0.5\nu\omega(\nu^2 - \omega^2)]^{-1}) \quad (4.32)$$

where N_A is Avogadro's number, c is the speed of light, R is the gas constant, ν is the vibrational mode leading toward reaction, ω is the frequency of the heat bath and \hbar is Planck's constant. Maximum efficacy of resonance transfer occurs when $\nu = \omega$, and Equation 4.32 simplifies to:

$$T_i = \frac{N_A \hbar c}{2R\nu} = 0.719\nu \quad (4.33)$$

According to this equation, the critical frequencies of vibration are 560 ± 20 and 536 ± 71 cm^{-1} for PMI and E-PMI, respectively. Somorjai and co-workers have reported T_i values of 443 ± 22 , 393 ± 77 , and 501 ± 7 cm^{-1} for benzene reduction on various platinum surfaces,⁹⁰⁻⁹² whereas using the T_i value reported by Keane gives a critical frequency of 634 ± 11 cm^{-1} for the xylenes over supported nickel catalysts.⁹³ These frequencies fall into the region of the metal- C_6H_6 , C-C-C out-of-plane stretching and ring deformation vibrational modes.⁹⁴⁻¹⁰⁰ Of these, the C-C-C out-of-plane mode is perhaps the most reasonable as Mittendorfer and Hafner found an imaginary vibrational frequency of 500 cm^{-1} at the transition state for the addition of the first hydrogen atom on the Ni(111) surface.¹⁰¹ This corresponded to the rotation of the molecule to the first partially hydrogenated intermediate.

Returning to the sensitivity of the Arrhenius parameters with temperature, this observation may be attributed to the changes in the amounts of adsorbed species as temperature is raised. The aromatic compounds display zero order behaviour, suggesting the surface concentration is invariant as it is strongly adsorbed. Hydrogen on the other hand has a reaction order between 0.5–1 depending on the temperature. An order greater than zero indicates the reactant is more weakly adsorbed and not saturating the surface. As temperature is raised, the desorption of hydrogen means the rate of reaction increases less rapidly than it would if the surface coverage were constant. The apparent activation energy values approaching a constant value suggests that the relative change in surface coverages above 50 bar hydrogen pressure is almost constant as one may anticipate at higher pressures. Nevertheless, this does not suggest the observed activation energies in this pressure region are beginning to approach the “true” values, as the desorption of hydrogen is still occurring. In the introduction, the Temkin equation was discussed (Equation 1.4) and this would indicate the “true” activation energies could be obtained by adding the enthalpy of adsorption of hydrogen multiplied by its reaction order. However, as pointed out by Bond,⁶⁸ performing this action would result in variable true activation energies, if adsorption heats are assumed to be constant, over the same catalyst, which seems improbable.

4.4 Conclusions

In this chapter, it is shown that the current industrial cyclic olefins yield of *ca.* 62 wt.%, obtained by the partial hydrogenation of GHC at 180 °C and 40 bar hydrogen pressure, can be surpassed if lower temperatures are employed. As the hydrogen pressure does not need to be increased for this improvement, it is possible to deploy this finding immediately and prevent hundreds, if not thousands, of tonnes of saturated product being produced per year, thereby alleviating the high energy process to reform the starting material. However, a possible limiting factor in the deployment of this finding is the lower reaction rate, explained by the Arrhenius equation, observed at lower temperatures. A higher hydrogen pressure could alleviate this issue, though this would require investment in new industrial equipment.

The observed sensitivity to temperature and hydrogen pressure was demonstrated to not be a consequence of an equilibrium or a mass transfer limitation as both were shown to be absent. Furthermore, as the selectivity to cyclic alkenes was constant at low conversions, attributing the temperature and pressure sensitivity of the yield to a change in reduction mechanism was discounted. Instead, the observed cyclic olefin yield enhancement was determined to be a consequence of Langmuir-Hinshelwood kinetics. Temperature effects were attributed to the larger exothermicity of aromatic adsorption, compared to cyclic alkene adsorption, leading to less competitive adsorption at higher reaction temperatures, thereby allowing the cycloalkenes to be more readily reduced. Whereas increasing hydrogen pressures led to a lowering of the surface π -allyl species, which are intermediates in isomerisation reactions and lead to the production of less sterically hindered alkenes. This effect was observed for E-THPMI, which contains the double bond adjacent to the bridging carbon atoms, and displayed lower yields than THPMI, which contains the double bond between the bridging carbon atoms, under all studied conditions. This strong sensitivity suggests further yield enhancements in this process may be possible if the synthesis of GHC is optimised to produce more PMI in favour of E-PMI.

4.5 References

- [1] S. Tadepalli, G. K. Tamy and A. P. Narula, *Circular economy methods of preparing unsaturated compounds*, US10435345B2, Oct. 2019.
- [2] Podkolzin, *Palladium catalysts supported on carbon for hydrogenation of aromatic hydrocarbons*, US20200001274A1, Jun. 2020.
- [3] C. Lopez Cruz, *Private communication*, 2018.
- [4] B. Li, X. Lichun and G. Yuncui, *Method for preparing polymethyl substituted tetrahydroindane by selective hydrogenation of polymethyl substituted indane*, CN1117037A, Feb. 1996.

- [5] L. Foppa and J. Dupont, *Chem. Soc. Rev.*, 2015, **44**, 1886–1897.
- [6] A. Borodziński and G. C. Bond, 2008, **50**, 379–469.
- [7] S. Siegel, J. Outlaw Jr and N. Garti, *J. Catal.*, 1979, **58**, 370–382.
- [8] D. E. Grove, *Platin. Mater. Rev.*, 2002, **46**, 92.
- [9] *Carbon Materials for Catalysis*, ed. P. Serp and J. L. Figueiredo, John Wiley & Sons, Inc., Hoboken, NJ, USA, 2008.
- [10] W. Kiciński and S. Dyjak, *Carbon*, 2020, **168**, 748–845.
- [11] Y. H. C. Chin, M. García-Diéguez and E. Iglesia, *J. Phys. Chem. C*, 2016, **120**, 1446–1460.
- [12] M. Thommes, K. Kaneko, A. V. Neimark, J. P. Olivier, F. Rodriguez-Reinoso, J. Rouquerol and K. S. Sing, *Pure Appl. Chem.*, 2015, **87**, 1052–1069.
- [13] J. Rouquerol, P. Llewellyn and F. Rouquerol, in *Stud. Surf. Sci. Catal.*, 2007, vol. 144, pp. 49–56.
- [14] Z. Q. Li, C. J. Lu, Z. P. Xia, Y. Zhou and Z. Luo, *Carbon*, 2007, **45**, 1686–1695.
- [15] P. Chou and M. A. Vannice, *J. Catal.*, 1987, **107**, 140–153.
- [16] M. Vasiur Rahaman and M. A. Vannice, *J. Catal.*, 1991, **127**, 251–266.
- [17] S. Lin and M. Vannice, *J. Catal.*, 1993, **143**, 539–553.
- [18] S. Lin and M. Vannice, *J. Catal.*, 1993, **143**, 554–562.
- [19] W. Taylor, *J. Catal.*, 1967, **9**, 99–103.
- [20] M. A. Keane and P. M. Patterson, *J. Chem. Soc. Faraday Trans.*, 1996, **92**, 1413.
- [21] M. Schoenmaker-Stolk, J. Verwijs, J. Don and J. Scholten, *Appl. Catal.*, 1987, **29**, 73–90.
- [22] J. Yoon and M. A. Vannice, *J. Catal.*, 1983, **82**, 457–468.
- [23] K. J. Yoon, P. L. Walker, L. N. Mulay and M. A. Vannice, *Ind. Eng. Chem. Prod. Res. Dev.*, 1983, **22**, 519–526.
- [24] C. P. Rader and H. A. Smith, *J. Am. Chem. Soc.*, 1962, **84**, 1443–1449.
- [25] A. Wheeler, *Adv. Catal.*, 1951, **3**, 249–327.

- [26] G. C. Bond, D. A. Dowden and N. Mackenzie, *Trans. Faraday Soc.*, 1958, **54**, 1537–1546.
- [27] M. K. Sabbe, G. Canduela-Rodriguez, J. F. Joly, M. F. Reyniers and G. B. Marin, *Catal. Sci. Technol.*, 2017, **7**, 5267–5283.
- [28] T. Bera, J. W. Thybaut and G. B. Marin, *ACS Catal.*, 2012, **2**, 1305–1318.
- [29] H. Spod, M. Lucas and P. Claus, *ChemCatChem*, 2016, **8**, 2659–2666.
- [30] C. Lopez Cruz, *Private communication*, 2021.
- [31] E. Elemensov, P. Zanolina, B. Zhanabaev and B. Utelbaev, *Zhurnal Fiz. Khimii*, 1988, **62**, 2515–2517.
- [32] C. U. Odenbrand and S. T. Lundin, *J. Chem. Technol. Biotechnol.*, 1980, **30**, 677–687.
- [33] J. Struijk, M. D'Angremond, W. L.-d. Regt and J. Scholten, *Appl. Catal. A Gen.*, 1992, **83**, 263–295.
- [34] J. Ning, J. Xu, J. Liu and F. Lu, *Catal. Letters*, 2006, **109**, 175–180.
- [35] J. Wang, Y. Wang, S. Xie, M. Qiao, H. Li and K. Fan, *Appl. Catal. A Gen.*, 2004, **272**, 29–36.
- [36] C. Milone, G. Neri, A. Donato, M. Musolino and L. Mercadante, *J. Catal.*, 1996, **159**, 253–258.
- [37] R. M. Rioux, B. B. Hsu, M. E. Grass, H. Song and G. A. Somorjai, *Catal. Letters*, 2008, **126**, 10–19.
- [38] Y. Zhao and D. G. Truhlar, *Theor. Chem. Acc.*, 2008, **119**, 525.
- [39] S. Grimme, J. Antony, S. Ehrlich and H. Krieg, *J. Chem. Phys.*, 2010, **132**, 154104.
- [40] J. Chai and M. Head-Gordon, *Phys. Chem. Chem. Phys.*, 2008, **10**, 6615.
- [41] C. Adamo and V. Barone, *J. Chem. Phys.*, 1999, **110**, 6158–6170.
- [42] M. Ernzerhof and G. E. Scuseria, *J. Chem. Phys.*, 1999, **110**, 5029–5036.
- [43] L. Goerigk and S. Grimme, *Phys. Chem. Chem. Phys.*, 2011, **13**, 6670.
- [44] T. H. Dunning, *J. Chem. Phys.*, 1989, **90**, 1007–1023.
- [45] NIST, *Benzene*, <https://webbook.nist.gov/cgi/cbook.cgi?ID=71-43-2>.
- [46] NIST, *Cyclohexene*, <https://webbook.nist.gov/cgi/cbook.cgi?ID=110-82-7>.

- [47] NIST, *Cyclohexane*, <https://webbook.nist.gov/cgi/cbook.cgi?ID=110-82-7>.
- [48] NIST, *Hydrogen*, <https://webbook.nist.gov/cgi/cbook.cgi?ID=1333-74-0>.
- [49] NIST, *1H-Indene, octahydro-, cis-*, <https://webbook.nist.gov/cgi/cbook.cgi?ID=C4551513^&'Mask=2>.
- [50] NIST, *1H-Indene, octahydro-, trans-*, <https://webbook.nist.gov/cgi/cbook.cgi?ID=C3296502^&'Mask>.
- [51] NIST, *Indane*, <https://webbook.nist.gov/cgi/cbook.cgi?ID=C496117^&'Mask=2>.
- [52] A. Stanislaus and B. H. Cooper, *Catal. Rev.*, 1994, **36**, 75–123.
- [53] S. A. Ali, *Pet. Sci. Technol.*, 2007, **25**, 1293–1304.
- [54] J. Kilpatrick, E. Prosen, K. Pitzer and F. Rossini, *J. Res. Natl. Bur. Stand.*, 1946, **36**, 559.
- [55] C. G. Frye and A. W. Weitkamp, *J. Chem. Eng. Data*, 1969, **14**, 372–376.
- [56] C. N. Satterfield, *Mass transfer in heterogeneous catalysis*, M.I.T. Press, 1969.
- [57] G. W. Roberts, in *Catalysis in Organic Synthesis*, ed. P. N. Rylander and H. Greenfield, Academic Press, 1976, pp. 1–48.
- [58] IUPAC, *Compendium of Chemical Terminology*, Blackwell Scientific Publications, Oxford (1997). Online version (2019-) created by S. J. Chalk., Research Triangle Park, NC, 2014.
- [59] B. E. Poling, J. M. Prausnitz and J. P. O'Connell, *The Properties of Gases and Liquids*, McGraw-Hill, 5th edn., 2000.
- [60] C. Wilke and P. Chang, *A.I.Ch.E. J.*, 1955, 264–270.
- [61] R. B. Scott and F. G. Brickwedde, *J. Chem. Phys.*, 1937, **5**, 736–744.
- [62] P. B. Weisz and C. D. Prater, *Adv. Catal.*, 1954, **6**, 143–196.
- [63] P. B. Weisz, *Zeitschrift für Phys. Chemie*, 1957, **11**, 1–15.
- [64] G. W. Watson, R. P. K. Wells, D. J. Willock and G. J. Hutchings, *J. Phys. Chem. B*, 2001, **105**, 4889–4894.
- [65] G. Canduela-Rodriguez, M. K. Sabbe, M. F. Reyniers, J.-F. Joly and G. B. Marin, *J. Phys. Chem. C*, 2014, **118**, 21483–21499.
- [66] E. Gonzo and M. Boudart, *J. Catal.*, 1978, **52**, 462–471.

- [67] P. C. Aben, H. van der Eijk and J. M. Oelderik, in *Proceedings of the Fifth International Congress in Catalysis Miami Beach, Florida*, ed. J. W. Hightower, Amsterdam: North-Holland, New York, 1973, vol. 4, pp. 717–728.
- [68] G. C. Bond, *Metal-catalysed reactions of hydrocarbons*, Springer, 2006.
- [69] I. Horiuti and M. Polanyi, *Trans. Faraday Soc.*, 1934, **30**, 1164–1172.
- [70] R. Sanchez-Delgado, I. Duran, J. Monfort and E. Rodriguez, *J. Mol. Catal.*, 1981, **11**, 193–203.
- [71] B. E. Koel, D. A. Blank and E. A. Carter, *J. Mol. Catal. A Chem.*, 1998, **131**, 39–53.
- [72] M. K. Sabbe, G. Canduela-Rodriguez, M. F. Reyniers and G. B. Marin, *J. Catal.*, 2015, **330**, 406–422.
- [73] D. Poondi and M. A. Vannice, *J. Catal.*, 1996, **161**, 742–751.
- [74] P. Chou and M. A. Vannice, *J. Catal.*, 1987, **107**, 129–139.
- [75] U. K. Singh and M. A. Vannice, *AIChE J.*, 1999, **45**, 1059–1071.
- [76] S. Lin and M. Vannice, *J. Catal.*, 1993, **143**, 563–572.
- [77] M. Vasiur Rahaman and M. Albert Vannice, *J. Catal.*, 1991, **127**, 267–275.
- [78] R. van Hardeveld and F. Hartog, 1972, **22**, 75–113.
- [79] A. Cinneide and J. Clarke, *J. Catal.*, 1972, **26**, 233–241.
- [80] H. Hoffmann, F. Zaera, R. Mark Ormerod, R. M. Lambert, Lu Ping Wang and W. T. Tysoe, *Surf. Sci.*, 1990, **232**, 259–265.
- [81] W. T. Tysoe, R. M. Ormerod, R. M. Lambert, G. Zgrablich and A. Ramirez-Cuesta, *J. Phys. Chem.*, 1993, **97**, 3365–3370.
- [82] A. F. Lee, K. Wilson, R. M. Lambert, A. Goldoni, A. Baraldi and G. Paolucci, *J. Phys. Chem. B*, 2000, **104**, 11729–11733.
- [83] M. Saeys, M. F. Reyniers, G. B. Marin and M. Neurock, *J. Phys. Chem. B*, 2002, **106**, 7489–7498.
- [84] G. Canduela-Rodriguez, M. K. Sabbe, M. F. Reyniers, J.-F. Joly and G. B. Marin, *Phys. Chem. Chem. Phys.*, 2014, **16**, 23754–23768.
- [85] W. G. Shim, J. W. Lee and S. C. Kim, *Appl. Catal. B Environ.*, 2008, **84**, 133–141.
- [86] G. C. Bond, M. A. Keane, H. Kral and J. A. Lercher, *Catal. Rev.*, 2000, **42**, 323–383.

- [87] R. Larsson, *Catal. Today*, 1987, **1**, 93–99.
- [88] R. Larsson, *J. Mol. Catal.*, 1989, **55**, 70–83.
- [89] D. Lomot, W. Juszczak, Z. Karpinski and R. Larsson, *J. Mol. Catal. A Chem.*, 2002, **186**, 163–172.
- [90] K. M. Bratlie, L. D. Flores and G. A. Somorjai, *J. Phys. Chem. B*, 2006, **110**, 10051–10057.
- [91] K. M. Bratlie, C. J. Kliewer and G. A. Somorjai, *J. Phys. Chem. B*, 2006, **110**, 17925–17930.
- [92] K. M. Bratlie, Y. Li, R. Larsson and G. A. Somorjai, *Catal. Letters*, 2008, **121**, 173–178.
- [93] M. A. Keane, *J. Catal.*, 1997, **166**, 347–355.
- [94] F. S. Thomas, N. S. Chen, L. P. Ford and R. I. Masel, *Surf. Sci.*, 2001, **486**, 1–8.
- [95] S. Lehwald, H. Ibach and J. Demuth, *Surf. Sci.*, 1978, **78**, 577–590.
- [96] C. Morin, D. Simon and P. Sautet, *J. Phys. Chem. B*, 2004, **108**, 5653–5665.
- [97] I. Jungwirthová and L. Kesmodel, *Surf. Sci.*, 2000, **470**, L39–L44.
- [98] V. H. Grassian and E. L. Muetterties, *J. Phys. Chem.*, 1987, **91**, 389–396.
- [99] G. D. Waddill and L. L. Kesmodel, *Phys. Rev. B*, 1985, **31**, 4940–4946.
- [100] G.-K. Liu, B. Ren, D.-Y. Wu, S. Duan, J.-F. Li, J.-L. Yao, R.-A. Gu and Z.-Q. Tian, *J. Phys. Chem. B*, 2006, **110**, 17498–17506.
- [101] F. Mittendorfer and J. Hafner, *J. Phys. Chem. B*, 2002, **106**, 13299–13305.

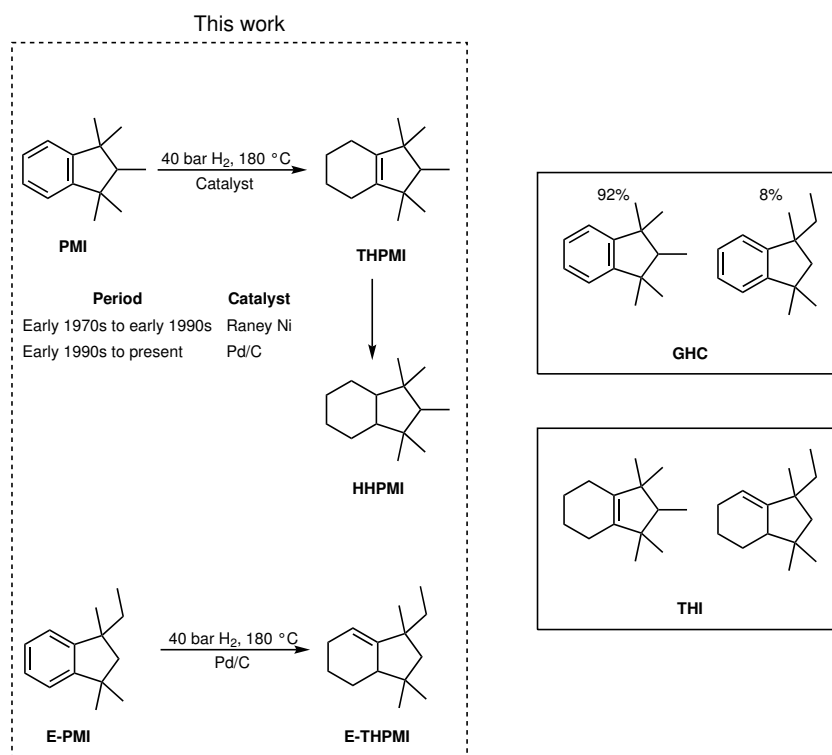
Chapter 5

The effect of metal (M = Ru, Rh, Pd, Ir, Pt) on the partial reduction of galaxolide hydrocarbon to cyclic alkenes

5.1 Introduction

IN the previous chapter, the partial reduction of GHC to tetrahydroindane products over the industrial Pd/C catalyst was studied (Scheme 5.1). The use of a palladium catalyst for this process is however surprising. Selective benzene hydrogenation towards cyclohexene is a mature industrial process performed on a scale of 160,000 tonnes per year in a tetraphasic (hydrogen, hydrocarbon, water, and catalyst) reactor using a ruthenium catalyst.¹⁻³ Since the development of this process in the 1980s, all but two literature articles have studied ruthenium-based catalysts under these optimum, industrially relevant conditions. One article employed a Rh/Al₂O₃ catalyst poisoned with mercury, which yielded similar performance to many ruthenium-based systems.^{4,5} Whilst the other article studied Pd/Al₂O₃ and Pt/Al₂O₃, which were reported as inactive for the reaction.⁶ In an early patent for the partial reduction of benzene, Drinkard screened a range of metals in a tetraphasic system.⁷ It was noted that although ruthenium-based catalysts were most selective, all other catalyst systems tested (Fe/CaCO₃, Raney cobalt, Raney nickel, Ni/CaCO₃, RhCl₃, PdCl₂, and IrCl₃) could produce the desired intermediate, albeit in lesser quantities.

The high performance of ruthenium catalysts for the partial reduction reaction was first noted by Hartog and Zwietering.⁸ They reported that Ru/C provided higher yields of dimethylcyclohexenes than Rh/C during the reduction of xylenes at atmospheric hydrogen pressure between 0–60 °C. This study also revealed that lesser intermediate yields were observed over Raney nickel, and Pd/C and Pt/C catalysts demonstrated no selectivity to dimethylcyclohexenes. The high performance of rhodium compared with palladium and platinum for the partial reduction reaction was also observed in the hydrogenation of 1,2-di- and



Scheme 5.1: The partial reduction of GHC to THPMI and E-THPMI.

1,3,5-tri-*tert*-butylbenzenes.^{9,10} Additionally, rhodium-based catalysts gave non-negligible yields of monounsaturated intermediates from 1,3- and 1,4-di-*tert*-butylbenzenes,^{11,12} various indanes,^{13,14} and in the production of the pentamethyl substituted octalins,¹⁵ though in these instances no comparisons to other metals were reported. Weitkamp researched the partial reduction of naphthalene over several metals and disclosed that Ru/C, Rh/C, and Ir/C selectively produced octalins in amounts totalling 0.2–1.9%, whereas palladium and platinum were again unselective.¹⁶

When IFF first developed a process for the preparation of tetrahydroindanes from GHC shortly after the work in the previous paragraph was published, they chose to employ Raney nickel as the catalyst and *not* ruthenium- or rhodium-based materials.¹⁷ Why Raney nickel was chosen is not clear as internal IFF documentation on this subject was not made available during the collaboration, but the choice is nevertheless interesting. Raney nickel was replaced by a Pd/C catalyst approximately 20 years later,¹⁸ but the use of both these materials is surprising if the work reviewed in the first two paragraphs is considered.

This chapter assesses the catalytic performance of 5 wt.% Ru, Rh, Pd, Ir, and Pt on graphene nanoplatelets (GNP) for the partial reduction of GHC to cyclic olefins. The catalysts have been prepared *via* an impregnation method previously reported by our group.¹⁹ Recent work by the Regalbuto group has demonstrated that metal nanoparticle surfaces are susceptible to poisoning by the “amorphous” carbon residue on the support,^{20,21} which leads to a loss of metal surface area during chemisorption experiments. Presumably, this may also affect

the behaviour of the catalyst. Therefore, each metal on GNP catalyst was subjected to two different thermal treatments, that is one sample being subjected only to a reductive treatment (denoted as “red. only”) whilst the other being subjected to a reductive treatment and an oxidative treatment (denoted as “red. + calc.”). These materials were then analysed by XRD, XPS, TGA-MS, and CO chemisorption. This preliminary work permitted the relative performance of these metals to be evaluated in the hydrogenation of GHC to cyclic alkenes under industrially relevant conditions.

5.2 Aims

- Prepare 5 wt.% Ru, Rh, Pd, Ir, and Pt on GNP catalysts and subject them to “red. only” and “red. + calc.” heat treatments.
- Characterise these materials by XRD, XPS, TGA-MS, and CO chemisorption.
- Evaluate the performance of these catalysts in the partial reduction of GHC to cyclic olefins and study any heat treatment effects.
- Vary the temperature and pressure of the system to study the reaction mechanism.
- Understand how the reaction proceeds on each supported metal catalyst and determine which metals are most suitable for this reaction.

5.3 Results and Discussion

5.3.1 Catalyst characterisation

5.3.1.1 Inductively coupled plasma mass spectrometry analysis

Inductively coupled plasma mass spectrometry (ICP-MS) analysis requires samples first be digested, that is taken into liquid form, prior to analysis. Attempts were made to analyse the as received graphene nanoplatelets (GNP) support using this method by utilising a microwave-assisted digestion procedure. The support did not, however, completely digest. This could mean that the results obtained using the filtered solution (Table 5.1) are lower than the actual values; though note that no characterisation of the undigested remnant by other methods, such as XPS or EDX, was performed to determine whether these elements (or others) were retained after this procedure. The loading of iridium is striking, even if the relatively large error is considered. This could alternatively be a consequence of spectral interferences from hafnium oxide or europium argide.²² Although iridium has been used to grow graphene films,²³ methods such as this are unrealistic to be used to produce material in large quantities owing to high costs.²⁴ Cheaper, scalable methods to prepare graphene materials involve

Table 5.1: ICP-MS characterisation of elements present in greater than 0.01 wt.% quantities in the as received graphene nanoplatelets after incomplete microwave digestion.

| Element | Composition (wt.%) ^a |
|---------|---------------------------------|
| Ir | 0.97±0.63 |
| Ca | 0.80±0.081 |
| Mg | 0.34±0.022 |
| Na | 0.12±0.017 |
| Fe | 0.091±0.0036 |
| Al | 0.060±0.0022 |
| Lu | 0.023±0.00077 |
| Sr | 0.019±0.0011 |
| Zn | 0.011±0.00043 |
| Br | 0.011±0.0043 |

^a Semi-quantitative analysis. Value given is average of three runs; error provided is the standard deviation of said runs.

the chemical, thermal, or mechanical exfoliation of graphite or graphitic oxide²⁵ and the encroachment of impurities may occur in this step or in the starting carbon material. However, XPS analysis of prepared catalysts could not detect the presence of iridium, hafnium, or europium, suggesting the surface concentration of these elements is below the detection limit, which for these elements on carbon is approximately 0.1 at %.²⁶ Further investigations into this matter are therefore required.

As the veracity of the digestion procedure was in doubt, the weight loadings of the catalyst were assumed to be equal to the nominal loadings for the “red. only” catalysts and the “red. + calc.” catalysts were taken to be fully oxidised to the metals most common oxide. This is not ideal, as trace residues of precursor material were visible on the round-bottom flask used in the synthesis of these materials, which suggests that not all of the precursor was incorporated into the final catalyst. Moreover, it is also unclear as to whether complete oxidation of the metal in the catalysts occurs under these conditions. For example, the XRD profile of the Pt/GNP “red. + calc.” catalyst only displays peaks for bulk platinum metal. Several potential methods to determine the actual weight loadings of the catalyst to alleviate this issue are discussed in the Conclusions and future work chapter (Section 6.2.3).

5.3.1.2 Nitrogen adsorption-desorption isotherms

The nitrogen adsorption-desorption isotherms measured at $-196\text{ }^{\circ}\text{C}$ for the blank support and supported catalysts are presented in Figure 5.1. Each isotherm can be classified as a composite of Type II and Type IVa isotherms due to large uptakes at the first recorded data point (at a P/P_0 value of 0.05) and the presence of hysteresis across all relative pressure values. This

indicates that micropores, mesopores, and macropores are present in these materials.

As micropores are present in this material, the use of the BET method in probing the surface areas is problematic. Therefore the criteria set forth by Rouquerol *et al.*²⁷—namely that (i) the BET C constant is positive, (ii) the $n(1 - P/P_0)$ term in the Rouquerol plot increases continuously with the relative pressure, and (iii) the relative pressure at which saturation occurs is within the BET plot—was used to assess the apparent surface areas.²⁸ The apparent surface areas and the relative pressure at which saturation occurs are stated in Table 5.2. A decrease in the apparent surface area of each catalyst is observed after impregnation of metal and thermal treatments. The lowering of apparent surface area is probably caused by a pore blocking in the micropore region. Extensive analysis of the micropore region was not possible owing to vacuum limitations on the instrument used for these measurements (the instrument used for the nitrogen sorption behaviour in the previous chapter was out of service during attempts to study these materials).

5.3.1.3 CO chemisorption and TGA-MS analysis

CO pulse chemisorption was performed on the bare support and supported catalysts at 35 °C (Table 5.2). The bare support did not have any detectable CO under these conditions, indicating that the results from the other samples are free from adsorption onto the support directly from the gas phase. CO uptake on the other materials, however, was dependent on the metal used and thermal treatment used in their preparation. Decreases in CO uptake, per gram of catalyst, after calcination are observed for ruthenium, rhodium, iridium, and platinum catalysts. The zero-uptake recorded for the Ru/GNP “red. + calc.” catalyst is surprising as Scherrer analysis of the RuO₂ (101) peak indicates a small volume-weighted particle size, d_v , of 4 nm and thus, a smaller surface-weighted particle size, d_s , would be expected as d_v must be greater than d_s (see table notes in Table 5.2 for definitions of these terms). This discrepancy could have several contributing factors. For instance, in this experiment the quantity of ruthenium in the sample tube was low as (i) only a small quantity of catalyst was used due to small amounts of sample available for analysis, and (ii) if all ruthenium metal is converted to ruthenium(IV) oxide during the calcination procedure, this would represent a 25% decrease in metal loading. Moreover, despite being widely used to study ruthenium catalysts, the adsorption stoichiometry is poorly understood as it has been suggested that the CO/Ru ratio can vary from 0.5 to 3.²⁹ It is therefore probable that a combination of these factors gives rise to few available surface sites for CO adsorption. For the rhodium, iridium, platinum, and perhaps the ruthenium catalysts, the decrease in uptake (per gram of sample) is probably to be a composite of sintering and oxidation of the metal nanoparticles, leading to fewer available surface sites.

An increase in CO uptake was observed for the Pd/GNP “red. + calc.” catalyst. This could not be attributed to experimental error as the associated error between samples was

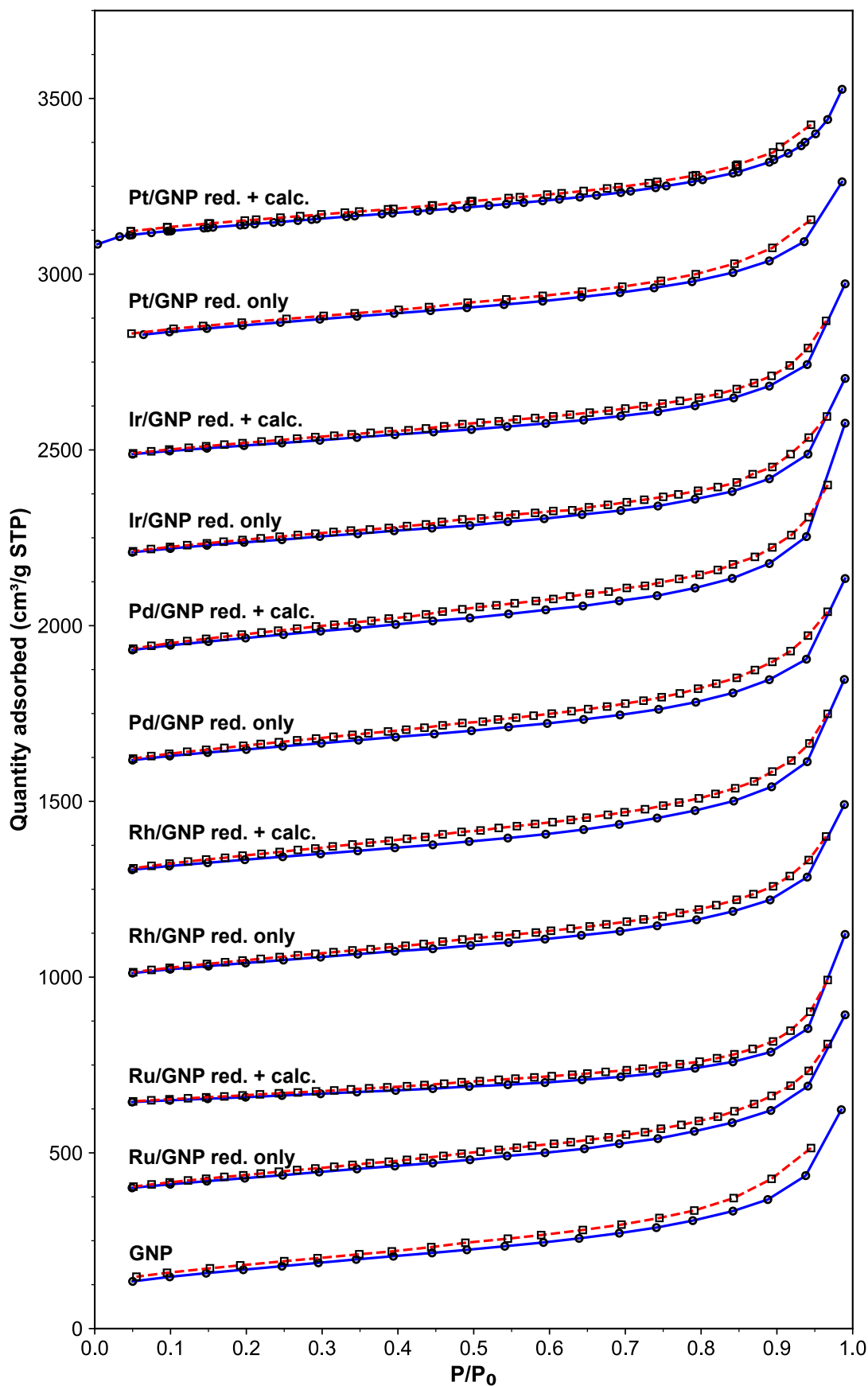


Figure 5.1: Nitrogen adsorption-desorption isotherms recorded at $-196\text{ }^{\circ}\text{C}$ for bare GNP and GNP-supported ruthenium, rhodium, palladium, iridium, and platinum “red. only” and “red. + calc.” catalysts.

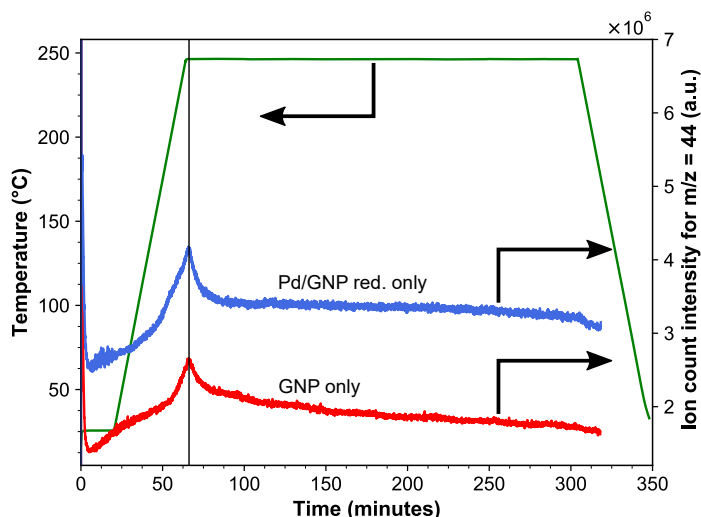


Figure 5.2: TGA-MS data for bare GNP and a Pd/GNP “red. only” catalyst. Note total ion count intensity has been smoothed using the Solvay-Golay filter.

found to be less than 2% during repeat measurements. Regalbuto has previously attributed lower than anticipated gas uptakes during chemisorption measurements to the decoration of the metal nanoparticles with carbon from the support during the catalyst’s preparation.^{20,21} A TGA-MS study was therefore conducted to investigate whether a similar effect was present in this work. The bare GNP support and the Pd/GNP “red. only” catalyst were subjected to the conditions used in the calcination procedure and the evolution of CO₂ was monitored by mass spectrometry. As shown in Figure 5.2, similar temperature-programmed oxidation profiles are observed with both these materials when the ion count is filtered for analytes with a m/z of 44. The detected mass changes in these samples was below 3%, which indicates the quantity of material removed during thermal treatment is small. With this data, it is not possible to definitively conclude that carbon decoration is occurring, as palladium would be expected to catalyse and hence lower the temperature of the removal of such species. Nevertheless, the removal of a carbonaceous species and the higher CO uptake requires further investigation.

5.3.1.4 X-Ray diffraction

X-Ray diffractograms for the blank support, “red. only”, and “red. + calc.” catalysts are presented in Figure 5.3. For the bare graphene nanoplatelets, Bragg peaks attributable to the (002), (100), (101), (004), and (110) reflections are located at 2θ angles of 26.7, 42.6, 43.6, 54.8, and 77.6°, respectively. This indicates that the GNP support is a highly crystalline material. These peaks are broader than those observed in pristine graphite, which is anticipated as there are fewer layers of graphene in this material. It is evident that the support structure is preserved during metal impregnation and subsequent heat treatments because no changes to the diffraction peaks of this material are observed. This evidences the hypothesis that the decrease is apparent surface areas of the catalysts, determined by use of the Rouquerol

Table 5.2: Properties of the catalysts used in this chapter.

| Material | Nominal loading (wt.%) | Apparent surface area ^a (m ² g ⁻¹) | P/P_0^{nb} | CO uptake ^c (mmol g ⁻¹) | Metal particle size (nm) | |
|-----------------------|---------------------------|---|--------------|---|--------------------------|----------------------------|
| | | | | | d_s^d | d_v^e |
| Bare GNP | 0 | 600 | 0.057 | 0 | n.a. | n.a. ^f |
| Ru/GNP “red. only” | 5.0 | 460 | 0.068 | 7.26 | 8.8 | n.a. ^f |
| Ru/GNP “red. + calc.” | 3.8 | 220 | 0.083 | 0 | n.a. | 4 (RuO ₂ (101)) |
| Rh/GNP “red. only” | 5.0 | 500 | 0.060 | 20.3 | 3.9 | n.a. ^f |
| Rh/GNP “red. + calc.” | 4.1 | 480 | 0.066 | 11.2 | 3.8 | n.a. ^f |
| Pd/GNP “red. only” | 5.0 | 590 | 0.060 | 6.13 | 8.6 | 4 (Pd(111)) |
| Pd/GNP “red. + calc.” | 4.3 | 520 | 0.057 | 6.37 | 3.5 | 3 (PdO(101)) 25 (Pd(111)) |
| Ir/GNP “red. only” | 5.0 | 490 | 0.062 | 7.42 | 3.9 | n.a. ^f |
| Ir/GNP “red. + calc.” | 4.3 | 400 | 0.074 | 3.98 | 6.2 | n.a. ^f |
| Pt/GNP “red. only” | 5.0 | 550 | 0.054 | 2.31 | 13 | 30 |
| Pt/GNP “red. + calc.” | 4.3 | 500 | 0.061 | 2.09 | 12 | 30 |

^a Determined using the BET method using the criteria set forth by Rouquerol^{27,28} between P/P_0 values of 0.0494 and 0.198.

^b P/P_0 value where monolayer is formed.

^c CO uptake determined using CO pulse chemisorption.

^d Surface-weighted particle size ($d_s = \frac{\sum n_i d_i^3}{\sum n_i d_i^2}$). Particle size assuming a hemisphere particle shape and weight loading equal to nominal metal loading.

^e Volume-weighted particle size ($d_v = \frac{\sum n_i d_i^4}{\sum n_i d_i^3}$). Calculated using the Scherrer equation.

^f Not applicable due to no added metal or no metal Bragg peaks observed.

BET method (Section 2.5.4.1.1), is a consequence of pore blockage effects and not due to deterioration of the bulk structure of the support.

The XRD patterns for the supported catalysts display a number of interesting similarities, particularly when the nature of the precursor is considered. Catalysts prepared from molecular chlorides—namely, RuCl_3 , RhCl_3 , and IrCl_3 —do not display diffraction peaks in the red. only catalysts. One possibility is that the synthesised phase is amorphous, as XRD requires crystallinity for detection. In this regard, Freakley *et al.* reported that the structure of bulk hydrated iridium oxide is amorphous,³⁰ which could explain the absence of peaks for this catalyst. The absence of peaks for the Ru/GNP red. only and both rhodium catalysts could be due to particle sizes being below the detection limit of the instrument, as the results from CO chemisorption suggest that well-dispersed nanoparticles exist. Particle growth is observed for each catalyst after the calcination procedure. This effect is most notable for the ruthenium catalyst, as a broad peak, corresponding to RuO_2 , is clearly visible in the diffractogram after calcination (Figure 5.3b red line). Very broad diffraction peaks for Rh_2O_3 and IrO_2 are also observed for the “red. + calc.” rhodium and iridium catalysts, respectively, but these are too broad to be reliably fitted.

On the other hand, the palladium and platinum catalysts were prepared using hydrogen tetrachloropalladate and chloroplatinic acids, where the metal is present in the anion, and display diffraction peaks in the XRD pattern. This indicates that (i) the metal in this catalyst has an ordered structure and (ii) the nanoparticles are of a detectable size. The diffractogram of the Pd/GNP “red. only” shows diffraction peaks for the (111), (200), and (220) planes of palladium metal. The intensity of the Pd(111) peak is sufficiently intense to note that the base of the peak is broad whilst the tip is sharp. This suggests that a bimodal particle size distribution may be present.³¹ Calcination results in the broad base peak of the Pd(111) disappearing and a new peak emerging at $34^\circ 2\theta$, which is attributable to the PdO(002) and PdO(101) peaks. The sharper region of the peak remains, suggesting that the bulk structure of the large palladium crystallite is not oxidised during the calcination step.

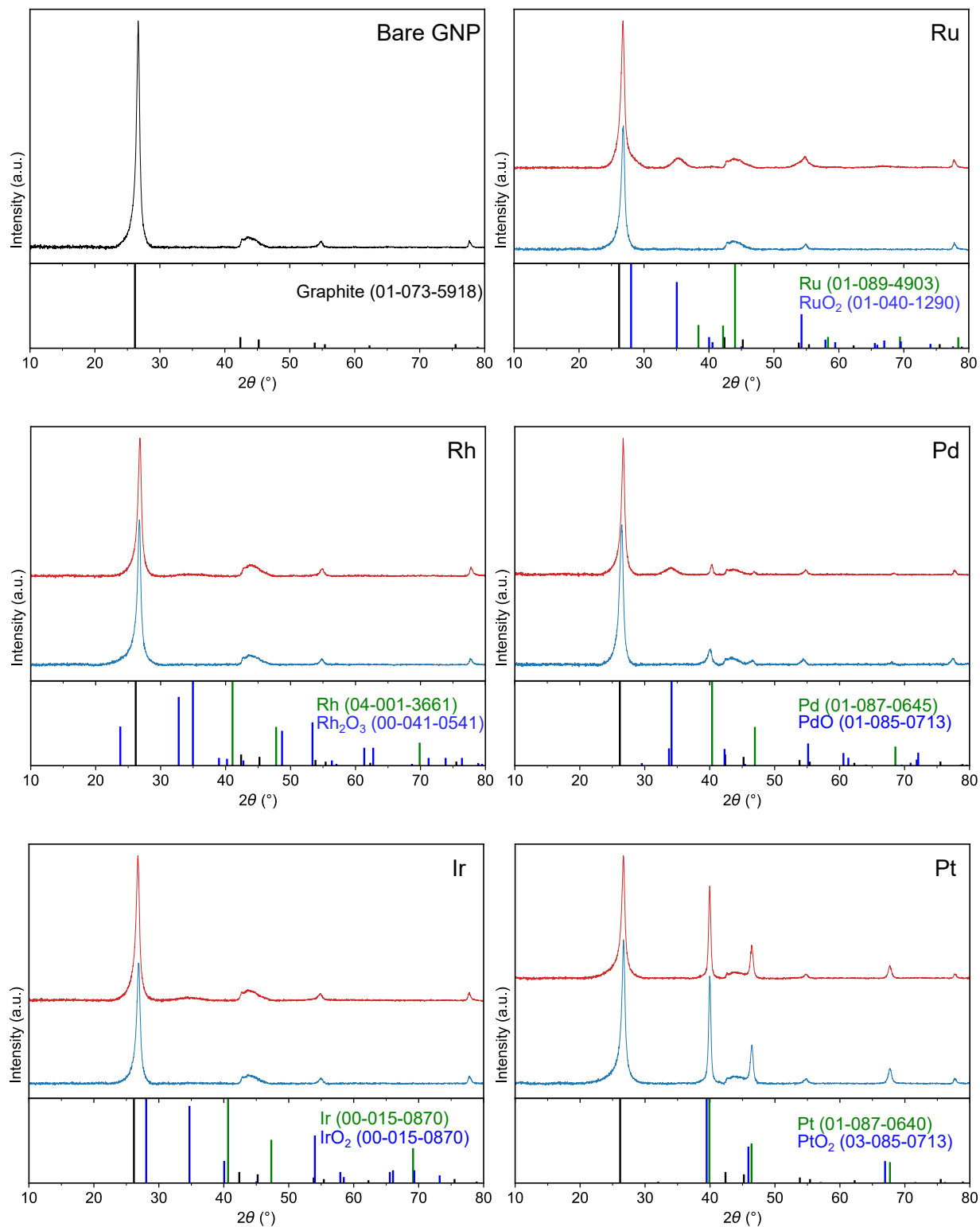


Figure 5.3: X-ray diffractograms for bare GNP and GNP-supported ruthenium, rhodium, palladium, iridium, and platinum “red. only” and “red. + calc.” catalysts. *Legend:* “red. only” (—) and “red. + calc.” (—).

5.3.2 Kinetic data

5.3.2.1 Effect of calcination on rate

The rates of GHC hydrogenation, expressed as the specific rate and turnover frequency (TOF), before and after calcination are presented in Figure 5.4. For all catalysts, an increase in both specific rate and TOF is observed for each catalyst after the calcination procedure. If the carbon support has indeed poisoned the nanoparticle surface prior to calcination, as alluded to previously, then a lower specific rate would be expected; the enhancement also observed for the TOFs meanwhile is less expected. The purpose of expressing a reaction rate as a TOFs is to normalise the rate to the number of surface atoms (or in some instances area), as the rate of reaction typically correlates linearly with this value. When there is no correlation between these terms, then the reaction is considered to be structure sensitive. Aromatic hydrogenation is generally not considered to be a structure sensitive reaction for practical materials unless very small particles are present (*ca.* > 1 nm)³² or an active metal is diluted with an inactive component (such as Pd-Cu nanoparticles).^{33,34} In these instances, it is considered to be an effect of geometric rather than electronic origin, as kinetic modelling estimates that three atoms are required for aromatic adsorption.³⁴ A similar effect could be present here, since the suspected removal of the carbonaceous material during the calcination step could break up the ensembles required for PMI and E-PMI to adsorb onto the surface. However, the contribution of the sintering of smaller, possibly inactive nanoparticles cannot be ruled out without further characterisation.

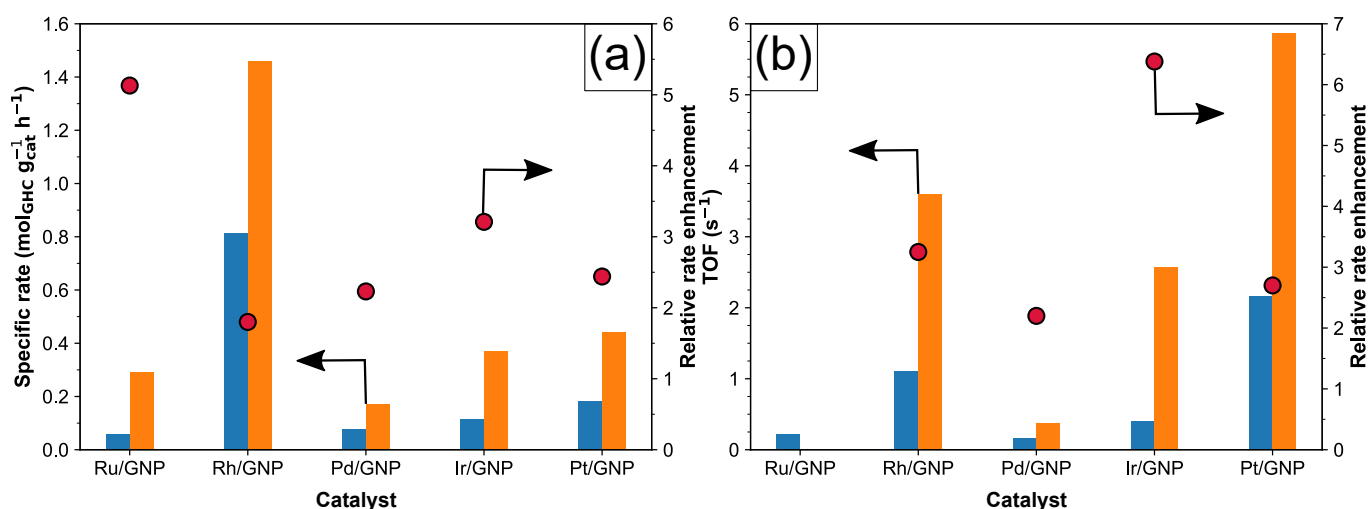


Figure 5.4: The effect of calcination on the specific rate (a) and the turnover frequency (b) with comparisons to the rate enhancement. Legend: “Red. only” (■), “Red. + calc.” (■), and relative rate enhancement (●).

5.3.2.2 Reaction orders and apparent activation energies for the “red. + calc.” catalysts

The reaction orders for PMI and E-PMI are dependent on the metal used for the reaction. For instance, on palladium the reaction orders for PMI and E-PMI are zero and negative one, respectively, according to integral analysis of the concentration time profiles. This is in accordance with what was observed over the industrial catalyst in the previous chapter. In contrast, the order of reaction with respect to PMI and E-PMI over ruthenium, rhodium, and platinum are both found to be zero when analysed using the integral method. This is further supported by analysis using log-log plots for the consumption of each substrate (Section 5.3.2.3). These findings indicate that on palladium catalysts the adsorption of PMI can inhibit the adsorption of E-PMI, whilst on ruthenium, rhodium, iridium, and platinum catalysts this inhibition is reduced or absent.

The reaction order with respect to hydrogen for the “red. + calc.” catalysts are presented in Figure 5.5 and summarised in Table 5.3. High errors are observed in each case, which can be attributed to the small number of data points used for the calculation. The reaction order for hydrogen over palladium at 170 °C between 40 and 60 bar hydrogen pressure equates to 0.6 ± 0.3 which is in good agreement with the value of 0.8 ± 0.1 found for the industrial catalyst. This indicates that similar kinetics exists for PMI and E-PMI reduction over palladium surfaces. Hydrogen orders over other metals are all greater than unity, which requires either the formation of hydrogen-deficient surface species or the rate determining step is not the first or second step. In the previous chapter, the selective energy transfer model was discussed, and it was shown that according to this theory, the transition state for nickel, palladium, and platinum catalysts probably involved the addition of hydrogen during a C-C-C out-of-plane vibration. Therefore, it seems more probable that the higher orders observed over these catalysts originate due to the formation of hydrogen-deficient surface species.

Apparent activation energies were evaluated at 50 bar between 160 and 180 °C and the resulting Arrhenius plots are shown in Figure 5.5 with the linear regression analysis summarised in Table 5.3. As with hydrogen reaction orders, errors are fairly large for these values. The apparent activation energies for PMI and E-PMI at 50 bar hydrogen pressure are within the expected range of $50 \pm 20 \text{ kJ mol}^{-1}$, with the exception of the Ir/GNP “red. + calc.” catalyst, which displays apparent activation energies of approximately 0 kJ mol^{-1} . Rate maxima are commonly observed for the gas phase hydrogenation of benzene and in some cases the liquid hydrogenation of aromatics.^{35,36} This is attributed to the rate constant increasing and the adsorption equilibrium constant decreasing with rising temperatures.³⁷ In the liquid phase, however, Singh and Vannice argue that the higher thermodynamic activity of benzene at a catalysts' surface in the liquid phase does not allow a rapid decline in surface coverage to occur as it does in the gas phase.³⁸ In addition, they state that observation of this behaviour could instead be attributable to catalyst deactivation. Traversing the temperature maxima is

Table 5.3: Kinetic parameters for the GNP-supported red. + calc. Ru, Rh, Pd, Ir, and Pt catalysts.

| Catalyst | PMI | | E-PMI | |
|------------------------------------|---|---|---|---|
| | Arrhenius parameter ^a lnA | Hydrogen reaction order ^b E_a^{app} | Arrhenius parameter ^a lnA | Hydrogen reaction order ^b E_a^{app} |
| Ru/GNP "red. + calc." | 16.2±5.6 | 64.1±20 | 13.1±5.9 | 62.0±22 |
| Rh/GNP "red. + calc." | 11.0 | 35.8±6.7 | 9.44±2.1 | 39.8±7.8 |
| Pd/GNP "red. + calc." | 14.7±3.2 | 58.3±12 | 14.0±1.2 | 66.5±4.3 |
| Ir/GNP "red. + calc." | 1.00±2.3 | 0.751±8.6 | -3.52 | -6.81±8.0 |
| Pt/GNP "red. + calc." ^c | 12.8 | 40.8 | 9.44 | 37.9 |
| | | | | 0.79±3 |
| | | | | 1.4±0.6 |
| | | | | 0.77±0.2 |
| | | | | 2.2±1 |
| | | | | 1.2 |

^a Determined between 160 and 180 °C at 50 bar hydrogen pressure.

^b Determined at 170 °C and between 40 and 60 bar hydrogen pressure.

^c Kinetic parameters determined using two points.

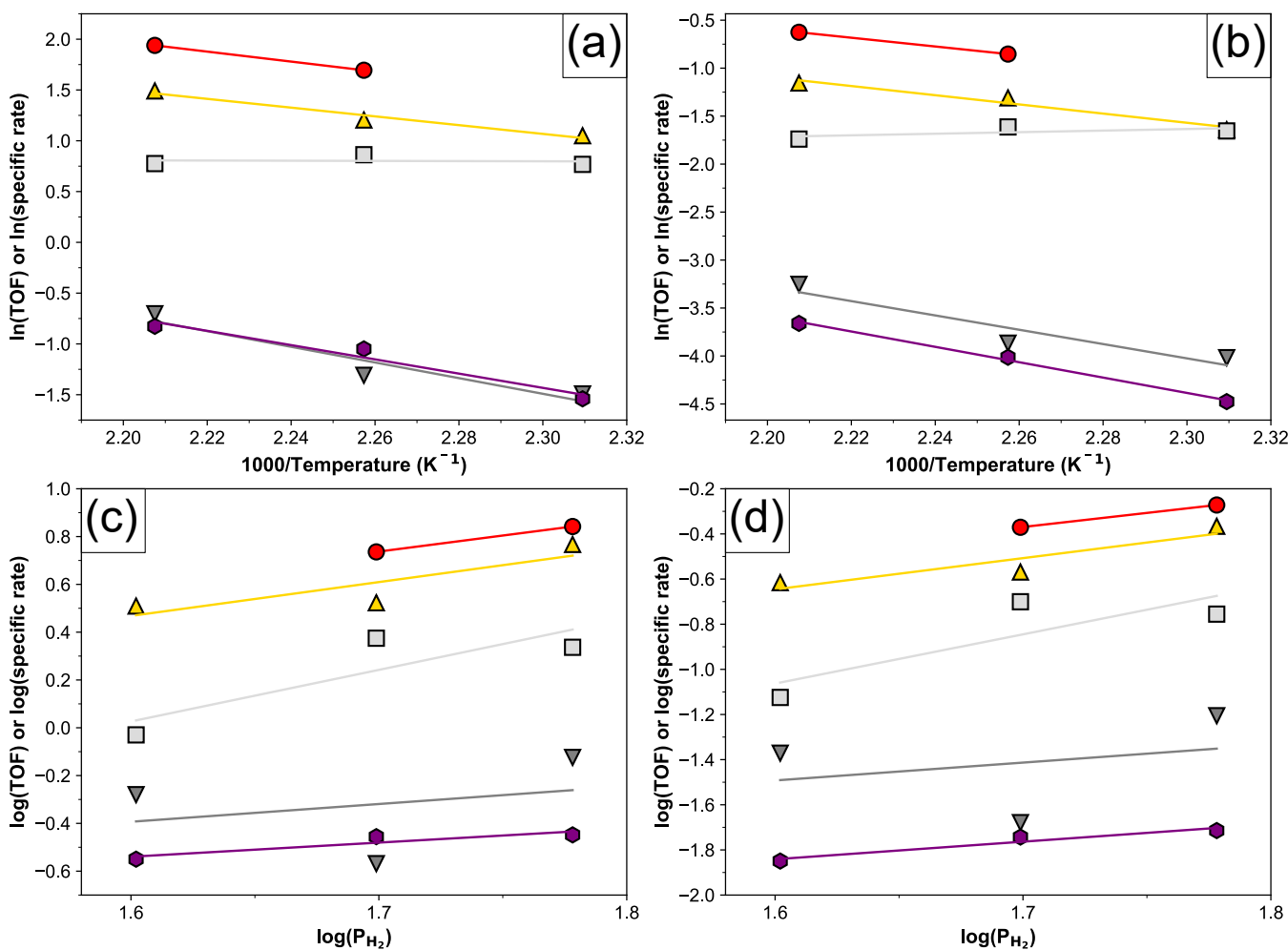


Figure 5.5: Arrhenius plots for PMI (a) and E-PMI (b) hydrogenation, and log rate-log hydrogen pressure plots for PMI (c) and E-PMI (d) hydrogenation over GNP-supported “red. + calc.” catalysts. Rate expressed as TOF for Rh, Pd, Ir, and Pt, and as a specific rate for Ru. Legend: Ru (∇), Rh (\blacktriangle), Pd (\blacklozenge), Ir (\square), and Pt (\bullet).

facile in many flow reactors, whereas in batch reactors it is not possible. For the other catalysts in the series, typical Arrhenius behaviour is observed, suggesting the presence of a maxima under these conditions is improbable. The high reaction order for hydrogen recorded for the Ir/GNP “red. + calc.” catalyst alludes that a dehydrogenation reaction is also occurring *via* a hydrogen-deficient surface species, which would therefore act as a poison for the addition reaction, or perhaps lead to its deactivation.

Performing a comparison of the relative activities of the metals based on the TOFs is complicated by the vast differences in particle sizes between catalyst samples. For instance, the TOFs observed for the Pt/GNP “red. + calc.” catalysts are higher than those observed for the Rh/GNP red. + calc. catalyst under various conditions. However, the surface-weighted and volume-weighted particle sizes estimated for these catalysts (Table 5.2) indicate that the platinum catalyst has a significantly larger particle size than the rhodium catalyst. As discussed above, the hydrogenation of benzene over practical catalysts generally does not

display structure-sensitive behaviour, unless the particle sizes are very small. However, no investigations into the structure sensitivity for these reaction systems were performed during the course of this work. Therefore, the possibility of particle size effects cannot be discounted.

Bearing this in mind, the relative ordering of these “red. + calc.” GNP-supported catalysts is Pt > Rh > Ir > Pd. Ruthenium is probably more active than palladium, but its activity compared to iridium and the more active metals is hard to determine without repeating the synthesis procedure and re-testing of the ruthenium catalyst. The finding that palladium is the least active metal in this series is in general accordance with the literature studies.^{39,40} The ordering of the other metals is less certain as the few studies which normalise rates to surface area or atoms are incongruous,³⁹⁻⁴¹ which could suggest that unidentified factors in the individual studies influenced the reaction kinetics. Moreover, in this study two aromatic compounds were present, so the ranking could differ if they were repeated with one substrate only.

5.3.2.3 The effect of metal on the relative surface equilibrium constant

The relative surface equilibrium constant ($K_{\text{PMI}}/K_{\text{EPMI}}$), derived in Section 4.3.2, for each catalyst as a function of hydrogen pressure and the reciprocal of temperature are presented in Figure 5.6. As with the commercial Pd/C catalyst studied in the previous chapter, the $K_{\text{PMI}}/K_{\text{EPMI}}$ ratio appears to be mostly insensitive of temperature and hydrogen pressure for all metals studied within experimental error. As no variation with temperature is observed, this means that the enthalpy of adsorption of PMI and E-PMI on each metal in isolation is equal, as no information on the absolute values is possible with this analysis method. Each line intersects the y-axis at different values however, which indicates that the difference in entropy of adsorption is sensitive to the metal, though the exact ordering is different due to overlapping standard error values. This ordering also does not reflect absolute values for adsorption enthalpies of PMI and E-PMI, and only reflects the relative value (Equation 4.30).

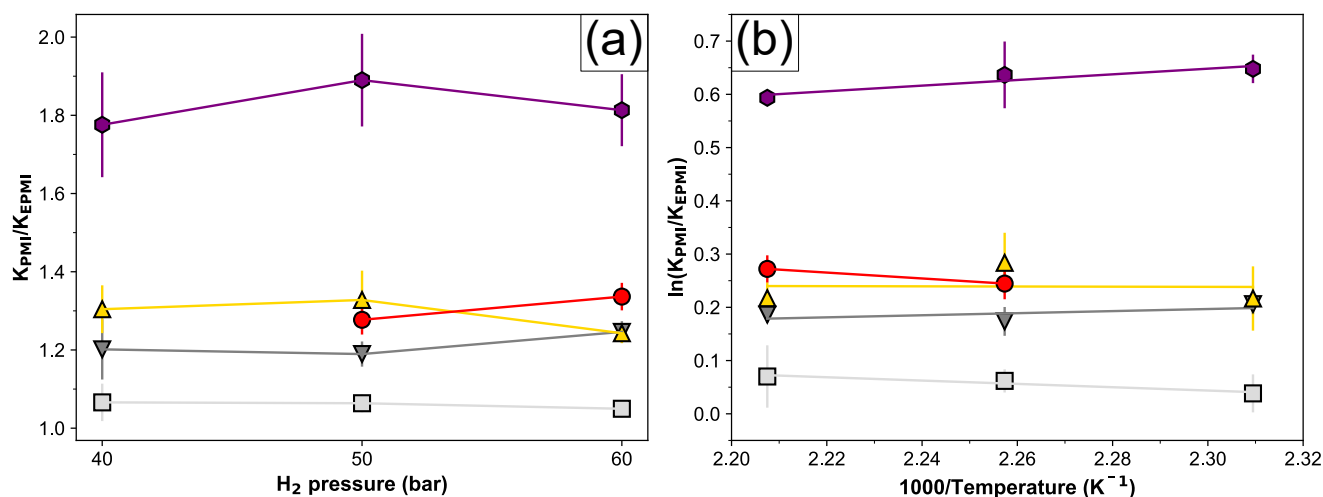


Figure 5.6: Plots of $K_{\text{PMI}}/K_{\text{EPMI}}$ versus hydrogen pressure (a) and the reciprocal of temperature (b) for GNP-supported “red. + calc.” catalysts. Legend: Ru (∇), Rh (\triangle), Pd (\bullet), Ir (\square), and Pt (\bullet). Error bars are representative of standard error of the slope on log-log plots used to calculate value.

5.3.3 Performance in the partial reduction reaction

5.3.3.1 Ru/GNP

The selectivity to and yield of THPMI and E-THPMI as a function of conversion over ruthenium catalysts is outlined in Figure 5.7. The Ru/GNP “red. only” catalyst is more selective to THPMI and E-THPMI than the Ru/GNP “red. + calc.” catalyst when conversions are below 20% at 170 °C and 50 bar hydrogen pressure. Selectivity to THPMI appears to initially decrease at differential levels of conversion before approaching an approximately constant value of *ca.* 5% for the “red. only” catalysts. The selectivity profile of E-THPMI is similar in that the selectivity decreases at low levels of conversion before reaching a constant value of 3%. This level of selectivity to THI is nearly constant until greater than 95% conversion under several different reaction conditions. The yields of the olefin intermediates increase as a function of conversion with the maximum yield for each substrate equal to 4 and 3 wt.% for THPMI and E-THPMI, respectively.

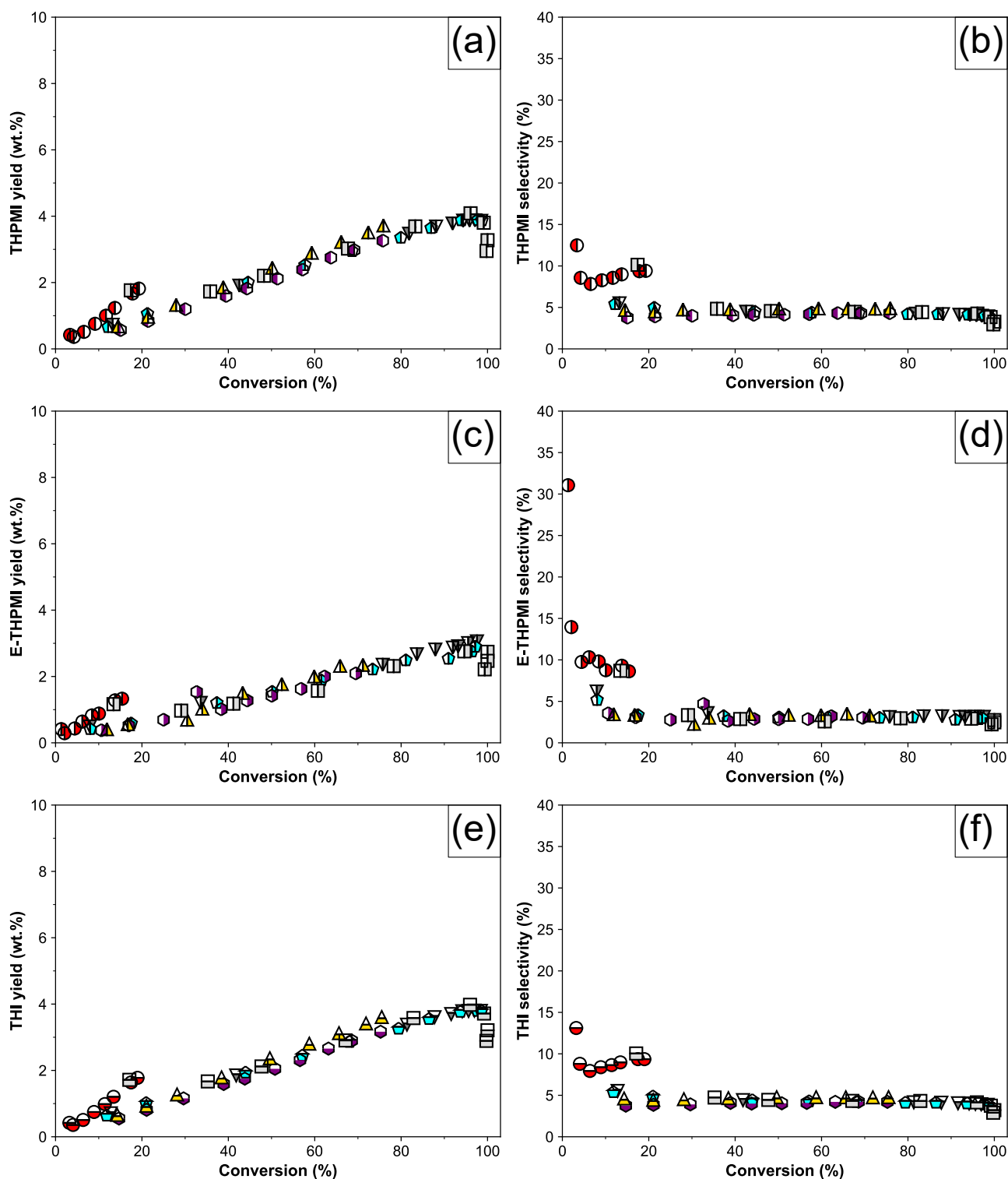


Figure 5.7: The effects of temperature and hydrogen pressure on the yield of THPMI (a), E-THPMI (c), and THI (e) for Ru/GNP “red. only” and Ru/GNP “red. + calc.” catalysts. The effects of temperature and hydrogen pressure on the selectivity to THPMI (b), E-THPMI (d), and THI (f) for Ru/GNP “red. only” and Ru/GNP “red. + calc.” catalysts. *Legend:* “red. only” catalyst tested at 170 °C and 50 bar hydrogen pressure (●), Ru/GNP “red. + calc.” catalyst tested at 170 °C and 50 bar hydrogen pressure (▼), Ru/GNP “red. + calc.” catalyst tested at 170 °C and 40 bar hydrogen pressure (▲), Ru/GNP “red. + calc.” catalyst tested at 170 °C and 60 bar hydrogen pressure (□), Ru/GNP “red. + calc.” catalyst tested at 160 °C and 50 bar hydrogen pressure (◆), and Ru/GNP “red. + calc.” catalyst tested at 180 °C and 50 bar hydrogen pressure (●).

5.3.3.2 Rh/GNP

Figure 5.8 displays the selectivity to and yield of THPMI and E-THPMI as a function of conversion. Under all conditions, the selectivity of the “red. only” and red. + calc. catalysts to THPMI increases over time before reaching a constant value dependent on the catalyst and reaction conditions. The selectivity to E-THPMI displays this behaviour to a lesser extent, though note that E-PMI is less reactive (see above) than PMI. Calcining the Rh/GNP “red. only” catalyst increases the selectivity and yield: THPMI selectivity increases from 37 to 57% whilst E-THPMI selectivity rises to 44 from 26%. The maximum yields of THPMI at 170 °C and 50 bar hydrogen pressure on the “red. only” and “red. + calc.” catalysts are 29 and 52%, respectively. Maximum yields of E-THPMI yields equate to 21% on the “red. only” catalyst and 41% on the “red. + calc.” catalyst but note that these values may vary slightly due to the limited number of points in the maximum region. Regarding the effect of experimental variables, the effects of hydrogen pressure at constant temperature is less pronounced than what was observed with palladium in the previous chapter, in that the maximum shows no discernible dependence. Altering the temperature on the hand is more complex; the reactions performed at 160 and 170 °C at 50 bar hydrogen pressure show a small decrease in the constant THPMI selectivity region as temperature is raised. When the temperature is increased to 180 °C, however, the selectivity to THPMI decreases sharply, from approximately 60% at 160 °C to 39% at 180 °C. The maximum yield at this higher temperature was not determined but in the optimum scenario, where selectivity remains constant until complete conversion, the yield would equal 39 wt.%—a drop of more than 10%. This is of course probably an overestimate since the maximum at other conditions occurred at *ca.* 95% conversion. Finally, the maximum yield of E-THPMI is approximately four-fifths of that of THPMI under all conditions.

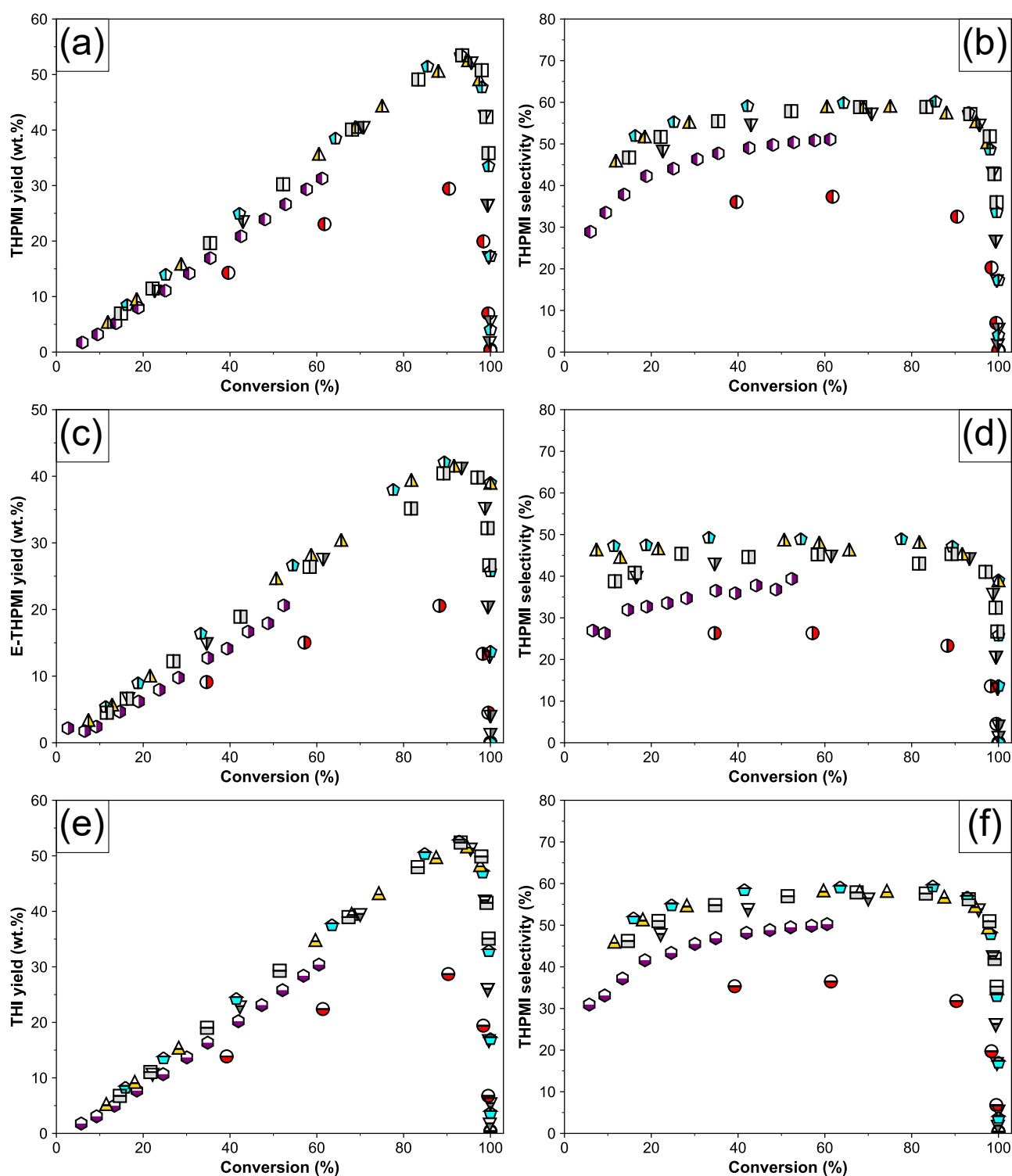


Figure 5.8: The effects of temperature and hydrogen pressure on the yield of THPMI (a), E-THPMI (c), and THI (e) for Rh/GNP “red. only” and Rh/GNP “red. + calc.” catalysts. The effects of temperature and hydrogen pressure on the selectivity to THPMI (b), E-THPMI (d), and THI (f) for Rh/GNP “red. only” and Rh/GNP “red. + calc.” catalysts. *Legend:* red. only catalyst tested at 170 °C and 50 bar hydrogen pressure (●), Rh/GNP “red. + calc.” catalyst tested at 170 °C and 50 bar hydrogen pressure (▼), Rh/GNP “red. + calc.” catalyst tested at 170 °C and 40 bar hydrogen pressure (▲), Rh/GNP “red. + calc.” catalyst tested at 170 °C and 60 bar hydrogen pressure (□), Rh/GNP “red. + calc.” catalyst tested at 160 °C and 50 bar hydrogen pressure (⬠), and Rh/GNP “red. + calc.” catalyst tested at 180 °C and 50 bar hydrogen pressure (⬡).

5.3.3.3 Pd/GNP

Selectivity and yield data for the palladium catalysts are presented in Figure 5.9. Mirroring the behaviour of the Rh/GNP catalysts, the initial selectivity to THPMI and E-THPMI increases by several percent upon calcination of the red. only catalyst. This extends, though to a lesser degree than the Rh/GNP catalysts, to high levels of conversion, where the maximum yields of THPMI and E-THPMI improve by around 20% after calcination. In agreement with what was observed in the previous chapter, altering temperature and hydrogen pressure does not result in noticeable changes to the initial selectivity but does lead to an improvement in the maximum observed yields of THPMI and E-THPMI. It should be noted, however, that the testing at 170 °C and 50 bar of pressure demonstrates a lower yield than expected, but this could be due to a small difference in dispersion with this sample (see later). As noted for the Pd/C catalyst in the previous chapter, the yield of E-THPMI is less than that of THPMI.

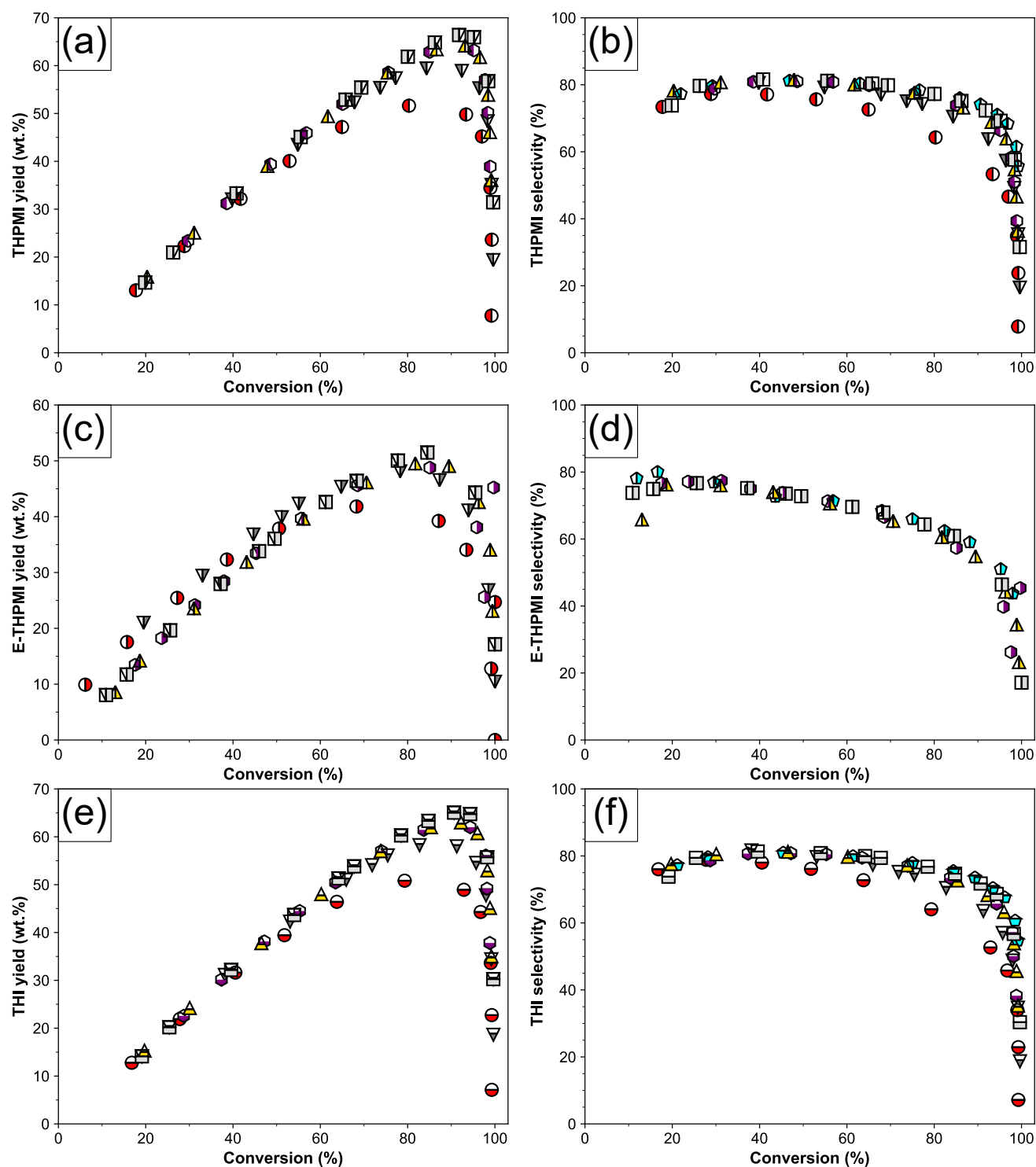


Figure 5.9: The effects of temperature and hydrogen pressure on the yield of THPMI (a), E-THPMI (c), and THI (e) for Pd/GNP “red. only” and Pd/GNP “red. + calc.” catalysts. The effects of temperature and hydrogen pressure on the selectivity to THPMI (b), E-THPMI (d), and THI (f) for Pd/GNP “red. only” and Pd/GNP “red. + calc.” catalysts. *Legend:* “red. only” catalyst tested at 170 °C and 50 bar hydrogen pressure (●), Pd/GNP “red. + calc.” catalyst tested at 170 °C and 50 bar hydrogen pressure (▼), Pd/GNP “red. + calc.” catalyst tested at 170 °C and 40 bar hydrogen pressure (▲), Pd/GNP “red. + calc.” catalyst tested at 170 °C and 60 bar hydrogen pressure (□), Pd/GNP “red. + calc.” catalyst tested at 160 °C and 50 bar hydrogen pressure (◆), and Pd/GNP “red. + calc.” catalyst tested at 180 °C and 50 bar hydrogen pressure (◆).

5.3.3.4 Ir/GNP

The yield and selectivity as a function of conversion for the Ir/GNP red. only and the Ir/GNP “red. + calc.” catalysts are presented in Figure 5.10. Oxidative treatment of the red. only Ir/GNP catalyst results in a decrease in selectivity from 15 to 10% for THPMI and from 13 to 7% for E-THPMI. The selectivity and yield of both THPMI and E-THPMI are essentially independent of temperature and pressure. Under no experimental condition was a maximum in the THPMI yield-conversion plot recorded, even at PMI conversions of 99%. A maximum yield for E-THPMI was observed at between 97 and 99% E-PMI conversion. Concerning the experimental yields of each reactive intermediate, the yields of E-THPMI were consistently lower than those of THPMI.

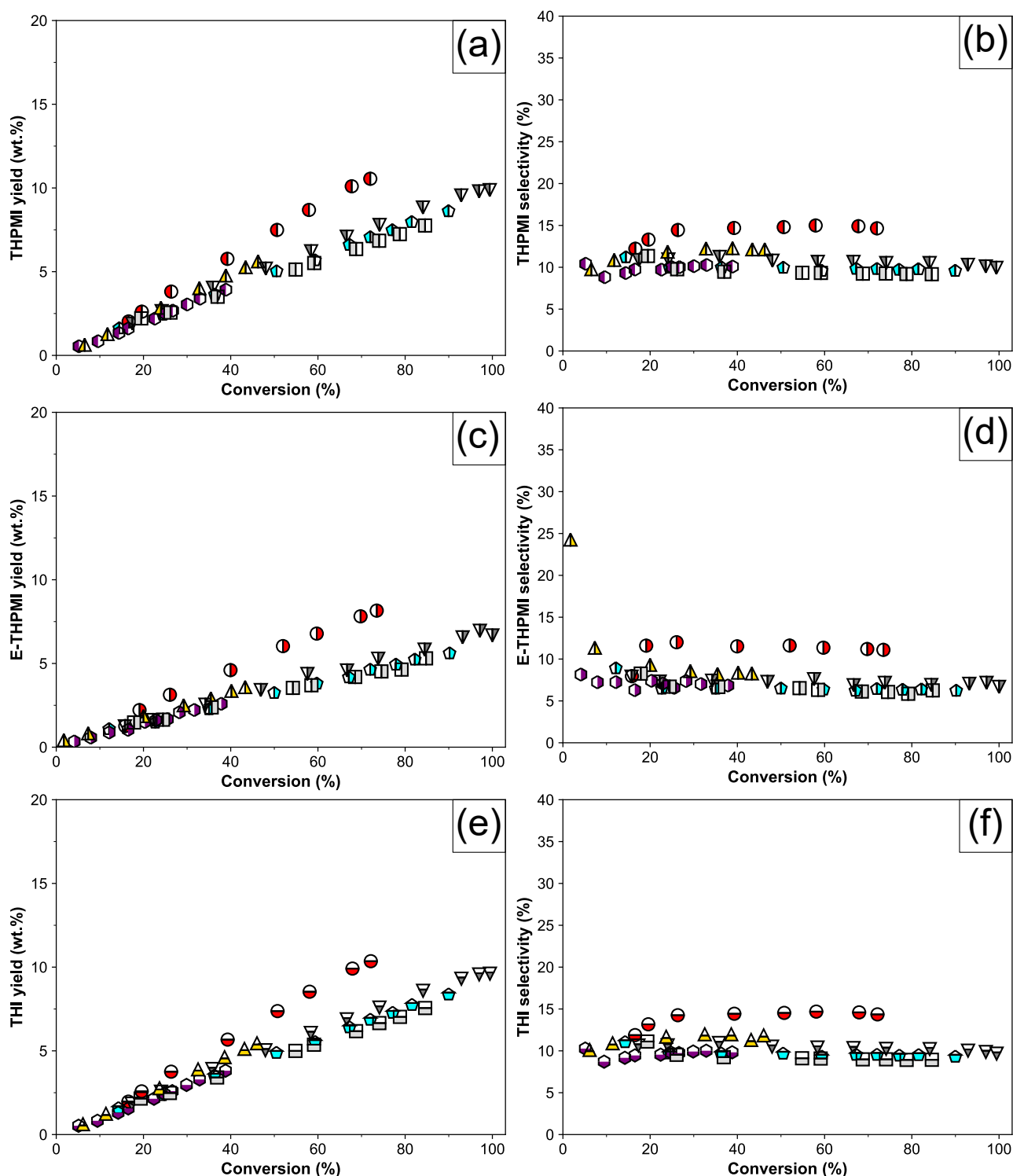


Figure 5.10: The effects of temperature and hydrogen pressure on the yield of THPMI (a), E-THPMI (c), and THI (e) for Ir/GNP "red. only" and Ir/GNP "red. + calc." catalysts. The effects of temperature and hydrogen pressure on the selectivity to THPMI (b), E-THPMI (d), and THI (f) for Ir/GNP "red. only" and Ir/GNP "red. + calc." catalysts. *Legend:* "red. only" catalyst tested at 170 °C and 50 bar hydrogen pressure (●), Ir/GNP "red. + calc." catalyst tested at 170 °C and 50 bar hydrogen pressure (▼), Ir/GNP "red. + calc." catalyst tested at 170 °C and 40 bar hydrogen pressure (▲), Ir/GNP "red. + calc." catalyst tested at 170 °C and 60 bar hydrogen pressure (□), Ir/GNP "red. + calc." catalyst tested at 160 °C and 50 bar hydrogen pressure (◈), and Ir/GNP "red. + calc." catalyst tested at 180 °C and 50 bar hydrogen pressure (●).

5.3.3.5 Pt/GNP

The initial testing of the Pt/GNP “red. only” and Pt/GNP “red. + calc.” catalysts are outlined in Figure 5.11. Calcination of the “red. only” catalysts results in a 4% increase in selectivity between 27 and 67% PMI conversion. In contrast, the yield of E-THPMI appears to decrease upon treatment in air. With regards to temperature effects, there appears to be no changes to PMI or E-PMI selectivity. As with all other catalysts, the selectivity and yield of E-PMI is lower than that of PMI.

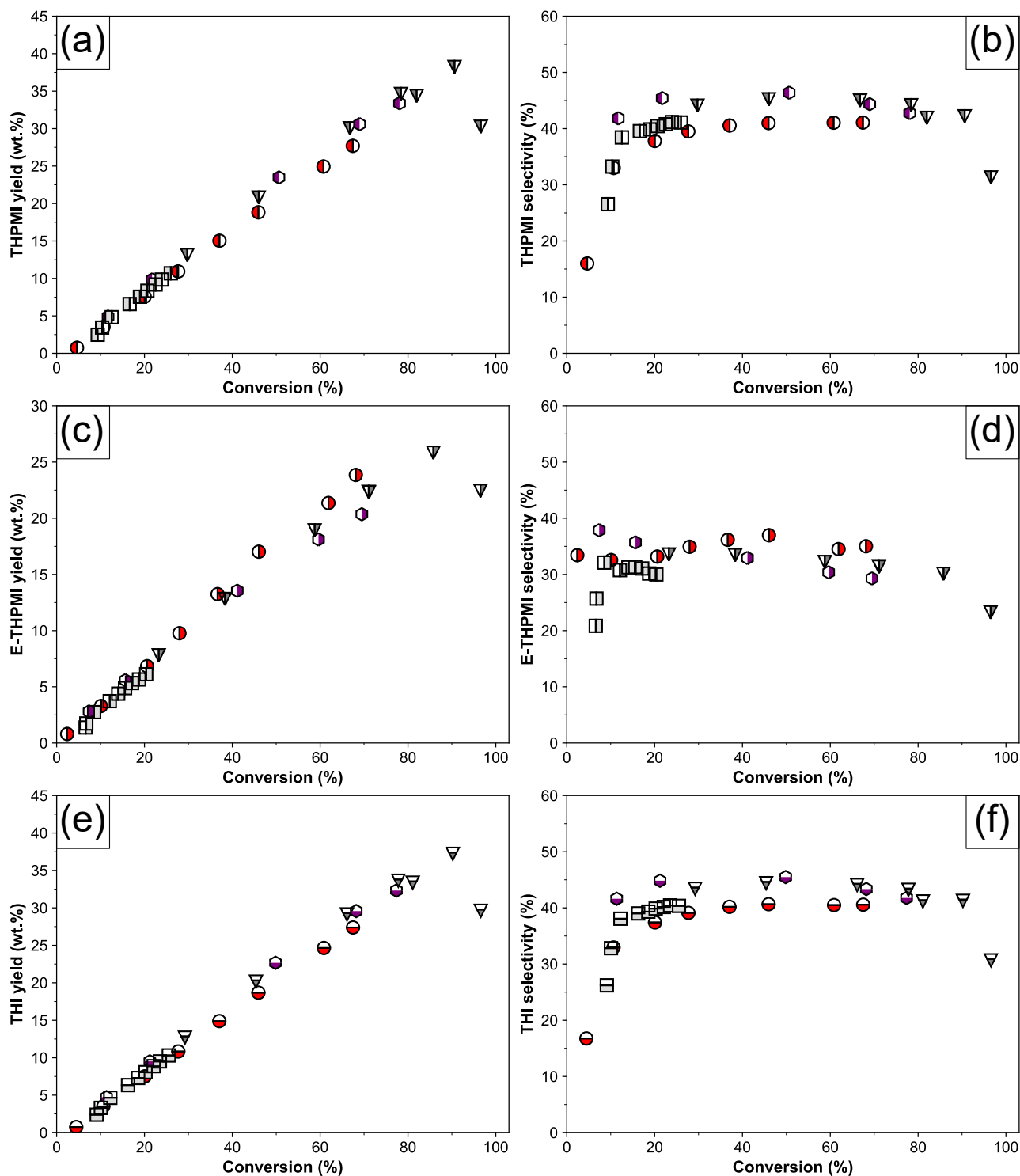


Figure 5.11: The effects of temperature and hydrogen pressure on the yield of THPMI (a), E-THPMI (c), and THI (e) for Pt/GNP "red. only" and Pt/GNP "red. + calc." catalysts. The effects of temperature and hydrogen pressure on the selectivity to THPMI (b), E-THPMI (d), and THI (f) for Pt/GNP "red. only" and Pt/GNP "red. + calc." catalysts. Legend: "red. only" catalyst tested at 170 °C and 50 bar hydrogen pressure (●), Pt/GNP "red. + calc." catalyst tested at 170 °C and 50 bar hydrogen pressure (▲), Pt/GNP "red. + calc." catalyst tested at 170 °C and 60 bar hydrogen pressure (□), and Pt/GNP "red. + calc." catalyst tested at 180 °C and 50 bar hydrogen pressure (◆).

5.3.3.6 The possible presence of an additional partially reduced product

During the course of experiments utilising ruthenium and iridium catalysts, a splitting of the E-THPMI peak was observed in the GC-FID trace. The area of this peak compared to the E-THPMI peak was approximately two-thirds and one-thirds for the ruthenium and iridium catalysts, respectively, although some variation in this value was noted. The compound that produced this peak could not be identified due to a merging of peaks in GC-MS column and being of too low in concentration to be characterised by NMR spectroscopy. This compound is possibly an isomer of THPMI or E-THPMI as Weitkamp reported that Ru/C produced larger quantities of an isomer of octalin from naphthalene than other group 8–10 metal catalysts.¹⁶

5.3.3.7 Summary

The relative selectivities to tetrahydroindane products of the “red. only” catalysts is in the order of Pd > Pt > Rh > Ir > Ru. Upon calcination, this ordering changes to Pd > Rh > Pt > Ir > Ru. Hydrogen pressure effects on the overall yield of the desired intermediate are observed for the Pd/GNP “red. + calc.” catalyst only. Temperature effects on the selectivity and overall yield of THPMI and E-THPMI are most profound for the Rh/GNP “red. + calc.” and Pd/GNP “red. + calc.” catalysts. The yield of E-THPMI is lower than THPMI over all catalysts under all conditions.

5.3.3.8 Discussion

The primary interest of this work is to establish the ordering of the selectivity of the platinum group metals in the partial reduction reaction. Since the data above indicates that (i) the initial selectivity to tetrahydroindane products varies before approaching a steady value, and (ii) that the ordering of the metals is sensitive to thermal treatments of the catalysts, it is therefore necessary to consider the origin of these effects before the behaviour of the metals can be interpreted. As the cause of these two observations may in principle lie in the same reasoning, the discussion offering possible explanations is combined for the sake of brevity.

The initial increase in selectivity observed on rhodium and platinum catalysts could be due to the formation of intermediate dienes, although it should be noted that such products were not identified during these experiments, possibly due to overlap with other products on the GC column. If dienes were to form on the catalyst surface, they would have a surface equilibrium constant and a rate constant for their hydrogenation. The relative values of these terms compared with those for the hydrogenation of the GHC and the THI would determine the selectivity *versus* conversion profile. If these terms were slightly greater, then the selectivity should increase over time as is observed here. If these terms were significantly greater, then an increase in selectivity would be observed, but only at very low levels of conversion. Therefore, when not observed during a reaction, it is possible that the reaction requires greater study at lower levels of conversion. Indeed, cyclohexadiene-¹⁴C is detected during the hydrogenation

of benzene-¹⁴C and cyclohexadiene mixtures at differential benzene conversions over a variety of metal powders (Fe, Ni, Ru, Rh, Pd, Os, Ir, Pt).^{42,43} Moreover, Siegel and co-workers concluded that dienes probably form during the reduction of *tert*-butylbenzenes but do not desorb from the surface.^{44,45}

Carbon deposition is widely reported to occur on metal surfaces during reactions involving hydrocarbons and hydrogen, including aromatic and olefin hydrogenation over many metals.⁴⁶ It is important to clarify here that despite noting the possibility of a carbonaceous species poisoning the surface above, the interaction of this carbon with the metal nanoparticle is not necessarily the same. Thus, any imparted effect may depend on the nature of the carbon species or phase. The overall effect could be attributable to a simple surface poisoning effect where the more or less selective sites, depending on the catalyst, become blocked with this carbonaceous overlayer. This concept has often been proposed as a selectivity modifier in a number of reactions, such as the partial reduction of acetylene,⁴⁷ the selective reduction of halogenated nitroaromatics,⁴⁸ and alkane hydrogenolysis.⁴⁹

An additional consideration is that metal surfaces, particularly those of nanoparticles, are dynamic and can reconstruct to form a lower energy surface during the reaction and in some instances, separate phases.⁵⁰ Unfortunately, there are no reports of the surface dynamics of catalysts exposed to a hydrogen aromatic feed to the extent of my knowledge. However, several authors have reported the activity during benzene hydrogenation to be highly sensitive to surface reconstruction process that occur during a catalyst's activation procedure.^{51,52} For instance, Aben *et al.* reported that the dispersion of Pt/Al₂O₃ catalysts bore no relationship to the metal dispersion but positively correlated with the height of peak observed at low temperatures in H₂-TPD spectra.⁵¹ The intensity of this peak was found to be sensitive to the thermal treatments used to prepare the catalysts. If this surface reconstruction process is indeed responsible for the differences in catalytic activity, which is also observed in this work, then this could also lead to a change in reaction selectivity.

Dynamic reconstruction has also been noted for hydrogen environments by various analytical methods.^{53,54} For example, Yakovina and Lisitsyn demonstrated that a hydrogen atmosphere could induce significant surface reconstruction in a Pt/Al₂O₃ catalyst but not in a Pt/SiO₂ catalyst, as determined by H₂-TPD.⁵³ However, surface reconstruction on silica supports appears to be sensitive to the relative environment. Nuzzo and co-workers reported that the coordination numbers of Pd/SiO₂ and Pt/SiO₂ catalysts, determined by X-ray adsorption spectroscopy, decreased by approximately half when changing from a hydrogen-rich to ethylene-rich environment and did not return to the original value when the atmosphere was reverted.⁵⁴ In this work, the reconstruction process is possibly justifiable when the manner of performing the reaction is considered. Recall that the neat solution of aromatic is heated in a nitrogen atmosphere with the catalyst without exposure to hydrogen to ensure that no conversion occurs during the long heating process. During this stage, the catalyst interacts with PMI and E-PMI only. When the temperature of the autoclave stabilises and hydrogen is

introduced, the environment to which the catalyst is exposed changes again and the catalyst may adapt as the surface becomes enriched with hydrogen. Thus, over a period of time the metal surface could reconstruct and lead to the observed product selectivity changes.

Similarly, the sintering of nanoparticles during the reaction is another possible explanation for the results. More characterisation of particle sizes of the fresh and used catalysts is needed for this point, but particle size effects are commonly used to explain the results of hydrocarbon chemistry that it would be amiss to not note their possible influence in this instance. This process leads to drastic changes to the electronic properties and geometry of the nanoparticles. For example, below approximately 2 nm the metallic character of a particle is lost and this could result in changes to the catalytic behaviour.⁵⁵ XPS allows the electronic state of metals to be probed. As large variations in selectivity as a result of heat treatments were observed for rhodium and iridium catalysts, the surface state of these catalysts was probed using XPS. The XPS data of the rhodium and iridium catalysts are presented in Figure 5.12. Two chemical states of rhodium were identified in the Rh 3d region of the XP spectrum of the Rh/GNP “red. only” catalyst, attributable to metallic rhodium (307.4 eV) and rhodium oxide (308.7 eV).⁵⁶ After calcination, the metallic rhodium peak must be excluded from the fitting procedure to ensure the model envelope matches the raw spectrum of this region, and the binding energy of the rhodium oxide increases by 0.2 eV to 308.9 eV. The binding energies of the Ir 4f_{7/2} peak in the Ir/GNP red. only and Ir/GNP “red. + calc.” catalysts are located at 61.7 eV and 61.9 eV, respectively. The XP spectra of iridium and its oxides and chlorides was recently studied in-depth by Morgan and co-workers.³⁰ They reported a binding energy for the Ir 4f_{7/2} peak in bulk IrO₂ at 62.5 eV when using the same fitting parameters used in this work.³⁰ However, the values observed in this study are within the range of bulk values documented for bulk IrO₂ in the NIST database,⁵⁶ and it also must be considered that core level shifts may occur with a change in particle size, which could also explain the shift in binding energy observed in the Rh/GNP catalysts.⁵⁷ Moreover, the presence of a metallic oxide peak in the XP spectra for both catalysts is probably attributable to surface oxidation over time, as this characterisation was performed several months after their initial preparation.

The geometric changes pertain to differing quantities of specific sites and changes in the crystal structure or interatomic distances. For example, the fraction of corner, edge, and face sites—which in a perfect fcc octahedra have coordination numbers of four, seven, and nine, respectively⁵⁸—will change dramatically below 5 nm for a nanoparticle with a well-defined shape.⁵⁵ The catalysts prepared in this study are probably not particles with a well-defined shape, but the model calculations still should apply to some degree. It should also be acknowledged that the nanoparticles are not monodispersed and thus the observed effects have contributions from all particles. Thus, if one particular reduction mechanism is sensitive to a specific site(s)/coordination number of the surface atom(s) involved in the reaction, then the sintering of nanoparticles could produce the observed changes in selectivity and yield.

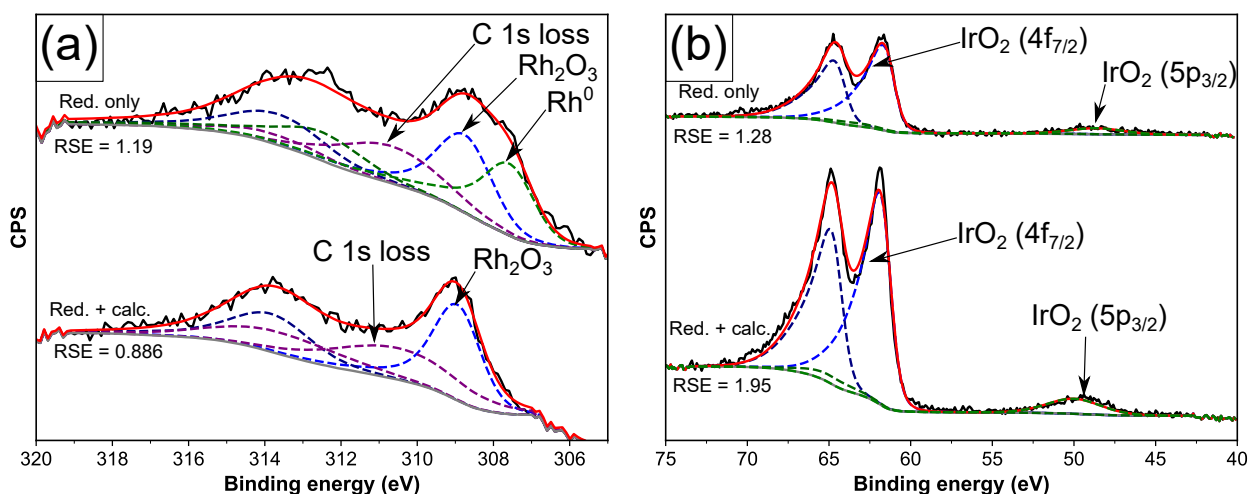
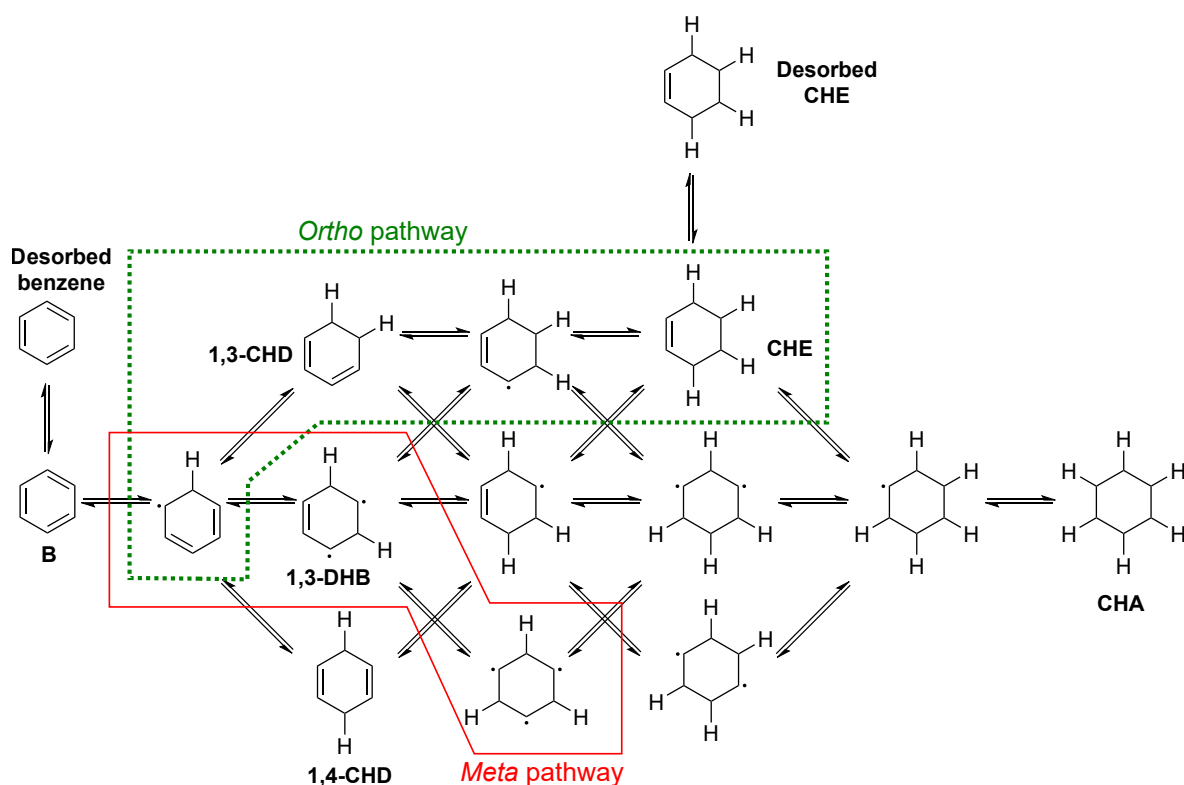


Figure 5.12: XPS spectra for the Rh/GNP (a) and Ir/GNP catalysts (b).

5.3.3.9 Reaction mechanisms

It is now necessary to consider the reaction mechanism to understand the origin of the selectivity and maximum yields observed over these catalysts. Theoretical studies on the Pd(111),⁵⁹ Pt(111),⁶⁰ and Ru(0001)⁶¹ surfaces indicate the reduction of benzene proceeds predominantly through the *ortho* mechanism, that is to say hydrogen is added in the *ortho* position relative to the previous addition step, such that the hydrogen proceeds as if benzene were equivalent to the cyclohexatriene structure. This process is enclosed within the dashed green lines in Scheme 5.2. Initial studies on the Pt(111) surface indicated that cyclohexene should not form as the reduction was calculated to be most favourable proceeding *via* 1,3,5-trihydrobenzene in the so-called *meta* pathway (Scheme 5.2 solid red line),⁶² but the methods employed in this theoretical study have since been further developed.

It is, of course, possible that the other metals and metal surfaces are less selective. For example, Somorjai and co-workers demonstrated experimentally that cyclohexene formation was possible over the Pt(111) plane, in agreement with theoretical studies, but not over the Pt(110) plane using metal films and structured unsupported nanoparticles.^{63–66} In addition, cyclohexene formed only at higher temperatures, which the authors attributed to a higher activation energy pathway for its formation. This could explain why the selectivity of the Rh/GNP “red. + calc.” catalysts declines with temperature as with increasing temperatures the *meta* pathway becomes more favourable. Similarly, Paál and Tétényi studied the reaction mechanism using benzene-¹⁴C and cyclohexadiene over metal powders (Fe, Ni, Ru, Rh, Pd, Os, Ir, Pt), which probably contain multiple surface planes.^{42,43} They calculated that if the addition of hydrogen were random, then the probability of cyclohexene forming would be 0.4. This value is in close agreement with the selectivity of Pt/GNP “red. + calc.” catalyst once a steady selectivity has been achieved, which may indicate the reduction mechanism



Scheme 5.2: Reaction network of the hydrogenation of benzene to cyclohexane. Abbreviations: B = benzene; 1,3-CHD = 1,3-cyclohexadiene; 1,4-CHD = 1,4-cyclohexadiene; CHE = cyclohexene; CA = cyclohexane; 1,3-DHB = 1,3-dihydrobenzene. Figure adapted from [62]

on the platinum surface is nearly random—a possible consequence of each pathway having similar kinetics. The experimental yields of cyclohexene in the studies of Paál and Tétényi were, however, far below this value and concluded that although the *ortho* mechanism takes place, the *meta* pathway is dominant on all metals.^{42,43} Theoretical studies utilising other metal surfaces could be greatly helpful in affording an explanation into these observations, but to the extent of my knowledge there are no reports on the energetically favoured reaction pathway for surfaces other than those discussed above.

If work where non-negligible yields of intermediate are detected, then the situation is made more complex still. van de Graaf *et al.* reported that a Rh/C catalyst was more selective in the partial reduction of 1,2-di-*tert*-butylbenzene to the cyclic alkene intermediate than Pt/C at atmospheric hydrogen pressure and room temperature in ethanol or acetic acid.⁹ Maximum yields for Rh/C and Pt/C were 45.2% and 7.5%, respectively, when acetic acid was used as the solvent compared with the yields in ethanol of 30.1 and 5.7% over Rh/C and Pt/C, respectively. Later, these authors studied the partial reduction of 1,3,5-tri-*tert*-butylbenzene on 5 wt.% Rh/C, 10 wt.% Pd/C, and 5 wt.% Pt/C under the same conditions, except employing *n*-heptane as solvent. The authors found the maximum cycloolefin yield to be in the order of Rh (67%) > Pt (46%) > Pd (14%). There are three important points to note before a comparison with these results can be made. Firstly, these articles do not perform any characterisation on the catalysts used in the study. Secondly, it is unclear whether the same carbon source and

preparation method was used, as all but one of the catalysts was purchased from a different manufacturer. Thirdly, the conditions used are vastly different, though the alkane solvent in the second mentioned study is similar to the solventless conditions used in this work.

At first glance these results appear to disagree with the findings of this work. However, the first two points are hard to determine due to the age of the article, but the third point may be considered if it assumed these first two points are unimportant. The yield of intermediate is dictated by (i) the reduction pathway followed and (ii) the rate of hydrogenation of the intermediate. Even if the reduction pathway proceeds entirely through the intermediate, the overall yield of the intermediate could be low if the rate of hydrogenation, determined by its rate constant and surface equilibrium constant, is significantly greater than the rate at which it is formed. Boudart and co-workers found that under ambient conditions, cyclohexene hydrogenation to cyclohexane could be inhibited by aromatic solvents, which were unreactive under these conditions when using nickel,⁶⁷ palladium,⁶⁸ and rhodium catalysts⁶⁹ but not platinum catalysts.⁷⁰ The inhibition was greatest for the rhodium catalysts, where the hydrogenation activity was almost entirely extinguished. This suggests that the aromatic compound is much more strongly adsorbed on the surface. Whereas for the palladium catalysts, cyclohexene could be hydrogenated, albeit at a slower rate. This could explain the seeming disparity between the results of van Bekkum *et al.*¹⁰ and those documented in this thesis: at the lower temperature the aromatic can still adsorb as its adsorption is more favourable, however, the rate constant for aromatic hydrogenation is reduced to a greater extent. In turn, this leads to a low overall yield as the rate of hydrogenation of the intermediate becomes greater. This could be why there is no difference observed between the THPMI yield reported in the patent for this process, which utilises a lower temperature, and the industrial process as it is performed currently. This highlights the importance of understanding a catalytic reaction on the basis of surface kinetics and not the power rate law, as it clearly evidences the need to understand the delicate balance between surface equilibrium constants and rate constants. In other words, studying a reaction under a narrow set of conditions may lead to false conclusions regarding the performance of certain metals in selective hydrogenation reactions.

In a similar view, the nature of yield and selectivity *versus* conversion plots can provide insight into the relative pathways and rates of each hydrogenation step. For instance, THPMI and E-THPMI increase with conversion and were observed to pass through a maximum at >90% conversion, whilst the selectivity in the mid-conversion region is flat and approaches and varies from 5%, in the case of Ru/GNP “red. + calc.”, to 80% for the Pd/GNP catalysts. Consider the scenario where the desired intermediate is desorbed entirely. If the adsorption of a reactive intermediate is able to compete more effectively for a surface site, then the maximum yield shifts towards earlier conversions and cannot occur at high conversions; this is observed for the palladium catalyst in the work of van Bekkum.¹⁰ The selectivity to intermediate products in this instance would be expected to decline as a function of conversion and not remain, or achieve, a stable value. The same curves would be found if the rate

Table 5.4: A comparison of the maximum intermediate yields obtained between IFF's Pd/C documented in the previous chapter and the Pd/GNP "red. + calc." catalyst used in this chapter.

| Temperature (°C) | Hydrogen pressure (bar) | Maximum yields observed (wt.%) | | | | | |
|---------------------|----------------------------|--------------------------------|--------|-----------------------|---------------------|----------|--------|
| | | THPMI | | E-THPMI | | THI | |
| | | IFF Pd/C | Pd/GNP | IFF Pd/C ^a | Pd/GNP ^b | IFF Pd/C | Pd/GNP |
| 170 | 40 | 68.2 | 64.2 | 51.2 | 49.6 | 66.6 | 63.0 |
| 170 | 50 | 66.9±0.4 | 59.4 | 50.6±2.6 | 48.2 | 65.4±0.4 | 58.3 |
| 180 | 50 | 65.2 | 63.2 | 48.9 | 47.8 | 63.8 | 62.0 |

^a Data taken from previous chapter.

^b Pd/GNP "red. + calc."

constants for a second step of a two-step process was greater.

For the curve maxima to be located at such levels of conversion, then a direct hydrogenation pathway must exist. Additionally, it is required that the surface equilibrium constant for the intermediate product be less than that of the parent molecule as otherwise the peak maxima again shifts to lower conversions. In this example the rate constant can be greater as it affects the intermediate yield to a lesser degree. These principles are in general agreement with experimental and theoretical reports. For example, computed heats of adsorption on Ru(0001), Rh(111), Pd(111), Pt(111), and Ir(111) surfaces state benzene is more strongly adsorbed than cyclohexene,^{59–61,71–74} which concurs with what has been determined experimentally using microcalorimetry,^{75–78} and what is observed in the kinetic studies of Boudart and associates as discussed above for nickel,⁶⁷ rhodium,⁶⁹ and palladium,⁶⁸ but not platinum,⁷⁰ catalysts.

Consideration of the preceding discussion indicates that palladium and rhodium catalysts are most selective to the cyclic alkene products in the partial reduction of PMI and E-PMI and ruthenium catalysts the least selective in this reaction. This result is surprising as ruthenium catalysts are almost exclusively employed for the partial reduction of benzene (Section 1.4.3.1).⁷⁹ On the basis of this work, more work should be conducted using palladium and rhodium catalysts in the industrially-relevant tetraphasic system, as such materials may offer improvements in cyclohexene yields in the benzene process.

5.3.3.10 A comparison of the Pd/GNP catalyst with the industrial Pd/C catalyst

The maximum observed yields of cyclic alkene obtained from the partial reduction of GHC over the Pd/GNP catalyst prepared in this chapter and the industrial catalyst used in the previous chapter are presented in Table 5.4. It is evident that the current industrial catalyst yields more desired product than the catalyst prepared in this work.

Inspection of the *trans/cis* ratio of these catalysts at 170 °C and 40 bar hydrogen pressure (Figure 5.13) indicates that more *trans* product forms over the Pd/GNP "red. + calc." catalyst. According to the mechanistic framework outlined in Section 4.3.3.2, this suggests that the isomerisation reaction is more prevalent on this catalyst. Identification of the responsible

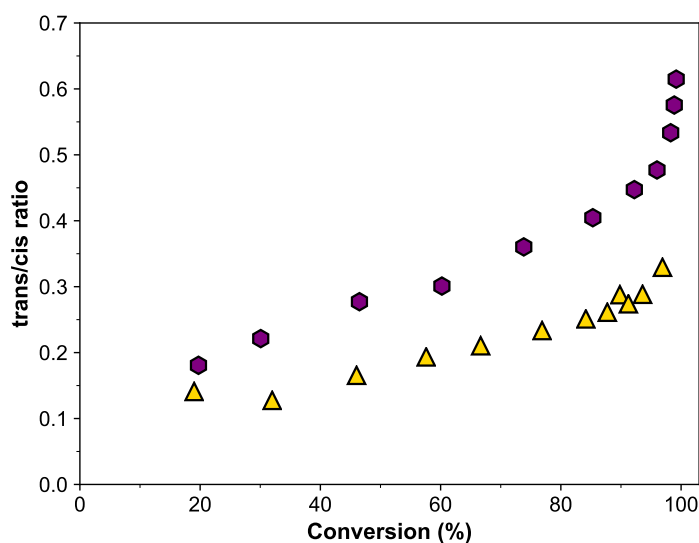


Figure 5.13: The trans/cis ratio of IFF's Pd/C catalyst (▲) and the Pd/GNP "red. + calc." catalyst (◆) at 170 °C and 40 bar hydrogen pressure.

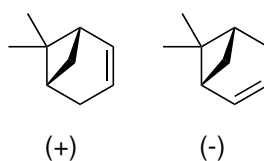


Figure 5.14: Structures of (+)- and (-)-apopinene.

factor could be a key strategy for the development of an improved catalyst. For example, each catalyst displays different particle size characteristics. The structure sensitivity of isomerisation reactions has not been extensively explored in literature as the separation of hydrogenation and isomerisation activity is difficult to separate and is presumably dependent on the structure of the alkene. Smith *et al.* studied the isomerisation of (+)-apopinene to (-)-apopinene (Figure 5.14) over Pd/Al₂O₃ catalysts at metal loadings of 0.03, 0.05, 1.0, and 5.0 wt.%.⁸⁰ This probably leads to the dispersion of the catalyst decreasing as the weight loading of palladium is increased. The isomerisation activity was shown to increase with metal loading and therefore the inverse of dispersion. Consideration of the particle size data for this catalyst alludes to the presence of a bimodal distribution consisting of both small and large crystallites (Figure 5.3). These larger particles, which probably contain a greater proportion of terraces,⁵⁸ could favour the formation of the π -allyl species required for isomerisation to occur. Although it should be noted that chemisorption measurements, which measure a surface-weighted particle size, suggest an improved dispersion with the Pd/GNP catalyst compared to the industrial Pd/C catalyst. However, the actual loading of the Pd/GNP "red. + calc." catalyst was not measured, so when this value is measured the dispersion could change. Moreover, this is an averaged value, so may not be representative if the particle size distribution is not monomodal.

5.3.3.11 Isomerisation processes on other catalysts

In contrast to the Pd/GNP “red. + calc.” catalyst, the Ru/GNP “red. + calc.” and the Rh/GNP “red. + calc.” catalysts did not display any detectable hydrogen pressure effects. Hydrogen pressure effects on palladium catalysts were attributed to isomerisation to more reactive cyclic alkenes and in this instance is possibly attributable to minimal isomerisation reactions occurring on these catalysts. The exact mechanism on ruthenium and rhodium surfaces is less well-studied compared with palladium and platinum, but Sanchez-Delgado *et al.* demonstrated that while the π -allyl and reversible stepwise addition isomerisation mechanisms can occur on ruthenium, the former mechanism is significantly slower than the latter.⁸¹ Nevertheless, both mechanisms become less favourable at increased hydrogen pressures. This is not to say that the isomerisation of the olefinic intermediates cannot occur on these surfaces, it only reflects that under these conditions, that is during the reduction of GHC, no such processes occur.

5.4 Conclusions

In this chapter, GNP-supported metals, where M = Ru, Rh, Pd, Ir, and Pt, catalysts were evaluated for their performance for the partial hydrogenation of GHC to cyclic olefins. Amongst all catalysts, the Pd- and Rh-based catalysts are the most promising metals for this reaction owing to providing good yields of the desired olefinic intermediates. For Pd-based catalysts, the high yields of the intermediate cyclic alkenes were lower than what was observed for the industrial Pd/C catalyst. This difference was tentatively attributed to a greater rate of isomerisation over this catalyst, which was promoted by larger particles of Pd observed in the XRD pattern for this catalyst. For Rh-based catalysts, the yields of cyclic alkene were lower than what could be achieved over Pd catalysts, however provided a TOF an order of magnitude higher. The selectivity to cyclic olefins of the Rh/GNP catalyst was also shown to improve upon calcination of the reduced catalyst. This suggests that further improvements may be obtained by further optimisation of the structure of this catalyst whilst offering a much higher productivity of desired product. It should be noted that whilst the other metals produce varying amounts of the desired alkene products, a mechanistic analysis of the yield *versus* conversion plots revealed Ru, Ir, and Pt-based catalysts proceed predominantly *via* a direct hydrogenation pathway. This means that these catalysts are probably unsuitable for this transformation and may serve as a foundation for other partial reduction of aromatic reactions, such as the partial hydrogenation of benzene.

There is a considerable room for improvement in a number of aspects relating to this preliminary study. The materials screened were not characterised extensively, so this must be addressed. This could also help identify the beneficial effect of calcination in terms of both catalytic activity and cyclic olefin yield, which may aid future catalyst development. In addition, it would be highly advantageous to discern how each metal surface controls which

pathway is followed in the course of the reduction, which could enable further improvements in yield.

5.5 References

- [1] O. Mitsui and Y. Fukuoka, *Process for producing a cycloolefin*, US4734536, Jul. 1987.
- [2] M. Konishi and H. Nagahara, *Process for producing cycloolefins*, US4734536, Mar. 1986.
- [3] H. Nagahara, M. Ono, M. Konishi and Y. Fukuoka, *Appl. Surf. Sci.*, 1997, **121-122**, 448–451.
- [4] E. Elemensov, P. Zanolina, B. Zhanabaev and B. Utelbaev, *Zhurnal Fiz. Khimii*, 1988, **62**, 2515–2517.
- [5] E. Elemensov, P. Zanolina, B. Zhanabaev and B. Utelbaev, *Russ. J. Phys. Chem.*, 1988, **62**, 1304–1308.
- [6] R. S. Suppino, R. Landers and A. J. G. Cobo, *Appl. Catal. A Gen.*, 2016, **525**, 41–49.
- [7] W. C. Drinkard, *Selective hydrogenation of aromatic hydrocarbons to cycloolefins*, US3767720, Oct. 1972.
- [8] F. Hartog and P. Zwietering, *J. Catal.*, 1963, **2**, 79–81.
- [9] B. van de Graaf, H. van Bekkum and B. M. Wepster, *Recl. des Trav. Chim. des Pays-Bas*, 1968, **87**, 777–785.
- [10] H. van Bekkum, H. M. A. Buurmans, G. van Minnen-Pathuis and B. M. Wepster, *Recl. des Trav. Chim. des Pays-Bas*, 2010, **88**, 779–794.
- [11] S. Siegel and N. Garti, in *Catalysis in Organic Synthesis*, Academic Press, 1977, pp. 9–23.
- [12] S. Siegel, J. Outlaw Jr and N. Garti, *J. Catal.*, 1979, **58**, 370–382.
- [13] V. S. Ranade, G. Consiglio and R. Prins, *J. Org. Chem.*, 1999, 8862–8867.
- [14] V. S. Ranade, G. Consiglio and R. Prins, *J. Org. Chem.*, 2000, **65**, 1132–1138.
- [15] J. B. Hall, L. K. Lala, M. G. J. Beets and T. W. I., *Bicyclic compounds and processes for making and using the same*, US3927083, Dec. 1975.
- [16] A. W. Weitkamp, *J. Catal.*, 1966, **6**, 431–457.

- [17] J. B. Hall, *Indane derivatives*, US3647826, Mar. 1972.
- [18] B. Li, X. Lichun and G. Yuncui, *Method for preparing polymethyl substituted tetrahydroindane by selective hydrogenation of polymethyl substituted indane*, CN1117037A, Feb. 1996.
- [19] M. Sankar, Q. He, M. Morad, J. Pritchard, S. J. Freakley, J. K. Edwards, S. H. Taylor, D. J. Morgan, A. F. Carley, D. W. Knight, C. J. Kiely and G. J. Hutchings, *ACS Nano*, 2012, **6**, 6600–6613.
- [20] J. M. M. Tengco, Y. K. Lugo-José, J. R. Monnier and J. R. Regalbuto, *Catal. Today*, 2015, **246**, 9–14.
- [21] R. Banerjee and J. R. Regalbuto, *Appl. Catal. A Gen.*, 2020, **595**, 117504.
- [22] N. Sugiyama and Y. Shikamori, *J. Anal. At. Spectrom.*, 2015, **30**, 2481–2487.
- [23] S. Nie, A. L. Walter, N. C. Bartelt, E. Starodub, A. Bostwick, E. Rotenberg and K. F. McCarty, *ACS Nano*, 2011, **5**, 2298–2306.
- [24] Y. Xu, H. Cao, Y. Xue, B. Li and W. Cai, *Nanomaterials*, 2018, **8**, 942.
- [25] M. Cai, D. Thorpe, D. H. Adamson and H. C. Schniepp, *J. Mater. Chem.*, 2012, **22**, 24992.
- [26] A. G. Shard, *Surf. Interface Anal.*, 2014, **46**, 175–185.
- [27] J. Rouquerol, P. Llewellyn and F. Rouquerol, in *Stud. Surf. Sci. Catal.*, 2007, vol. 144, pp. 49–56.
- [28] M. Thommes, K. Kaneko, A. V. Neimark, J. P. Olivier, F. Rodriguez-Reinoso, J. Rouquerol and K. S. Sing, *Pure Appl. Chem.*, 2015, **87**, 1052–1069.
- [29] C. H. Bartholemew and R. J. Farrauto, *Fundamentals of Industrial Catalytic Processes*, John Wiley & Sons, Inc., Hoboken, New Jersey, 2nd edn., 2005, pp. 147–148.
- [30] S. J. Freakley, J. Ruiz-Esquius and D. J. Morgan, *Surf. Interface Anal.*, 2017, **49**, 794–799.
- [31] V. Uvarov and I. Popov, *CrystEngComm*, 2015, **17**, 8300–8306.
- [32] R. Burch, in *Catalysis*, ed. G. C. Bond and G. Webb, Royal Society of Chemistry, Cambridge, 1985, vol. 7, pp. 149–196.
- [33] D. A. Cadenhead and N. G. Masse, *J. Phys. Chem.*, 1966, **70**, 3558–3566.
- [34] C. A. Leon and M. Albert Vannice, *Appl. Catal.*, 1991, **69**, 305–321.

- [35] C. U. Odenbrand and S. T. Lundin, *J. Chem. Technol. Biotechnol.*, 1980, **30**, 677–687.
- [36] S. R. Konuspayev, M. Schaimardan and D. Y. Murzin, *Res. Chem. Intermed.*, 2009, **35**, 1–11.
- [37] J. Yoon and M. A. Vannice, *J. Catal.*, 1983, **82**, 457–468.
- [38] U. K. Singh and M. A. Vannice, *AIChE J.*, 1999, **45**, 1059–1071.
- [39] H. Kubicka, *J. Catal.*, 1968, **12**, 223–237.
- [40] A. Amano and G. Parravano, *Adv. Catal.*, 1957, **9**, 716–726.
- [41] P. Mériaudeau, O. H. Ellestad, M. Dufaux and C. Naccache, *J. Catal.*, 1982, **75**, 243–250.
- [42] Y. I. Derbentsev, Z. Paál and P. Tétényi, *Zeitschrift fur Phys. Chemie*, 1972, **80**, 51–62.
- [43] P. Tétényi and Z. Paál, *Zeitschrift fur Phys. Chemie*, 1972, **80**, 63–70.
- [44] J. R. Cozort, J. F. Outlaw, A. Hawkins and S. Siegel, *J. Org. Chem.*, 1983, **48**, 4190–4197.
- [45] J. F. Outlaw, J. R. Cozort, N. Garti and S. Siegel, *J. Org. Chem.*, 1983, **48**, 4186–4190.
- [46] G. C. Bond, *Metal-catalysed reactions of hydrocarbons*, Springer, 2006.
- [47] A. Borodziński and G. C. Bond, 2008, **50**, 379–469.
- [48] K. Li, R. Qin, K. Liu, W. Zhou, N. Liu, Y. Zhang, S. Liu, J. Chen, G. Fu and N. Zheng, *ACS Appl. Mater. Interfaces*, 2021, **13**, 52193–52201.
- [49] G. C. Bond, *Appl. Catal. A Gen.*, 1997, **149**, 3–25.
- [50] F. Zaera, *ACS Catal.*, 2017, **7**, 4947–4967.
- [51] P. C. Aben, H. van der Eijk and J. M. Oelderik, in *Proceedings of the Fifth International Congress in Catalysis Miami Beach, Florida*, ed. J. W. Hightower, Amsterdam: North-Holland, New York, 1973, vol. 4, pp. 717–728.
- [52] A. F. Flores, R. L. Burwell and J. B. Butt, *J. Chem. Soc. Faraday Trans.*, 1992, **88**, 1191.
- [53] O. A. Yakovina and A. S. Lisitsyn, *Langmuir*, 2016, **32**, 12013–12021.
- [54] U. Jung, A. Elsen, Y. Li, J. G. Smith, M. W. Small, E. A. Stach, A. I. Frenkel and R. G. Nuzzo, *ACS Catal.*, 2015, **5**, 1539–1551.
- [55] M. Che and C. O. Bennett, *Adv. Catal.*, 1989, **36**, 55–172.

- [56] *NIST X-ray Photoelectron Spectroscopy Database*, <https://srdata.nist.gov/xps/Default.aspx>.
- [57] P. R. Davies and D. J. Morgan, *J. Vac. Sci. Technol. A*, 2020, **38**, 033204.
- [58] R. van Hardeveld and F. Hartog, 1972, **22**, 75–113.
- [59] M. K. Sabbe, G. Canduela-Rodriguez, J. F. Joly, M. F. Reyniers and G. B. Marin, *Catal. Sci. Technol.*, 2017, **7**, 5267–5283.
- [60] M. K. Sabbe, G. Canduela-Rodriguez, M. F. Reyniers and G. B. Marin, *J. Catal.*, 2015, **330**, 406–422.
- [61] C. Fan, Y. A. Zhu, X. G. Zhou and Z. P. Liu, *Catal. Today*, 2011, **160**, 234–241.
- [62] M. Saeys, M. F. Reyniers, M. Neurock and G. B. Marin, *J. Phys. Chem. B*, 2005, **109**, 2064–2073.
- [63] K. M. Bratlie, L. D. Flores and G. A. Somorjai, *J. Phys. Chem. B*, 2006, **110**, 10051–10057.
- [64] K. M. Bratlie, M. O. Montano, L. D. Flores, M. Paaanen and G. A. Somorjai, *J. Am. Chem. Soc.*, 2006, **128**, 12810–12816.
- [65] K. M. Bratlie, C. J. Kliewer and G. A. Somorjai, *J. Phys. Chem. B*, 2006, **110**, 17925–17930.
- [66] K. M. Bratlie, H. Lee, K. Komvopoulos, P. Yang and G. A. Somorjai, *Nano Lett.*, 2007, **7**, 3097–3101.
- [67] M. Boudart and W. C. Cheng, *J. Catal.*, 1987, **106**, 134–143.
- [68] E. Gonzo and M. Boudart, *J. Catal.*, 1978, **52**, 462–471.
- [69] M. Boudart and D. J. Sajkowski, *Faraday Discuss.*, 1991, **92**, 57.
- [70] R. J. Madon, J. P. O’Connell and M. Boudart, *AIChE J.*, 1978, **24**, 904–911.
- [71] B. E. Koel, D. A. Blank and E. A. Carter, *J. Mol. Catal. A Chem.*, 1998, **131**, 39–53.
- [72] X. Li, M. S. M. Wong and K. H. Lim, *Theor. Chem. Acc.*, 2010, **127**, 401–409.
- [73] Y. Xia, C. Fan, Z. L. Zhou, Y. A. Zhu and X. G. Zhou, *J. Mol. Catal. A Chem.*, 2013, **370**, 44–49.
- [74] H. He, R. J. Meyer, R. M. Rioux and M. J. Janik, *ACS Catal.*, 2021, **11**, 11831–11842.

- [75] H. Ihm, H. M. Ajo, J. M. Gottfried, P. Bera and C. T. Campbell, *J. Phys. Chem. B*, 2004, **108**, 14627–14633.
- [76] O. Lytken, W. Lew, J. J. W. Harris, E. K. Vestergaard, J. M. Gottfried and C. T. Campbell, *J. Am. Chem. Soc.*, 2008, **130**, 10247–10257.
- [77] A. Schießer, P. Hörtz and R. Schäfer, *Surf. Sci.*, 2010, **604**, 2098–2105.
- [78] S. J. Carey, W. Zhao and C. T. Campbell, *Surf. Sci.*, 2018, **676**, 9–16.
- [79] L. Foppa and J. Dupont, *Chem. Soc. Rev.*, 2015, **44**, 1886–1897.
- [80] G. Smith, O. Zahraa, A. Molnar, B. Rihter, M. Khan and W. Brower, *J. Catal.*, 1983, **83**, 238–241.
- [81] R. Sanchez-Delgado, I. Duran, J. Monfort and E. Rodriguez, *J. Mol. Catal.*, 1981, **11**, 193–203.

Chapter 6

Conclusions and future work

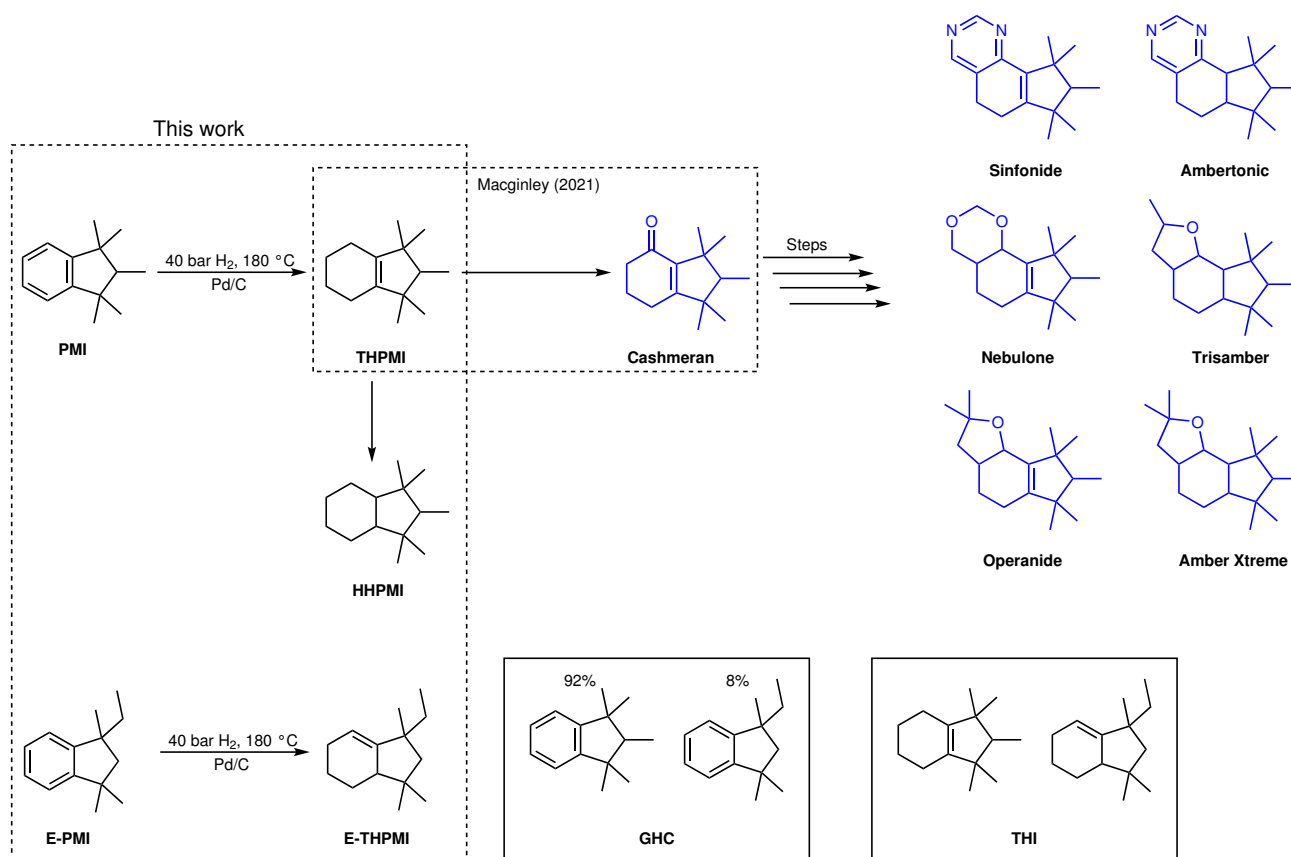
6.1 Introduction

The partial reduction of GHC to tetrahydroindane intermediates is a very important step in synthesis of the Cashmeran family of fragrances (Scheme 6.1). At present, this process is performed solventless in a semi-batch reactor at 180 °C under 40 bar hydrogen pressure over a Pd/C catalyst, yielding between 62 and 65 wt.% of the desired intermediate alkenes.^{1,2} The aim of this thesis was to study this process, and desirably formulate a strategy that would allow for improvements in the yield without lowering reactor throughput. This section will reflect on the work documented in this thesis, whilst also offering some suggestions for future work that could be performed.

6.2 Conclusions and future work relating to work presented in this thesis

6.2.1 Chapter 3: The characterisation of galaxolide hydrocarbon and an industrial product mixture

Chapter 3 initially sought to identify the compounds present in the starting and product materials, as these were industrial feedstocks with multiple compounds present. Two analytical methods were used for this, namely, GC-MS and ¹H NMR spectroscopy. The chromatogram for GHC revealed there were primarily two chemical components present that constituted approximately 98% of the solution. PMI could be readily identified because the NIST database present on the instrument had a reference file for this compound. There was, however, no reference file available for E-PMI, and in order to more confidently assign the fragmentation pattern, an artificial intelligence-generated mass spectrum for this molecule was generated using the method of Wei *et al.*³ This method was successful and was subsequently used



Scheme 6.1: Commercial fragrances obtained from the partial reduction of GHC.

to generate a library of all possible reduction products that was used to identify the major components of a typical industrial product mixture taken from a plant.

However, several low intensity peaks were also observed in the chromatogram that could not be identified using this strategy. The closest spectral matches for these compounds, though the similarity scores were still low, suggests that they are probably side-products of the cycloaddition reaction that forms GHC and their hydrogenated products. It is, nevertheless, imperative that the compounds are identified as understanding the nature of these products may improve the understanding of the synthesis of GHC and also eliminate the possibility that they are side-products of the hydrogenation reaction. As discussed in Chapter 3, structural elucidation of a compound based upon a fragmentation pattern alone is challenging. The artificial intelligence method outlined above afforded a method for generating mass spectra based on an inputted structure and a recently developed program performs the reverse of this: using an experimental mass spectrum to generate possible matches.⁴ Therefore, attempts to identify these compounds using this technique should be performed next.

An interesting finding of the GC-MS study was that the double bond of the intermediate obtained from E-PMI was not located between the bridging carbon atoms as in THPMI but adjacent to this location. To further evidence this assignment, the typical industrial product mixture was examined using ¹H NMR spectroscopy, as vinylic signals would be observed in

the resulting NMR spectrum if this were correct. The ^1H NMR spectrum was unfortunately inconclusive, as the trace impurities discussed previously coupled with the anticipated small intensity of this peak meant an unambiguous assignment was not possible. However, this supported the assignment that no isomers of THPMI were present in significant quantities.

Several physical properties of said materials, which were required to understand transport phenomena, were then reported. Firstly, the densities of GHC and a typical industrial product mixture were determined using a density bottle at atmospheric pressure from room temperature to 100 °C, with this limit being set for safety reasons. In this region, the density of GHC was found to be slightly higher than the industrial product mixture. These data were then fitted to an equation proposed by Francis⁵ to extrapolate the densities to the temperature range used in experiments, *viz.*, 145 to 210 °C. A discussion on possible pressure effects was also provided based on experimental data for decalin and tetralin. It was concluded that the use of high pressures will only have small effects on the liquid phase densities; thus, the densities determined in this work could be used for their intended purpose. If it desired to record these values, then measurement of the density at elevated temperatures and pressures can be performed using a vibrating tube densimeter.⁶

Next, the viscosity of both mixtures was assessed using an Oswald-type viscometer under atmospheric pressure between 25 and 65 °C. The viscosity of the industrial product mixture was determined to be slightly greater than the viscosity of GHC. These data were subsequently modelled using an Arrhenius-type equation, so that again the viscosity in the desired temperature region could be known. The linear regression parameters were then interpreted using absolute rate theory, as this would provide insight into the boiling points, which were also required for mass transfer calculations. This analysis estimated that both compounds have a boiling point of *ca.* 285 °C, which was in good agreement to what was predicted using the Joback group contribution method.

In contrast to density, a greater effect of pressure on viscosity was considered probable when literature data for tetralin and declain was used, though this difference approached negligible differences at higher temperatures. For example, if GHC and the industrial product mixture were considered to behave identically to these model compounds, then the effect of increasing the pressure from the lowest pressure used in this study, 15 bar, to the highest pressure, 85 bar, at 145 °C, the lowest temperature employed, results in a 10% difference in viscosity. However, at the highest temperature studied, 210 °C, the viscosity increase between these pressures is only 5%. Future work for this section should be to examine the viscosities at elevated temperatures and pressures to assess viscosities under experimentally relevant conditions. This could be done, for instance, using the vibrating tube apparatus mentioned above if configured appropriately.

The final section of this chapter concerned the solubility of hydrogen in these mixtures. Unfortunately, no experimental measurements were performed due to limitations of the controller box used for this work and ongoing issues related to the covid-19 pandemic.

Therefore, Henry's constants were therefore calculated using literature data—for benzene, cyclohexane, *m*-xylene, tetralin, decalin, cumene, and mesitylene—in an attempt to gain insight into the solubility behaviour in the liquids used in this work. This study revealed that literature solubility data could be used to potentially predict hydrogen solubility but was sensitive to the manner in which Henry's constant was expressed. For example, a r^2 value of 0.569 was observed when expressing the units of the Henry's constant in $\text{bar dm}^3 \text{mol}^{-1}$. Moreover, compounds with a higher molecular weight displayed greater Henry's constants. In contrast, expressing Henry's constant in bar mol mol^{-1} gave r^2 values of 0.874, with deviations present in the data showing no dependence on molecular structure and most probably attributable to experimental error within the data itself. The equation which provided this fitting was $H_{\text{bar mol mol}^{-1}} = 5.8129 + 689.24/T$, and the calculated Henry's constant converted using known properties of the desired liquid.

It is nonetheless still desirable to record the solubility of hydrogen in these solutions. A convenient experimental technique to accomplish this is to use a gas absorption method, since this has an additional benefit of allowing the volumetric gas–liquid mass-transfer coefficient to be determined.⁷ In this process, a liquid is purged with gas under agitation to form a starting state of known pressure, P_i , at temperature, T . Subsequently, stirring is stopped and the reactor is pressurised to the desired value, P_d . The reactor is then agitated again and the pressure change over time is monitored until no further pressure changes are observed, P_f .

The Henry constant can be calculated using this data by:

$$H = \frac{P_f - P_i}{P_d - P_f} \frac{V_L}{V_G} RT \quad (6.1)$$

where H is the Henry constant for gas g , V_L and V_G are the liquid and gas volumes, respectively and R is the gas constant. The gas volume is readily determined separately through gas displacement.

Mass transfer coefficients are then determined from using the pressure *versus* time data by considering that the concentration of gas in the liquid depends on the pressure drop in the autoclave. After mathematical treatment, this gives:

$$\ln \frac{\alpha P_i - \beta}{\alpha P - \beta} = \alpha \frac{k_L A R T}{V_G} t \quad (6.2)$$

where:

$$\alpha = \frac{1}{H} + \frac{V_G}{V_L R T} \quad (6.3)$$

$$\beta = \frac{P_i - P_l}{H} + \frac{V_G P_D}{V_L R T} \quad (6.4)$$

and P_l is the liquid phase partial pressure, k_L is the liquid side mass transfer coefficient, and A is the interfacial area.

In consequence, the volumetric gas–liquid mass-transfer coefficient is obtained by plotting $\ln((\alpha P_i - \beta)/(\alpha P - \beta))$ against time and multiplying the gradient of the line by $V_G/(\alpha V_L R T)$.

6.2.2 Chapter 4: The effect of some process variables in the partial reduction of galaxolide hydrocarbon to cyclic alkene intermediates

Chapter 4 studied the partial reduction reaction using the current industrial catalyst under a wide range of conditions. This was done to firstly ensure that the optimum conditions were in use at the industrial scale, but also to gain an understanding of the sensitivity of the yield/selectivity to some process variables. It also represents the first study in open literature on the hydrogenation of this substrate.

The chapter began with characterisation of this catalyst. ICP-MS revealed that the weight loading of palladium in the dried as-received catalyst, which was labelled as “Palladium on Carbon, 5 wt.% loading, nominally 50% water”, was 4.2 wt.%. This discrepancy was attributed to the formation of palladium oxide, which if reduced would give a loading of 5 wt.%. The textural properties of the catalyst were subsequently analysed, and as the carbon support exhibited microporosity, the criteria of Rouquerol were used to reliably assess the apparent BET surface area,⁸ which equalled 890 m² g⁻¹. The palladium particle size was then evaluated using TEM, CO chemisorption, and XRD. The first mentioned technique gave a number-average particle size of 2.6±0.9 nm, and harmony was observed when this data was used to calculate the surface-weighted and volume-weighted particles size measured by the other two techniques, respectively.

Initial catalytic testing was conducted, under industrial conditions ($P_{H_2} = 40$ bar, $T = 180$ °C), to compare the performance of the laboratory scale reactor used in this work and the commercial scale reactor. Good alignment between the two reactors was found, as the laboratory scale cyclic alkene yield was within the 62–65 wt.% obtainable on the commercial scale.

Next, the effects of temperature and hydrogen were explored as many selective hydrogenation reactions show a sensitivity to these parameters. Preliminary studies were performed under conditions close to the current industrial conditions, that is between 150 and 210 °C under 40 bar hydrogen pressure and at 180 °C under hydrogen pressures from 20 to 60 bar. It was found that higher yields of the desired products could be obtained when either lower temperature or higher hydrogen pressures were used. In addition, the yield of THPMI was noted as always being greater than that of E-THPMI, which was attributed to the second mentioned molecule being more reactive on account of its lower steric protection.

Because of this sensitivity, the reaction conditions were optimised using the design of experiments methodology, utilising a central composite design between 145 and 195 °C under hydrogen pressures of 15 to 85 bar. Under all conditions the selectivity to THI at the start of the reaction equalled 80%, which was attributed to the remaining 20% being hydrogenated directly to saturated products. The contour plot for each substrate indicated that the reaction went through a maximum as a function of pressure but experiments to verify this model

could not substantiate the claim and it was therefore rejected. This appearance of a maximum was thought to perhaps be a consequence of utilising the maximum observed experimental yields rather than the quadratic model used in the design of experiments optimisation being inappropriate. For this reason, it would be useful to obtain absolute maximum yields by obtaining more data points in the maximum region. In addition, the accuracy of models improves with more data and thus, repeats of already obtained points and studying additional data points would be greatly beneficial for the modelling process.

When the raw data points were examined without the contour plots, the same trend as above was generally observed with the exception that the hydrogen pressure sensitivity appeared to be less pronounced at lower temperatures. There were no satisfactory explanations in literature that could account for this behaviour, as few prior studies have systematically explored the effect of temperature and hydrogen pressure on the intermediate yield in selective aromatic reduction. Those which do map parameters generally find contrasting results; the intermediate alkenes in these reports display a different relationship as hydrogen pressure and temperature are varied.^{9–15} This could indicate that every reaction system is unique, so two overarching concepts were considered: (i) a physical effect, and/or (ii) a catalytic effect.

At first, the physical effect was considered from a thermodynamic perspective, since a catalyst cannot form an amount of product that exceeds what is expected by the equilibrium of a reaction. As no thermodynamic data for the compounds used in this study was not available, they were computed using density-functional theory. To verify this approach, a benchmarking study was performed for benzene-cyclohexene-cyclohexane-hydrogen and indane-hexahydroindane-hydrogen systems with M06-D3, ω B97X-D, and PBE0-D3 functionals with a cc-pVTZ basis set. The M06-D3 functional provided the smallest errors on reaction enthalpies, of less than 10%, whilst the PBE0-D3 functional gave the largest errors, which approached 20%. Errors associated with the free energy of the reaction were typically of several orders of magnitude, which resulted in equilibrium constants being overestimated in many instances.

Errors were greatest for the indane to hexahydroindane reaction and was therefore examined to assess whether this data could be used to calculate equilibrium conversions to an acceptable standard for application in this reaction. Equilibrium conversions calculated using experimentally measured thermochemical values were in agreement with reported equilibrium conversions for the reaction.¹⁶ In contrast, however, equilibrium conversions calculated using DFT computed chemicals resulted in the predicted onset of equilibrium occurring approximately 50 °C higher than what was found experimentally when using the best performing M06-D3 functional. This meant that equilibrium conversion for the PMI-THPMI-hydrogen system of interest was probably overestimated with this method. As a consequence, the computed equilibrium conversions, based on calculations using the M06-D3/cc-pVTZ method, were mirrored at 50, 100, and 150 °C lower temperatures to highlight possible error margins. In all cases, no experimental yields were observed within 50 °C of the calculated equilibrium

conversion and treating data as if it were limited by equilibrium resulted in unrealistic, that is too low, reaction enthalpies. This means that the observed experimental yields were probably not limited by equilibrium. Future efforts should attempt to perform theoretical calculations at higher levels of theory to reduce these errors further, so that a better understanding of the possible role of equilibrium is achieved.

Mass transfer limitations present under reaction conditions were then assessed. Much of the kinetic data obtained suggested that no limitations were present owing to apparent activation energies equating to $50 \pm 10 \text{ kJ mol}^{-1}$, which is significantly greater than the 20 kJ mol^{-1} or less expected if this were the case. This was further evidenced by the Carberry number and Weisz-Prater criterion—which measure extraparticle and intraparticle diffusion, respectively—being below the thresholds required for mass transfer effects to be present. This indicated that the results obtained were not influenced by liquid-solid mass transfer or pore diffusion but did not definitely rule out the presence of gas-liquid diffusion. The probable absence of this mass transfer resistance should be investigated by conventional testing, where the stirring speed and catalyst mass are varied, or by measuring the volumetric mass transfer calculated as outlined above.

Possible catalytic effects were then considered. Firstly, possible changes to the catalysts structure were examined. A comparison of the XRD patterns of the fresh and used catalysts revealed that no changes to the bulk structure of the palladium particle occurred during the reaction. However, the surface area of the used catalyst was measured to be lower than that of the fresh catalyst using CO chemisorption. In Chapter 5, the possible role of carbonaceous species was considered to possibly influence the performance of catalysts in the reaction, therefore it would be interesting to study if the selectivity/activity were to change during catalyst re-use. Furthermore, if this is shown to be an issue, then the calcination procedure outlined in Chapter 5 could perhaps be employed to regenerate the catalyst.

The effect of temperature and pressure were then considered from a surface mechanistic perspective. Temperature effects were explained by hypothesising that a single adsorption site for all hydrocarbon molecules existed, which was based on experimental and theoretical studies for benzene and cyclohexene.^{17,18} Then, using reported adsorption thermodynamics for these compounds, van't Hoff plots were presented, revealing that the surface coverage of benzene decreased more rapidly than it does for cyclohexene with rising temperature, owing to a more exothermic adsorption for the first mentioned molecule. This offered an explanation as to why lower yields were obtained at higher temperatures.

The effects of hydrogen pressure on intermediate yield could not, however, be accounted for with this explanation. As palladium catalysts are notorious for the isomerisation of alkenes,¹⁹ it was proposed that THPMI and E-THPMI isomerised into less sterically protected and more reactive alkenes, as has been observed in low pressure studies during the reduction of 1,3-di-*tert*-butylbenzenes.²⁰ This was evidenced by the ratio of *trans* to *cis* products increasing with decreasing pressure, before approaching constant behaviour and was attributed to the

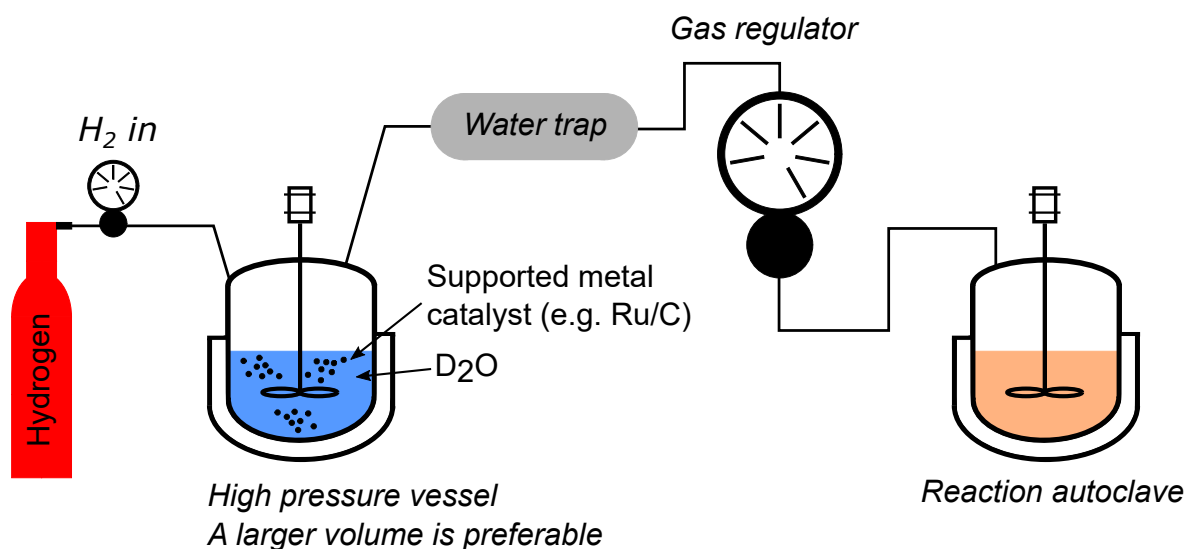


Figure 6.1: Drawing of high-pressure deuterium generator.

hydrogen pressure dependence of the π -allyl surface species required for the formation of isomers. Attempts were made to synthesise isomers of these molecules by heating the reduced industrial Pd/C catalyst and a solution more enriched with THPMI than the industrial product mixture but this instead resulted in a transfer hydrogenation reaction occurring with no isomers detectable by ^1H NMR or gas chromatography. This should be further explored to assess whether isolation of isomeric products is possible. If so, then the reactivity of all isomers should be examined.

Experiments with deuterium *in lieu* of hydrogen were also considered to probe the isomerisation process. The use of cylinders of deuterium obtained from commercial suppliers is problematic though, as cylinders of suitable pressure are too large for use in the laboratory where this work was performed (due to storage space) and of considerable cost. Therefore, a system was devised based on the method outlined by Sajiki *et al.*²¹ (Figure 6.1). It was envisaged that an autoclave was initially used instead of a round-bottom flask and balloon. After generation of deuterium in head space of the autoclave, the gas would be dried to ensure no traces of water were present. This system would be more expensive per mole of deuterium but would allow a greater flexibility of available pressure and alleviate the need to keep additional highly flammable gas cylinders.

The design of experiments data points were also used for kinetic studies. The reaction order for PMI and E-PMI were determined to be equal to zero and negative unity using the integral method. This was interpreted as PMI inhibiting the adsorption of E-PMI, which was supported by the calculation of the relative surface equilibrium constants of the two compounds using the method of Smith and Rader.²² The reaction order for hydrogen on the other hand was observed to increase as a function of temperature, from 0.5 at 150 °C to 1 at 190 °C, which was previously observed by Chou and Vannice in the gas phase hydrogenation of benzene over palladium catalysts.²³ One possible explanation for this behaviour was the

rate determining step, if present, shifting to a later step, as observed in computational studies for benzene hydrogenation,¹⁸ but no such studies were performed in this instance. If such studies were performed, then it could support or oppose this hypothesis.

The apparent activation energies were also observed to generally increase as hydrogen pressure was raised for PMI and E-PMI. The Arrhenius parameters derived from these plots were observed to exhibit compensation phenomena, that is, they fit to a straight line on a Constable plot.²⁴ The gradient was then used to derive an isokinetic temperature, which predicted the reaction would proceed at the same rate at 385 K, though this was never verified. The isokinetic temperature was then interpreted using the selective energy transfer model²⁵ and this hinted that the transition state involved a C-C-C out-of-plane vibration, which was calculated to be the transition state for the rate determining step during a DFT study on benzene hydrogenation over the Ni(111) surface.²⁶

6.2.3 Chapter 5: The effect of metal in the partial reduction of galaxolide hydrocarbon to cycloalkene intermediates

The purpose of the research conducted in Chapter 5 was to evaluate the performance of five carbon-supported platinum, group metals (ruthenium, rhodium, palladium, iridium, and platinum) to assess the relative performance of each metal under various industrially relevant conditions. This was motivated by previous studies, which suggest that palladium should have a lower selectivity to the partial reduction reaction than ruthenium or rhodium.^{27–29} Inspired by the work of the Regalbuto group, who demonstrated that carbon supports can decorate the surface of nanoparticles and lower the gas uptake during chemisorption measurements if not removed,^{30,31} the possibility of the carbon support affecting the catalytic performance was also explored by performing an additional calcination step post-reduction. The labels of red. only and red. + calc. were used to denote that the catalysts were reduced only or reduced and calcined, respectively.

These catalysts were prepared using a modified impregnation method and used a vendor-purchased graphene nanoplatelets as the support. Subsequently, they were characterised by N₂ physisorption, XRD, CO chemisorption, and TGA-MS. The N₂ physisorption measurements revealed the presence of micropores and the Rouquerol method⁸ was used to evaluate the apparent surface areas once more. A decrease in the apparent surface areas occurred after impregnation and heat treatments compared to the blank supports. This was attributed to pore blocking in the microporous region as (i) the shape of the isotherm was largely unchanged at intermediate pressures, and (ii) the XRD patterns of all catalysts did not display any changes to the diffraction peaks relative to the blank support. Further investigations into the nature of the pore blocking could not be performed owing to the vacuum limitations on the instrument used for this analysis. Therefore, future work should be conducted on an instrument capable of micropore analysis.

XRD and CO chemisorption were used to gain an understanding of volume-weighted and surface-weighted particle sizes, respectively, with the latter technique also being used to quantify active sites. The ruthenium, rhodium, and iridium catalysts were prepared from the molecular chloride salts of these metals and displayed no diffraction peaks in the red. only catalysts. The Ru/GNP red. + calc. catalyst exhibited broad peaks attributable to RuO₂ of approximately 4 nm in diameter, whereas only very broad peaks that could not be separated from the baseline were observed for the Rh/GNP and Ir/GNP red. + calc. catalysts. Whether this was a result of particle sizes being below the detection limit of the instrument or due to being amorphous was uncertain, as surface-weighted particle sizes, which are estimated from CO chemisorption, indicated that small particles were present on the Rh/GNP red. + calc. catalyst (3.8 nm), whilst the Ir/GNP red. + calc. had larger particles of 6.2 nm. It should also be noted that no CO uptake was observed for the Ru/GNP red. + calc. catalyst, but this was perhaps due to a combination of the small amount of catalyst used in the experiment, so should be repeated when more sample becomes available. For the Pd/GNP and Pt/GNP catalysts, diffraction peaks were observable in both the red. only and red. + calc. catalysts. In the case of the former metal, the red. only catalyst appeared to show a bimodal distribution of reduced particles, which separated into small oxidised particles and unoxidised reduced particles after calcination. Meanwhile, the Pt/GNP catalyst displayed very large crystallites (~30 nm) of platinum metal in both red. only and red. + calc. catalysts, which was in stark contrast to the 10 nm particles expected from CO chemisorption. Of course, these two techniques will not usually lead to the same value, but such a difference was viewed as most unusual.

The possibility of a carbonaceous species decorating the surface of metal nanoparticle was investigated using TGA-MS. Two samples were studied, *viz.*, the Pd/GNP red. only catalyst, as the dispersion of this catalyst was observed to decrease after oxidative treatment, and the blank GNP support. The evolution of CO₂ as a function of temperature was observed to be approximately equal on both materials at temperatures around 250 °C. This was ascribed to a lack of strong interactions between the carbonaceous material removed and the metal surface. However, the low removal temperature may suggest that this species is relatively volatile and therefore performing a washing step prior to impregnation could have a similar effect to calcination, but this would require further investigations.

The aforementioned techniques generally only provide average values and therefore the particle size distribution is not readily obtained from their use. Therefore, it is vital to perform electron microscopy on these catalysts to gain an understanding of the particle size characteristics. Moreover, this would allow for surface-weighted particle sizes to be calculated and compared to the data obtained from chemisorption studies, providing more insight into the possible carbon decoration effect.

The metal loading of these catalysts was not determined, as the blank support could not be digested using the most powerful method of doing so within the university. This means

the metal loadings used to estimate particle size using CO chemisorption measurements are probably erroneous to some degree. This is a problem commonly encountered with carbon-supported metal catalysts within the group and other approaches need to be considered. One possible strategy to overcome these issues is to place the catalyst in a crucible and expose it to a high temperature calcination step to burn off a majority of the support, so that the metal that remains can be more readily digested and quantified.³²

An initial comparison of the activity of the red. only and red. + calc. catalysts was then performed at 170 °C under 50 bar hydrogen pressure. Significant activity enhancements were observed for all catalyst when the specific rate and TOFs were considered. It was suggested that this was caused by the carbonaceous species breaking up the active ensembles required for aromatic adsorption, or possible particle size effects. Possible future work for these effects will be discussed below.

Kinetic analysis was then performed on the red. + calc. catalysts under 50 bar hydrogen pressure between 160 and 180 °C and at 170 °C at hydrogen pressures in the range of 40 to 60 bar. These data were then used to obtain Arrhenius parameters and reaction orders for hydrogen, respectively. In both instances errors on the obtained values were fairly large and as such, more data points should be acquired to reduce this error. However, this data revealed consistently that the relative activity of these metals was in the order of Pt > Rh > Ir > Pd, with the placing of Ru uncertain due to difficulties with CO chemisorption measurements with this sample. It should be noted, however, that this ordering was not taken as being definitive owing to widely different metal particle sizes between samples. To make such a conclusion, understanding how particle size affects the rate of reaction should be examined, or by preparing catalysts that have very similar, if not identical, particle size distributions.

The selectivity of the catalysts was then studied. The relative selectivity of the metals was sensitive to the thermal treatments used in their synthesis. For the red. only catalysts the selectivity of the metals decreased in the order of Pd > Pt > Rh > Ir > Ru, whereas for the red. + calc. catalysts gave ordering was determined to be Pd > Rh > Pt > Ir > Ru. Furthermore, improvements in selectivity were observed for the Pd/GNP, Rh/GNP, Ir/GNP, and Pt/GNP catalysts, but not for the Ru/GNP catalyst, after calcination. It was also noted that for some catalysts, particularly Rh/GNP, the selectivity increased at low conversions until it approached a constant value.

These changes in selectivity were first considered before the possible differences in the metals were discussed. It was suggested that initial increase in selectivity could be due to the formation of dienes, however, no such compounds were detected during the experiments. As no reference compounds for the dienes that would form from PMI and E-PMI were available, future work should attempt their synthesis to rule out the possibility of overlapping with other compounds on the GC column. The classical Birch reduction method could be used, but this is quite hazardous to perform, owing to the use of condensed ammonia and metallic lithium. Safer alternatives include electrochemical methods³³ or a recently reported technique utilising

ethylenediamine and metallic lithium in THF.³⁴

Other proposals explaining the rise in selectivity and the changes in selectivity after calcination were also forwarded. For example, the possibility of the carbon species, or a coke deposited during the reaction, altering the selectivity profile through blocking more or less sites were discussed. This was not probed further because in the instances where large differences in behaviour were observed, small amounts of catalysts were used to ensure the reactor temperature remained constant. Thus, very little sample remained after each reaction for analysis methods that could detect coke deposition, such as temperature-programmed oxidation. A more advanced autoclave could be useful in this regard, as some models have simultaneous heating and cooling for better thermal stability. Alternatively, the reaction could be repeated enough times to gather enough sample for analysis. Surface reconstruction, which could be investigated to some degree using H₂-TPD³⁵ or by utilising X-ray absorption spectroscopies, leading to differing selectivity behaviour was proposed, but no evidence for this occurring was obtained during these studies. Similarly, possible particle size effects on selectivity were suggested as changes to the type of site and the electronic nature of a particle change with increasing size are possible, but the limited catalyst characterisation provided in this chapter could not substantiate this hypothesis. As stated above, the use of electron microscopy to gain a better understanding of the particle size distribution of the fresh and used catalysts would be greatly beneficial.

The origin of the selectivity behaviour was then considered. For all catalysts examined, the maximum intermediate yield occurred at high substrate conversions. It was reasoned that there must be a direct hydrogenation pathway, where the saturated products form during one residence on the surface due to forming non-isolable surface radicals, with the cyclic olefin intermediates being hydrogenated at a lower rate than the starting aromatic compound. The contribution of the direct pathway was most noticeable on the Ru/GNP catalyst which suggested approximately 5% of intermediate was desorbed with the remaining 95% being hydrogenated directly. At the opposite end of the scale was the Pd/GNP catalysts, which desorbed the majority, *ca.* 80%, of the desired intermediate.

As a result, it was concluded that future work should study palladium- and rhodium-based catalysts. Moreover, despite being more selective, it could be that rhodium-based catalysts are found to be more suitable from an industrial perspective owing to their near order of magnitude activity and only slightly inferior selectivity. For example, the continuous flow system outlined in the introduction—where GHC is reduced in a flow reactor before being separated into starting material, desired intermediate, and saturated product, which is subsequently dehydrogenated back to GHC (Section 1.2.3)³⁶—could be a suitable application of this material if the reaction exotherm is suitably controlled.

The high performance of these catalysts towards the selective reduction reaction could also impact in the partial reduction of benzene. This reaction was discussed extensively in Section 1.4.3.1, where the near sole use of ruthenium catalysts in an unusual tetraphasic

reactor (hydrogen, hydrocarbon, water, catalyst) was discussed.³⁷ This work shows that other platinum group metals can afford a greater selectivity to the partially reduced product obtained from bulky aromatic compounds than ruthenium and therefore should be explored in this optimised reactor system for selective benzene hydrogenation.

Another point of discussion in this chapter was that for other aromatic bulky aromatic substrates, palladium is not very selective for this reaction in comparison with platinum or rhodium when the reduction is performed at lower temperatures. It was suggested that when decreasing the temperature, there may become a point at which the greater surface coverage of the aromatic, which promotes improved reaction yields, is counteracted by the lowering of rate constant for the hydrogenation of the aromatic; meanwhile, the rate constant of the reduction of the tetrahydroindane intermediates is less impacted. In other words, it was proposed that the reaction yield may never reach the theoretical maximum of 80% as dictated by the proposed reaction mechanism. Therefore, this should be borne in mind when studying the reaction at lower temperature. In addition, it would be highly advantageous to have a kinetic model that describes the hydrogenation of these substrates over a wide temperature range.

The intermediate yields obtained over the industrial Pd/C catalyst and the Pd/GNP red. + calc. catalyst employed in this investigation were also compared. It was reported that when tested under the same conditions, the THPMI and E-THPMI were lower when using the Pd/GNP red. + calc. catalyst compared to the industrial catalyst. This could not be attributed to differences in mechanism as the yield at low conversions was found to be approximately 80% over each catalyst. Instead, it was proposed that isomerisation reactions took place to a greater extent when using this catalyst, which was evidenced by the higher *trans/cis* ratio observed during testing of this catalyst. This was hypothesised to be catalysed by the large palladium crystallites that were detected in the Pd/GNP catalyst and not in the industrial Pd/C catalyst. Future work should verify that larger particles promote the isomerisation reactions, as it will permit further rational catalyst design.

The final section questioned why no pressure effects were observed for the other catalysts in this study. It was concluded that under the high hydrogen pressures used during experiments, isomerisation processes over these metals were disfavoured. However, it would be interesting to study whether these catalysts were active in the isomerisation reaction at lower hydrogen pressures.

6.3 Final comments

This thesis documents the first open studies on the partial reduction of GHC to cyclic olefins. The most important finding in this thesis was that the current industrial yield can be improved, simply by lowering the reaction temperature without requiring higher hydrogen pressures, which would require new reactors due to operational limits. For example, a THI yield

of 62.1 wt.% was obtained under the industrial conditions of 180 °C and 40 bar hydrogen pressure; when the temperature is reduced to 150 °C and the pressure is kept constant at the industrial reactor limit, THI yields of 68.5 wt.% were attainable. This was ascribed to a more exothermic adsorption of the aromatic compounds. However, employing a lower temperature results in a significant reduction in hydrogenation rate, owing to the exponential relationship rate shares with temperature. This would therefore limit reactor throughput. Moreover, if this yield enhancement can be extended to even lower temperatures is uncertain because of possible rate constant effects.

The reduced rate at lower temperatures can be offset slightly by using higher hydrogen pressures, since kinetic studies revealed that the rate of GHC hydrogenation increases approximately to the square root of hydrogen pressure. However, this would require new industrial reactors. A more effective solution would be to increase the mass of catalyst (or palladium weight loading if dispersion can be kept constant) as the rate of reaction should be directly proportional to its loading (under mass transfer free conditions). An alternative improvement would be to utilise higher hydrogen pressures at the current reaction temperature as small increments in yield were possible, though the yield appeared to approach a limiting value. This was attributed to the surface coverage of the π -allyl species responsible for the undesirable isomerisation reaction, which leads to the formation of more reactive cyclic alkene, reaching a constant value.

Two other catalyst-based modifications of the current operation should also be considered. Firstly, if an understanding of what promotes the isomerisation reactor, such as particle size, is obtained, then it may afford a catalyst design strategy for an improved palladium catalyst. Secondly, the marginally less selective, but far more active rhodium-based catalyst in a continuous flow reactor within a circular economy reactor system could be considered. This catalyst would significantly increase the possible throughput in that reactor system and perhaps make the energy intensive mode of operation viable from an industrial perspective.

A separate important consideration is that E-PMI consistently yielded less intermediate product than PMI. This was attributed to the partial reduction product of E-PMI being the cyclic alkene where the double bond was located adjacent to the bridging carbons. This is an interesting difference (academically), and theoretical studies on palladium surfaces could afford an explanation. However, it would be favourable from an industrial perspective to synthesise PMI more selectively. A discussion of the patent literature on the synthesis of GHC was provided in the introduction (Section 1.2.2) and it should be recalled that an early study observed that the ratio of PMI to E-PMI was 2 to 1 and independent of the cycloaddition reagents (amylene or 2-methyl-1-butene) and catalyst ($\text{BF}_3 \cdot \text{Et}_2\text{O}$ or H_2SO_4) used.³⁸ Whether this is still the case is uncertain, as few details on any purification steps to give the current PMI to E-PMI ratio found in GHC of 11 to 1 are publicly available. If there is no limit imposed by thermodynamics in the synthesis of these compounds, then shape-selective materials which are suitable catalysts for this cycloaddition reaction should be explored.

Finally, the possible impact of this work should be considered. This is a process that is performed on the kilotonne scale. Any improvements in the industrial process would be highly profitable and perhaps offer a more sustainable synthesis of a precursor used in highly popular commercial products.

6.4 References

- [1] B. Li, X. Lichun and G. Yuncui, *Method for preparing polymethyl substituted tetrahydroindane by selective hydrogenation of polymethyl substituted indane*, CN1117037A, Feb. 1996.
- [2] C. Lopez Cruz, *Private communication*, 2018.
- [3] J. N. Wei, D. Belanger, R. P. Adams and D. Sculley, *ACS Cent. Sci.*, 2019, **5**, 700–708.
- [4] H. Ji, H. Deng, H. Lu and Z. Zhang, *Anal. Chem.*, 2020, **92**, 8649–8653.
- [5] A. Francis, *Ind. Eng. Chem.*, 1957, **49**, 1779–1786.
- [6] D. González-Salgado, J. Troncoso and L. Romani, in *Volume Properties: Liquids, Solutions and Vapours*, Royal Society of Chemistry, Cambridge, 2014, pp. 100–114.
- [7] S. Ledakowicz, H. Nettelhoff and W. D. Deckwer, *Ind. Eng. Chem. Fundam.*, 1984, **23**, 510–512.
- [8] J. Rouquerol, P. Llewellyn and F. Rouquerol, in *Stud. Surf. Sci. Catal.*, 2007, vol. 144, pp. 49–56.
- [9] E. Elemensov, P. Zanolina, B. Zhanabaev and B. Utelbaev, *Zhurnal Fiz. Khimii*, 1988, **62**, 2515–2517.
- [10] E. Elemensov, P. Zanolina, B. Zhanabaev and B. Utelbaev, *Russ. J. Phys. Chem.*, 1988, **62**, 1304–1308.
- [11] C. U. Odenbrand and S. T. Lundin, *J. Chem. Technol. Biotechnol.*, 1980, **30**, 677–687.
- [12] J. Struijk, M. D'Angremond, W. L.-d. Regt and J. Scholten, *Appl. Catal. A Gen.*, 1992, **83**, 263–295.
- [13] J. Ning, J. Xu, J. Liu and F. Lu, *Catal. Letters*, 2006, **109**, 175–180.
- [14] H. Spod, M. Lucas and P. Claus, *ChemCatChem*, 2016, **8**, 2659–2666.
- [15] J. Wang, Y. Wang, S. Xie, M. Qiao, H. Li and K. Fan, *Appl. Catal. A Gen.*, 2004, **272**, 29–36.

- [16] C. G. Frye and A. W. Weitkamp, *J. Chem. Eng. Data*, 1969, **14**, 372–376.
- [17] E. Gonzo and M. Boudart, *J. Catal.*, 1978, **52**, 462–471.
- [18] M. K. Sabbe, G. Canduela-Rodriguez, J. F. Joly, M. F. Reyniers and G. B. Marin, *Catal. Sci. Technol.*, 2017, **7**, 5267–5283.
- [19] G. C. Bond, *Metal-catalysed reactions of hydrocarbons*, Springer, 2006.
- [20] S. Siegel, J. Outlaw Jr and N. Garti, *J. Catal.*, 1979, **58**, 370–382.
- [21] H. Sajiki, T. Kurita, H. Esaki, F. Aoki, T. Maegawa and K. Hirota, *Org. Lett.*, 2004, **6**, 3521–3523.
- [22] C. P. Rader and H. A. Smith, *J. Am. Chem. Soc.*, 1962, **84**, 1443–1449.
- [23] P. Chou and M. A. Vannice, *J. Catal.*, 1987, **107**, 129–139.
- [24] G. C. Bond, M. A. Keane, H. Kral and J. A. Lercher, *Catal. Rev.*, 2000, **42**, 323–383.
- [25] R. Larsson, *J. Mol. Catal.*, 1989, **55**, 70–83.
- [26] F. Mittendorfer and J. Hafner, *Surf. Sci.*, 2001, **472**, 133–153.
- [27] F. Hartog and P. Zwietering, *J. Catal.*, 1963, **2**, 79–81.
- [28] B. van de Graaf, H. van Bekkum and B. M. Wepster, *Recl. des Trav. Chim. des Pays-Bas*, 1968, **87**, 777–785.
- [29] H. van Bekkum, H. M. A. Buurmans, G. van Minnen-Pathuis and B. M. Wepster, *Recl. des Trav. Chim. des Pays-Bas*, 2010, **88**, 779–794.
- [30] J. M. M. Tengco, Y. K. Lugo-José, J. R. Monnier and J. R. Regalbuto, *Catal. Today*, 2015, **246**, 9–14.
- [31] R. Banerjee and J. R. Regalbuto, *Appl. Catal. A Gen.*, 2020, **595**, 117504.
- [32] C. Ge, F. Lao, W. Li, Y. Li, C. Chen, Y. Qiu, X. Mao, B. Li, Z. Chai and Y. Zhao, *Anal. Chem.*, 2008, **80**, 9426–9434.
- [33] B. K. Peters, K. X. Rodriguez, S. H. Reisberg, S. B. Beil, D. P. Hickey, Y. Kawamata, M. Collins, J. Starr, L. Chen, S. Udyavara, K. Klunder, T. J. Gorey, S. L. Anderson, M. Neurock, S. D. Minteer and P. S. Baran, *Science*, 2019, **363**, 838–845.
- [34] J. Burrows, S. Kamo and K. Koide, *Science*, 2021, **374**, 741–746.
- [35] O. A. Yakovina and A. S. Lisitsyn, *Langmuir*, 2016, **32**, 12013–12021.

- [36] S. Tadepalli, G. K. Tampy and A. P. Narula, *Circular economy methods of preparing unsaturated compounds*, US10435345B2, Oct. 2019.
- [37] L. Foppa and J. Dupont, *Chem. Soc. Rev.*, 2015, **44**, 1886–1897.
- [38] D. B. Spoelstra, S. H. Weber and R. J. C. Kleipool, *Recl. des Trav. Chim. des Pays-Bas*, 1963, **82**, 1100–1106.